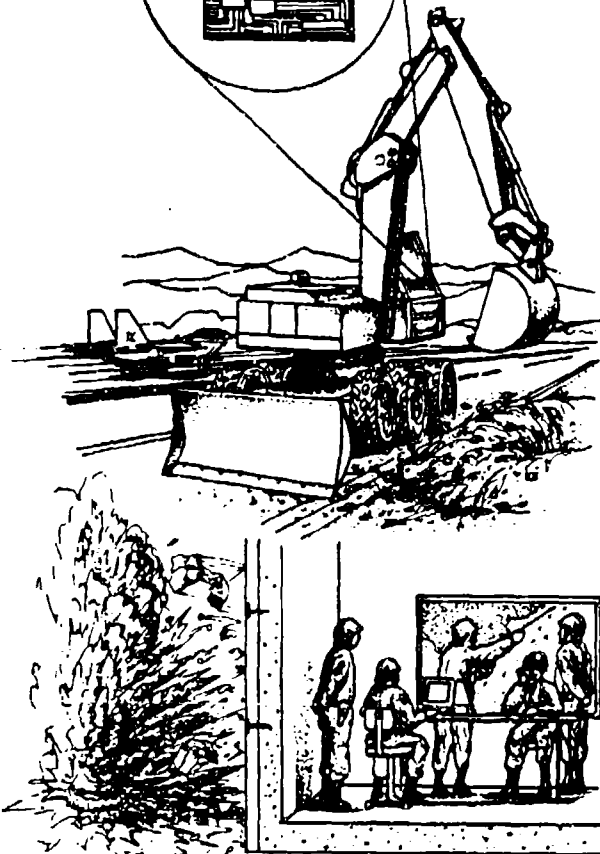
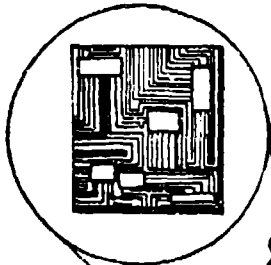




AD-A270 194



ESL-TR-92-46



# CENTRIFUGE MODELING OF EXPLOSION-INDUCED CRATERS IN UNSATURATED SAND

K.C. BROWNELL, W.A. CHARLIE

COLORADO STATE UNIVERSITY  
FORT COLLINS, COLORADO 80523

NOVEMBER 1992

FINAL REPORT

MAY 1991 - AUGUST 1991

APPROVED FOR PUBLIC RELEASE:  
DISTRIBUTION UNLIMITED



93-23187



ENGINEERING RESEARCH DIVISION  
Air Force Civil Engineering Support Agency  
Civil Engineering Laboratory  
Tyndall Air Force Base, Florida 32403



93 10 4 008

**NOTICE**

**PLEASE DO NOT REQUEST COPIES OF THIS REPORT FROM HQ AFCESA/RA (AIR FORCE CIVIL ENGINEERING SUPPORT AGENCY). ADDITIONAL COPIES MAY BE PURCHASED FROM:**

**NATIONAL TECHNICAL INFORMATION SERVICE  
5285 PORT ROYAL ROAD  
SPRINGFIELD, VIRGINIA 22161**

**FEDERAL GOVERNMENT AGENCIES AND THEIR CONTRACTORS REGISTERED WITH DEFENSE TECHNICAL INFORMATION CENTER SHOULD DIRECT REQUESTS FOR COPIES OF THIS REPORT TO:**

**DEFENSE TECHNICAL INFORMATION CENTER  
CAMERON STATION  
ALEXANDRIA, VIRGINIA 22314**

# REPORT DOCUMENTATION PAGE

Form Approved  
OMB No. 0704-0188

Public reporting burden for this collection of information is estimated to average 1 hour per response, including the time for reviewing instructions, searching existing data sources, gathering and maintaining the data needed, and completing and reviewing the collection of information. Send comments regarding this burden estimate or any other aspect of this collection of information, including suggestions for reducing this burden, to Washington Headquarters Services, Directorate for Information Operations and Reports, 1215 Jefferson Davis Highway, Suite 1204, Arlington, VA 22202-4302, and to the Office of Management and Budget, Paperwork Reduction Project (0704-0188), Washington, DC 20503.

1. AGENCY USE ONLY (Leave blank)	2. REPORT DATE Nov 92	3. REPORT TYPE AND DATES COVERED
----------------------------------	--------------------------	----------------------------------

4. TITLE AND SUBTITLE Centrifuge Modeling of Explosion-Induced Craters in Unsaturated Sand	5. FUNDING NUMBERS F08635-90-C-0306
---	--

6. AUTHOR(S) Kenneth C. Brownell, Wayne A. Charlie	
---	--

7. PERFORMING ORGANIZATION NAME(S) AND ADDRESS(ES) Colorado State University Fort Collins, Colorado 80523	8. PERFORMING ORGANIZATION REPORT NUMBER
---	--

9. SPONSORING / MONITORING AGENCY NAME(S) AND ADDRESS(ES) Air Base Survivability Branch HQ Air Force Civil Engineering Support Agency 139 Barnes Drive Tyndall AFB FL 32403-5319	10. SPONSORING / MONITORING AGENCY REPORT NUMBER
--	--

11. SUPPLEMENTARY NOTES This report was conducted under the Air Force Palace Knight Program
--

12a. DISTRIBUTION AVAILABILITY STATEMENT Approved for Public Release Distribution Unlimited	12b. DISTRIBUTION CODE
---	------------------------

13. ABSTRACT (Maximum 200 words) Craters, induced by explosive detonations, were modeled in dry and partially saturated sand in a geotechnical centrifuge. The apparent dimensions of the explosion-induced craters are analyzed as dimensional terms and dimensionless pi terms. Analysis of dimensional terms through a comparison of yield exponents shows that the scaling laws for apparent crater dimensions are the same for dry and partially saturated sand. Analysis of the dimensionless pi terms derived by Schmidt and Holsapple (1977) for buried charges, shows apparent crater volume ( $\pi_1 = \pi_v$ ) and depth ( $\pi_1 = \pi_d$ ) do not follow the same scaling laws in partially saturated sand. Normalized (divided by the cube root of the charge mass) apparent crater diameter and depth data fit the best-fit prediction curves for sand derived by the U.S. Army Engineer Waterways Experiment Station. However, the apparent crater diameter data do not fall within the range from dry to wet sand predicted by the Air Force Protective Construction Design Manual. Scaled apparent crater dimensions of crater volume, radius, and depth increase at a point between 0 and 20 percent compaction saturation. Between 20 to 70 percent the influence of compaction saturation on apparent crater dimensions appears to remain constant.
--

14. SUBJECT TERMS Centrifuge, Centrifuge Modeling, Sand, Unsaturated Sand, Explosive Modeling, Explosions, Craters, Cratering	15. NUMBER OF PAGES 236
--	----------------------------

	16. PRICE CODE
--	----------------

17. SECURITY CLASSIFICATION OF REPORT Unclassified	18. SECURITY CLASSIFICATION OF THIS PAGE Unclassified	19. SECURITY CLASSIFICATION OF ABSTRACT Unclassified	20. LIMITATION OF ABSTRACT UL
---	--	---	----------------------------------

PREFACE

This report was submitted as a thesis to Colorado State University. Funding was provided by the U.S. Air Force Palace Knight program and by the U.S. Air Force contract (No. FO8635-90-C-0306) between HQ Air Force Civil Engineering Support Agency/Air Force Air Base Survivability, Tyndall AFB, Florida 32403-5319 and Colorado State University.

This report is being published in its original format by this laboratory because of its interest to the worldwide scientific and engineering community. This report covers work performed between May 1991 and August 1991.

This report has been reviewed by the Public Affairs Officer (PA) and is releasable to the National Technical Information Service (NTIS). At NTIS, it will be available to the general public, including foreign nationals.

This report has been reviewed and is approved for publication.

*Kenneth C. Brownell*  
KENNETH C. BROWNELL  
Project Officer

*Felix T. Uhlík*  
FELIX T. UHLIK, Lt Col, USAF  
Chief, Engineering Research  
Division

*William S. Strickland*  
WILLIAM S. STRICKLAND  
Chief, Air Base  
Survivability Branch

*Frank P. Gallagher III*  
FRANK P. GALLAGHER III, Col, USAF  
Director, Engineering Support  
Agency

1990 QUALITY INSPECTION

Accession For	
NTIS	<input checked="" type="checkbox"/>
DTIC TAB	<input type="checkbox"/>
Unannounced	<input type="checkbox"/>
Justification	
By	
Distribution/	
Availability Codes	
Dist	Avail and/or Special
A-1	

## TABLE OF CONTENTS

Section	Title	Page
I.	INTRODUCTION . . . . .	1
	A. Objective . . . . .	1
	B. Background . . . . .	2
	C. Significance . . . . .	3
	D. Approach . . . . .	4
II.	EXPLOSION-INDUCED CRATERING . . . . .	6
	A. Cratering Dimensions . . . . .	6
	B. Cratering Terminology . . . . .	8
	C. Cratering Mechanisms . . . . .	9
	D. Historical Cratering Results at 1 G . . . . .	10
III.	CENTRIFUGE MODELING . . . . .	15
	A. Principle of Centrifuge Operation . . . . .	15
	B. Assumptions in Centrifuge Modeling . . . . .	17
	C. Sources of Error in Centrifuge Modeling . . . . .	21
	D. Modeling of Models . . . . .	27
IV.	CRATERING ON THE CENTRIFUGE . . . . .	28
	A. Dimensional Analysis - Pi Terms . . . . .	28
	1. Surface Detonations . . . . .	28
	2. Material Strength Model . . . . .	34
	3. Subsurface Detonations . . . . .	39
	B. Slope Stability in Cratering . . . . .	40
	C. Moisture Content Effect on Crater Dimensions . . . . .	41
	D. Scale Effect in Cratering . . . . .	41
	E. Soil Density Effect on Crater Volume . . . . .	41
	F. Coriolis Effect on Crater Shape . . . . .	42

TABLE OF CONTENTS  
(CONTINUED)

Section	Title	Page
V.	MODEL DESCRIPTION . . . . .	48
	A. Explosives . . . . .	48
	B. Test Matrices . . . . .	51
	1. Constant Normalized Depth of Burial . . . . .	51
	2. Varied Normalized Depth of Burial . . . . .	55
VI.	SPECIMEN PREPARATION . . . . .	57
	A. Soil Description . . . . .	57
	B. Saturation Procedure . . . . .	60
	C. Placement Methods . . . . .	60
	1. Vibration . . . . .	62
	2. Pluviation . . . . .	62
VII.	TEST PROCEDURES . . . . .	67
	A. Centrifuge Facility . . . . .	67
	B. Detonator Placement . . . . .	69
	C. Centrifuge Operation . . . . .	71
	D. Apparent Crater Measurement . . . . .	71
	1. Inside Diameter and Depth . . . . .	71
	2. Volume . . . . .	72
	E. Moisture Content Measurement . . . . .	72
VIII.	RESULTS AND ANALYSIS . . . . .	75
	A. Scaled-Crater Dimension versus Scaled Explosive Mass . . . . .	75
	B. Material Strength Model . . . . .	87
	C. Crater Dimensions versus Depth of Burial . . . . .	91
	D. Desaturation Analysis . . . . .	100
	E. Crater Dimension versus Saturation at Compaction . . . . .	106
	F. Aspect Ratio versus Saturation at Compaction . . . . .	110
	G. Coriolis Effects on Crater Shape . . . . .	121

TABLE OF CONTENTS  
(CONCLUDED)

Section	Title	Page
IX.	CONCLUSIONS AND RECOMMENDATIONS . . . . .	128
	A. Conclusions . . . . .	128
	1. Scaling Laws for Dry and Moist Sand . . . . .	128
	2. Depth of Burial Effect . . . . .	131
	3. Desaturation during Centrifugation . . . . .	132
	4. Saturation Versus Crater Dimensions . . . . .	132
	5. Effect of Moisture on Apparent Crater Aspect Ratio . . . . .	133
	6. Coriolis Effects on Crater Shape . . . . .	133
	B. Recommendations . . . . .	134
	LIST OF REFERENCES . . . . .	136
	APPENDIX	
	A. Measured, Scaled, And Normalized Apparent Crater Data . . . . .	141
	B. Crater Mold Photographs . . . . .	166
	C. Moisture Content-Saturation Conversion Curve for Tyndall Beach Sand . . . . .	179
	D. Moisture Content Data . . . . .	181
	E. Water Retention (Desaturation) Curve . . . . .	185
	F. Actual Dry Density of Pluviated Specimens . . . . .	187
	G. Apparent Crater Measurement Procedure . . . . .	189
	H. Crater Mold Profile Measurement Procedure . . . . .	197
	I. Apparent Crater Dimensions Versus Charge Mass, TNT Equivalent, (Figures 8.1 - 8.6) Without 1 G Data . . . . .	200
	J. Torque Placed on the Soil Mass of the Crater by the Coriolis Acceleration . . . . .	208
	K. Centrifuge Crater Rotation Versus G-Level . . . . .	211
	L. Variation of Normalized Apparent Crater Dimensions with G-Level . . . . .	213

LIST OF TABLES

Table	Title	Page
3.1	SCALING RELATIONS FOR CENTRIFUGE MODELING . . . . .	18
4.1	CENTRIFUGE CRATERING PI TERMS . . . . .	29
5.1	STANDARD AND MODIFIED RP-83 DETONATORS . . . . .	49
5.2	TEST MATRICES FOR THE CURRENT RESEARCH:	
	a) CONSTANT NORMALIZED DOB TEST SERIES . . . . .	52
	b) 1-G TEST SERIES . . . . .	54
	c) RANGE OF DOB TEST SERIES . . . . .	56
6.1	SOIL PARAMETERS FOR TYNDALL BEACH SAND . . . . .	57
8.1	CENTRIFUGE TEST SPECIFICATIONS . . . . .	76
8.2	YIELD COMPONENTS FOR CHARGE MASS, W . . . . .	84
8.3	YIELD EXPONENTS REPORTED BY WES (ROOKE ET AL., 1974) . . . . .	86
8.4	CORRELATION COEFFICIENTS FOR THE CURRENT RESEARCH AT ALL G-LEVELS . . . . .	86
8.5	AVERAGE ASPECT RATIO AND APPARENT CRATER WALL ANGLE AS TAKEN FROM FIGURE 8.21 . . . . .	112
8.6	THE DECREASE IN ACTUAL APPARENT CRATER DIMENSIONS DUE TO CENTRIFUGATION AT 57 G (179.5 RPM) PRIOR TO TESTING AT 1 G . . . . .	121
8.7	APPARENT CRATER ASYMMETRY DUE TO THE CORIOLIS ACCELERATION . . . . .	125
9.1	YIELD EXPONENTS FOR CHARGE MASS, W . . . . .	129

## LIST OF FIGURES

Figure	Title	Page
2.1	Half-Crater Profile Taken about a Vertical Centerline . . . . .	7
3.1	Centrifuge Schematic: (a) Centrifuge Components; (b) Payload Platform Rotation During Centrifuge Operation and Force Directions . . . . .	16
3.2	Variation of Centripetal Acceleration within the Specimen, Side View (NTS) . . . . .	24
3.3	Model Stress Error with Depth (Joseph et al., 1988) . . . . .	25
4.1	Agreement of Cratering Data Between Schmidt and Holsapple (1978) and Piekutowski (1974, 1975) . . . . .	32
4.2	Cratering Efficiency Versus Gravity-Scaled Yield for Various Soil-Explosive Combinations (Holsapple et al., 1978) . . . . .	35
4.3	General Form of the Material Strength Model for Crater Volume (Holsapple et al., 1978) . . . . .	37
4.4	Compass Directions Assigned to the Centrifuge Specimen as Pictured from the Center of Rotation . . . . .	43
4.5	Soil Particle Trajectories Assumed by Steedman (1990) . . . . .	45
4.6	Scaled Crater Profiles Measured by Gill and Kuennen (1991) . . . . .	46
5.1	Reynolds Industries RP-83 Detonator . . . . .	50
6.1	Particle Size Distribution for Tyndall Beach Sand . . . . .	58
6.2	Photograph Showing the Characteristic Shape of Tyndall Beach Sand . . . . .	59

LIST OF FIGURES  
(CONTINUED)

Figure	Title	Page
6.3	Chiyoda Flexible Wall Mixer . . . . .	61
6.4	FMC Corporation Syntron Magnetic Vibrator . . . . .	63
6.5	Tyndall Air Force Base Pluviator . . . . .	64
6.6	Pluviator Schematic (Fragaszy and Taylor, 1989) . . . . .	65
7.1	Miletus Video Camera and Pacific Data Acquisition System Mounted on the Centrifuge . . . . .	68
7.2	Detonator Placement Guide . . . . .	70
7.3	Sampling Locations of the Moisture Content Analysis, Top View . . . . .	74
8.1	Scaled Apparent Crater Volume Versus Scaled Explosive Mass, TNT Equivalent (Compared to Cratering Tests in Dry Ottawa Sand) . . . . .	77
8.2	Scaled Apparent Crater Radius Versus Scaled Explosive Mass, TNT Equivalent (Compared to Cratering Tests in Dry Ottawa Sand) . . . . .	78
8.3	Scaled Apparent Crater Depth Versus Scaled Explosive Mass, TNT Equivalent (Compared to Cratering Tests in Dry Ottawa Sand) . . . . .	79
8.4	Scaled Apparent Crater Volume Versus Scaled Explosive Mass, TNT Equivalent (Compared to Cratering Tests in Moist Desert Alluvium) . . . . .	81
8.5	Scaled Apparent Crater Radius Versus Scaled Explosive Mass, TNT Equivalent (Compared to Cratering Tests in Moist Desert Alluvium) . . . . .	82
8.6	Scaled Apparent Crater Depth Versus Scaled Explosive Mass, TNT Equivalent (Compared to Cratering Tests in Moist Desert Alluvium) . . . . .	83
8.7	Cratering Efficiency ( $\pi_v$ ) Versus Gravity-Scaled Yield ( $\pi_2$ ), Tyndall Beach Sand: a) S = 0%, 20; b) S = 0%, 60%. . . . .	83

LIST OF FIGURES  
(CONTINUED)

Figure	Title	Page
8.8	Apparent Crater Dimensions Versus Gravity-Scaled Yield ( $\pi_2$ ), Tyndall Beach Sand, $S = 0\%$ , $20\%$ , $60\%$ : a) Depth $\pi_d$ ; b) Radius $\pi_r$ . . . . .	89
8.9	Normalized Apparent Inside Crater Diameter Compared to the U.S. Army Engineer Waterways Experiment Station Prediction Curve. (Strange, 1961) . . . . .	92
8.10	Normalized Apparent Crater Depth Compared to the U.S. Army Engineer Waterways Experiment Station Prediction Curve. (Strange, 1961) . . . . .	93
8.11	Normalized Apparent Crater Depth and Inside Diameter Compared to the Air Force Protective Construction Design Manual Prediction Curves . . . . .	94
8.12	Normalized Apparent Crater Depth and Inside Diameter Compared to the Apparent and True Crater Dimensions Predicted by the Air Force Conventional Weapons Computer Program (CONWEP): a) Dry Sand; b) Partially Saturated Sand . . . . .	96
8.13	Crater Profile Comparison Between the Centrifuge Apparent Crater and the Crater Generated by the CONWEP Computer Program . . . . .	98
8.14	Scaled Crater Efficiency Versus Scaled Depth of Burial Showing Data from the Current Research, Viktorov and Stepenov (Schmidt, 1979), and a Best-Fit Line Developed by Schmidt (1979) from 86 Cratering Events. . . . .	99
8.15	Specimen Elevation Versus Saturation: a) $S_c = 20\%$ , $40\%$ ; b) $S_c = 60\%$ , $70\%$ . . . . .	101
8.16	Capillary Pressure Versus Saturation, 19 G . . . . .	102
8.17	Capillary Pressure Versus Saturation, 26 G . . . . .	103
8.18	Capillary Pressure Versus Saturation, 49 G . . . . .	104
8.19	Capillary Pressure Versus Saturation, 67 G . . . . .	105

LIST OF FIGURES  
(CONCLUDED)

Figure	Title	Page
8.20	Apparent Crater Dimensions Versus Compaction Saturation: a) Scaled Dimensions; b) Normalized Dimensions . . . . .	107
8.21	Aspect Ratio Versus Compaction Saturation . . . . .	111
8.22	Crater Wall Angle Calculation . . . . .	113
8.23	Measured Apparent Crater Depth Versus Compaction Saturation . . . . .	114
8.24	Decrease of the Cohesion Component of Soil Strength Relative to the Total Shear Strength with an Increase in G-Level (Stress) . . . . .	116
8.25	Crater Profiles Showing the Differences in Aspect Ratio due to Apparent Crater Depth and Wall Angle at 26 G, 49 G, and 67 G . . . . .	118
8.26	Differences in Aspect Ratio due to Centrifugation Prior to Testing at 1 G . . . . .	119
8.27	Crater Profiles Showing the Differences in Aspect Ratio due to Centrifugation Prior to Testing at 1 G . . . . .	120
8.28	Typical Location of Crushed Sand Grains in the East-West Direction: a) Photograph: b) Schematic . . . . .	122
8.29	Crater Mold Profiles in the East-West and North-South Directions . . . . .	123
8.30	Direction of Coriolis Force Components Drawn in the Plane of the Original Ground Surface About the Edge of a Spherical Crater . . . . .	126

## LIST OF SYMBOLS AND UNITS

a	spherical explosive charge radius (mm)
a	acceleration (m/s <sup>2</sup> or G)
a <sub>c</sub>	Coriolis acceleration
c	seismic velocity (m/s)
cc	cubic centimeters
°C	degree Celsius
c <sub>u</sub>	coefficient of uniformity
c <sub>c</sub>	coefficient of curvature (or gradation)
cm	centimeter
d	crater depth (m)
D <sub>r</sub>	relative density (%)
D <sub>50</sub>	diameter corresponding to 50% finer (mm)
DOB	depth of charge burial (m) (+DOB below ground surface) (-DOB above ground surface)
e	void ratio
F <sub>c</sub>	Coriolis force (N)
°F	degree Fahrenheit
G	gravitational acceleration (9.81 m/s <sup>2</sup> )
g	gram
h	crater lip height (m)
i	unit vector, x direction
j	unit vector, y direction
k	unit vector, z direction
K	total unit weight (N/m <sup>3</sup> )
kg	kilogram
L	length
m	meter
mg	milligram
mm	millimeter
M	mass (kg)
N	scale factor
P	blast pressure (kPa)
Q <sub>c</sub>	specific energy of explosive (erg/g)
r	crater radius (m)
r	unit vector for particle velocity
R	centrifuge rotor radius
rpm	revolutions per minute
s	second
S <sub>c</sub>	compaction saturation (%)
t	time
T	torque (N-m)

LIST OF SYMBOLS AND UNITS  
(CONCLUDED)

U	explosive Chapman-Jouget particle velocity (m/s)
$u_a$	pore-air pressure (kPa)
$u_w$	pore-water pressure (kPa)
v	particle velocity (m/s)
V	crater volume (m <sup>3</sup> )
W	explosive charge mass (kg) The symbol W represents the total energy of an explosive, however, for a given chemical explosive weight and mass are proportional to energy.
Y	material strength (kPa)
$\alpha$	crater wall angle (degree)
$\tau$	shear stress (kPa)
$\sigma$	normal stress (kPa)
$\delta$	charge density (kg/m <sup>3</sup> )
$\rho$	soil density (kg/m <sup>3</sup> )
$\pi$	pi term
$\lambda$	normalized depth of burial (m/kg <sup>1/3</sup> )
$\phi'$	effective angle of internal friction
$\phi^b$	angle of shear strength increase with an increase in ( $u_a - u_w$ )
$\omega$	angular velocity (rad/s)
-	overbar designating a vector quantity

SECTION I  
INTRODUCTION

A. OBJECTIVE

The objectives of this research are to determine:

- 1) scaling laws for explosion-induced apparent crater dimensions of volume, radius, and depth for dry and partially saturated sand for buried, fully coupled explosives;
- 2) the effect of the depth of charge burial (DOB) on crater formation;
- 3) to what extent desaturation occurs in beach sand during centrifugation;
- 4) the effect of moisture on the apparent crater dimensions;
- 5) the effect of moisture on the apparent crater aspect ratio;
- 6) and the effect of the Coriolis acceleration on the shape of the apparent crater.

For the first objective, the apparent crater dimensions are analyzed as dimensional terms and as dimensionless pi terms. In the analysis of dimensional terms, the apparent

crater dimensions in dry and partially saturated sand are plotted against the TNT equivalent weight of the explosive mass. The slope of the best-fit lines, the yield exponents, are compared to determine the similarity between scaling laws. Comparisons of the yield exponents derived in this subscale centrifuge research are also made with the yield exponents derived from: 1) other centrifuge tests (Goodings et al., 1988); Schmidt and Holsapple, 1978 and 1980); 2) field explosive tests by the U.S. Army Engineer Waterways Experiment Station (Strange et al., 1961; Rooke et al., 1974); and 3) crater scaling relations given in the Air Force Protective Construction Design Manual and the Army design manual, Fundamentals of Protective Design for Conventional Weapons.

The dimensionless pi terms used to analyze crater dimensions produced by buried charges are those derived by Schmidt and Holsapple (1977). In the analysis of the pi terms, a direct comparison is made between the consistency of the apparent crater dimensions with increasing charge size in dry sand and in partially saturated sand.

#### B. BACKGROUND

Theoretical research in cratering consists of numerical methods that either combine a cavity growth and surface mounding model with a free-fall throw out model, or use quasi-static calculations to treat cratering as an earth pressure problem (Dillon, 1972). The experimental research has

concentrated on the development of scaling relations that allow the crater dimensions resulting from one charge size to be scaled to another. The vast majority of the cratering data generated through experimental research comes from full-scale field tests. Unfortunately, much of the field test data includes little, if any, information on the soil properties.

### C. SIGNIFICANCE

Cohesionless soils are commonly placed and compacted around and over strategic structures. The influence of the moisture content of cohesionless soils on ground shock and cratering from conventional weapons detonations is unknown. Unsaturated soil mechanics theory predicts saturation level will influence soil behavior (Fredlund, 1986).

Split-Hopkinson Pressure Bar tests conducted by Ross et al. (1989) and Pierce (1989) indicate that, in sands, the saturation during compaction influences stress transmission. Uniaxial explosive tests conducted on the centrifuge by Charlie and Walsh (1990) indicate trends similar to those of the Split-Hopkinson Pressure Bar.

Centrifuge test results on the material strength model proposed by Schmidt and Holsapple (1978, 1980) indicate that explosive induced crater dimensions scale differently for soils with cohesion (moist alluvium and clays) than for dry frictional cohesionless soils (sands and gravels). The difference in scaling occurs when cohesion is large compared

to the total shear strength. Therefore, the test results to date indicate that the moisture content of compacted sands may influence the conventional weapon effects on airbase structures.

#### D. APPROACH

The observational method of analysis through centrifuge modeling is used to study explosion-induced cratering. Centrifuge modeling allows soil properties to be well-controlled and provides the gravitational field required for similarity between model and prototype. Stiffness and strength of dry cohesionless soils are derived from the self-weight stresses. Therefore, only by increasing the gravitational acceleration can the self-weight stresses be equivalent in the model and prototype.

The scale of the model determines the gravitational acceleration required to equate the soil properties in the model and prototype. A  $1/N$  scale model will require  $N$  times the earth's gravitational constant ( $G = 9.81 \text{ m/s}^2$ ) to maintain similarity between the model and prototype. For similarity of explosive energy, a  $1/N$  scale model at  $N$  times the earth's gravitational constant will require  $1/N^3$  times the explosive mass of the prototype. In a  $1/N$  scale crater, the depth and diameter scale with  $1/N$ , whereas the crater volume scales with  $1/N^3$ . Centrifuge tests will be conducted at four G-levels to

verify the application of these and other scaling laws to unsaturated sands.

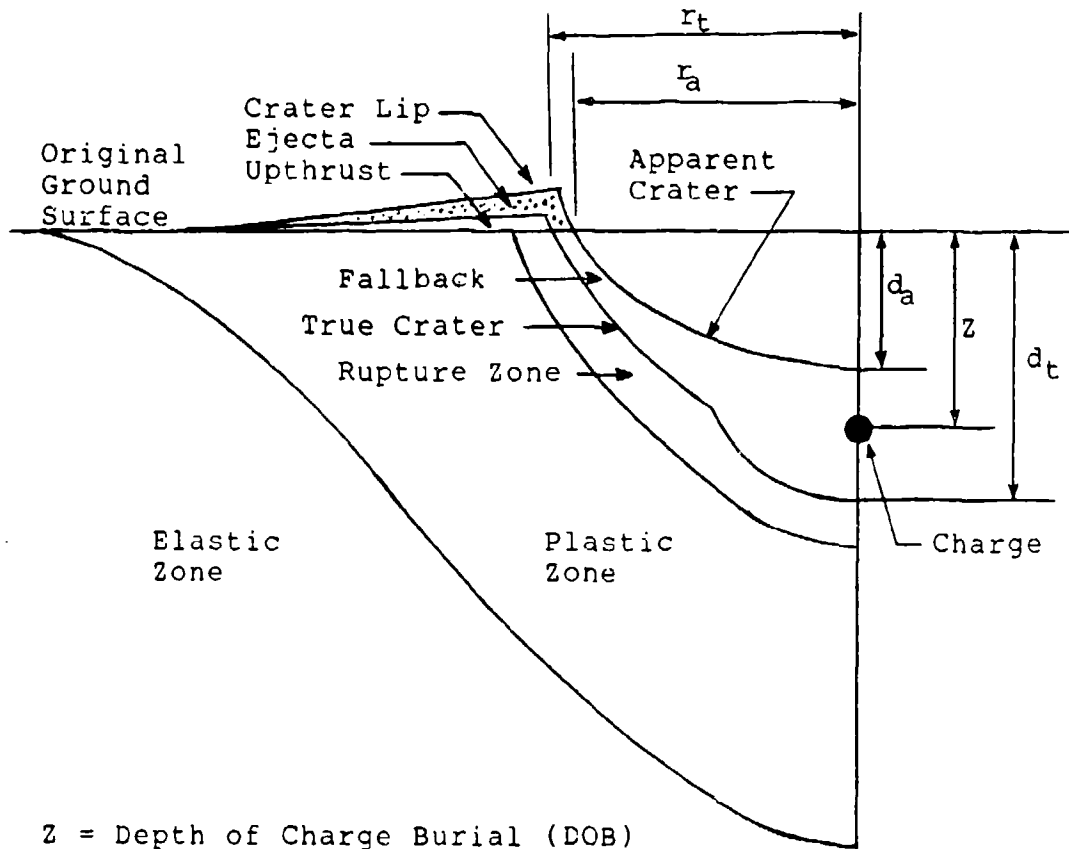
## SECTION II

### FULL SCALE EXPLOSION-INDUCED CRATERING

#### A. CRATER DIMENSIONS

Figure 2.1 shows the dimensions used to describe a crater. The ejected material deposited on the ground surface surrounding the crater by the blast is referred to as the ejecta. The airborne material that falls back into a newly formed crater is referred to as fallback. The subscripts  $a$  and  $t$  indicate the apparent and true crater dimensions, respectively. The apparent crater is the visible crater below the level of the original ground surface. The true crater is defined by the boundary below the original ground surface between the fallback and the crushed, fractured material that did not experience significant displacement or disarrangement (Dillon, 1972).

The crushed and fractured material that does not undergo significant displacement or disarrangement makes up the rupture zone. The plastic zone defines the region in which permanent deformation has occurred without crushing or fracturing. The deformation resembles a flow of the material. Within the plastic zone is a shear boundary beyond which no shearing of the material is assumed to occur. The elastic



- $Z$  = Depth of Charge Burial (DOB)
- $r_a$  = Apparent Crater Radius
- $d_a$  = Apparent Crater Depth
- $r_t$  = True Crater Radius
- $d_t$  = True Crater Depth

Figure 2.1 Half-Crater Profile taken about a Vertical Centerline.

zone contains material that has not undergone permanent deformation (Rooke et al., 1974).

#### B. CRATERING TERMINOLOGY

Centrifuge crater dimensions are described as measured, scaled, or normalized. Scaled crater dimensions are measured model dimensions multiplied by  $N$ , where  $N$  is a multiple of the earth's gravitational acceleration ( $G = 9.81 \text{ m/s}^2$ ). Thus, scaled crater dimensions are the prototype crater dimensions.

In crater modeling, dimensions are divided by  $W^n$  to eliminate the dependence on explosive energy. Charge mass ( $W$ ) is commonly used to represent explosive energy because for a given chemical explosive, charge mass is proportional to explosive energy. With all other variables held constant, the charge mass exponent,  $n$ , is referred to as the yield exponent. When the yield exponent is unknown, a value of  $1/3$  has been found to be a good approximation for dimensions of radius and depth (Strange et al., 1961). The procedure of dividing by  $W^n$  is referred to as normalization. Thus, the normalized crater dimensions are scaled dimensions divided by the cube root of the charge mass.

Depth of burial (DOB) significantly effects crater size. To determine the functional relationship between DOB and crater size, normalized crater dimensions are plotted against normalized DOB ( $\lambda$ ). As with crater radius and depth, DOB is divided by  $W^{1/3}$ . By convention, a positive DOB refers to a

buried charge, and a negative DOB refers to an airblast. The height of burst (HOB) is also used to denote the distance of an airblast from the ground surface.

### C. CRATERING MECHANISMS

Near surface blasts produce craters. The size and shape of the crater are controlled by the energy of the explosion, the properties of the soil or rock, DOB, and gravity (Dillon, 1972). For all other variables held constant, the greater the energy release, the larger the crater. Conversely, the greater the shear strength of the soil, the smaller the crater for a given release of energy and DOB.

The fraction of the released energy that impacts the medium is a function of DOB. Initially as DOB increases, the crater becomes larger because more energy is directed into the medium. Then beyond a certain DOB, the impact of the energy released on the surface becomes less and less and the size of the crater begins to decrease. The optimum DOB is the DOB that maximizes a crater dimension. The optimum DOB for crater volume, radius, or depth are not necessarily the same (Dillon, 1972).

Gravity is a significant factor in crater formation. First, the explosive energy must overcome the gravitational force to excavate the soil or rock. Second, gravity controls the distribution of fallback. Third, gravity controls the properties of frictional materials

There are three mechanisms for nonnuclear crater production. In chronological order these mechanisms are the formation of a shock front, explosive gas acceleration and gravity. The shock front is the pressure discontinuity developed from the explosive detonation. The shock front impacts the soil first and causes crushing, compaction, fracturing, and plastic deformation of the soil surrounding the blast cavity. Compression waves are reflected at the ground surface as a tensile wave. When the magnitude of the reflected wave exceeds the tensile strength of the material, spalling occurs (Dillon, 1972).

During the gas-acceleration phase, the crushed and fractured material is accelerated by the adiabatic expansion of the trapped gases. The magnitude of the acceleration vector determines the flight of the material particles. Following the gas expansion, the gravitational force pulls the airborne particles down into and around the crater.

#### D. HISTORICAL CRATERING INVESTIGATION AT 1 G

Initial research on crater prediction and scaling relied on field test data. The goal was to derive the functional relationship between apparent crater radius ( $r_a$ ), depth ( $d_a$ ) and explosive energy ( $W$ ). These functional relationships are commonly referred to as scaling laws, and are named after the yield exponent. For example, the cube root scaling law describes a condition in which the linear dimensions of the

model crater scale to prototype dimensions with the cube root of the explosive energy ( $r, d \propto W^{1/3}$ ). In cube-root scaling, crater volume is proportional to explosive energy ( $V \propto W$ ) because volume is proportional to the cube of a linear dimension.

Other variables included in the research on cratering were DOB, soil strength ( $\sigma$ ) expressed in dimensions of stress, and the total unit weight of the soil ( $K$ ). The soil strength variable,  $\sigma$ , was used to represent the constitutive effects of the medium on the crater dimension, and the unit weight variable,  $K$ , was used to represent the effect of gravity. Through dimensional analysis (a variable manipulation technique used to generate the conditions for model and prototype similarity and discussed in section IV) the functional relationship including all of the above named variables was found to be

$$\frac{r}{DOB} = f \left\{ \frac{W^{1/3}}{\sigma^{1/3}DOB}, \frac{W^{1/4}}{K^{1/4}DOB} \right\} \quad (2.1)$$

The constitutive effects term ( $W^{1/3}/\sigma^{1/3}DOB$ ) follows the cube root scaling law, and the gravitational effects term ( $W^{1/4}/K^{1/4}DOB$ ) follows the quarter-root scaling law (Baker et al., 1973).

To reduce the three-dimensional functional relationship to two dimensions, several researchers ignored either the

constitutive effects or the gravitational effects. Chabai (1965) recognized that neither the constitutive effects term nor the gravitational effects term alone were sufficient to describe apparent crater radius. Chabai (1965) stated that, for small differences in explosive energy, the cube-root scaling law applied, but that for large differences in explosive energy the quarter-root scaling law provided a better estimate of apparent crater dimensions. Earlier, in a regression analysis, Chabai (1959) found the  $r/DOB$  term could be approximated by the function  $W^{1/3.4}/DOB$ . The fact that the exponent for the charge mass was between  $1/3$  and  $1/4$  was taken by Baker et al. (1981) as an indication that in cratering, both the constitutive effects and the gravitational effects are significant.

In 1960 and 1961, the U.S. Army Engineer Waterways Experiment Station (WES) published a two-volume technical report entitled "Cratering from High Explosive Charges." The report shows cube-root scaling best describes crater radius and a yield exponent of 0.3 best describes crater depth (Strange et al., 1961). However, the authors of the WES report state that the cube-root scaling law is only accurate for charges ranging from 0.5 kg to 450 kg of TNT. They attribute the deviations from the principles of similitude to the dependence of soil strength on gravity and the difficulty in scaling soil density, particle size, and soil strength

properties in proportion to the ratio of the cube root of the model and prototype charge masses.

The data are also normalized to allow comparison of the various test series and to form prediction curves. The prediction curves show normalized crater radius ( $r/W^{1/3}$ ) and normalized crater depth ( $d/W^{1/3}$ ) plotted against normalized DOB ( $\lambda = \text{DOB}/W^{1/3}$ ). The maximum apparent crater radius and depth are shown to occur when  $1.0 < \lambda < 1.5$ , and the maximum true crater radius and depth are shown to occur near  $\lambda = 2.0$ .

Rooke et al. (1974) updated the WES report. Data from nuclear explosions are included with the high explosive data. The data were also separated by moisture content, as well as by medium and DOB.

Dillon (1972) performed a regression analysis on existing crater data to develop prediction equations for apparent crater dimensions as a function of DOB, and to determine the effect of material properties on the apparent crater dimensions. Dillon (1972) used 10 nuclear events with yields ranging from 308,000 kg to 91,000,000 kg TNT equivalent, and 200 high explosive events with yields ranging from 0.45 kg to 454,000 kg of TNT. The densities of the materials ranged from 960 kg/m<sup>3</sup> to 2,720 kg/m<sup>3</sup>. A bell shaped curve was selected for the regression model and a value of 5/16, the average of 1/3 and 7/24, was used as the yield exponent.

Dillon (1972) states the "best regression equations" occurred when the soil property variables consisted of total

unit weight, percent saturation, specific gravity, shearing resistance, and seismic velocity. Of these variables, percent saturation and total unit weight appeared to be the most significant. At the "optimum" (undefined, presumably for crater diameter) DOB, "larger" (undefined, presumably also in terms of crater diameter) craters were produced at low and high levels of saturation in granular soils. The "largest" craters at the "optimum" DOB occurred in dry soil.

SECTION III  
CENTRIFUGE MODELING

A. PRINCIPLE OF CENTRIFUGE OPERATION

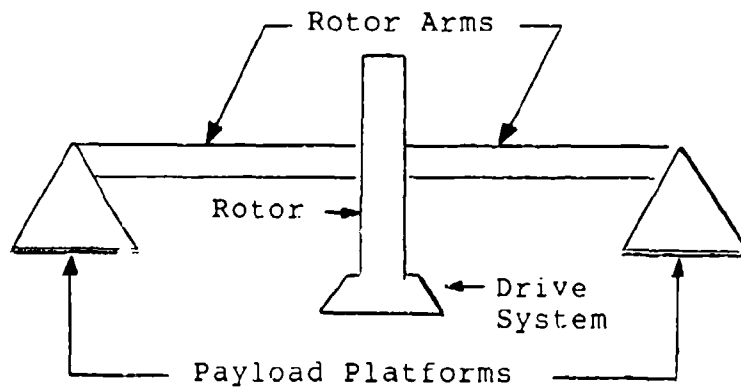
Centrifuge modeling was first applied to geomechanical testing in 1931 by P. B. Bucky at Columbia University, and in 1932 by G. I. Pokrovsky and N. N. Davidenkov in the U.S.S.R. The basic components of a centrifuge used for geomechanical testing are shown in Figure 3.1a. The centrifuge increases the acceleration applied to a specimen on the payload platform by rotating in the horizontal plane. Centripetal acceleration,  $\bar{a}_{co}$ , is directed radially toward the center of rotation and is defined as

$$\bar{a}_{co} = \bar{\omega}^2 r \quad (3.1)$$

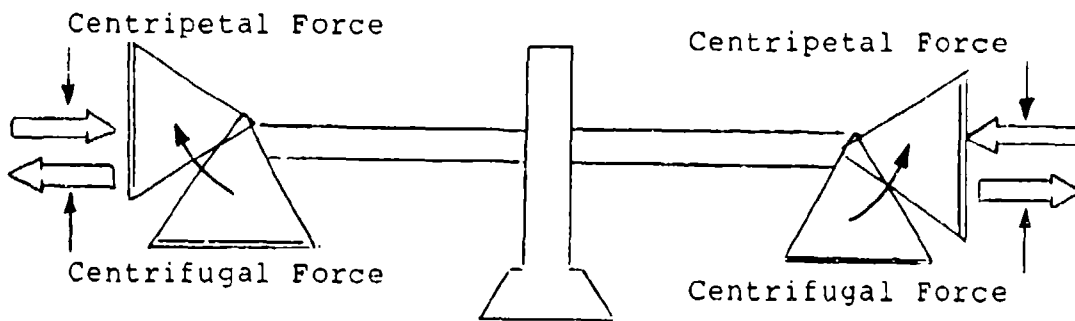
where  $\bar{\omega}$  is the angular velocity in radians per second and  $r$  is the radial distance to the specimen. The centripetal force,  $\bar{F}_c$  is

$$\bar{F}_c = M\bar{\omega}^2 r \quad (3.2)$$

where  $M$  is the specimen mass. Centripetal force is present when the frame of reference is outside the rotating frame and is therefore defined as a real force. The equal and



(a)



(b)

Figure 3.1 Centrifuge Schematic: a) Centrifuge Components; b) Payload Platform Rotation During Centrifuge Operation and Force Directions.

oppositely directed force is the centrifugal force (Figure 3.1b). The centrifugal force acts only in the rotating frame and is therefore a pseudo force.

#### B. ASSUMPTIONS IN CENTRIFUGE MODELING

The centrifuge modeling of a process or event assumes: 1) the model is an accurate scaled version of the prototype; 2) a 1/N scale model at N G behaves like the prototype at 1 G; and 3) the centrifuge produces an N G gravitational field that is constant throughout the specimen (Joseph et al., 1988).

The accuracy of the model depends on the scaling relations between the model and the prototype. A scaling relation is the expression relating the prototype variable at 1 G to the model variable at N G. For example, the scaling relation for a linear dimension, L, is

$$L_p = NL_m \quad (3.3)$$

where the subscripts p and m refer to prototype and model, and the constant N is the G-level. Table 3.1 shows the scaling relationships used in centrifuge modeling.

The second assumption in centrifuge modeling states that whatever happens in the prototype will happen in the model. Dynamic similarity between model and prototype exists only when the nondimensional parameters or pi terms formed from prototype variables equal the equivalent nondimensional parameters formed from model variables. For example, when

TABLE 3.1. SCALING RELATIONS FOR CENTRIFUGE MODELING.

<u>Quantity</u>	<u>Full Scale (Prototype)</u>	<u>Centrifuge Model at N G</u>
Linear Dimension	1	1/N
Area	1	1/N <sup>2</sup>
Volume	1	1/N <sup>3</sup>
Time		
In Dynamic Terms	1	1/N
In Diffusion Terms	1	1/N <sup>2</sup>
In Viscous Flow Cases	1	1
Velocity (Distance/Time)	1	1
Acceleration (Distance/Time <sup>2</sup> )	1	N
Mass	1	1/N <sup>3</sup>
Force	1	1/N <sup>2</sup>
Energy	1	1/N <sup>3</sup>
Stress (Force/Area)	1	1
Strain (Displacement/Unit Length)	1	1
Density	1	1
Energy Density	1	1
Frequency		
In Dynamic Problems	1	N

$$\pi_p = \frac{V_p \rho_p}{W_p} = \frac{V_m \rho_m}{W_m} = \pi_m \quad (3.4)$$

where V is apparent crater volume,  $\rho$  is soil density, and W is charge mass. Therefore, the development of a good model depends on the identification of the controlling variables and the generation of the associated pi terms.

There are three methods used to generate the pi terms for a physical phenomenon such as an explosion. If the physical factors controlling the phenomenon can be identified, then a

governing differential equation can often be written to describe the phenomenon. The use of a governing equation is the first method that can be used to insure the existence of similarity.

Pi terms are created from a governing equation through a normalization procedure. Kline (1980) defines normalization as "making the governing equations and conditions nondimensional in terms of nondimensional variables of standard magnitude." The procedural steps are first to make the variables dimensionless (divide each variable by itself defined at the limit of the domain of interest), substitute the dimensionless variables into the governing equation, and lastly to make the coefficient of each term dimensionless (divide each coefficient by the coefficient of one of the terms). The remaining coefficients are the pi terms.

The first step is the more difficult because the appropriate scales of the problem must be known. The main advantage of using a governing equation is that all the controlling variables are known to be included in the analysis. The list of pi terms is complete and physically meaningful.

The second method used to create the pi terms for a physical phenomenon is the method of similitude. The method of similitude involves identifying the forces controlling the phenomenon, defining the forces in the term of relevant variables, and creating force ratios. The force ratios are

the pi terms. Thus, the method of similitude is useful when the physical process is not well understood but the controlling forces are.

When the physical process is not well-understood and the forces cannot be well-defined, the method of dimensional analysis is used to generate a list of pi terms. Dimensional analysis is an extension of the Buckingham pi theorem (Buckingham, 1914) which states that given a relation among  $m$  parameters of the form

$$F_1\{p_1, p_2, \dots, p_m\} = 0 \quad (3.5)$$

an equivalent relation among  $n$  terms of dimensionless parameters, pi terms, can be found of the form

$$F_2\{\pi_1, \pi_2, \dots, \pi_n\} = 0 \quad (3.6)$$

where  $n$  is usually  $m$  less the number of primary units represented by the parameter.

The dimensional analysis of a physical phenomenon begins with the listing of all relevant variables expressed in primary units. There are two systems of primary units; force, length, and time or mass, length, and time. The mass-length-time system should be selected for centrifuge modeling as force, unlike mass, varies with G-level.

Dimensionless combinations of the variables, the pi terms, are created through algebraic or matrix manipulation.

The pi terms are complete for the variables selected as long as each pi term is independent of the others, and any pi term not generated by the analysis can be formed by taking the product of two or more of the terms raised to some power. However, the pi terms are not absolute if important variables are missing. Thus, the possible exclusion of important variables is the main weakness of dimensional analysis.

There are two significant advantages of using pi terms to study a physical phenomenon other than to insure similarity. The first is that combinations of variables allows certain variables to vary between model and prototype. Only the combinations themselves must remain equal. Second, the process of generating the pi terms may give physical meaning to seemingly unrelated variables.

The third assumption of centrifuge modeling is that the uniform nature of the earth's gravitational field at the surface can be accurately reproduced at higher G-levels.

#### C. SOURCES OF ERROR IN CENTRIFUGE MODELING

One obvious source of error in centrifuge modeling is the boundary effect. The specimen has to be placed in a container of one form or another. However, boundary effects can usually be shown to be negligible in comparison to the measured event.

A second source of error occurs when one or more of the scaling relations can not be met. Under these conditions the model becomes distorted. Limited distortion of a model is

acceptable as long as the physical phenomenon is not affected, or the test results are corrected for the distortion.

Distorted models occur in geotechnical centrifuge modeling when the prototype sand is used in the model. No attempt is made to scale the particle grain size, because to do so would necessitate the use of clay-sized particles having different material properties. The difficulty with not using a scaled grain size in the model is that the linear dimensions of the sand grains scale to a larger material in the prototype. However, as long as the grain size distortion does not affect other areas of the model such as the number of contact points with a structure or instrument, the model distortion is considered to be of secondary importance. The primary consideration is that the behavior of the soil be the same in the model and prototype.

Through a similarity analysis of cratering using the thermomechanical response of a continuum, Schmidt and Holsapple (1980) showed that dynamic similarity between tests in the same material will occur as long as the constitutive behavior of the material is independent of the scale factors for time and size.

Constitutive behavior independent of the scale factors for time is rate independent. Thus, sand used in centrifuge modeling should ideally be rate-independent. However, Felice et al. (1985) showed sand exhibits strain-rate dependence when the strain is greater than the initial gas porosity. Farr

(1990) measured 20 to 100 percent increases in constrained modulus due to differences in loading rate. In addition, recent Split-Hopkinson Pressure Bar tests show a strain-rate dependence in moist Eglin sand<sup>1</sup>. Thus, additional research is required to determine to what extent rate dependence affects the conditions of similarity.

A third source of error lies in the use of centripetal acceleration to increase the G-level. Centripetal acceleration varies with distance from the axis of rotation. Thus, within a cylindrical specimen, lines of constant acceleration follow lines of equal radii (Figure 3.2).

The linear increase in G-level with specimen depth creates a nonlinear stress distribution in the model (Figure 3.3). Whereas, a uniform gravitational field in the prototype leads to self-weight stresses that increase linearly with depth. Therefore, the model stresses equal the prototype stresses at only one depth. Above this depth, the model stresses are lower than the prototype stresses, while below this depth, the model stresses are higher than the prototype stresses. The error associated with this stress difference is a function of the ratio between the model depth and the radius of the centrifuge rotor arm (Joseph et al., 1988). A long rotor arm and a shallow model can be used to minimize the error.

---

<sup>1</sup>Personal Communication, C. Allen Ross, Professor Emeritus, University of Florida, Gainesville, Florida; Consultant, HQ AFCESA/RACS, Tyndall AFB, Florida.

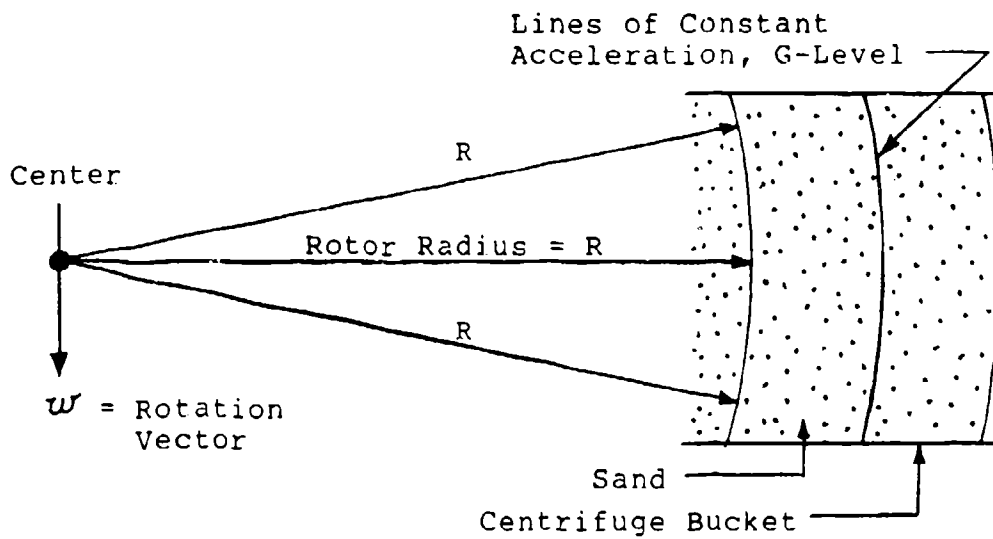


Figure 3.2 Variation of Centripetal Acceleration Within a Specimen, Side View. (NTS)

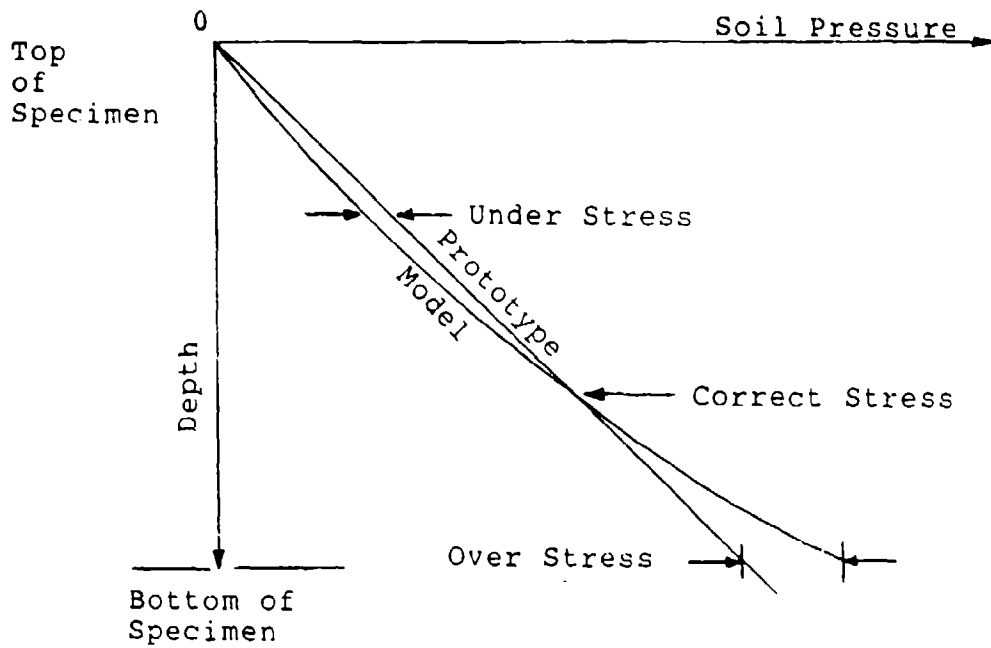


Figure 3.3 Model Stress Error with Depth (Joseph et al., 1988).

A second acceleration, the Coriolis acceleration, is added to the system when the blast occurs. The Coriolis acceleration is defined as

$$\bar{a}_c = 2\bar{\omega} \times \bar{v} \quad (3.7)$$

where  $\bar{\omega}$  is angular velocity, and  $\bar{v}$  is particle velocity. Therefore, to determine the movement of particles in a rotating frame, the Coriolis acceleration must be included. In the centrifuge environment, the change in particle movement due to the Coriolis acceleration is referred to as the Coriolis effect.

Lastly, the earth's gravitational acceleration cannot be overlooked at low G-levels. The acceleration on the specimen is the resultant of the centripetal and gravitational acceleration:

$$\bar{a}_{resultant} = \sqrt{\bar{a}_{centripetal}^2 + \bar{a}_{gravitational}^2} \quad (3.8)$$

In summary, the centrifuge does not meet exactly all of the assumptions made to justify its use. However, the errors can usually be made insignificant. The container size should be large enough to reduce boundary effects. The particle size should be small enough to maintain sufficient points of contact, but not so small as to alter the material properties of the soil. The model size should be limited to some fraction of the rotor arm length, and tests should be run at

speeds high enough to make the gravitational acceleration a small percentage of the resultant.

D. MODELING OF MODELS

The modeling of models technique refers to the comparison of similar centrifuge tests at G-levels bounding the domain of interest. If the measurements from each test are approximately equal, then the scaling relations are shown to be accurate over the domain. No scale effects, errors introduced through the scaling process, are present and the model should accurately simulate the prototype. The advantage of a test series that includes the modeling of models is that centrifuge modeling can be performed without a prototype.

## SECTION IV

### CRATERING ON THE CENTRIFUGE

#### A. DIMENSIONAL ANALYSIS - PI TERMS

##### 1. Surface Detonations

Schmidt and Holsapple (1978) performed a series of tests in dry Ottawa sand to verify the similarity relations generated by their thermomechanical analysis of a continuum, and to study surface blast phenomena. The variables selected by Schmidt and Holsapple (1978) were apparent crater volume (V), the heat of detonation per unit mass (Q), initial density of the explosive ( $\delta$ ), initial density of the soil ( $\rho$ ), material strength of the soil (Y), spherical explosive charge radius (a), depth of charge burial (DOB), and the gravitational constant (G). The pi terms used in their analysis are listed in Table 4.1. Crater radius (r) and depth (d) are also analyzed using the same set of variables such that:

$$\pi_1 = \pi_r = r \left( \frac{\rho}{W} \right)^{1/3} \quad \text{or} \quad \pi_1 = \pi_d = d \left( \frac{\rho}{W} \right)^{1/3} \quad (4.1)$$

TABLE 4.1. CENTRIFUGE CRATERING PI TERMS.

I. Surface (Half-Buried) Detonations  
(Schmidt and Holsapple, 1980)

A. Mass Set

$$\pi_1 = \pi_v = \frac{V\rho}{W} \quad \text{Cratering Efficiency}$$

$$\pi_2 = \left(\frac{G}{Q_0}\right) \left(\frac{W}{\delta}\right)^{1/3} \quad \text{Gravity Scaled Yield}$$

$$\pi_3 = \frac{Y}{\delta Q_0}$$

$$\pi_4 = \frac{\rho}{\delta}$$

B. Energy Set

$$\pi_1 = \frac{VQ_v}{E}$$

$$\pi_2 = \frac{\rho GE^{1/3}}{Q_v^{1/3}}$$

$$\pi_3 = \frac{Y}{Q_v}$$

$$\pi_4 = \frac{\rho}{\delta}$$

C. Gravity Set

$$\pi_1 = V \left(\frac{\rho G}{E}\right)^{3/4}$$

$$\pi_2 = \frac{1}{Q_0} \left(\frac{G^3 E}{\delta}\right)^{1/4}$$

$$\pi_3 = \frac{Y}{\delta Q_0}$$

$$\pi_4 = \frac{\rho}{\delta}$$

**TABLE 4.1. CENTRIFUGE CRATERING PI TERMS  
(CONTINUED).**

II. Buried Detonations  
(Schmidt and Holsapple, 1977)

$\pi_1, \pi_2, \pi_4$  from I.A, the mass set, and

$$\pi_3 = DOB \left( \frac{\rho}{W} \right)^{1/3}$$

III. Material Strength Model  
(Schmidt and Holsapple, 1979)

$\pi_1, \pi_2$  from I.A, the mass set, and

$$\pi_3 = \frac{\rho}{\delta}$$

$$\pi_4 = \frac{C}{\rho Q_0}$$

$$\pi_5 = \tan \phi$$

When tests of half-buried charges are performed in the same soil with the same explosive,  $\pi_3=0$  and both  $\pi_4$ , and  $\pi_5$  are constant. Thus, using the Buckingham Pi theorem (Buckingham, 1914), Schmidt and Holsapple (1978) wrote the functional relationship as:

$$\pi_1 = F \{ \pi_2 \} \quad (4.2)$$

Schmidt and Holsapple (1978) found the power law could be used to relate  $\pi_1$  to  $\pi_2$ .

$$\pi_1 \pi_2^\alpha = k = \text{constant} \quad (4.3)$$

The expansion of the pi terms to their physical definitions, resulted in scaling rules for dynamically nonsimilar tests in Ottawa sand:

$$V = k_v \left(\frac{W}{\rho}\right) \left[\frac{G}{Q} \left(\frac{W}{\delta}\right)^{1/3}\right]^{-\alpha} \quad (4.4a)$$

$$r = k_r \left(\frac{W}{\rho}\right)^{1/3} \left[\frac{G}{Q} \left(\frac{W}{\delta}\right)^{1/3}\right]^{-\beta} \quad (4.4b)$$

$$d = k_d \left(\frac{W}{\rho}\right)^{1/3} \left[\frac{G}{Q} \left(\frac{W}{\delta}\right)^{1/3}\right]^{-\gamma} \quad (4.4c)$$

For the apparent crater dimensions, Schmidt and Holsapple (1978) defined the yield exponents as

$$V \propto W^{(1-\alpha)/3} \quad (4.5a)$$

$$r \propto W^{(1-\beta)/3} \quad (4.5b)$$

$$d \propto W^{(1-\gamma)/3} \quad (4.5c)$$

where the exponents  $\alpha$ ,  $\beta$ , and  $\gamma$  represent the material properties of the soil.

Using the power law, Schmidt and Holsapple (1978) found their data agreed with the 1 G test data reported by Piekutowski (1974, 1975). Figure 4.1 shows the agreement

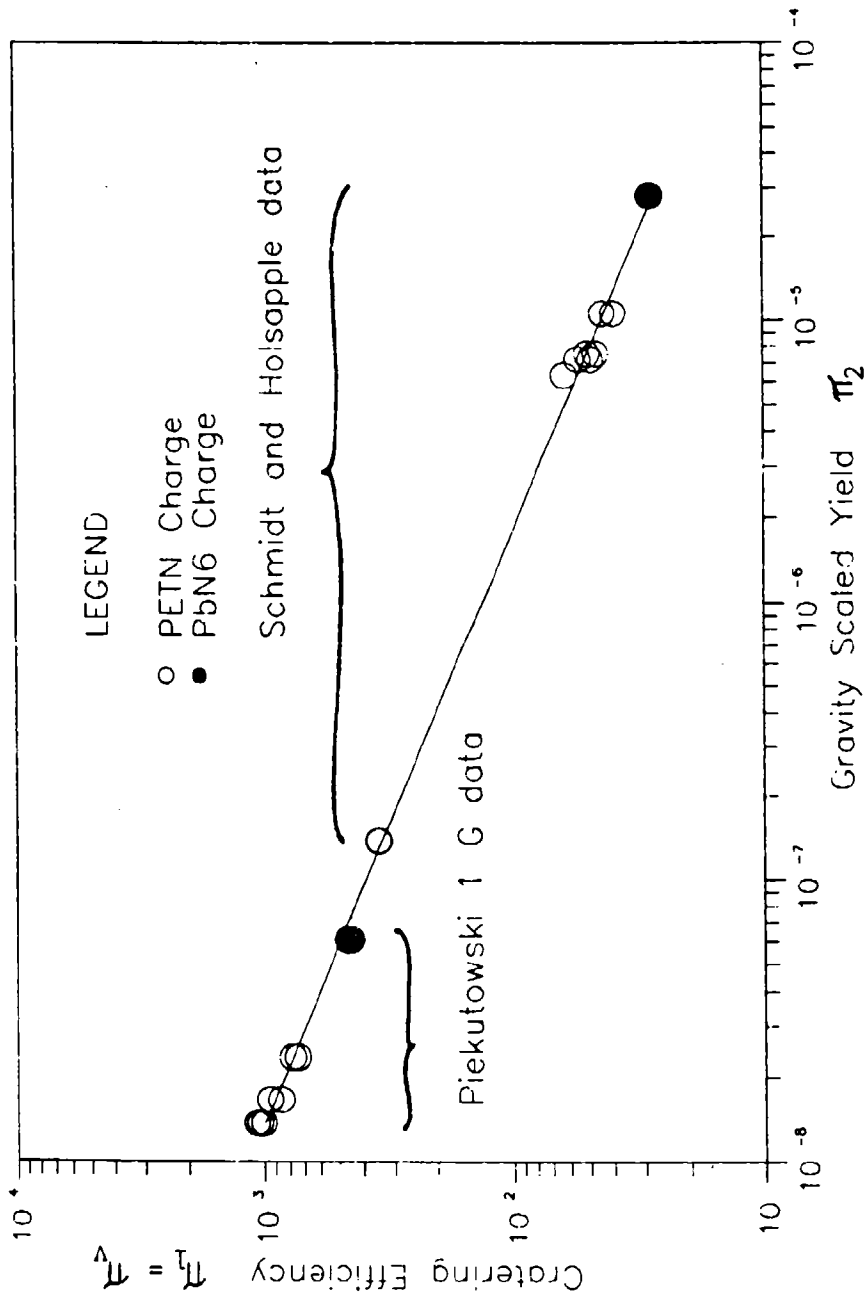


Figure 4.1 Agreement of Cratering Data Between Schmidt and Holsapple (1978) and Piekutowski (1974, 1975).  $\pi_v = vC/W$ ,  $\pi_2 = G/(Q(W/d)^{1/3})$ .

between the two sets of data for apparent crater volume. From such figures, Schmidt and Holsapple (1978) concluded that large explosive yields at 1 G could be accurately simulated by small charges at elevated gravity, and that for half-buried charges the effect of increasing the gravitational acceleration on a fixed charge is equal to increasing charge size at fixed gravity.

The gravity-scaled yield  $((G/Q_0)(W/\delta)^{1/3})$  accounted for variation in explosive properties as well as the variation in gravity. Therefore, Schmidt and Holsapple (1978) also concluded that use of a gravity-scaled yield term would permit large explosive yields to be simulated by a small scale equivalent charge of a different type.

When all other variables are fixed, the power-dependence of apparent crater dimensions in Ottawa sand on charge mass were reported by Schmidt and Holsapple (1978) as  $W^{0.842 \pm 0.002}$  for apparent crater volume,  $W^{0.280 \pm 0.001}$  for apparent crater radius, and  $W^{0.279 \pm 0.002}$  for apparent crater depth.

Schmidt and Holsapple (1980) concluded that different scaling laws do not result from different variables and pi term sets. The scaling laws from different pi term sets appear different because each requires different testing procedures to hold the pi terms constant and to maintain conditions of similarity. If all of the variables used to relate the variables in one pi term set to the variables in another set are included in the pi term sets, any one set of

$\pi$  terms can be converted to any other through the product of powers-transformation procedure. Thus, as long as specific energy of the explosive is included in the analysis, charge mass is interchangeable with explosive energy.

If the soil type is fixed, a variation in gravity as required by similarity produces the cube-root scaling law. The quarter-root scaling law will only result if gravity is kept constant, but no two similar tests ( $\pi_2, \pi_3, \pi_4 = \text{constant}$ ) can fulfill these restrictions. Therefore, Schmidt and Holsapple (1980) showed that when the soil type is fixed, quarter-root scaling is impossible.

## 2. MATERIAL STRENGTH MODEL

Figure 4.2 (Holsapple et al., 1978; Schmidt and Holsapple, 1979) shows that when the cratering efficiency  $\pi$  term ( $\pi_1$ ) is plotted against the gravity scaled yield  $\pi$  term ( $\pi_2$ ), those materials having some cohesion, apparent or real, do not fall on the curve for dry sand. At low G-levels or low explosive yield, the cratering efficiency is constant. The apparent crater volume is proportional to the charge mass, and the cube root scaling rule applies.

At high G-levels, the data becomes asymptotic to lines parallel to the dry sand curve. Beyond some G-level or charge size, the cube root scaling rule is not appropriate. The crater dimensions exhibit a dependence on charge mass.

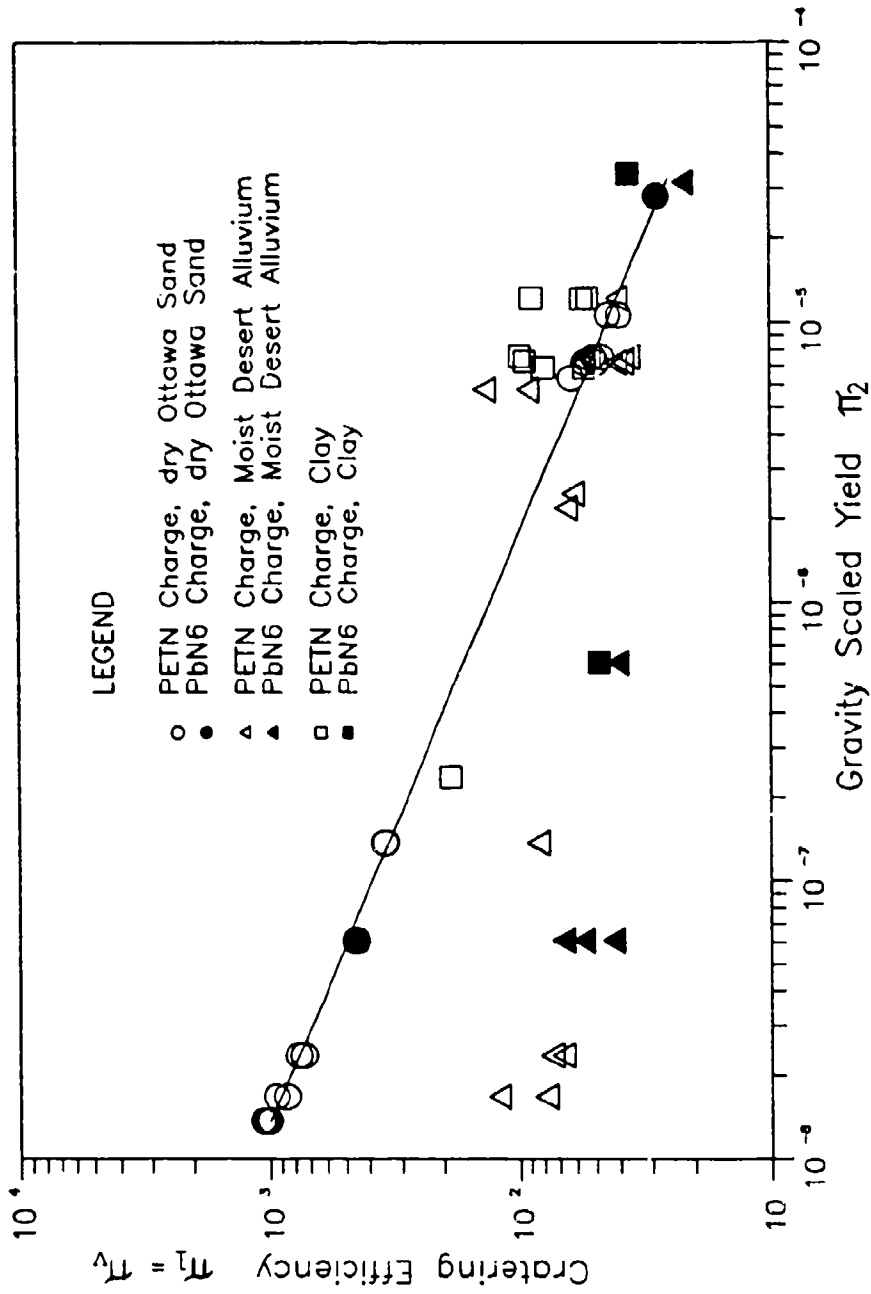


Figure 4.2 Cratering Efficiency Versus Gravity-Scaled Yield for Various Soil-Explosive Combinations (Holsapple et al., 1978).  $\pi_v = ve/w$ ,  $\pi_2 = G/Q(w/\Delta)^{1/3}$ .

To account for this observed deviation in scaling, Schmidt and Holsapple (1979) used an energy balance approach to derive a modified gravity scaled yield term:

$$\pi_{2m} = k_2 \frac{c}{\rho Q_e} + \pi_2 [k_3 \tan\phi + k_1] \quad (4.6)$$

where  $c$  is cohesion,  $\tan\phi$  is the frictional shear resistance, and  $k_1$ ,  $k_2$ , and  $k_3$  are dimensionless constants. The first constant ( $k_1$ ) was defined as a measure of the work done against gravity. The second constant ( $k_2$ ) was defined as a measure of the work required to overcome cohesion, and the third constant ( $k_3$ ) was defined as a measure of the work done against the material strength increase due to the increase in confining pressure. Holsapple et al. (1978) found  $k_1$  empirically for Ottawa sand to be 0.1. Both  $k_2$  and  $k_3$  were found to be approximately 1.0.

Figure 4.3 is a graphical presentation of the material strength model for crater volume (Holsapple et al., 1978). At low gravity scaled yields, the cohesion dominates the cratering process. The curve is horizontal and crater volume is proportional to charge mass. The cube root scaling law applies. Then at an increased gravity-scaled yield the curve becomes aligned with the craters formed in cohesionless soil. The soil strength due to the frictional shear resistance dominates the cratering process. Holsapple et al. (1978) concluded their analysis, stating that the observed change in

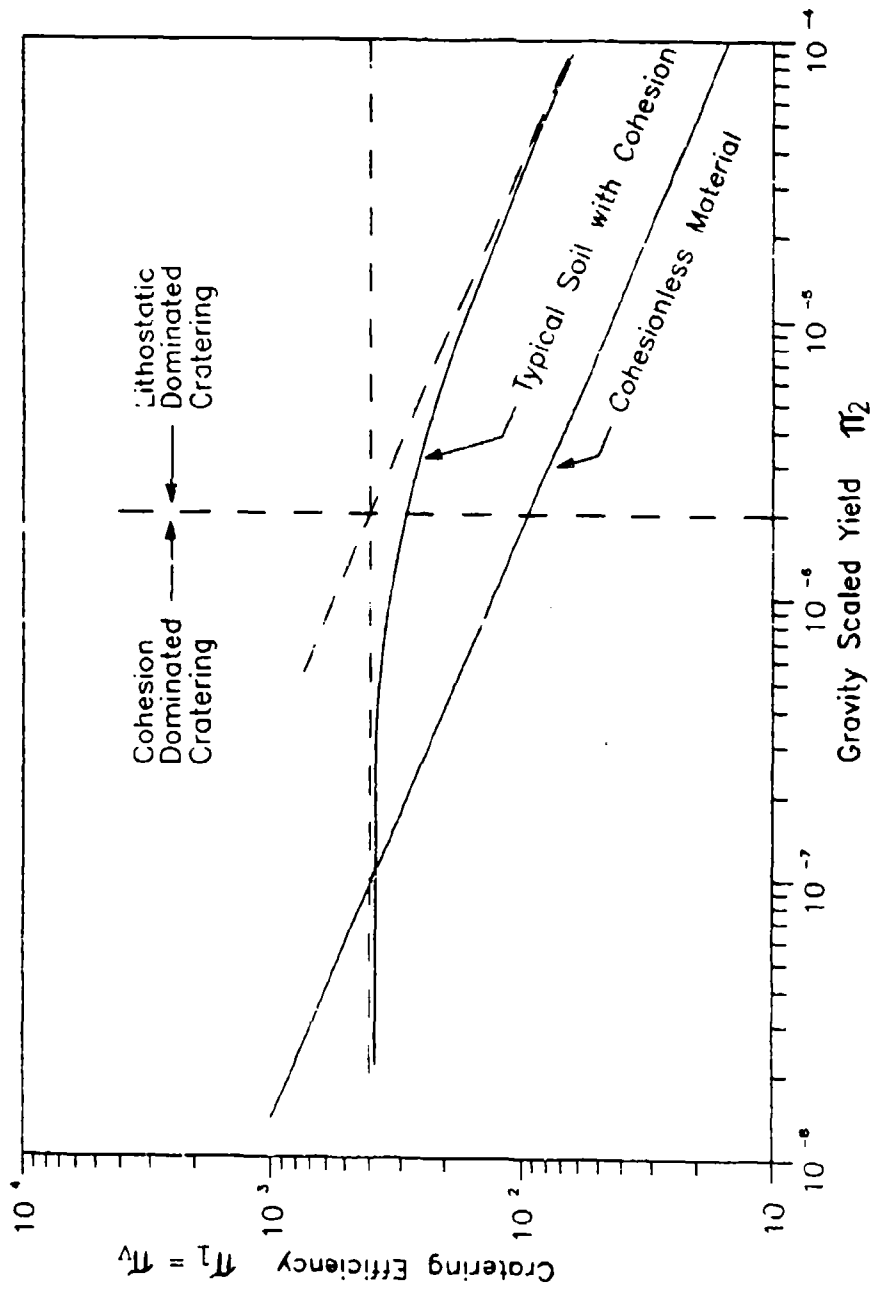


Figure 4.3 General Form of the Material Strength Model for Crater Volume (Holsapple et al., 1978).  $\pi_v = ve/w$ ,  $\pi_2 = G/Q(w/a)^{1/3}$ .

scaling law is the reason small-scale 1 G tests in soil with cohesion can not extrapolated to large-scale 1 G tests.

Holsapple et al. (1978) used the material strength model as represented by  $\pi_{2m}$  to explain the differences in crater volume in clay and in sand. Sand has a relatively high frictional shear resistance and, therefore, has a strength that increases with confining pressure. As the centrifugal acceleration increases, the strength of the sand increases because the confining pressure increases. In the short term under undrained conditions, clay is assumed to have no frictional shear resistance, but a relatively large cohesion. However, cohesion is not affected by gravitational acceleration, so the strength of clay remains constant. Therefore, Holsapple et al. (1978) stated that at high G-levels, an explosive charge will produce a larger crater in clay than in sand.

Schmidt and Holsapple (1979) stated the apparent crater radius and depth data may not necessarily fit the material strength model proposed for crater volume. Their reason was that the model was based on available energy and the work to excavate the soil. No parameters for shape were included. However, the radius may fit the model to some extent because volume is proportional to the crater depth multiplied by the radius squared.

Overall, Schmidt and Holsapple (1979) concluded that subscale craters cannot be accurately modeled without

increased gravity, and that the material strength model based on cohesion and frictional shear resistance accurately predicts apparent crater volume for various soils and explosive sources.

From a plot of scaled crater volume (V/W) versus scaled-charge mass ( $N^3W$ ), Gaffney et al. (1989) concluded that the transition point between strength (cohesion) dominated scaling to gravity (frictional shear resistance) dominated scaling occurs at scaled yields of a few kilograms. However, differences in medium, medium density, and explosive type were ignored. The slope of the decreasing scaled crater volume was found to be -0.175 which was less than the slope of -0.2 calculated by Schmidt et al. (1986).

### 3. Subsurface Detonations

Schmidt (1977) used four pi terms to analyze charges buried in artist modeling clay (Table 4.1). Through the application of the product of powers rule which permits the combination of pi terms, a scaling law for crater volume in terms of the depth of charge burial (DOB) was derived:

$$\pi_1 \pi_2^{1/4} = F \{ \pi_3 \pi_2^{1/6} \} \quad (4.7)$$

The scaling law was shown to fit the data from 86 cratering events with a charge yield energy range of 12 orders of magnitude. Schmidt and Holsapple (1977) concluded that tests in an accelerated reference improve the prediction of large-

scale events and attributed the accuracy of the crater volume scaling law to the gravity-scaled yield term ( $\pi_2$ ).

Schmidt (1979) repeated the analysis of the effects of charge burial on apparent crater volume. When the gravity scaled yield ( $\pi_2$ ) was expanded to include the material strength effects of cohesion and frictional shear resistance, the scaling law became:

$$\pi_1 \pi_2^{0.472} = F(\pi_3) \quad (4.8)$$

The exponential coefficient for  $\pi_2$  on the right-hand side of Equation (4.7) did not vary within the range of the data, and was therefore set to zero.

#### B. SLOPE STABILITY IN CRATERING

Schmidt and Holsapple (1979) added that crater shape will be effected by slope stability. When the side of the crater becomes unstable, slumping will occur. Slope stability and slumping are functions of the crater depth, cohesion, and angle of internal friction. Therefore, Schmidt and Holsapple (1979) concluded limits exist on apparent crater radius and depth combinations. The lower limit on the aspect ratio (radius/depth) of the apparent crater was defined as  $1/\tan\phi$  for desert alluvium where  $\phi$  is the angle between the crater wall and the original ground surface. Cohesion decreases crater aspect ratio for a given crater depth.

#### C. MOISTURE CONTENT EFFECT ON CRATER DIMENSIONS

Schmidt and Holsapple (1979) also analyzed the effect of moisture content on apparent crater dimensions in Desert Alluvium. They found small differences in moisture content produced large differences in crater size and structure. A decrease in moisture content resulted in flatter craters, whereas at a larger moisture content the crater shape became more hemispherical. Thus, Schmidt and Holsapple (1979) concluded the decrease in cohesion at the lower moisture content caused the flattening of the apparent craters.

#### D. SCALE EFFECT IN CRATERING

Goodings et al. (1988) concluded there are no detectable scale effects due to centripetal acceleration between 31 G and 101 G. Given the same soil and explosive, craters formed on a centrifuge at G-levels ranging from 1 G to 463 G will all follow the same scaling law. The power dependence (yield exponent) of crater dimensions on a half-buried charge mass in Ottawa sand were found to be  $W^{0.84}$  for apparent crater volume,  $W^{0.29}$  for apparent crater radius, and  $W^{0.28}$  for apparent crater depth.

#### E. SOIL DENSITY EFFECT ON CRATER VOLUME

Goodings et al. (1988) included tests at different soil densities ranging from 1590 kg/m<sup>3</sup> to 1720 kg/m<sup>3</sup>. The tests showed an 8 percent decrease in density (36 percent decrease

in relative density) produced a 72 percent increase in apparent crater volume.

F. CORIOLIS EFFECT ON CRATER SHAPE

Kutter et al. (1985) studied the effect of blast loading on tunnels. When compass directions are assigned to the specimen surface (Figure 4.4), the authors found the apparent crater profiles exhibited "marked asymmetry" in the East-West direction, and attributed this distortion to the Coriolis effect and the close proximity of the tunnel. The apparent crater profile in the North-South direction remained symmetrical.

Schmidt et al. (1986) and Steedman (1990) analyzed the Coriolis effect on the flight of the centrifuge crater ejecta. In both analyzes, particle flight was a function of ejection angle and particle velocity. Schmidt et al. (1986) stated the Coriolis acceleration shortens the ballistic range of the particles ejected towards the East and extends the ballistic range of the particles ejected towards the West. Thus within the crater, the ejecta will become more concentrated in the West. The result is an asymmetrical apparent crater profile.

Schmidt et al. (1986) observed asymmetrical crater profiles in dry Ottawa Flintshot Sand where the ejection angles typically ranged from 40 to 45 degrees. The Coriolis effect was shown to increase with ejection angle. However,

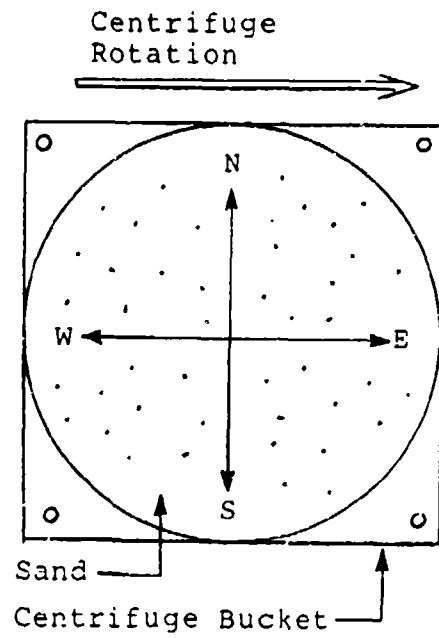


Figure 4.4 Compass Directions Assigned to the Centrifuge Specimen as Pictured from the Center of Rotation.

Schmidt et al. (1986) stated that below 55 to 60 degrees, the Coriolis effect should not be significant.

Steedman (1990) assumed the trajectory of the ejecta was a straight line directed ahead of the centrifuge bucket due to the initial tangential velocity (Figure 4.5). Thus, at certain combinations of centrifuge speed and particle velocity, the particles will return to the bucket. Steedman (1990) attributed the accumulation of ejecta ahead of the original detonator location to the high absolute velocity of the particles and the shorter distance traveled by the particles relative to the centrifuge bucket.

Steedman (1990) noted that his analysis did not include the strong wind created by the rotation of the centrifuge which may prevent the ejecta from following the theoretical straight line trajectories. From a series of centrifuge tests designed to model the effects of blast loading on piles located in saturated sand, Steedman concluded there was no evidence that the Coriolis effect distorted the shape of the apparent crater.

Figure 4.6 shows the apparent crater profiles measured by Gill and Kuennen (1991) in the East-West direction. The average crater profile (test number 500-00 ave.) of the tests produced by a half-buried charge is symmetrical about a vertical axis located at the origin of the blast. In contrast, the crater profiles produced by buried charges all appear to shift to the right. The centrifuge was reported by

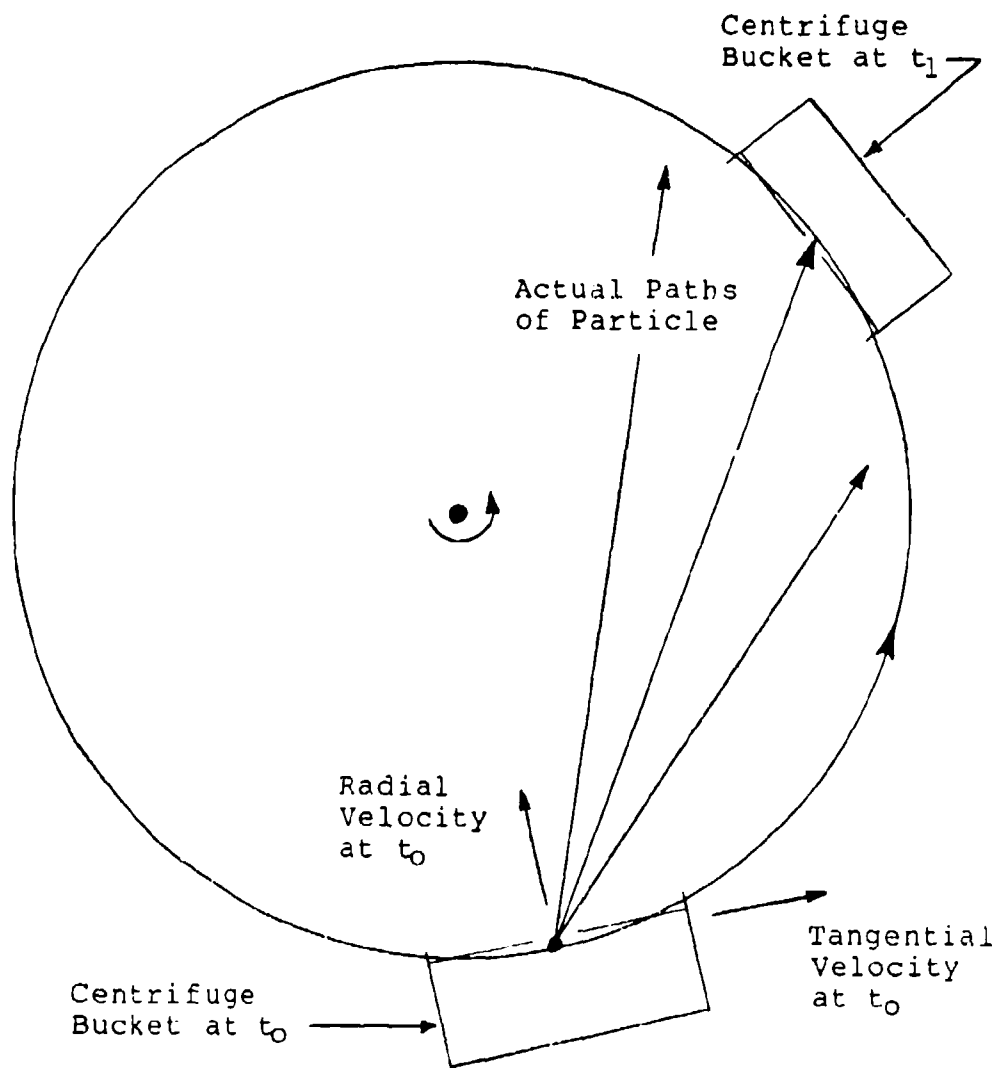


Figure 4.5 Soil Particle Trajectories Assumed by Steedman (1990).

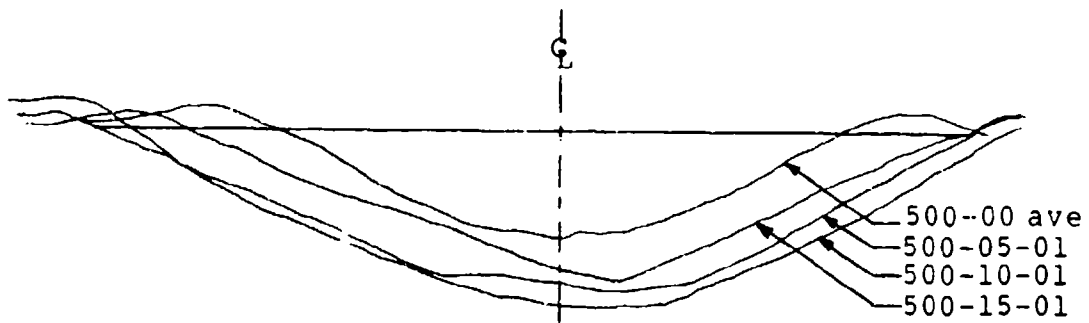


Figure 4.6 Scaled Crater Profiles Measured by Gill and Kuennen (1991).

Gill and Kuennen to rotate clockwise so that the movement of the specimen was from right to left. Thus, the apparent crater profile from buried charges appear to become skewed in the direction opposite the direction of centrifuge rotation.

## SECTION V

### MODEL DESCRIPTION

#### A. EXPLOSIVES

Explosives used in this research were RP-83 detonators specially prepared by Reynolds Industries Systems, Inc of San Ramon, California. Four different sizes of the detonator were used to model several explosive weights. The make-up of each detonator is shown in Table 5.1. The output charge consists of a multiple of 220 mg cyclotetramethyl enetetranitramine (PBX 9407) pressings (Figure 5.1). Each 220 mg pressing is 4.4 mm in length by 7.0 mm in diameter. Thus, each larger detonator is 4.4 mm longer than the next.

The total charge mass is converted to an equivalent weight of TNT for the data analysis. PBX 9407 is 94 percent cyclotrimethylene trinitramine (RDX) and 6 percent Exon 461 (Baker et al., 1980). Based on the heat of detonation, the TNT equivalent weights for PBX 9407 and RDX are 1.136 and 1.149 respectively. For cratering, the Air Force uses a factor of 1.115 to convert RDX to TNT. Thus, the equivalent mass of TNT can be expressed as:

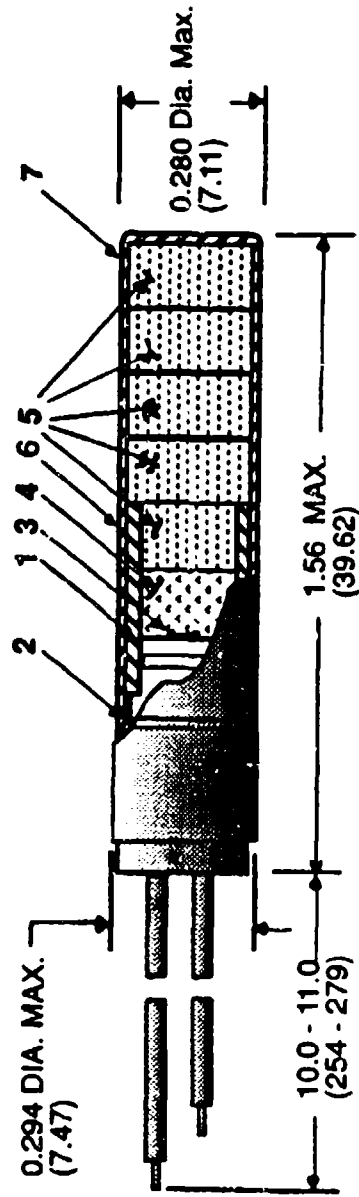
$$(1.09) \text{ PBX} = \text{TNT}.$$

(5.1)

TABLE 5.1. STANDARD AND MODIFIED RP-83 DETONATORS.\*

	Charge			Detonator Explosive Size (mg)			
	Type	Density (g/cc)	Specific Energy (erg = N-m)	"880" (standard)	"660"	"440"	"220"
Initiating Explosive	PETN	0.88	$5.95 \times 10^{-7}$	39	39	39	39
Pellet	PBX 9407	1.60	$5.35 \times 10^{-7}$	124	124	124	124
Output Charge	PBX 9407	1.60	$5.35 \times 10^{-7}$	880	660	440	220
	TOTAL CHARGE SIZE (PBX Equivalent)			1043	825	603	383

\*Personal Communication, Ron Varosh, Reynolds Industries Systems, Inc., San Ramon, California.



#### PARTS DESCRIPTION

1. MOLDED HEAD: FM #4005 Phenolic.
2. "O" RING.
3. BRIDGEWIRE: Gold, .0015 dia., .040 long
4. INITIATING EXPLOSIVE: 80 mg of PETN.
5. TOTAL OUTPUT CHARGE: 1031 mg of RDX with binder (13.5 grains @ 1.55-1.70 gm/cc density).
6. ALUMINUM CUP: .007 thick.

Figure 5.1 Reynolds Industries RP-83 Detonator. (From Reynolds Industries Systems, Inc. Technical Data Sheet).

B. TEST MATRICES

Table 5.2, shows the test matrix for this research. The G-levels ( $1\text{ G} = 9.81\text{ m/s}^2$ ) presented in the matrix are the G-levels at the center of mass of the detonator.

1. Constant Normalized Depth of Burial

$(\lambda = 0.73\text{ m/kg}^{1/3})$

Detonators were buried at a normalized depth of charge burial ( $\lambda$ ) equal to  $0.73\text{ m/kg}^{1/3}$  to insure as much of the explosive energy as possible was released into the soil. Drake and Little (1983) introduced an equivalent effect coupling factor to adjust the explosive energy directed into a medium according to the depth of charge burial. For soil, the maximum explosive energy is shown to be released into the medium at normalized depths of burial of  $0.56\text{ m/kg}^{1/3}$  and greater.

The centrifuge test series was designed to study explosive-induced stress wave transmission and crater size as a function of saturation. This test series formed the first part of the matrix (Table 5.2a). The modeling of models technique was used to simulate a prototype charge mass of 7 kg of TNT. The largest (880 mg) RP-83 detonators were fired at 19 G and the smallest (220 mg) RP-83 detonators were fired at 26 G. Each detonator was fired in dry specimens and specimens saturated at compaction levels of 20, 40, 60, and 70 percent.

**TABLE 5.2a. TEST MATRIX FOR THE CONSTANT NORMALIZED DOB SERIES ( $\lambda = 0.73 \text{ m/kg}^{1/3}$ ).**

Test Number (rpm-S-#)	Scaled Explosive (kg TNT)	RP-83 size (mg)	G-Level (Detonator) (G)	Preparation Method	Compaction Saturation (%)
102-0-7	7	"880"	19	vibration	0
120-0-8	7	"220"	26	vibration	0
120-0-9	7	"220"	26	vibration	0
102-20-3	7	"880"	19	vibration	17
120-20-2	7	"220"	26	vibration	17
165-20-5	46	"220"	49	vibration	20
192-20-4*	116	"220"	67	vibration	20
102-40-2	7	"880"	19	vibration	35
120-40-1**	7	"220"	26	vibration	35
165-40-4	46	"220"	49	vibration	40
192-40-3	116	"220"	67	vibration	40
102-60-2	7	"880"	19	vibration	53
120-60-1	7	"220"	26	vibration	53
165-60-4	46	"220"	49	vibration	60
192-60-3	116	"220"	67	vibration	60
102-70-1	7	"880"	19	vibration	70
102-70-3***	7	"880"	19	vibration	70
120-70-2	7	"220"	26	vibration	70
120-70-4***	7	"220"	26	vibration	70

\* Centrifugation to 93 G prior to test at 67 G.  
 \*\* Centrifugation to 43 G prior to test at 26 G.  
 \*\*\* First (bottom) layer consisted of 2 inches of dry sand.

Two more test series were added to include tests at higher G-levels. The series modeled 49 and 124 kg of TNT, and subjected the specimens to 49 G and 67 G respectively. In these series, the tests were conducted at compaction saturation levels of 0, 20, 40, and 60 percent

Last, six tests were conducted without centrifugation at 1 G (Table 5.2b). Tests were conducted at 1 G because 1 G tests are legitimate tests in and of themselves, and to show how the use of a centrifuge changes the results. From the centrifuge scaling relations it is apparent the 1 G tests are in no way related to the centrifuge tests. The 1 G tests only model a detonator buried in a few centimeters of sand, whereas the centrifuge tests model several kilograms of explosive buried in a few meters of sand.

The compaction saturation levels selected were 0, 20, and 60 percent. All of the tests were conducted in the centrifuge buckets. Two of the 1 G tests, one at 20 percent compaction saturation and one at 60 percent compaction saturation were spun on the centrifuge to 57.3 G before being tested. The two 1 G tests conducted in dry beach sand did not have the same method of compaction. One specimen was vibrated while the other was pluviated.

TABLE 5.2b. TEST MATRIX FOR THE 1-G SERIES ( $\lambda = 0.73 \text{ m/kg}^{1/3}$ ).

Test Number (rpm-S-#)	Scaled Explosive (kg TNT)	RP-83 size (mg PBX)	Detonator G-level (G)	Preparation Method	Compaction Saturation (%)
( 0-20-1)	0.00062	"440"	1	vibration	20
(179-20-3)	0.00062	"440"	1	vibration	20
( 0-60-2)	0.00062	"440"	1	vibration	60
(179-60-4)	0.00062	"440"	1	vibration	60
( 0-00-5)	0.00062	"440"	1	vibration	0
( 0-00-6)	0.00062	"440"	1	pluviation	0

2. Varied Normalized Depth of Burial

( $\lambda = 0.23$  to  $0.99 \text{ m/kg}^{1/3}$ )

A separate series of 11 tests was conducted to study the variation in crater size and shape with depth of charge burial (Table 5.2c). In this test series,  $\lambda$  ranged from 0.23  $\text{m/kg}^{1/3}$  to 0.99  $\text{m/kg}^{1/3}$ . All of the tests used oven-dry Tyndall Beach Sand, and all of the specimens were compacted through pluviation. In the design of this test matrix, the modeling of models technique was used whenever possible.

TABLE 5.2c. TEST MATRIX FOR THE SERIES OVER A RANGE OF DOB.

Test Number	Scaled Explosive (kg TNT)	RP-83 size (mg) (PBX)	G-Level (Detonator)	Preparation Method	S (%)	Normalized DOB ( $m, kg^{1/3}$ )
(rpm-S-#)			(G)			
(194-V0-1)	231	"660"	65	pluviation	0	0.23
(186-V0-2)	231	"880"	60	pluviation	0	0.43
(167-V0-3)	46	"220"	49	pluviation	0	0.73
(195-V0-4)	116	"220"	67	pluviation	0	0.73
(202-V0-5)	231	"440"	72	pluviation	0	0.79
(139-V0-6)	46	"880"	35	pluviation	0	0.99
(179-V0-7)	116	"440"	57	pluviation	0	0.99
(190-V0-8)	231	"660"	65	pluviation	0	0.99

## SECTION VI

### SPECIMEN PREPARATION

#### A. SOIL DESCRIPTION

The soil used in this research, termed Tyndall Beach Sand, was quartz beach sand found on Tyndall Air Force Base in Florida. The sand was washed, oven-dried, and passed through a number 20 sieve prior to use. As shown in Figure 6.1, this sand has an almost uniform particle size distribution. The characteristic shape of the sand is classified as subrounded to subangular (Figure 6.2). The calculated parameters for Tyndall Beach Sand are listed in Table 6.1.

TABLE 6.1. SOIL PARAMETERS FOR TYNDALL BEACH SAND.

$D_{10}$ (mm)	0.17 mm
$D_{50}$ (mm)	0.24 mm
$C_u$	1.53
$C_c$	0.95
Density of solids	2,650 kg/m <sup>3</sup>

The sand was compacted either through vibration or pluviation to a dry density of 1522 kg/m<sup>3</sup>. The minimum and

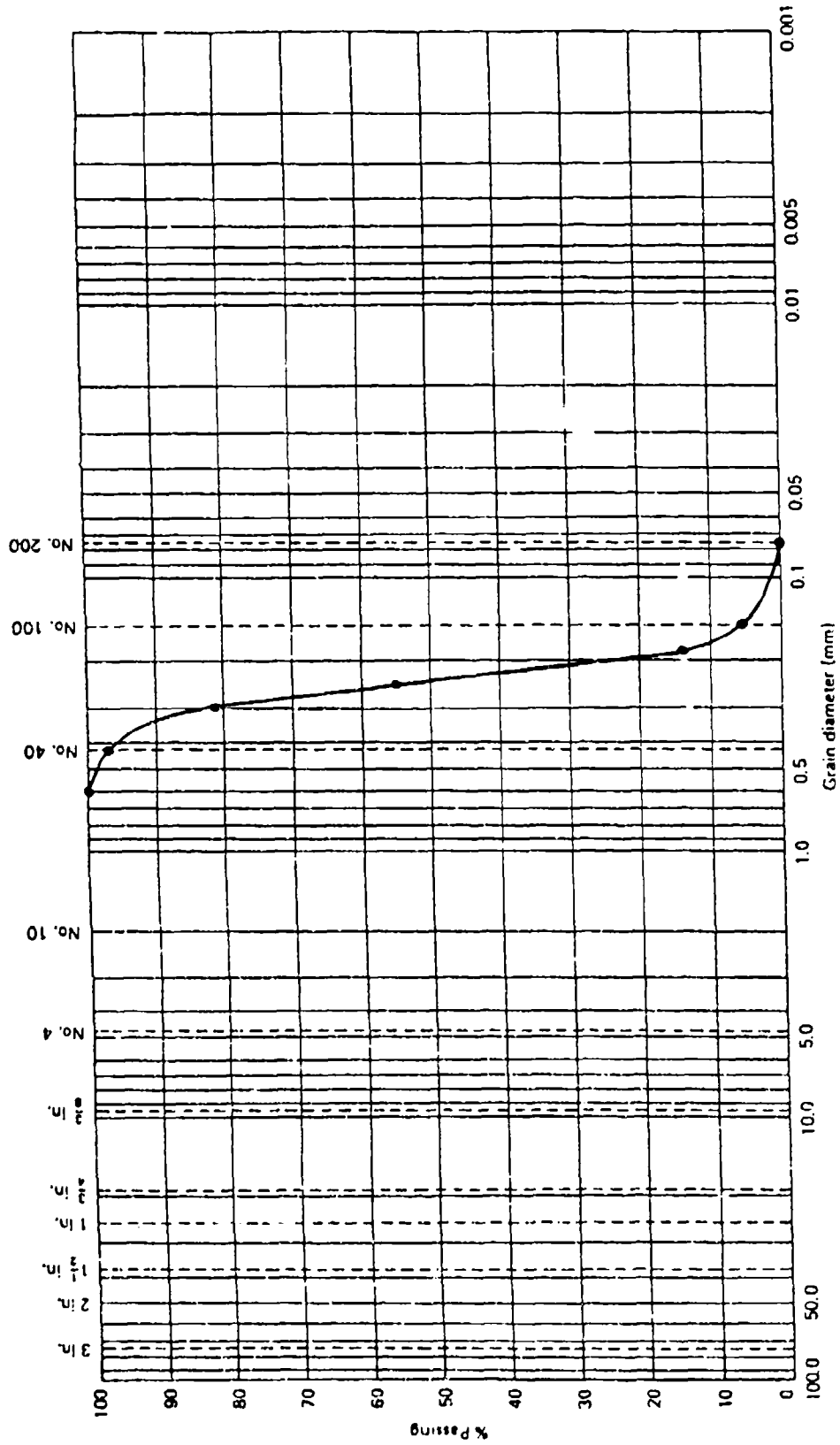


Figure 6.1 Particle Size Distribution for Tyndall Beach Sand.

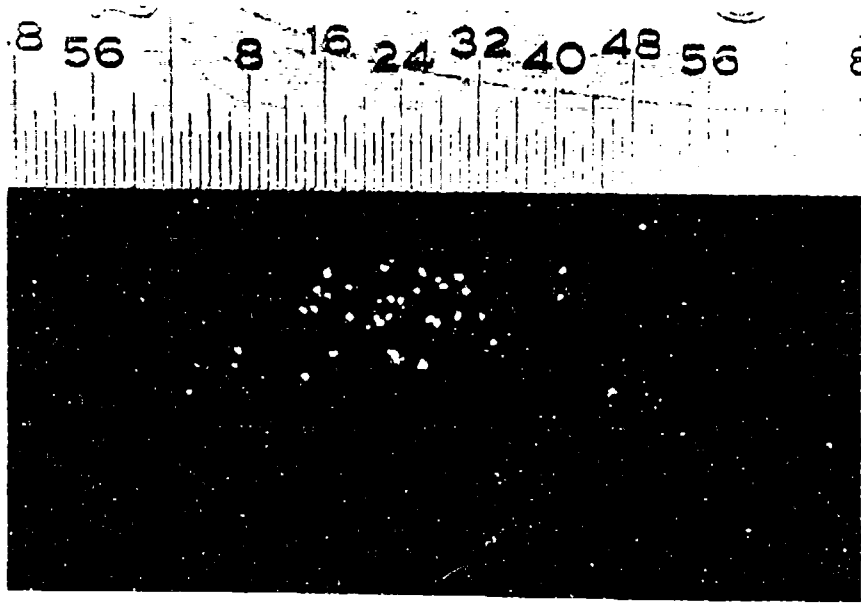


Figure 6.2 Photograph Showing the  
Characteristic Shape of Tyndall  
Beach Sand.

maximum dry densities for the sand are 1450 kg/m<sup>3</sup> and 1630 kg/m<sup>3</sup> respectively (ASTM D4253 and D4254). At a dry density of 1522 kg/m<sup>3</sup>, the void ratio is 0.74 which leads to a relative density of 39 percent.

#### B. SATURATION PROCEDURE

For tests in partially saturated sand, distilled water was added to the specimen prior to placement. The procedure involved weighing out enough dry sand for one lift in the centrifuge buckets, adding the desired weight of distilled water, and mixing the moist sand in a Chiyoda flexible wall mixer (Omni-Mixer model OM-10, Figure 6.3).

Five lifts were used to fill the aluminum centrifuge buckets measuring 457 mm in inside diameter and 305 mm in height. The first four lifts were 50 mm in height. The height of the fifth lift was determined by the normalized depth of charge burial ( $\lambda$ ) which in turn was determined by the test G-level and charge size. Therefore, for similar tests, the depth of the overburden was varied instead of the charge elevation.

#### C. PLACEMENT METHODS

All partially saturated specimens were compacted using the vibratory method. In the constant normalized DOB test series, the dry specimens were compacted using the vibratory method to maintain a consistent method of preparation. In the



Figure 6.3 Chiyoda Flexible Wall Mixer.

test series spanning a range of DOB, all specimens were pluviated.

### 1. Vibration

A top-down, vertical vibration technique was used to compact the partially saturated specimens. A Syntron magnetic vibrator (model No. V51 D1) was attached to an circular aluminum plate cut to 0.44 m in diameter. Each lift was compacted separately by placing the plate down against the sand (Figure 6.4).

The compaction was controlled by lift height markings painted around the inside of the bucket. Once the leveled lift matched the appropriate markings, the dry density of 1522 kg/m<sup>3</sup> had been attained. As a final check, the full bucket was weighed at the completion of compaction.

### 2. Pluviation

The pluviator used in this research was designed by Dr. Taylor of Virginia Polytechnic Institute and State University<sup>2</sup> and is shown in Figure 6.5. In pluviation, the soil is rained, allowed to free-fall, through holes and several sieves (wire screens) into the specimen bucket (Figure 6.6). For a specific soil and set free-fall heights, the final density of the soil as it falls into the bucket is a

---

<sup>2</sup>Personal Communication, Mike Purcell, Engineering Assistant, Applied Research Associates, Inc., Tyndall AFB, Florida.



Figure 6.4 FMC Corporation Syntron Magnetic Vibrator.



Figure 6.5 Tyndall Air Force Base Pluviator.

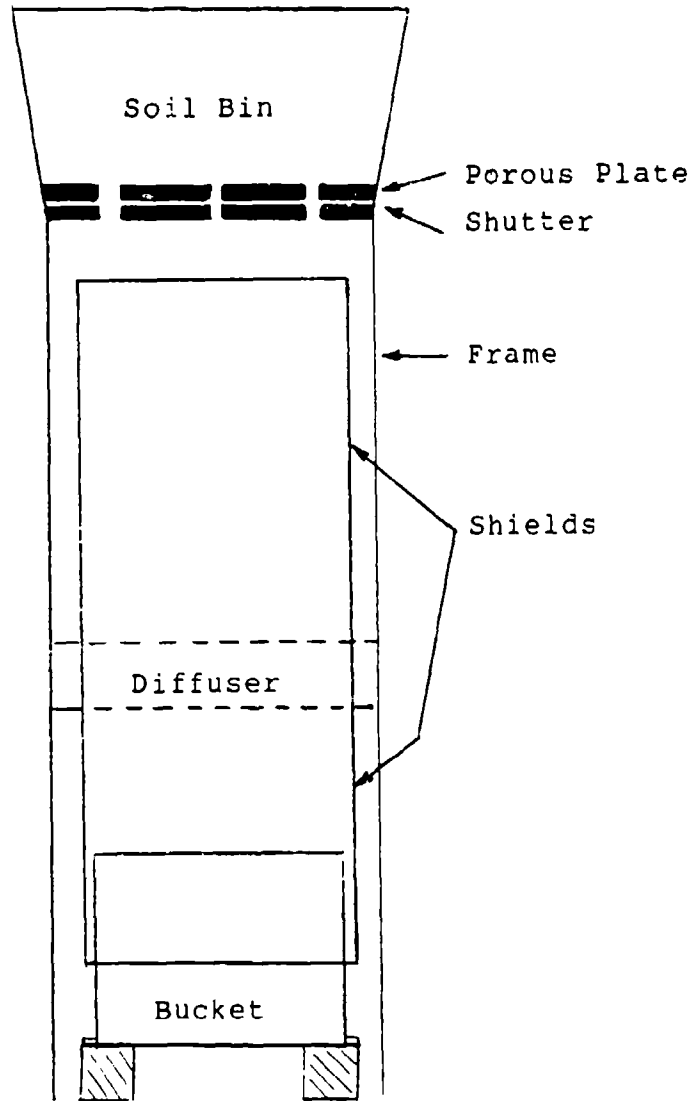


Figure 6.6 Pluviator Schematic (Fragoszy and Taylor, 1989).

function of the number and size of the holes in the board, and the opening sizes of the sieves (Fragaszy and Taylor, 1989).

SECTION VII  
TEST PROCEDURES

A. CENTRIFUGE FACILITY

The centrifuge facility at Tyndall Air Force Base was utilized for this research. The facility contains a 133 G-KN centrifuge (Genisco model E-185) enclosed in a circular concrete structure. The centrifuge radius is 1.83 m, and the payload platforms each measure 76 cm x 76 cm. The payload platforms are attached to the centrifuge by two symmetrical cantilever arms and are thus allowed to swing freely during the operation of the centrifuge (Figure 3.1.b). Weights were added to the opposing arm to balance the centrifuge. An electronic balancing system assisted this manual balancing process and automatically kept the centrifuge in balance during flight.

The data acquisition system (Pacific Transient Data Recorder model 5700) and a Miletus Associates (model 0) video camera have been mounted on the central axis of the centrifuge (Figure 7.1). These additions allow on-board data capture and the photographic recording of all centrifuge tests. The centrifuge is operated by a hydraulic drive system from a nearby control room. The video is connected to a monitor in

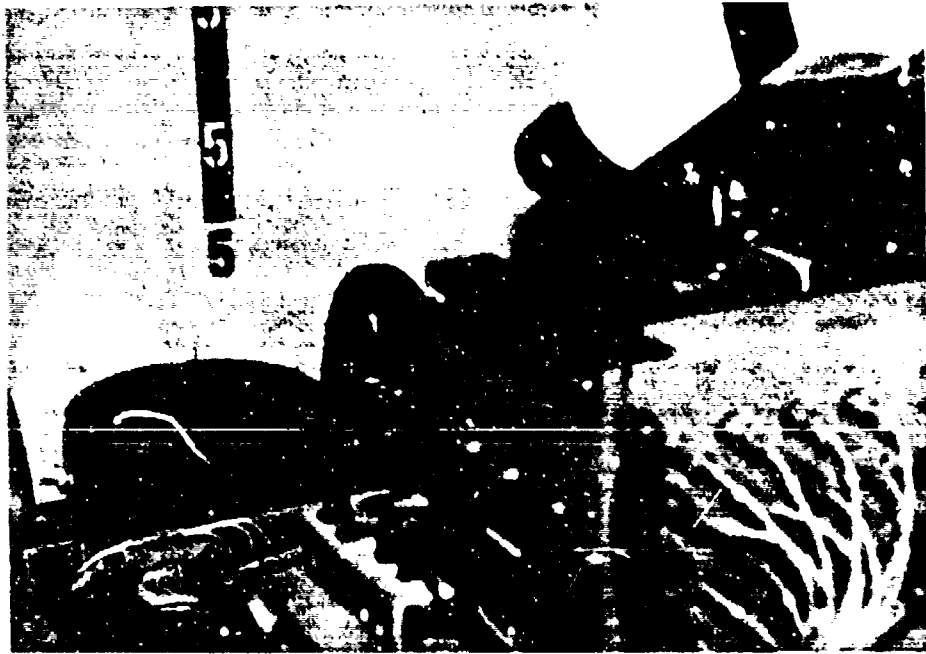


Figure 7.1 Miletus Video Camera and Pacific Data Acquisition System Mounted on the Centrifuge.

the control room such that real-time viewing of a test is possible.

#### B. DETONATOR PLACEMENT

The RP-83 detonators were placed in the specimens just prior to centrifuge start-up. Detonator placement could not be made during compaction because of safety regulations.

For the partially saturated specimens, an 8 mm diameter hole was manually drilled into the sand. Capillary forces within the sand were strong enough to prevent the walls of the hole from caving in. For the dry specimens, a glass tube with an inside diameter of 10 mm was used to retain the surrounding soil and permit excavation. Using a guide and suction to remove sand grains from inside the glass tube, the glass tube was gently pushed into the sand.

When the detonator was placed into the drilled hole or the glass tube, a mark on the detonator wires corresponding to the sand surface verified the correct placement of the detonator. The guide designed to place the detonator at the center of the bucket and to keep the drill or glass tube oriented in the vertical direction is pictured in Figure 7.2. Markings along the side of the guide allowed the depth to the bottom of the hole to be measured within 1 mm. All depth of burial distances are measured from the surface to the center of mass of the charge.



Figure 7.2 Detonator Placement Guide.

Dry sand was poured back into the hole to keep the detonator vertical and to hold the detonator in place. Knudson et al. (1972) found that the choice of material used to stem, backfill, a charge was not critical, and that significant increases in crater radius or depth did not occur with stemming beyond 50 percent of the emplacement hole length. For the dry tests, the glass tube was removed once the hole had been stemmed.

#### C. CENTRIFUGE OPERATION

The operation of the centrifuge during a test consisted of running the centrifuge up to the desired G-level, firing the detonator, and decelerating the centrifuge back down to a stationary position. Each test required approximately 10 minutes from centrifuge start-up to shut-down.

The electronic connection of the Reynolds Industries EBW firing system (model FS-17) to the detonator passed through one of the 28 slip rings of the centrifuge. The firing sequence was manually armed and operated. When the desired G-level was attained, the charge was detonated.

#### D. APPARENT CRATER MEASUREMENT

##### 1. Inside Diameter and Depth

The crater depth and inside diameter were measured immediately after the centrifuge came to rest. No changes in the apparent crater shape were observed during centrifuge

deceleration. The measurements were taken in two different directions, one perpendicular to the other. Thus, the reported dimensions are an average. Both depth measurements were taken at the deepest point in the crater.

## 2. Volume

Crater volume measurements were made from a clay replica. The clay replica was made from a concrete mold taken after the crater diameter and depth had been measured. When the clay replica was filled with water, the weight of water in grams equaled the crater volume in cubic centimeters.

## E. MOISTURE CONTENT MEASUREMENT

The downward migration of water that occurs during a centrifuge test quickly became evident. The centripetal acceleration of a centrifuge desaturates the specimen as gravity would desaturate the prototype soil layer. To determine the extent of the desaturation, the specimen was sampled immediately following the test. The moisture content present at the completion of the test was assumed to approximate the moisture content present during the test, and the upward migration of water during the deceleration of the centrifuge was assumed to be minimal.

Samples were taken from the top, middle, and bottom 51 mm of the specimen. After being weighed, the samples were dried in an oven at 120 °C for 24 hours. One hole was located

towards the center of the bucket at the crater edge, while a second was located at the side of the bucket. Initially, four holes were used to sample the specimen, two at the 12 o'clock position, and two at the 3 o'clock position (Figure 7.3). After several tests, however, four holes proved to be redundant. The moisture content at the crater edge or at the side of the bucket did not vary significantly from one position to the other; therefore, sampling at the 3 o'clock position was discontinued.

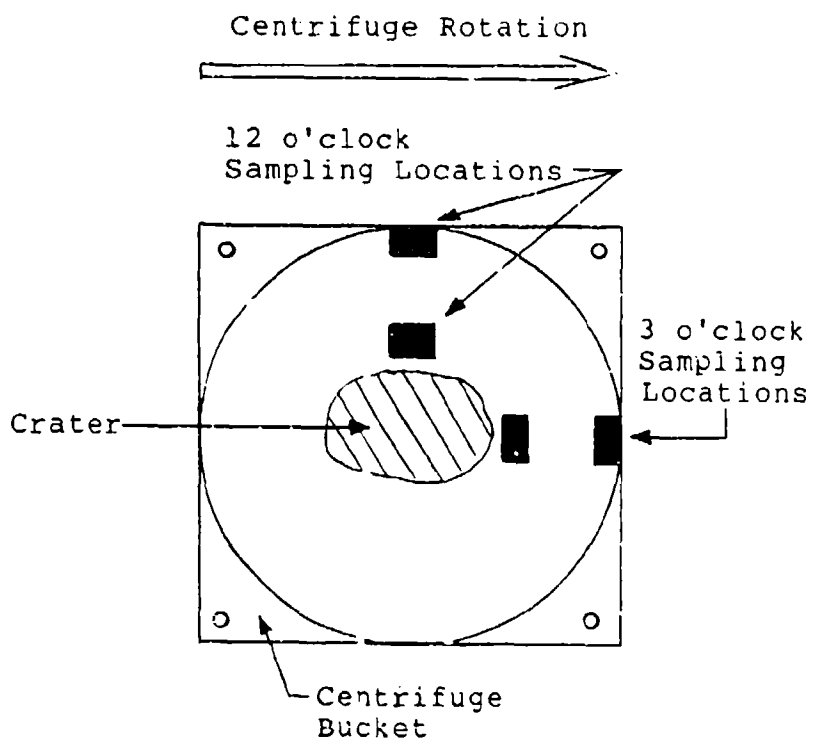


Figure 7.3 Sampling Locations of the Moisture Content Analysis, Top View. (NTS)

SECTION VIII  
RESULTS AND ANALYSIS

A. SCALED CRATER DIMENSION VERSUS SCALED EXPLOSIVE MASS

The current research differs from the previous centrifuge cratering studies in soil type, saturation, and density (Table 8.1). Figures 8.1, 8.2, and 8.3 show the scaled apparent crater volume, radius, and depth plotted against scaled explosive mass.<sup>3</sup> The best-fit lines for these relationships developed from the current research have the same general slope and plot above those developed from the data presented by Goodings et al. (1988) and Schmidt and Holsapple (1978, 1980). The constant slope confirms the independence of soil type, saturation, and density from explosive mass.

Schmidt and Holsapple (1980) and Goodings et al. (1988) were able to relate 1 G tests with centrifuge tests because the charges were placed at the soil surface (half-buried). Surface charges have confining pressures of zero at all G-levels. For buried charges, the confining pressures are a function of depth and G-level which makes the comparison of tests at 1 G and high-G unreasonable for frictional materials

---

<sup>3</sup>Plotted in english and metric units to allow comparison with other work; conversion equations provided in figures. Scaled crater dimensions are prototype crater dimensions.

**TABLE 8.1. CENTRIFUGE TEST SPECIFICATIONS.**

	<u>Current Research (1992)</u>	<u>Goodings et al. (1988)</u>	<u>Schmidt &amp; Holsapple (1978)</u>	<u>Schmidt &amp; Holsapple (1979)</u>
Soil Type	Tyndall Beach Sand	Ottawa Sand	Ottawa Sand	Desert Alluvium
Sat. (%)	0 - 70	0	0	15 <sup>a</sup>
Dry Density (kg/m <sup>3</sup> )	1522	1704	1779 <sup>b</sup>	1572 <sup>c</sup>
DOB (m/kg <sup>1/3</sup> )	Fully Buried (0.23 to 0.99)	Half- Buried (0)	Half- Buried (0)	Half- Buried (0)
<p>a. Average value for 21 tests with saturations ranging from 3 to 29 percent.</p> <p>b. Average value for 19 tests with dry densities ranging from 1677 kg/m<sup>3</sup> to 1802 kg/m<sup>3</sup>.</p> <p>c. Average value for 21 tests with dry densities ranging from 1429 kg/m<sup>3</sup> to 1657 kg/m<sup>3</sup>.</p>				

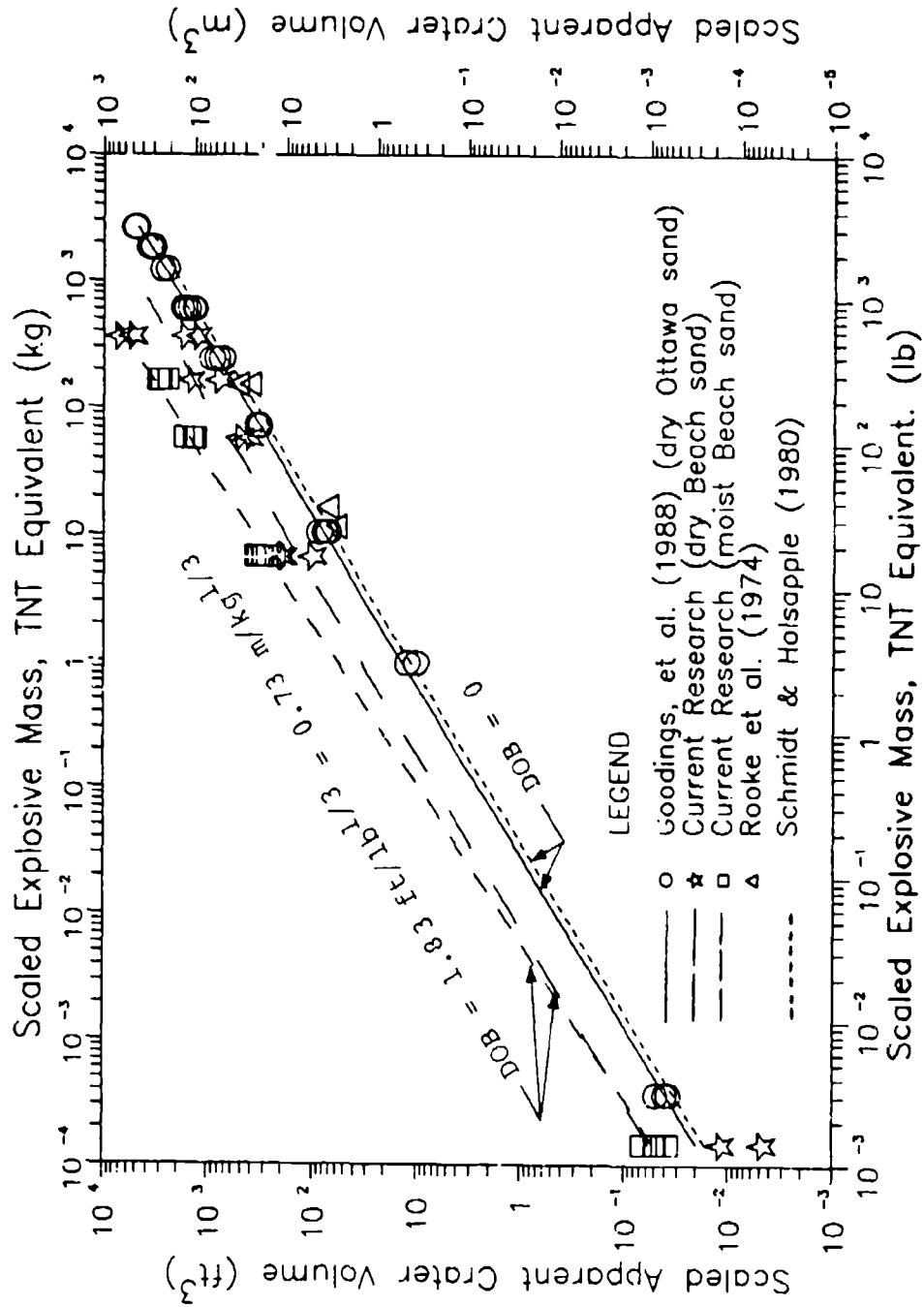


Figure 8.1 Scaled Apparent Crater Volume Versus Scaled Explosive Mass, TNT Equivalent. (Conversions:  $0.0283 \text{ ft}^3 = 1.0 \text{ m}^3$ ,  $0.454 \text{ lb} = 1.0 \text{ kg}$ )

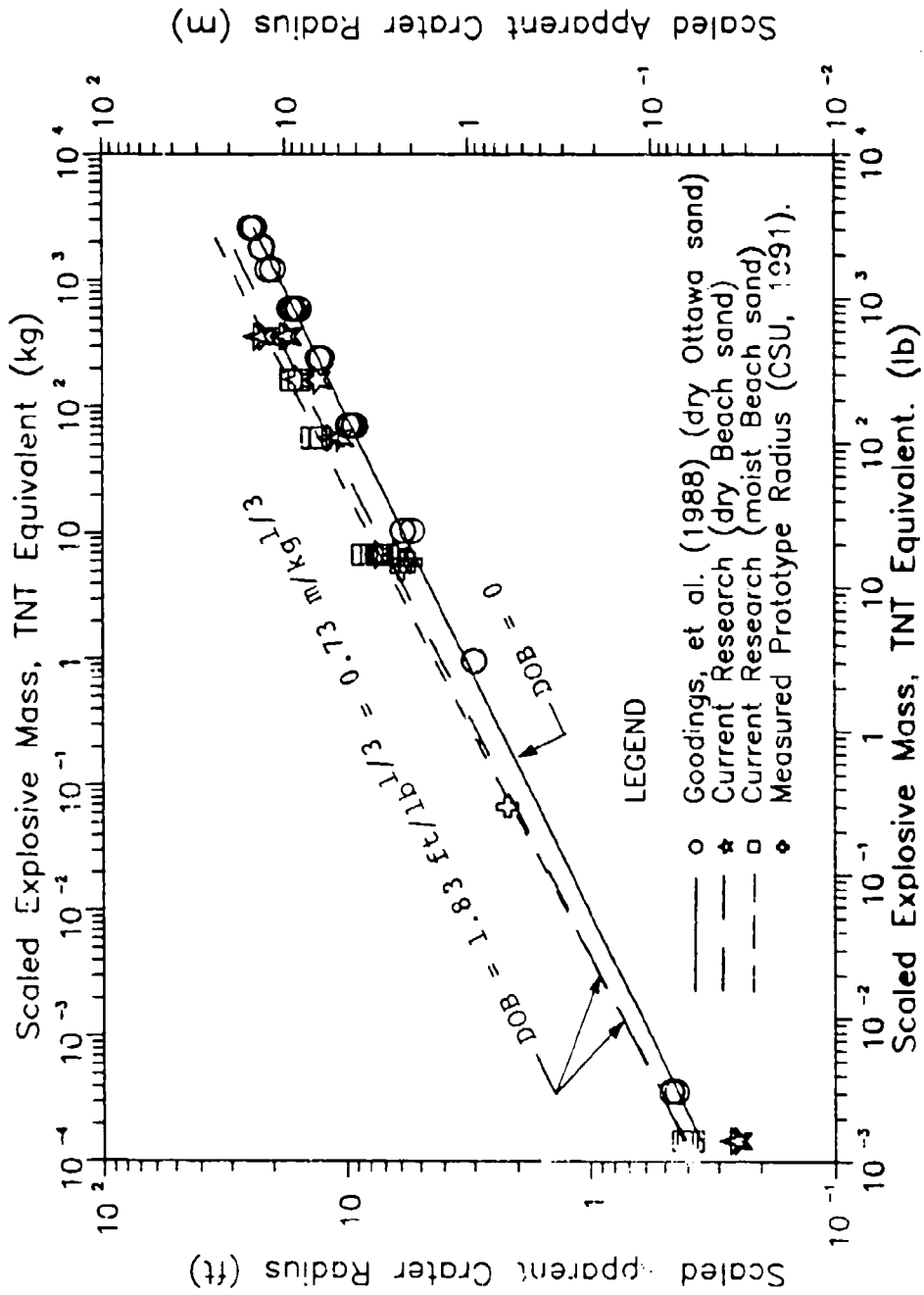


Figure 8.2 Scaled Apparent Crater Radius Versus Scaled Explosive Mass, TNT Equivalent. (Conversions: 0.305ft = 1.0m, 0.454lb = 1.0kg)

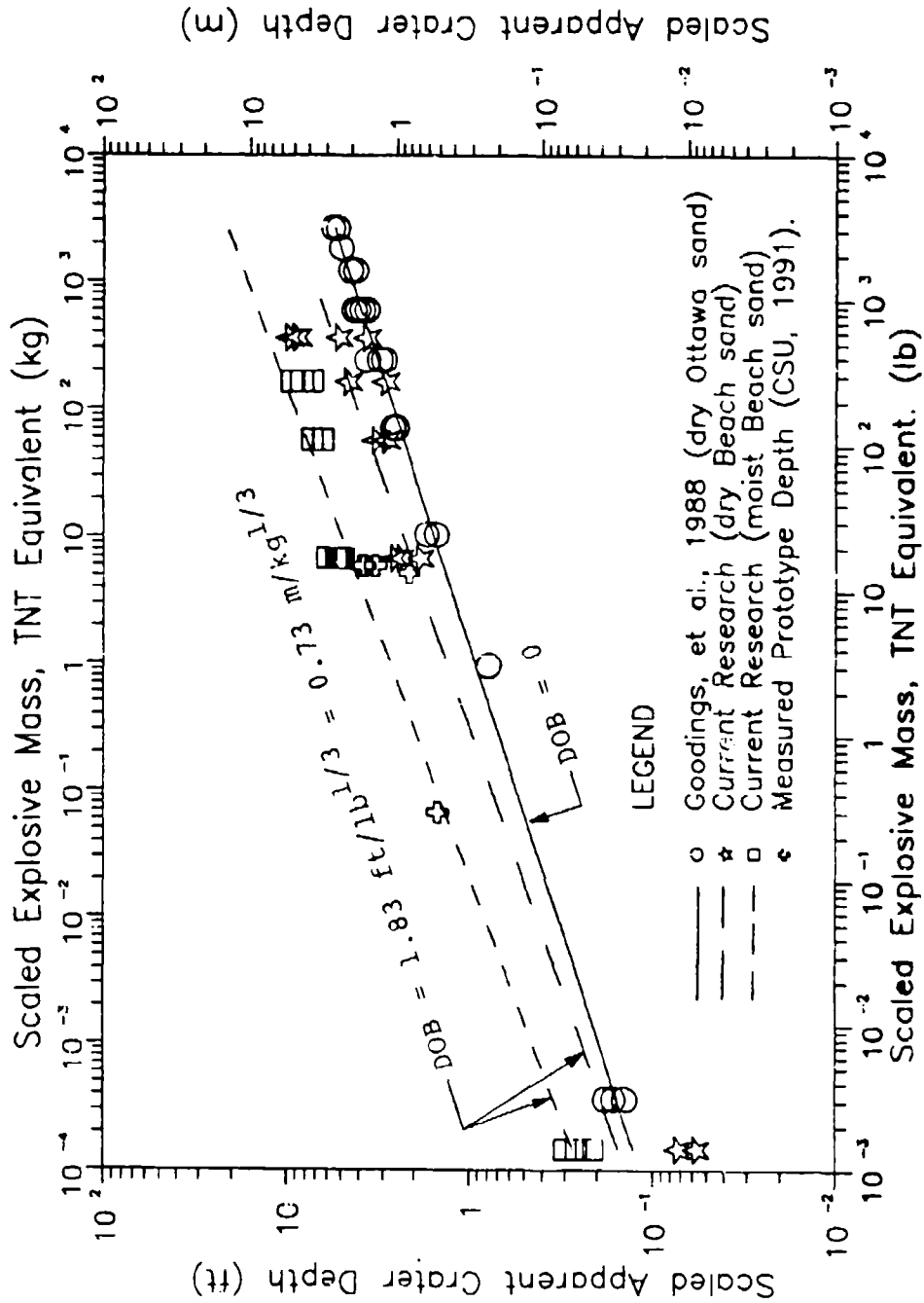


Figure 8.3 Scaled Apparent Crater Depth Versus Scaled Explosive Mass, TNT Equivalent. (Conversions: 0.305ft = 1.0m, 0.4541b = 1.0kg)

including dry sand. For cohesive materials, a comparison of 1 G and high-G tests may not be meaningless. As shown in section 8.B, the capillary forces within the sand produce an apparent cohesion which controls crater formation at elevated G-levels as well as at 1 G. Therefore, the partially saturated 1 G tests were included in the derivation of the centrifuge scaling laws whereas the dry 1 G tests were not.

The partially saturated tests are also compared to tests in moist ( $\approx$  4 percent moisture content,  $\approx$  15 percent saturation) desert alluvium (Schmidt and Holsapple, 1979) (Figures 8.4, 8.5, 8.6). Again, the best-fit lines for the data from the current research are greater than and parallel to the best-fit lines of other centrifuge research. The best-fit lines drawn through the data on a log-log scale have the form  $Y \propto W^n$  where the slope  $n$ , in these figures, is the yield exponent (see section II),  $W$  is the explosive mass, and  $Y$  is the scaled apparent crater dimension (volume, radius, depth).

Table 8.2 lists the yield exponents from this research as well as from the research by Goodings et al. (1988), Schmidt and Holsapple (1978, 1980), and the U.S. Army Engineer Waterways Experiment Station (Strange et al., 1961 ; Rooke et al., 1974). The yield exponents of the current research are closely aligned with the yield exponents of the other research. The yield exponents for the dry Tyndall Beach Sand are almost identical to the yield exponents of the dry Ottawa Sand, and the yield exponents for the moist Tyndall Beach Sand

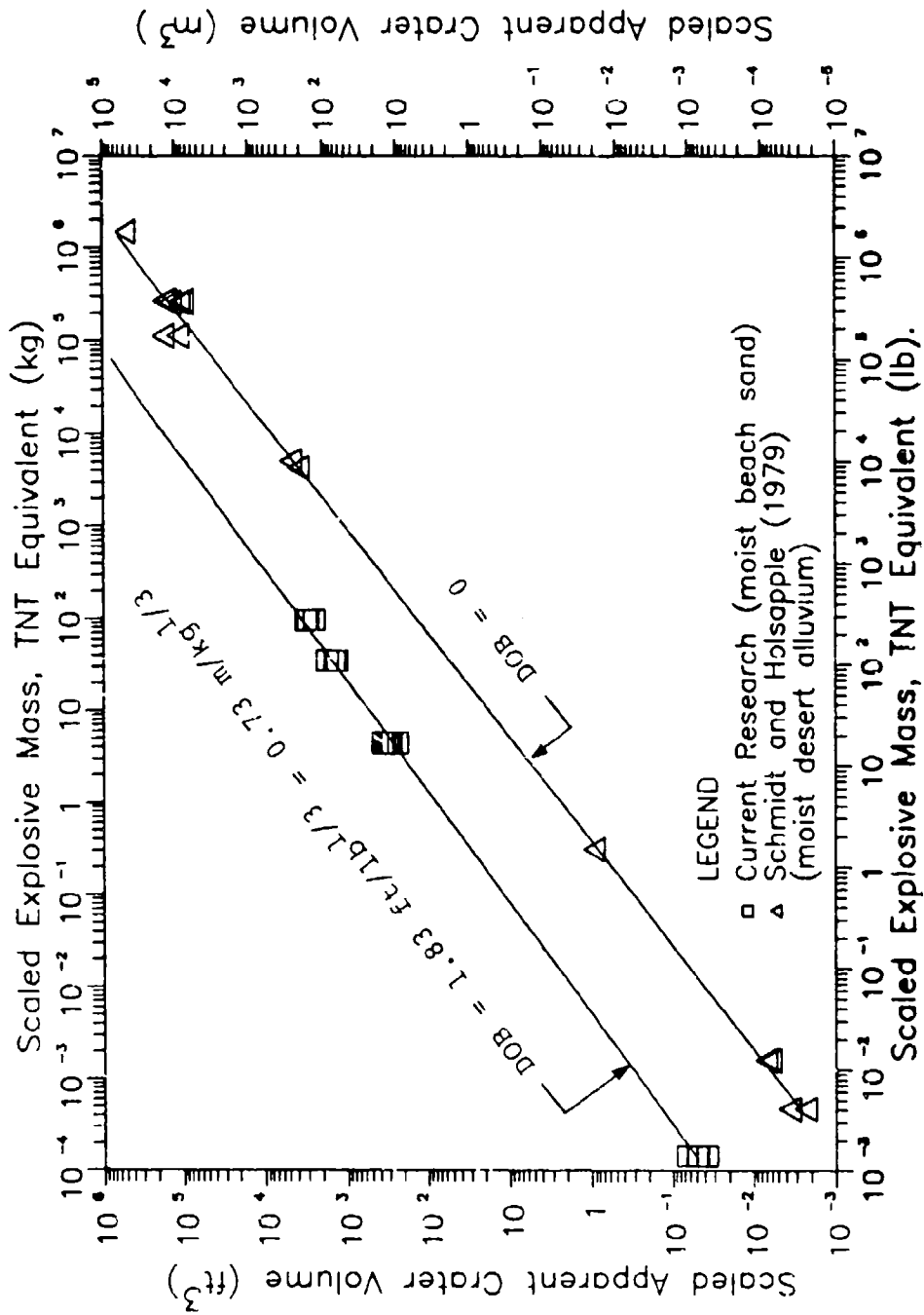


Figure 8.4 Scaled Apparent Crater Volume Versus Scaled Explosive Mass, TNT Equivalent. (Conversions: 0.0283ft<sup>3</sup> = 1.0m<sup>3</sup>, 0.454lb = 1.0kg)

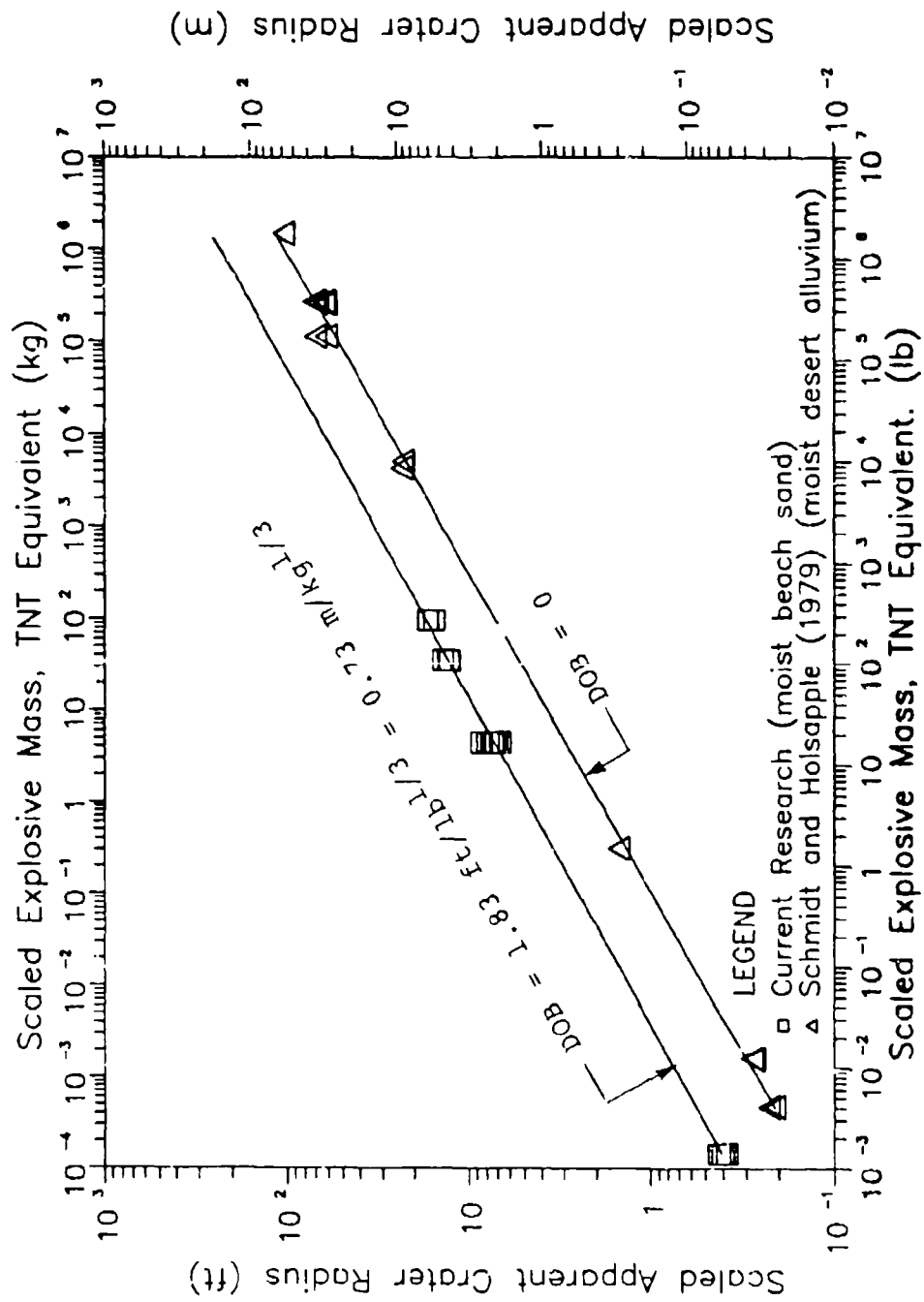


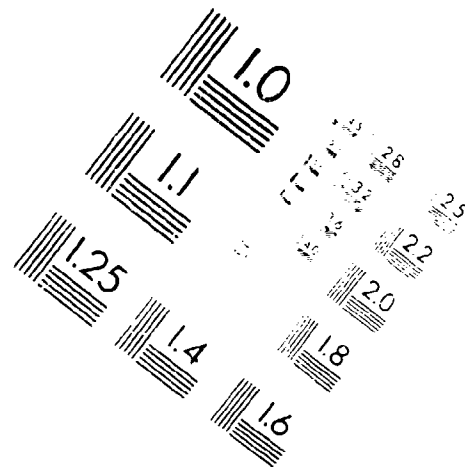
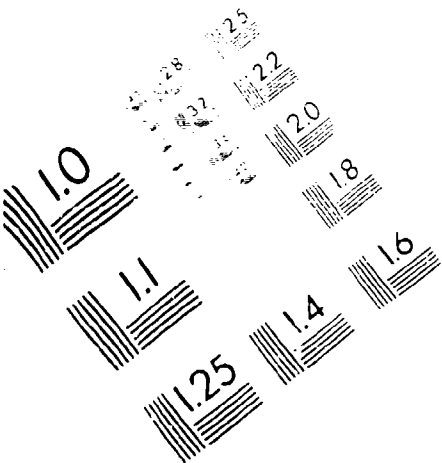
Figure 8.5 Scaled Apparent Crater Radius Versus Scaled Explosive Mass, TNT Equivalent. (Conversions: 0.305ft = 1.0m, 0.454lb = 1.0kg)



**AIM**

**Association for Information and Image Management**

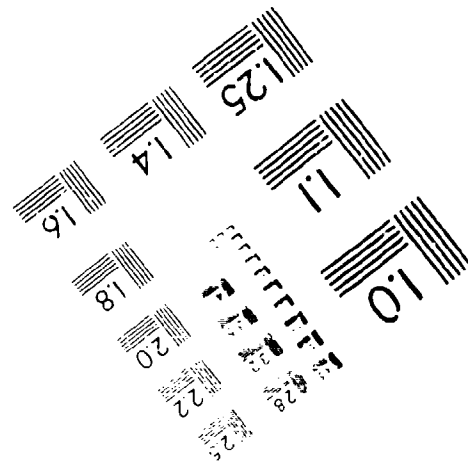
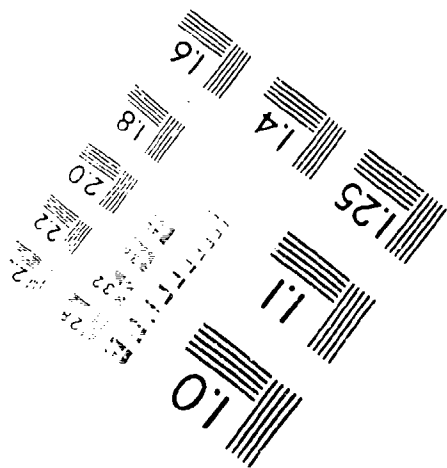
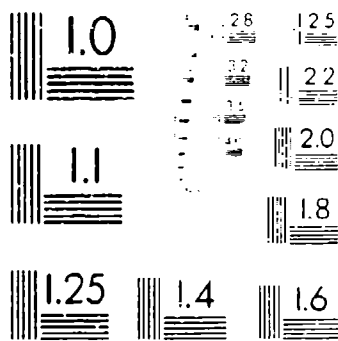
180 Wayne Avenue, Suite 1104  
Silver Spring, Maryland 20910  
301 581 9302



Centimeter



Inches



MANUFACTURED TO AIM STANDARDS  
BY APPLIED IMAGE, INC.

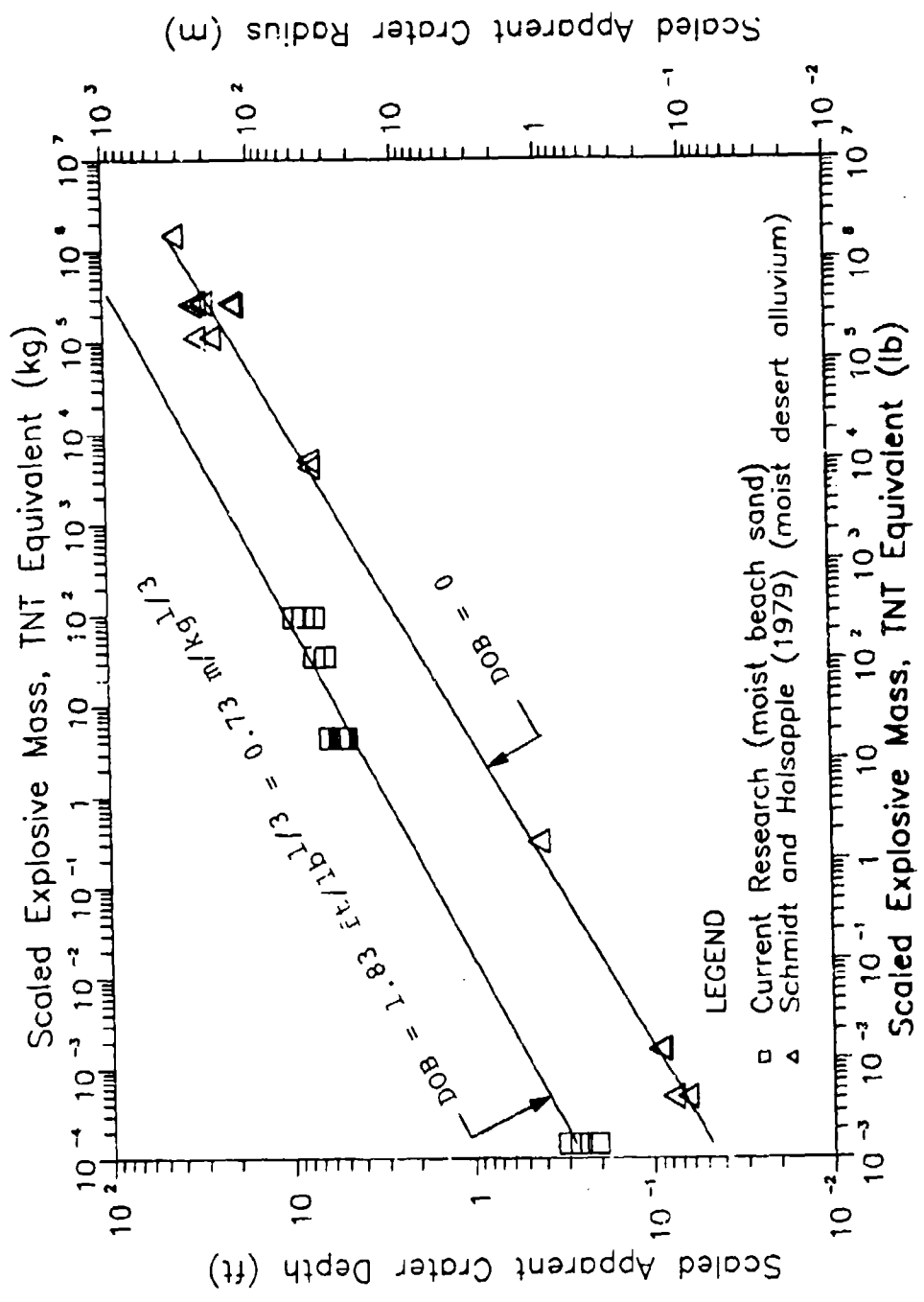


Figure 8.6 Scaled Apparent Crater Depth Versus Scaled Explosive Mass, TNT Equivalent. (Conversions: 0.305ft = 1.0m, 0.454lb = 1.0kg)

TABLE 8.2. CRATER DIMENSION YIELD EXPONENTS FOR CHARGE MASS, W.

Crater Dimension	Current Research	Goodings et al.	Schmidt & Holsapple			WES		
			(1988)	(1978)	(1980)	(1974) <sup>b</sup>	(1974) <sup>b</sup>	(1961) <sup>c</sup>
	(1992)* Tyndall Beach Sand	Ottawa Sand	Ottawa Sand	Ottawa Sand	Desert Alluvium	Unspec. Sand	Desert Alluvium	Unspec. Sand
Volume - Dry	0.831	0.84	0.842					
Volume - Moist	0.914			0.974		0.951	0.963	
Radius - Dry	0.297	0.29	0.280					0.270
Radius - Moist	0.308			0.316		0.306	0.305	
Depth - Dry	0.279	0.28	0.279					0.240
Depth - Moist	0.297			0.326		0.355	0.238	

\* Yield Exponents for the dry test data do not include 1 G test results.  
Yield Exponents for the moist test data include 1 G test results.

<sup>b</sup> Rooke et al. (1974),  $1.1 < \lambda < 2.0$ .

<sup>c</sup> Strange et al. (1961),  $0.9 < \lambda < 1.1$ .

are in agreement with the yield exponents for the moist Ottawa Sand and moist Desert Alluvium. In contrast to the WES report (Strange, 1961), apparent crater radius and depth both appear to scale by 0.3 rather than by 1/3.

The specimens tested in the current research were compacted to a dry density of 1522 kg/m<sup>3</sup> which is less than the 1704 kg/m<sup>3</sup> used by Goodings et al. (1988) and less than the 1779 kg/m<sup>3</sup> for Ottawa Sand used by Schmidt and Holsapple (1978, 1980) (Table 8.1). Therefore, the data plot as expected, above the data reported by Goodings et al. (1988) and Schmidt and Holsapple (1979, 1980).

Table 8.3 lists by depth of charge burial (DOB), the yield exponents for dry to moist sand, "wet" (unsaturated) sand, and moist desert alluvium established by Rooke et al. (1974) for full-scale tests. No consistent trend can be identified in these data for a variation in yield exponent with DOB. However, the yield exponents generated by the current research are in reasonable agreement with the variable results reported by Rooke et al. (1974).

The correlation coefficients ( $R^2$  values) from a regression analysis using the method of least squares on the log of the current research data for the constant DOB series ( $\lambda = 0.73 \text{ m/kg}^{1/3}$ ) are listed in Table 8.4. The  $R^2$  values for the crater dimensions in dry sand are lower than the  $R^2$  values for the crater dimensions in partially saturated sand in part because no 1 G tests are included. All of the  $R^2$  values for

**TABLE 8.3.** YIELD EXPONENTS REPORTED BY WES (Rooke et al., 1974).

<u>Normalized DOB</u>	<u>Crater Dimension</u>	<u>Dry to Moist Sand</u>	<u>Wet Unsat Sand</u>	<u>Moist Desert Alluvium</u>
0.05 < $\lambda$ < 0.2	Radius	0.280	0.304	
	Depth	0.270	0.313	
	Volume	0.906	1.012	
0.2 < $\lambda$ < 0.5	Radius	0.279	0.323	
	Depth	0.262	0.263	
	Volume	0.815	-----	
0.5 < $\lambda$ < 0.9	Radius		0.365	0.259
	Depth		0.266	0.327
	Volume		1.059	0.840
0.9 < $\lambda$ < 1.1	Radius		0.268	0.282
	Depth		0.237	0.280
	Volume		-----	0.859
1.1 < $\lambda$ < 2.0	Radius		0.305	0.306
	Depth		0.238	0.335
	Volume		0.863	0.951

**Table 8.4.** CORRELATION COEFFICIENTS FOR THE CURRENT RESEARCH AT ALL G-LEVELS.

<u>Dry</u>		<u>Partially Saturated</u>	
Volume	R <sup>2</sup> = 82.5%	Volume	R <sup>2</sup> = 99.8%
Radius	R <sup>2</sup> = 93.9%	Radius	R <sup>2</sup> = 99.8%
Depth	R <sup>2</sup> = 62.3%	Depth	R <sup>2</sup> = 98.2%

the crater dimensions in partially saturated sand are above 0.95. The lower observed scatter in the data presented by Goodings et al. (1988) may be attributed to a higher soil density. Greater consistency is expected for denser specimens.

#### B. MATERIAL STRENGTH MODEL.

The current research data at compaction saturation ( $S_c$ ) levels of 20 and 60 percent are applied to the material strength model proposed by Schmidt and Holsapple (1979) (see section III). Figures 8.7, and 8.8 show the pi terms for apparent cratering efficiency ( $\pi_v = V_p/W$ ), apparent crater radius ( $\pi_r = r(\rho/W)^{1/3}$ ) and apparent crater depth ( $\pi_d = d(\rho/W)^{1/3}$ ) plotted against the gravity scaled yield pi term ( $\pi_2 = G/Q[W/\delta]^{1/3}$ ). These figures follow the material strength model presented in Figure 4.3. In the derivation of the gravity scaled yield, the soil density, explosive density, and explosive specific energy were taken to be 1522 kg/m<sup>3</sup>, 1467 kg/m<sup>3</sup>, and 5.35 x 10<sup>10</sup> ergs/g (Meyer, 1987) respectively.

At 60 percent compaction saturation, the cratering efficiency appears to follow the model closely (Figure 8.7.b). At low yields, the curve is horizontal and the apparent cohesion dominates the cratering process. Then at a gravity scaled yield of approximately 3 x 10<sup>-7</sup>, the frictional component of soil strength begins to dominate the cratering

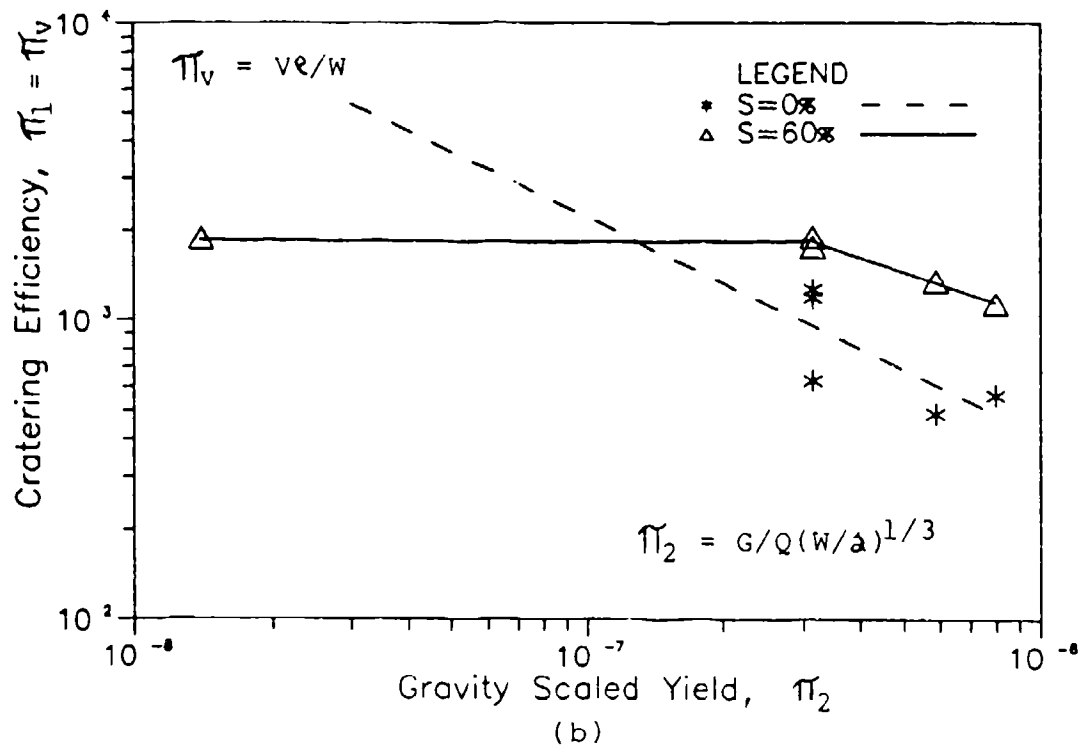
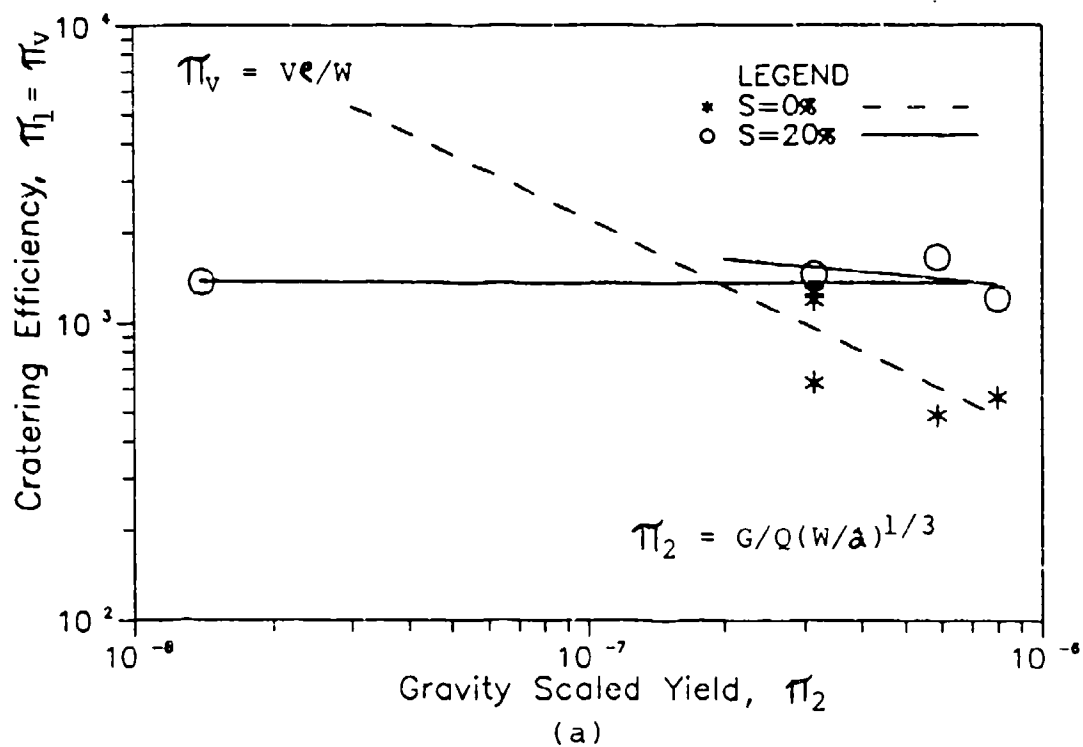
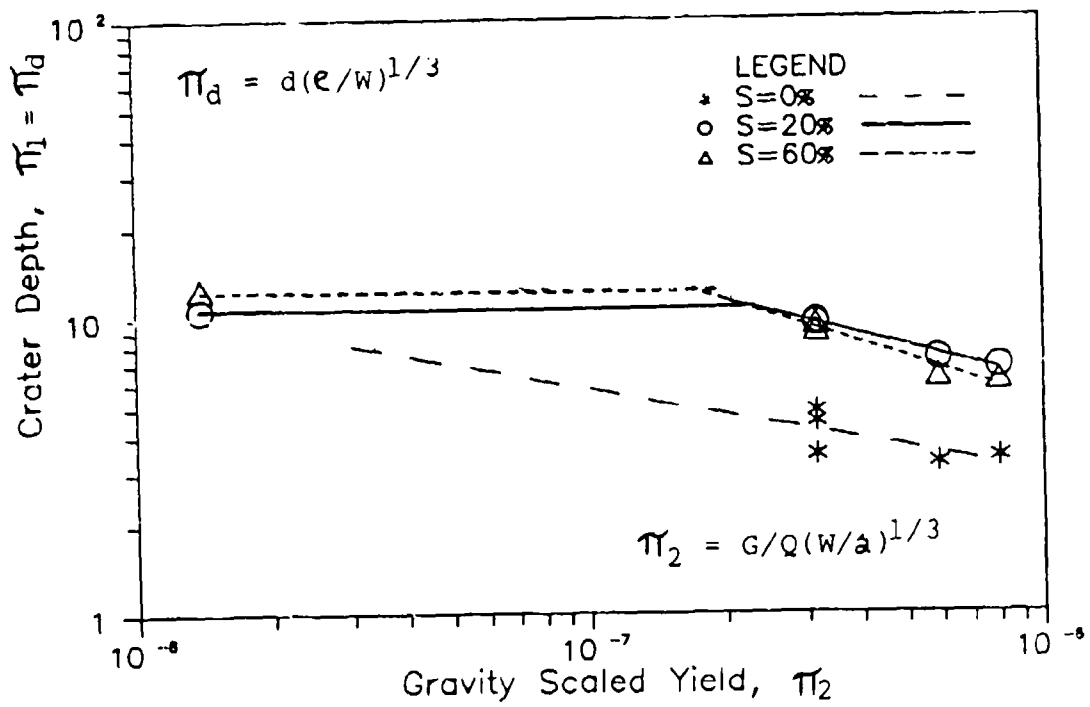
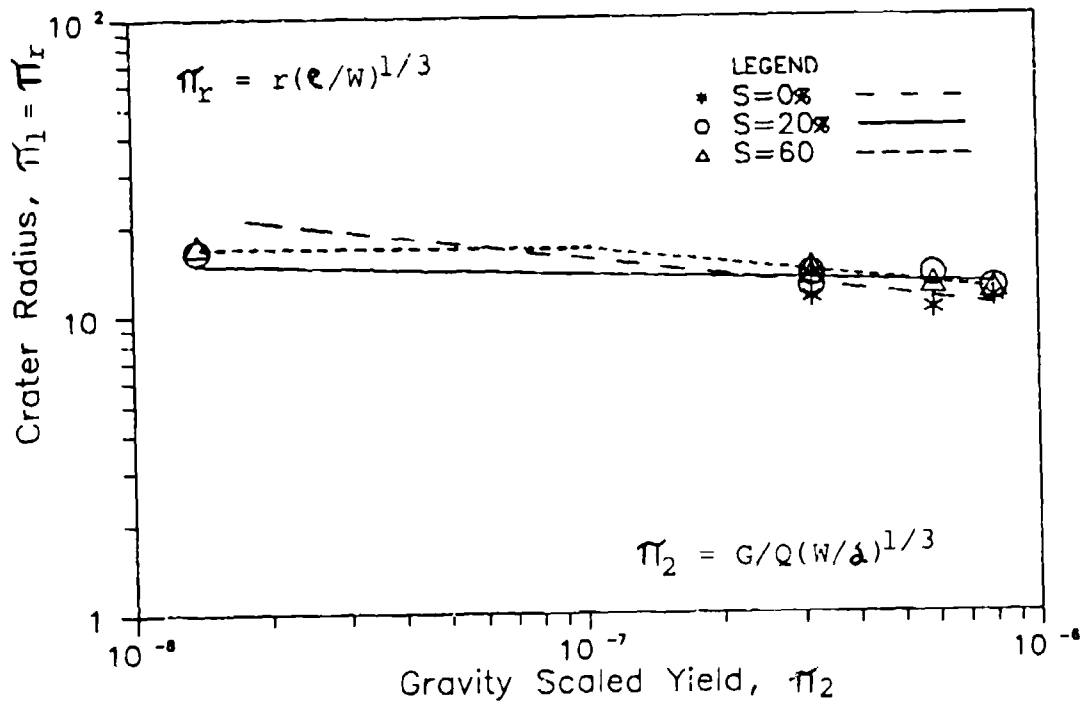


Figure 8.7 Cratering Efficiency ( $\pi_v$ ) Versus Gravity Scaled Yield ( $\pi_2$ ), Tyndall Beach Sand: a)  $S = 0\%$ ,  $20\%$ ; b)  $S = 0\%$ ,  $60\%$ .



(a)



(b)

Figure 8.8 Apparent Crater Dimensions Versus Gravity Scaled Yield ( $\pi_2$ ), Tyndall Beach Sand: a) Depth ( $\pi_d$ ); b) Radius ( $\pi_r$ ).

process. The apparent crater volume declines with increasing gravity scaled yield.

Figure 8.7.a showing cratering efficiency at 20 percent saturation is not as definitive. The transition point between cohesion and friction-dominated cratering appears to be just at or beyond the yields tested. Thus, there is an indication that cohesion dominates the cratering process to a higher yield at 20 percent compaction saturation than at 60 percent compaction saturation. The additional moisture in the specimens compacted at 60 percent may have a weakening effect. Overall, the cratering efficiency data support the results of Gaffney et al. (1989). In Tyndall Beach Sand, the transition point occurs at a few kilograms of explosive not a few thousand kilograms as reported by Schmidt et al. (1986). Apparent crater depth (Figure 8.8.a) also appears to follow the material strength model proposed by Schmidt and Holsapple (1979) which, for reasons mentioned in section IV, is unexpected. As for the cratering efficiency, the transition yield point for apparent crater depth at 60 percent compaction saturation is below the transition yield point at 20 percent compaction saturation.

Figure 8.8.b showing apparent crater radius is less clear because the best-fit line through the dry data is almost horizontal. The data at 60 percent compaction saturation take the form described above, but no transition point can be located for the data at 20 percent compaction saturation (The

best-fit line for the data at 20 percent compaction saturation does not include the point at 1 G, the lowest gravity scaled yield).

C. CRATER DIMENSIONS VERSUS DEPTH OF BURIAL

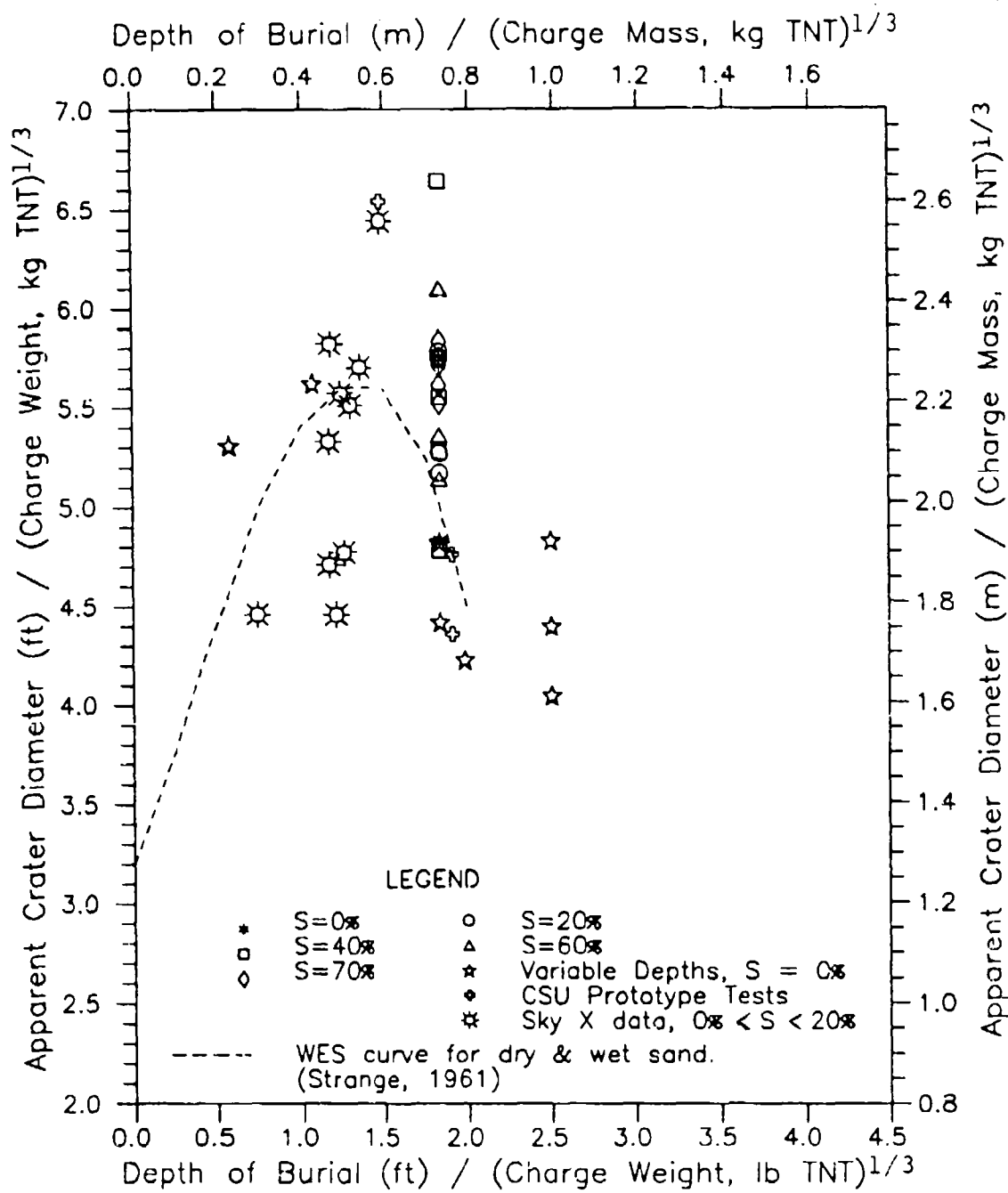
The graphs of apparent crater diameter versus depth of burial (DOB), and apparent crater depth versus DOB are presented in Figures 8.9 and 8.10. The data have been normalized to remove the influence of charge mass. Data from prototype tests at Colorado State University (CSU) and the full scale Sky X test area<sup>4</sup> at Tyndall AFB are included. The tests in dry sand plot below the tests in the partially saturated sand. No trend associated with the degree of saturation during compaction is apparent.

The best-fit curve for sand at  $0 < \lambda < 2.0$  generated from field tests at WES (Strange et al., 1961) is also included in Figures 8.9 and 8.10. These curves show an optimum DOB in the range of 1.25 to 1.5. The centrifuge tests of the current research in dry and partially saturated sand appear to indicate an optimum DOB for apparent crater diameter and depth near 1.75.

Figure 8.11 is a reproduction of Figure V-10 of the Air Force Protective Construction Design Manual. The figure shows the predicted range in apparent crater dimensions from dry

---

<sup>4</sup>Personal communication, Walter Buchholtz, Structural Research Engineer, HQ AFCEA/RACS, Tyndall AFB, FL 32403.



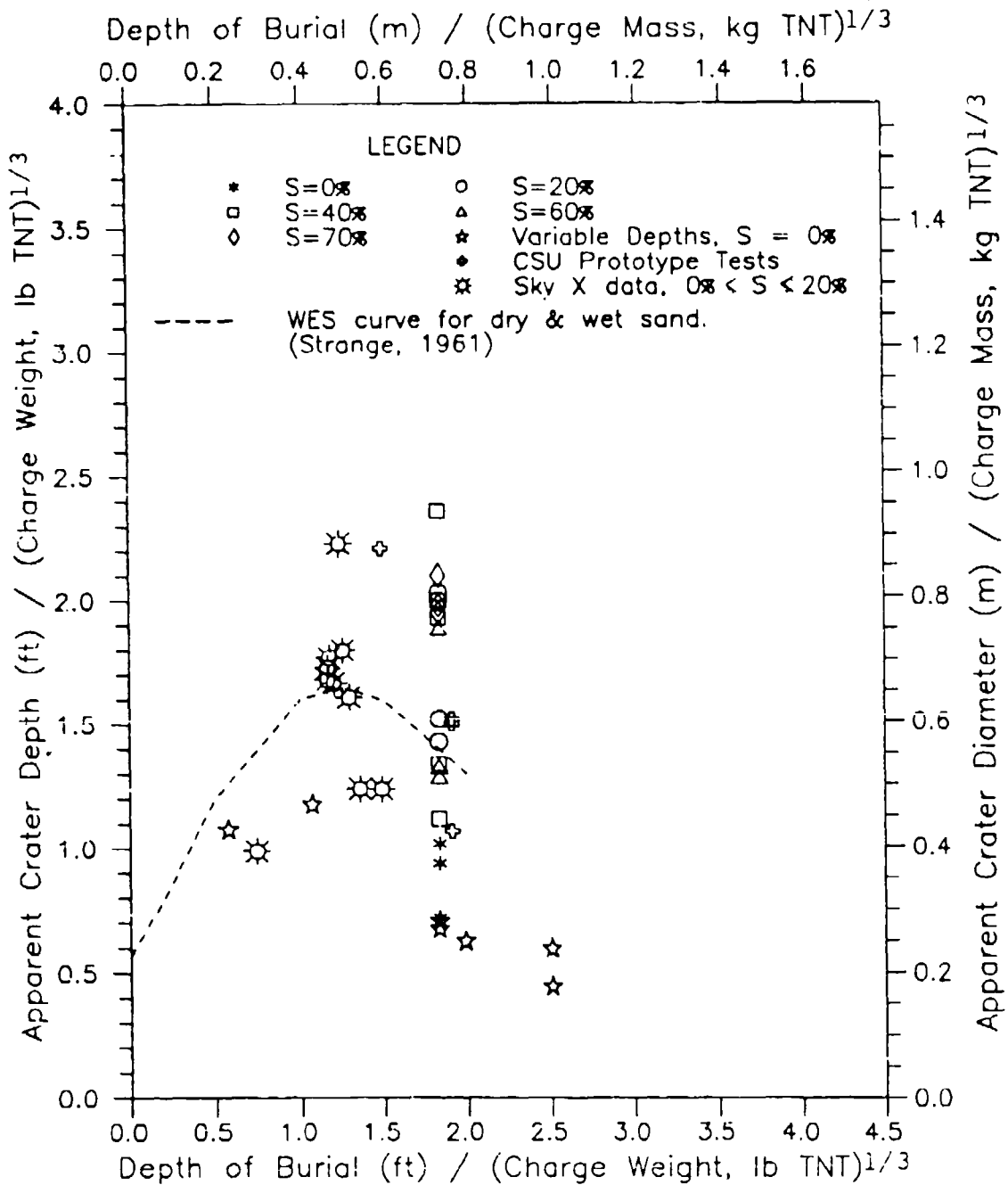


Figure 8.10 Normalized Apparent Crater Depth Compared to the U. S. Army Engineer Waterways Experiment Station Prediction Curve (Strange, 1961). (Conversion: 0.3967ft/lb<sup>1/3</sup> = 1.0m/kg<sup>1/3</sup>)

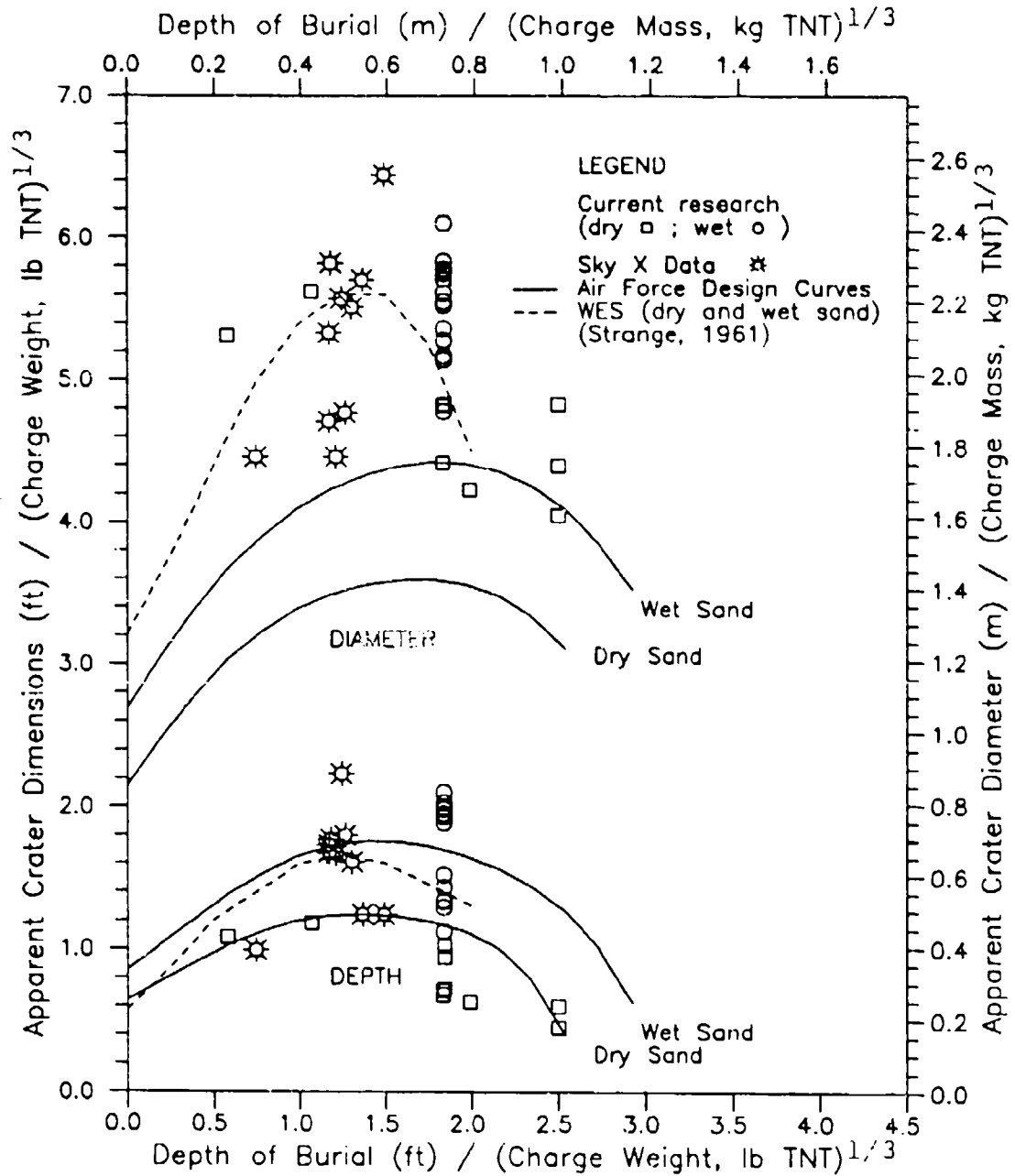


Figure 8.11 Normalized Apparent Crater Depth and Inside Diameter Compared to the Air Force Protective Construction Design Manual Prediction Curves.  
 (Conversion:  $0.3967 \text{ft}/\text{lb}^{1/3} = 1.0 \text{m}/\text{kg}^{1/3}$ )

(S = 0%) to wet (S > 0%) sand for different normalized depths. The Air Force design curves were generated using the conventional weapons computer program (CONWEP, 17 February 1988 version) which references Figure V-10.

Two observations concerning apparent crater diameter are evident from Figure 8.11. First, the majority of the field and centrifuge data lie above the range predicted by the CONWEP program. Second, the WES (Strange et al., 1961) best-fit curve also lies above the range predicted by the CONWEP program. The WES curve correlates better with centrifuge and full scale data than the curve generated by the CONWEP computer program.

In contrast, the range predicted by the CONWEP computer program for apparent crater depth appears to fit the test data well. The range contains the central data from the Sky X and centrifuge tests, and encompasses the WES curve.

Figure 8.12 shows graphical comparisons of the current research data with the apparent and true crater dimensions in "dry" and "wet" sand predicted by the CONWEP computer program. As in Figure 8.11, the data are normalized to remove the influence of charge mass. These figures illustrate how the apparent crater dimensions of the centrifuge tests fit the prediction curves of the Air Force Protective Construction Design Manual.

The scaled apparent crater depth data from the dry tests of the current research follow the apparent crater depth curve

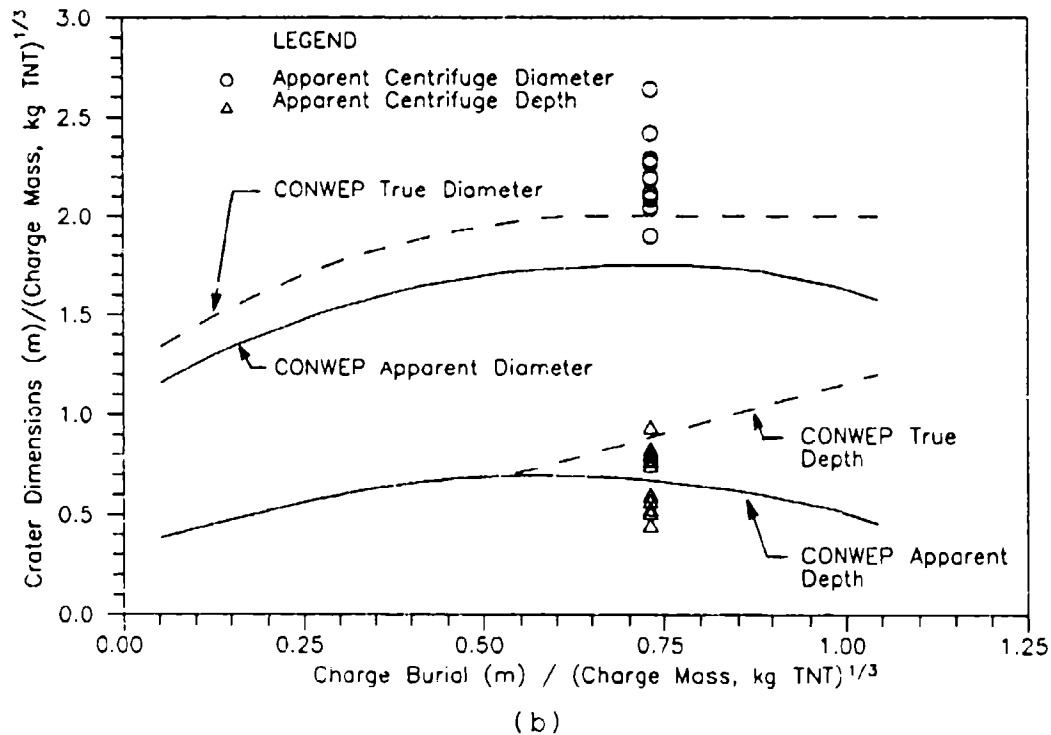
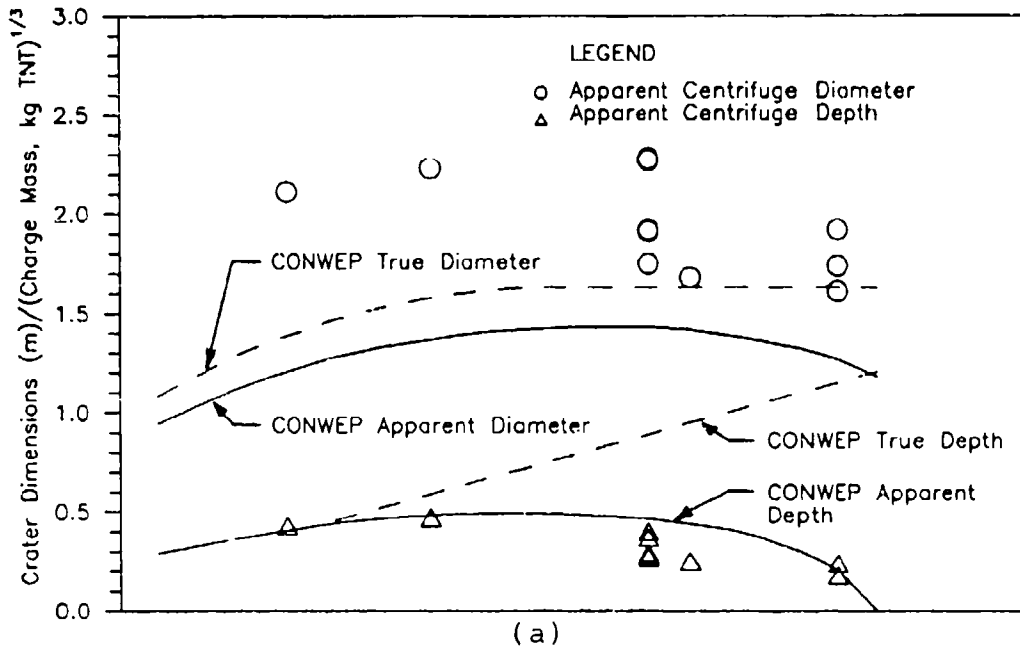


Figure 8.12 Normalized Apparent Crater Depth and Inside Diameter Compared to the Apparent and True Crater Dimensions Predicted by the Air Force Conventional Weapons Computer Program (CONWEP): a) Dry Sand; b) Partially Saturated Sand.

predicted for "dry" sand, whereas the scaled apparent crater depth data from the partially saturated tests vary from values less than the apparent depth curve to values greater than that true depth curve predicted for "wet" sand. Due to the unknown moisture content of the sand data used by the CONWEP computer program, the accuracy of the partially saturated apparent crater depth data can not be assessed.

The majority of the scaled apparent crater diameter data measured in the current research are larger than the predicted true crater diameter in both the "dry" and "wet" sand. Thus, the shape of the craters produced on the centrifuge is different than the shape of the craters predicted by the CONWEP computer program (Figure 8.13).

A best-fit curve from the DOB analysis by Schmidt (1979) is superimposed on the data from the current research (Figure 8.14). The data match the curve at the lower scaled crater efficiencies defined as  $\pi_1 \pi_2^{1/4}$  (see section III). Unfortunately, these particular data points have the largest confidence intervals (see section VII). The data points having the smallest confidence intervals are the points furthest from the curve. However, data collected at similar G-levels (25 G - 65 G) by Viktorov and Stepenov (Schmidt, 1979) are also not well predicted at the higher-scaled crater efficiencies. Thus, the data from the current research are in reasonable agreement with the best-fit curve derived by Schmidt (1979).

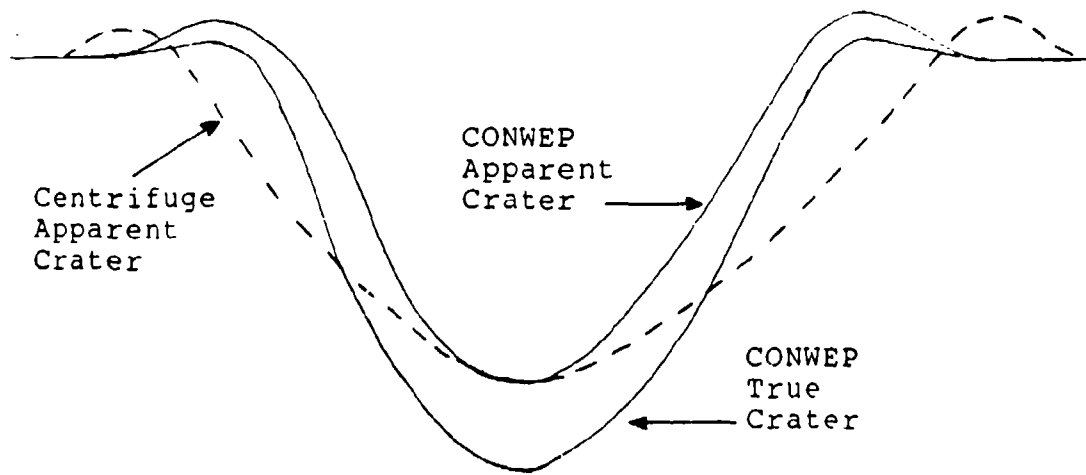


Figure 8.13 Crater Profile Comparison Between the Centrifuge Apparent Crater and the Crater Generated by the CONWEP Computer Program.

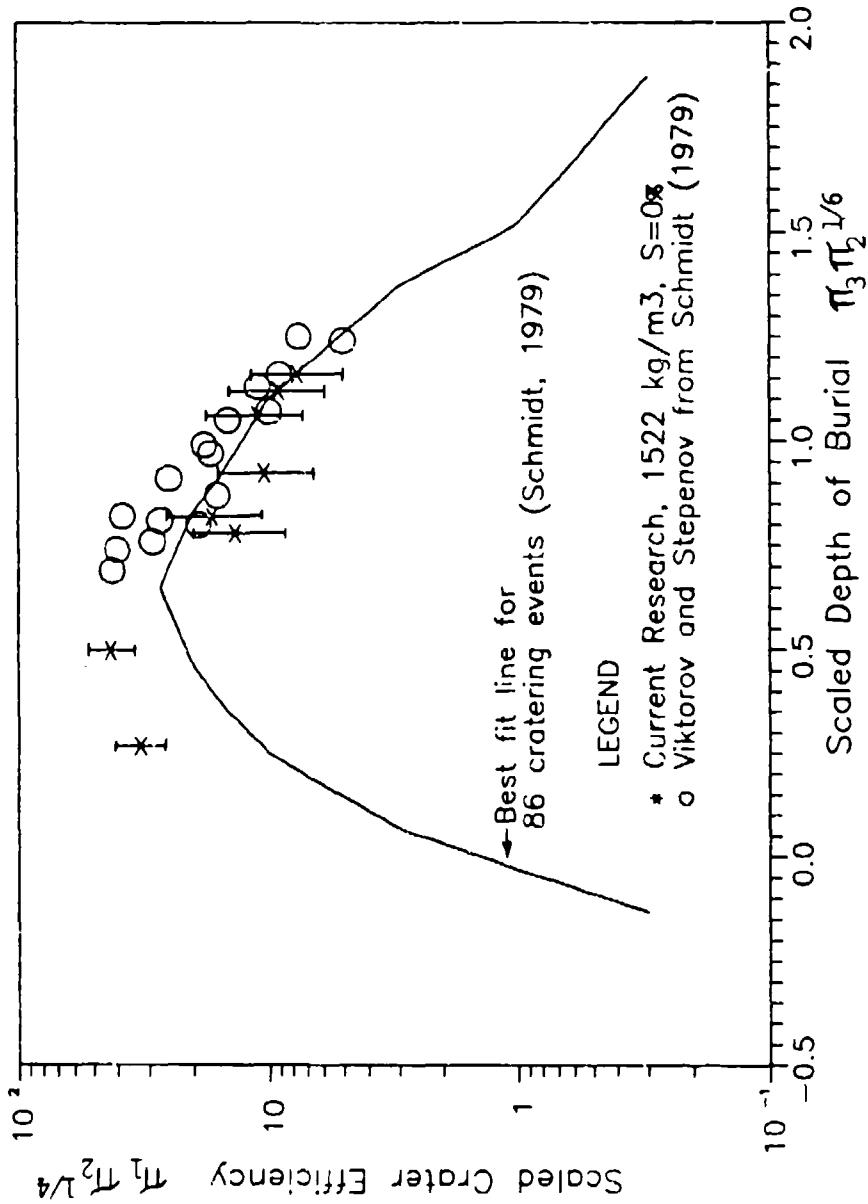


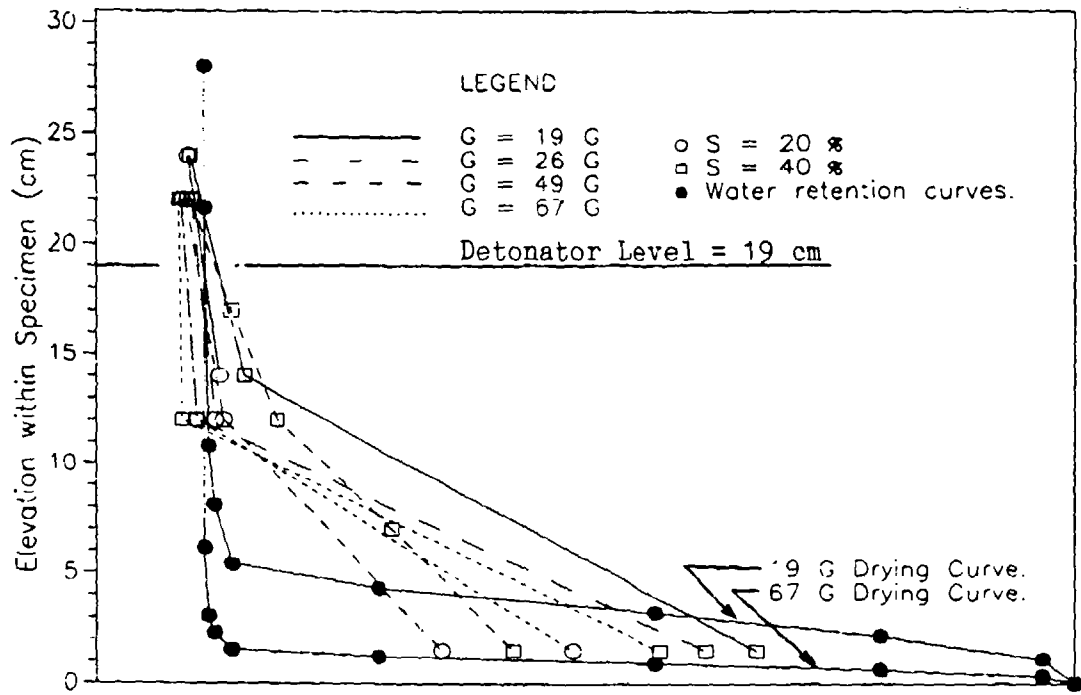
Figure 8.14 Scaled Crater Efficiency Versus Scaled Depth of Burial Showing Data from the Current Research, Viktorov and Stepenov (Schmidt, 1979), and a Best-Fit Line Developed by Schmidt (1979) from 86 Cratering Events.

#### D. DESATURATION ANALYSIS

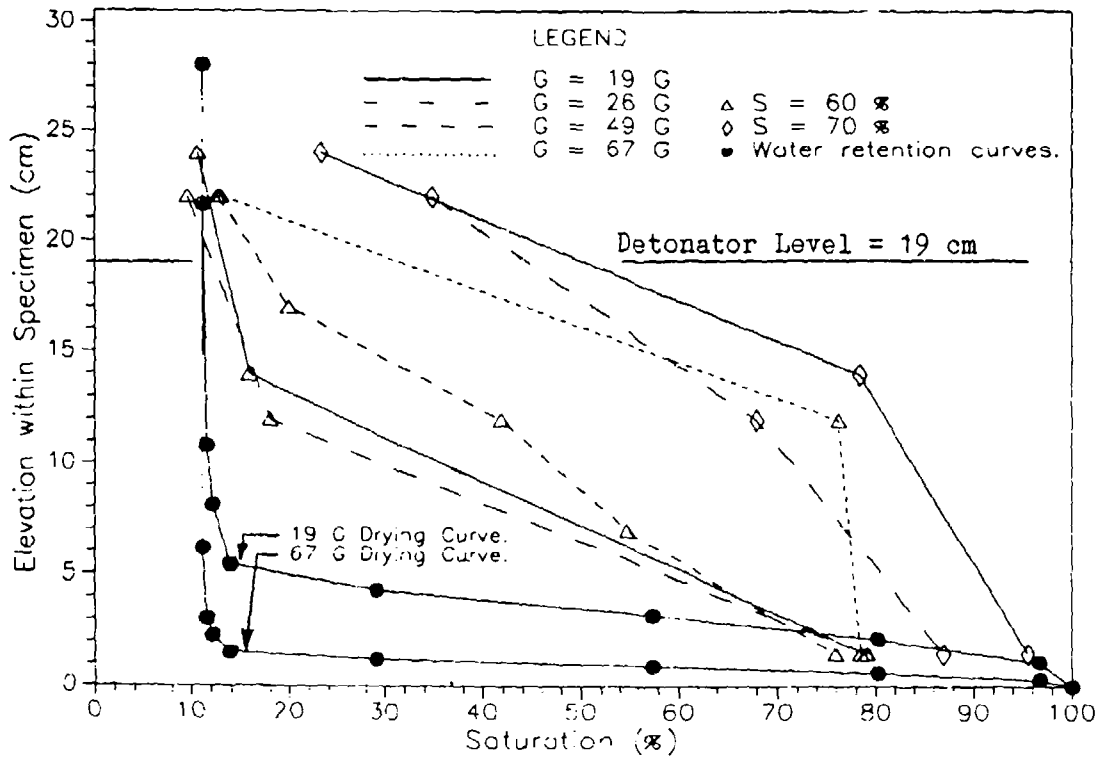
The moisture content profile in the sand during the test is analyzed in two ways. First, the desaturation curve as shown in Appendix E is scaled to model dimensions (divided by 19 G and 67 G). Second, the bucket elevations are scaled to field elevations (multiplied by 19 G and 67 G) allowing comparison to desaturation occurring in the field.

Using the first approach, the moisture content analysis shows that desaturation is the greatest in the top layer of sand, and decreases with increasing depth. The higher the G-level attained during the test, the greater the desaturation. At 20 percent compaction saturation the top 10 cm of sand desaturated to approximately the residual water content of approximately 10 percent at all G-levels (Figure 8.15). Similar trends are shown for 30.5, 60, and 70 percent compaction saturation.

The second approach for analyzing the moisture content profile allows the direct comparison of moisture content data with the water retention curve for Tyndall Beach Sand. In Figures 8.16 through 8.19, which show compaction saturation plotted against capillary pressure, the centrifuge data have been separated by G-level. The formation of a water table within the specimen bucket due to desaturation during centrifugation shifts the water retention curve upward.



(a)



(b)

Figure 8.15 Specimen Elevation Versus Saturation:  
 a)  $S_c = 20\%$ ,  $40\%$ ; b)  $S_c = 60\%$ ,  $70\%$ .

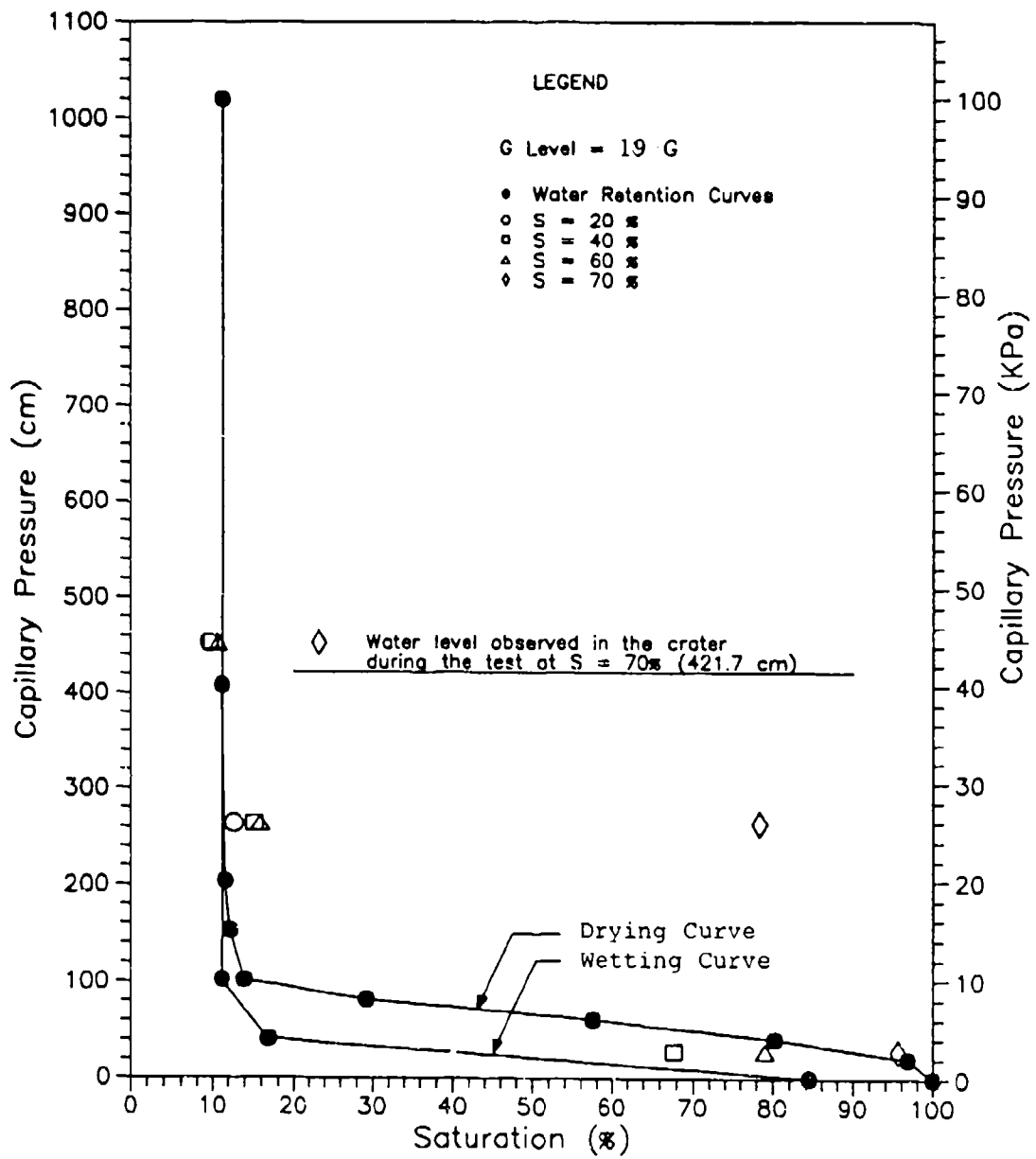


Figure 8.16 Capillary Pressure Versus Saturation, 19 G. (Conversion:  $10.20\text{cmH}_2\text{O} = 1.0\text{kPa}$ )

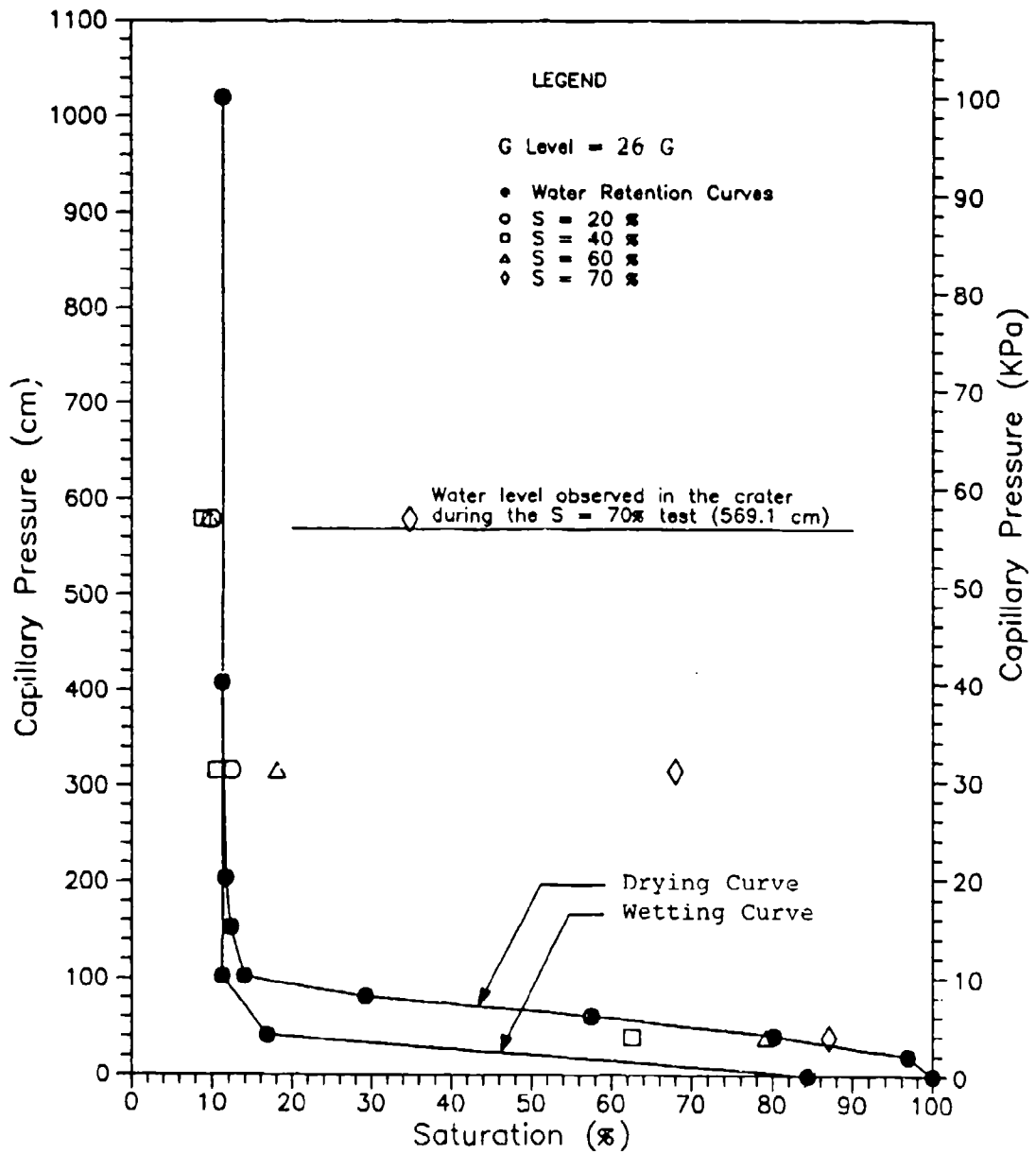


Figure 8.17 Capillary Pressure Versus Saturation, 26 G. (Conversion:  $10.20\text{cmH}_2\text{O} = 1.0\text{kPa}$ )

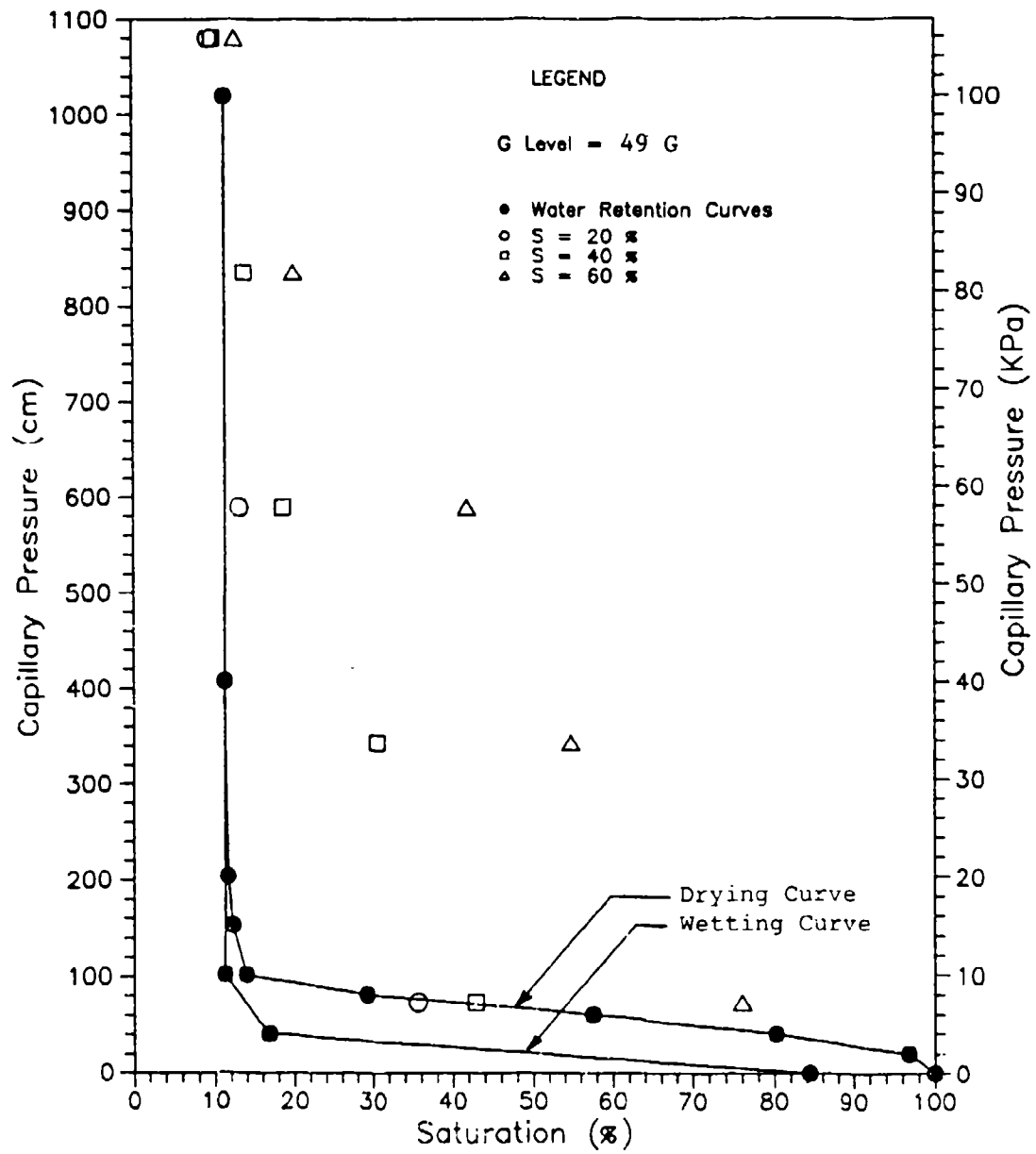


Figure 8.18 Capillary Pressure Versus Saturation, 49 G. (Conversion:  $10.20 \text{ cmH}_2\text{O} = 1.0 \text{ kPa}$ )

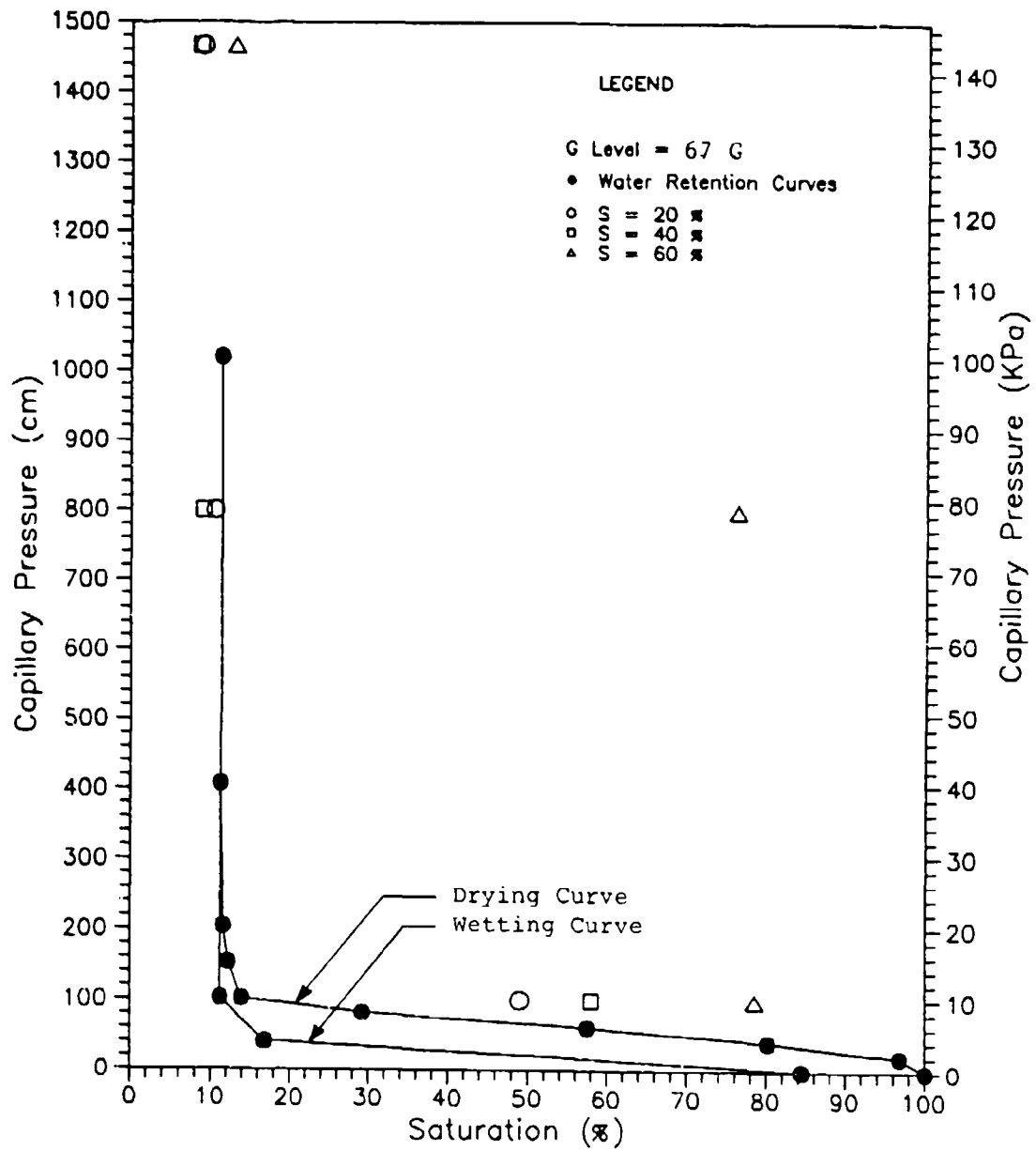


Figure 8.19 Capillary Pressure Versus Saturation, 67 G. (Conversion: 10.20cmH<sub>2</sub>O = 1.0kPa)

#### E. CRATER DIMENSION VERSUS SATURATION AT COMPACTION

In Figure 8.20 the scaled apparent crater dimensions are plotted by G-level against compaction saturation. As stated previously (section V), the tests at 19 G and 26 G were designed to use the modeling of models technique. The tests use different charge sizes to model craters produced by 7 kg of TNT. Thus, the apparent crater dimensions from these tests should be identical. If the apparent crater dimensions are significantly different, then a charge size effect exists.

Figure 8.20 shows the apparent crater dimensions for the tests at 19 G and 26 G are the same within the bounds of experimental error. As Goodings et al. (1988) and Schmidt and Holsapple (1978) show, no charge size effect exists and the modeling of models is valid.

The slight rise of the 26 G test crater radius and depth at the compaction saturation of 35 percent (test number 120.63-40-1) may be explained by experimental procedure. Because the payload platform had not rotated the full 90 degrees at 26 G, the centrifuge speed was increased to 43 G at which point full rotation occurred. With the payload platform held in the vertical position, at a 90 degree rotation, the centrifuge was slowed to 26 G.

Figure 8.15.a shows that for tests at 40 percent compaction saturation, the saturation at the detonator elevation at the conclusion of the test was significantly lower at 26 G (S = 9 percent, long dash) than at 19 G and 49

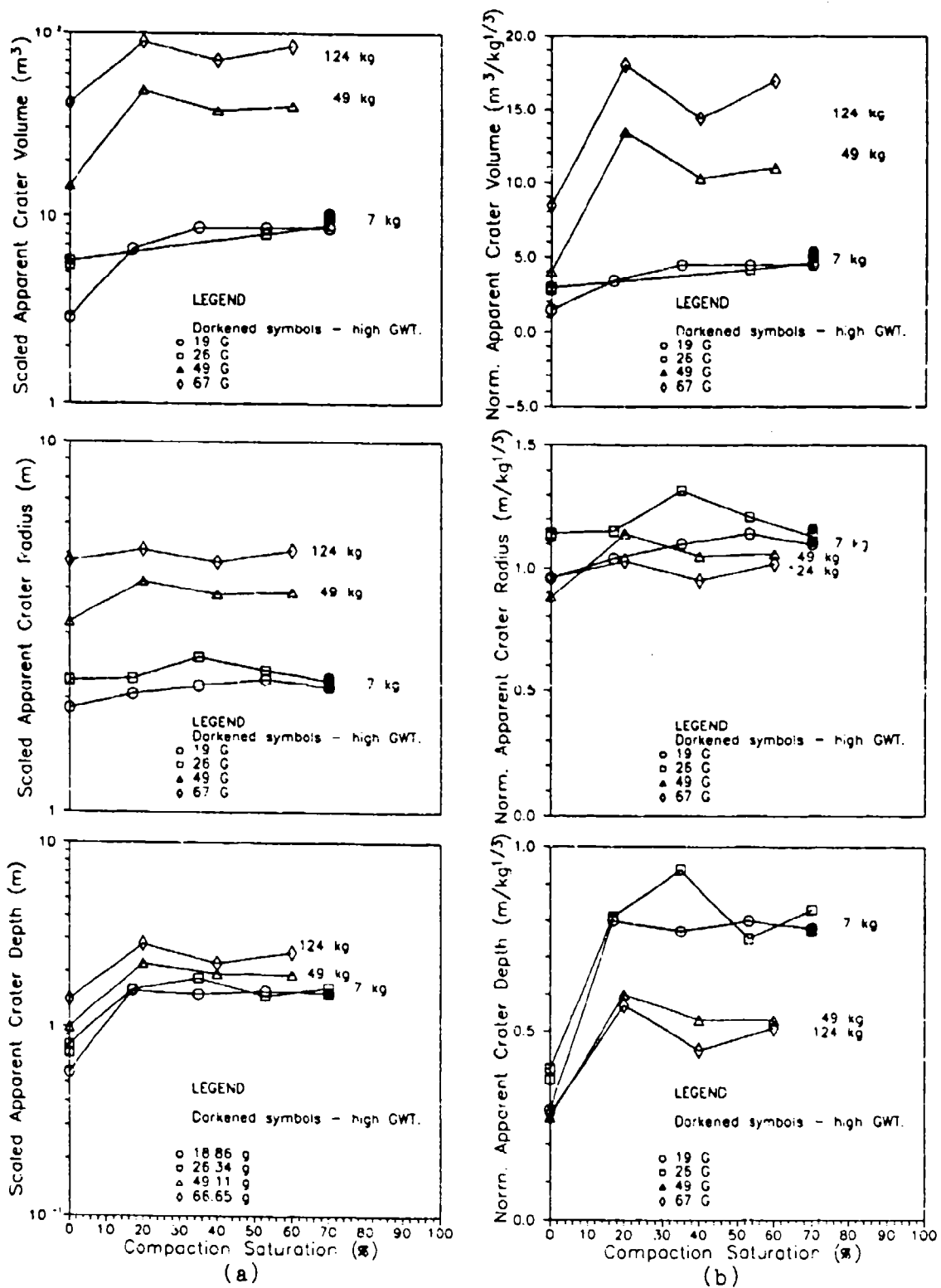


Figure 8.20 Apparent Crater Dimensions Versus Compaction Saturation: a) Scaled Dimensions; b) Normalized Dimensions.

G (S = 12 percent, solid line and medium dash respectively). In moist sand, a lower pore-water pressure induced by the lower saturation increases the apparent cohesion component of shear strength. The equation given by Fredlund (1986) for the shear strength of unsaturated soil is

$$\begin{aligned}
 s &= (u_a - u_w) \tan \phi^b + (\sigma_n - u_a) \tan \phi' \\
 &= \text{Apparent Cohesion} \\
 &\quad + \text{Frictional Shear Resistance} \qquad (8.1)
 \end{aligned}$$

where  $u_a$  is the pore-air pressure,  $u_w$  is the pore-water pressure,  $\phi^b$  is the angle of shear strength increase with an increase in  $(u_a - u_w)$ ,  $\sigma_n$  is the total effective normal stress, and  $\phi'$  is the effective angle of internal friction.

For the centrifuge tests,  $u_a$  was at atmospheric pressure ( $u_a = 0$ ). In unsaturated soils,  $u_w$  is always less than the air pressure,  $u_a$ , thus  $u_w$  must be negative (Fredlund, 1986). For dry soil,  $u_w$  is zero, becoming negative as moisture is added to the soil (Fredlund, 1986). However, as the soil moisture increases,  $u_w$  becomes less negative. Therefore, theoretically, the apparent crater dimensions of the 26 G specimen spun to 43 G should be smaller than the apparent crater dimensions of the 19 G specimen because the sand had a lower saturation and therefore a higher shear strength. An equivalent explosive mass should have ejected more sand from the weaker 19 G specimen than the stronger 26 G specimen.

The test at a compaction saturation of 20 percent and 67 G (test number 191.89-20-40) was also spun to a higher G-level (93 G) to correct the orientation of the payload platform. However, in this case, the apparent crater dimensions at 67 G increase and decrease at the same compaction saturation levels as the apparent crater dimensions at 49 G. By 67 G, the sand at the detonator had already been desaturated to the residual level (9 to 10 percent).

Figure 8.20 also shows that scaled apparent crater volume, radius, and depth increase with G-level. When the G-level is multiplied by a factor of 2.5 (from 26 G to 67 G) which corresponds to increasing the prototype explosive charge from 7 to 124 kg, apparent crater volume increases by an order of magnitude from 7 m<sup>3</sup> to 70 m<sup>3</sup> and doubles apparent crater radius from 2.3 m to 4.6 m.

The scaled apparent crater volume, radius, and depth remain constant from 20 to 70 percent compaction saturation. A noticeable increase in scaled apparent crater volume and depth is observed between 0 and 20 percent compaction saturation. An increase in scaled apparent crater dimensions is expected to occur as low as the residual level of saturation where the capillary forces are the largest.

An increase in stress transmission has been observed to occur in Ottawa Sand between 0 and the residual level of

compaction saturation.<sup>5</sup> As shown by Fredlund (1986), the apparent cohesion component of soil shear strength increases as the pore-water pressure decreases, becomes more negative. Thus, in that cratering is controlled by soil strength, the effects of moisture should increase as the degree of saturation approaches the residual level. Conversely, at saturations greater than the residual level, the less effect capillarity should have on crater formation.

#### F. ASPECT RATIO VERSUS SATURATION AT COMPACTION

To analyze crater shape, the aspect ratio, as defined as apparent crater radius divided by apparent crater depth ( $r/d$ ), was plotted against compaction saturation (Figure 8.21). The data are separated by G-level. The observations from this graph are: 1) craters in dry sand have a larger aspect ratio at all G-levels; 2) charge size does not alter aspect ratio; and 3) the addition of moisture significantly reduces the aspect ratio. Also, based on a few tests at  $1602 \text{ kg/m}^3$ , there is strong indication that under dry conditions, an increase in density will lower the aspect ratio.

Figure 8.21 reinforces the influence of water in the specimen. The average aspect ratio of the dry specimens is 3.17 with a range between 2.82 and 3.40, whereas the aspect ratios of the partially saturated specimens range from 1.3 to

---

<sup>5</sup>Personal Communication, C. Allen Ross, Professor, University of Florida, Gainesville, Florida; Consultant, HQ AFCEA/RACS, Tyndall AFB, Florida.

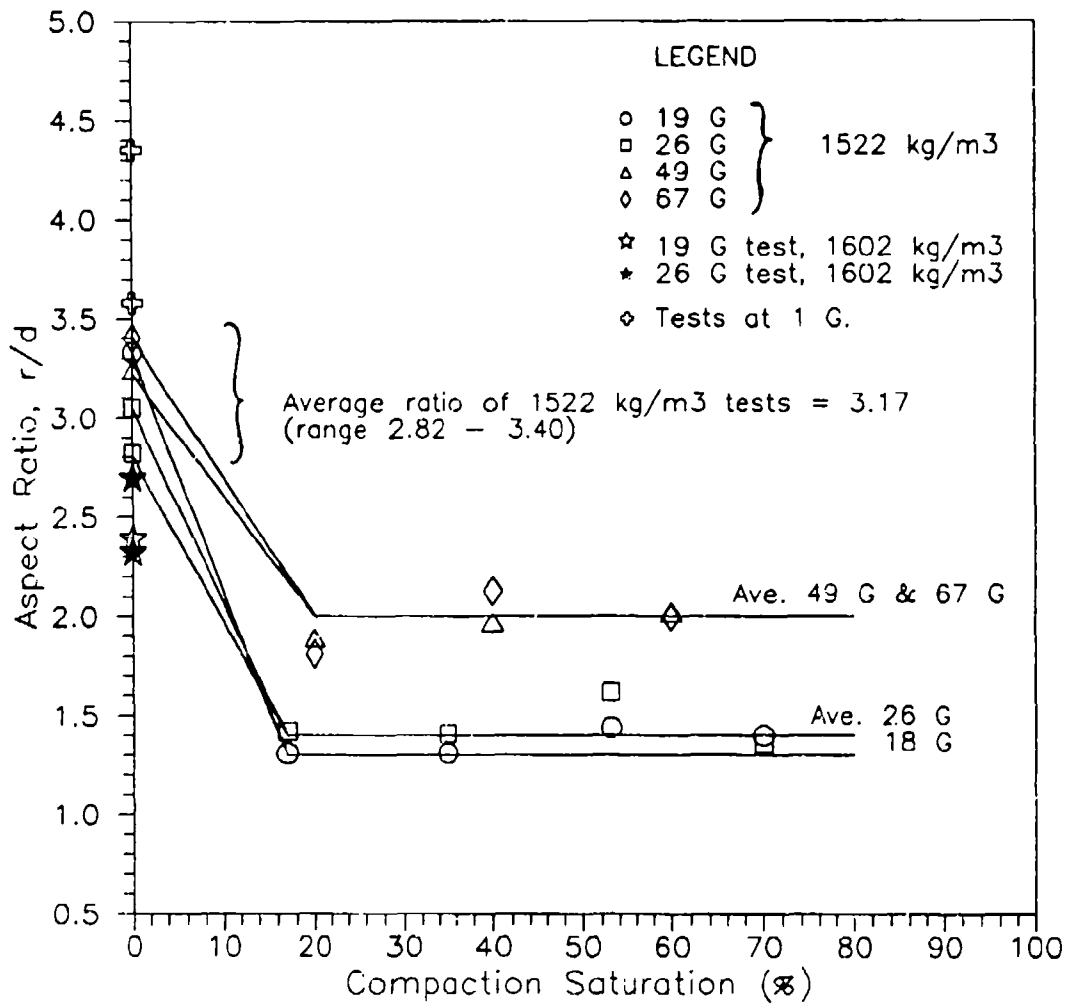


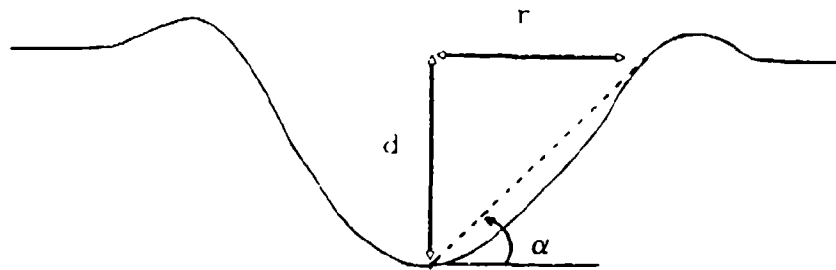
Figure 8.21 Aspect Ratio Versus Compaction Saturation.

2.0. Lines of average aspect ratios are drawn through the partially saturated data. Table 8.5 lists the average aspect ratio and the apparent crater wall angle for each G-level. The crater wall angle ( $\alpha$ ) is calculated from the equation  $\tan \alpha = d/r$  (Figure 8.22).

**TABLE 8.5. AVERAGE ASPECT RATIO AND APPARENT CRATER WALL ANGLE AS TAKEN FROM FIGURE 8.21.**

<u>S<sub>c</sub></u> <u>(%)</u>	<u>G</u>	<u>PBX</u> <u>(gm)</u>	<u>Scaled</u> <u>TNT EQ.</u> <u>(kg)</u>	<u>DOB</u> <u>(cm)</u>	<u>r/d</u>	<u>α</u> <u>(deg)</u>
17 to 70	18.86	1.043	7.6	7.6	1.3	37.6
17 to 70	26.34	0.383	7.6	5.44	1.4	35.5
20 to 60	49.11	0.383	49.4	5.44	1.9	27.8
20 to 60	66.65	0.383	123.6	5.44	2.0	26.6
0	18.86	1.043	7.6	7.6	3.2	17.5
	26.34	0.383	7.6	5.44	Ave.	Ave.
	49.11	0.383	49.4	5.44		
	66.65	0.383	123.6	5.44		

One possible explanation for the high aspect ratio for the craters in dry sand is slope failure. Slumping of the side wall would decrease the crater depth, increase the crater radius, and raise the aspect ratio. The measured apparent crater depth is shallower in dry craters (Figure 8.23), and



$$\tan \alpha = d/r = 1/(r/d)$$

Figure 8.22 Crater Wall Angle Calculation.

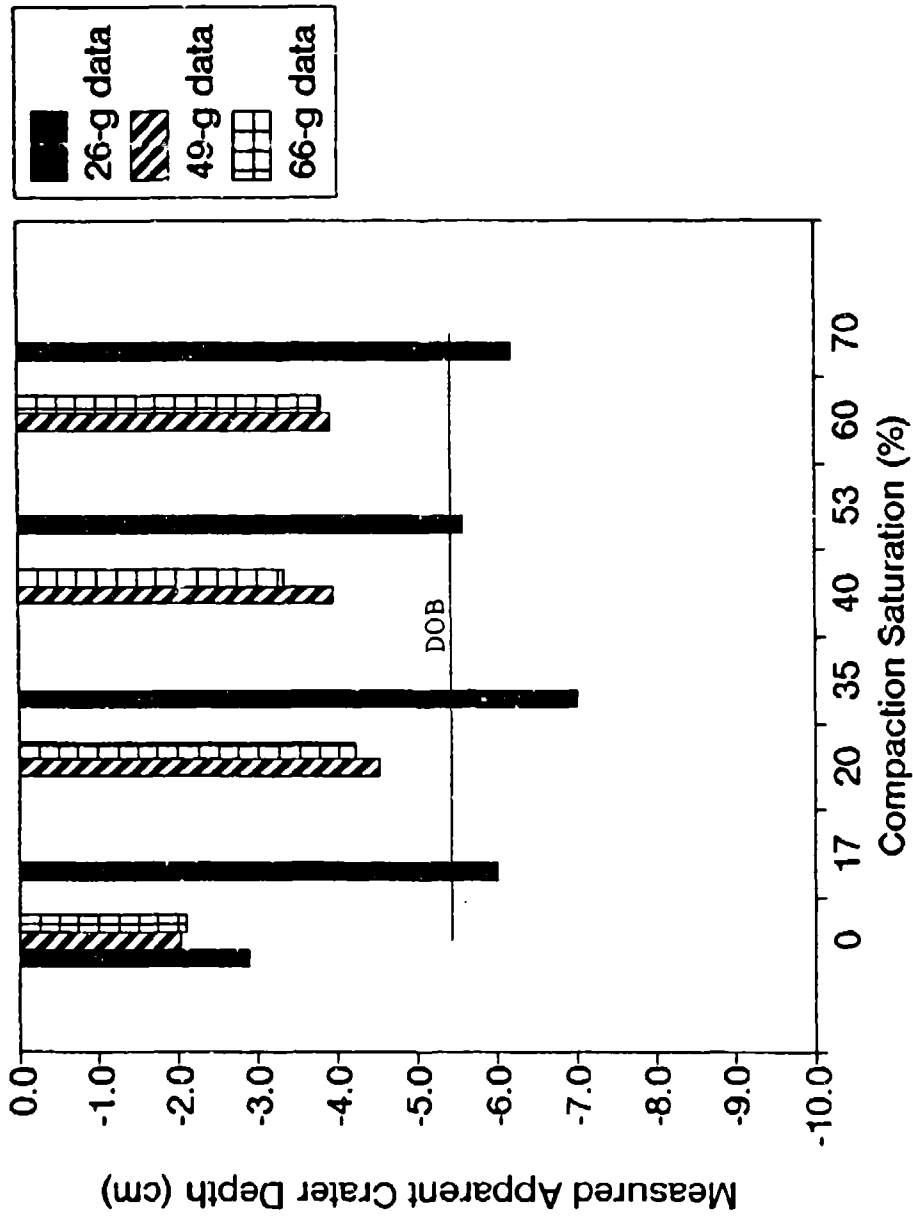


Figure 8.23 Measured Apparent Crater Depth Versus Compaction Saturation. All Data are from Charges Containing an Equivalent of 383 mg of PBX.

the crater wall angle of  $17.5^\circ$  (Table 8.5) is much lower than the angle of repose for beach sand (approximately  $30^\circ$ - $35^\circ$ ).

With moisture, sand develops capillary forces which create an apparent cohesion. Evidence in support of the capillary forces and an apparent cohesion is provided by the high crater wall angles of  $37.6^\circ$  and  $35.5^\circ$  calculated for the specimens at 19 G and 26 G (Table 8.5). Higher wall angles permit deeper craters which result in lower aspect ratios. Thus, slope failure did not occur in the craters formed at 19 G and 26 G.

Figure 8.20 shows apparent crater depth increases more between degrees of compaction saturation of 0, and 20 percent than in apparent crater radius. As previously discussed, 20 percent compaction saturation is not expected to be the limiting degree of compaction saturation. Due to the rise in capillarity with decreasing moisture, the residual level of saturation is instead expected to be the limit to increasing apparent crater dimensions.

As the G-level increases to 49 G and 67 G, the apparent cohesion component of sand shear strength becomes a smaller percentage of the total strength (Figure 8.24), and slope failure reoccurs. The measured apparent crater depth for tests at 49 G and 66 G is less than the DOB of 5.44 cm (Figure 8.23), and the crater wall angles of  $27.8^\circ$  and  $26.6^\circ$  (Table 8.5) are significantly lower than the crater wall angles for tests at 19 G and 26 G. For degrees of compaction saturation

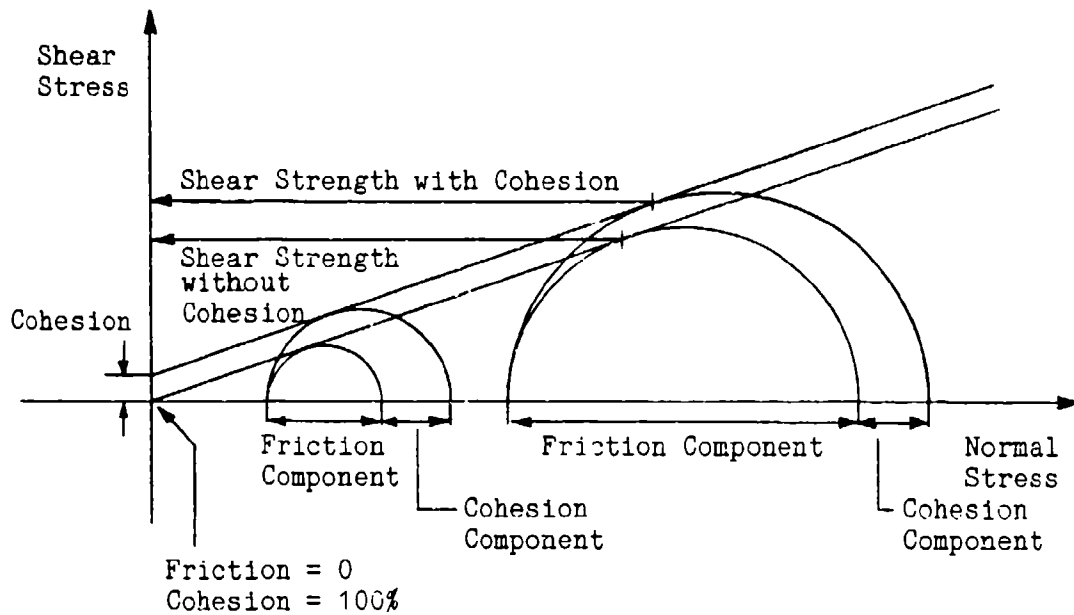


Figure 8.24 Decrease of the Cohesion Component of Soil Strength Relative to the Total Shear Strength with an Increase in G-Level (Stress).

from 20 to 60 percent, the apparent crater depth increases less than the apparent crater radius (Figure 8.20) which leads to the greater aspect ratios shown in Figure 8.21 for the tests at 49 G and 67 G. Figure 8.25 depicts these differences in aspect ratio for the tests at 26 G, 49 G, and 67 G through the crater profile.

Figures 8.26 and 8.27 show how subjecting specimens to elevated G's prior to a test at 1 G raises the aspect ratio. The apparent craters become proportionally shallower, and both the apparent crater depth and apparent crater diameter decrease (Table 8.6). Moisture is drained from the detonator elevation which increases the capillary forces and in turn increases the soil strength.

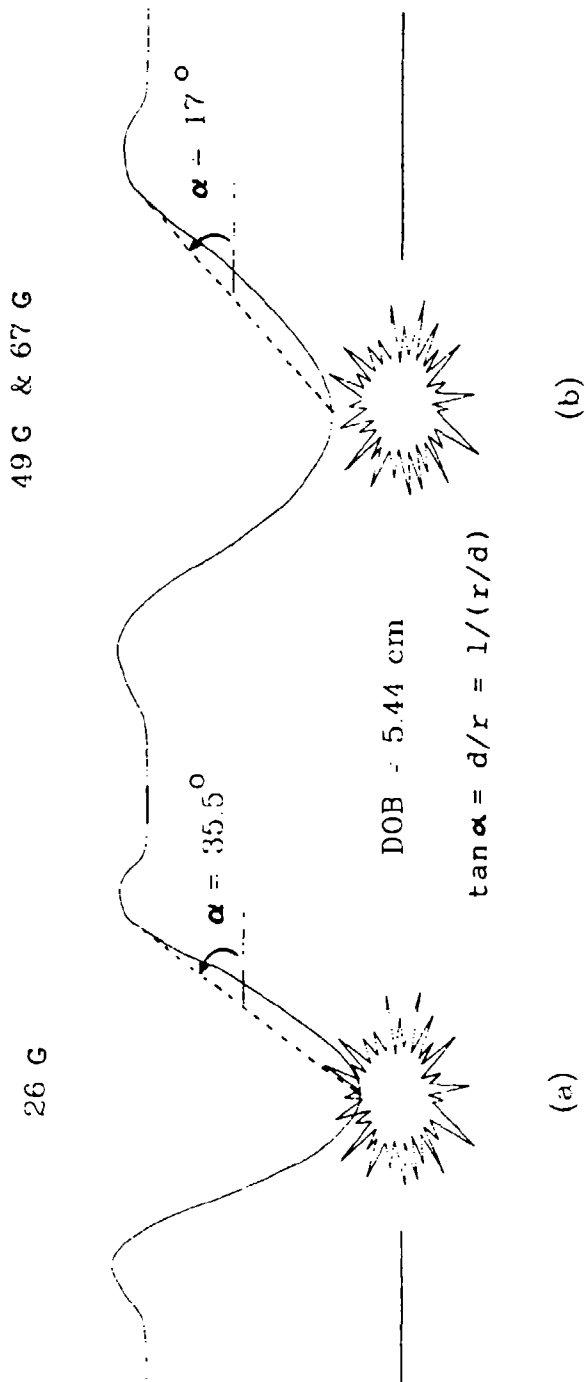


Figure 8.25 Crater Profiles Showing the Differences in Aspect Ratio due to Apparent Crater Depth and Wall Angle at 26 G, 49 G, and 67 G.

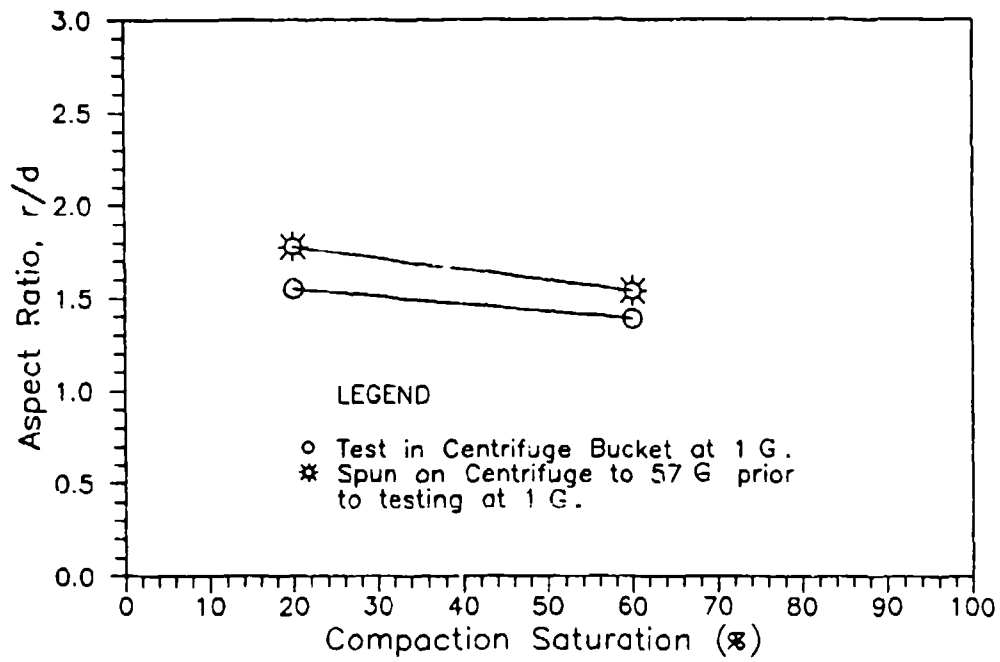
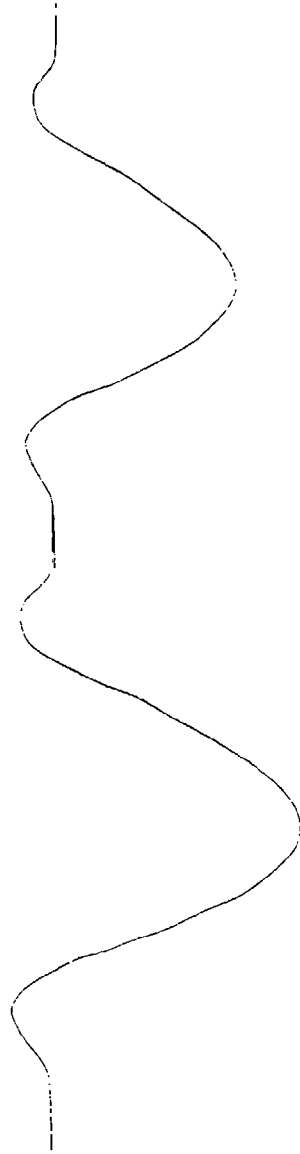


Figure 8.26 Differences in Aspect Ratio due to Centrifugation Prior to Testing at 1 G.



Test at 1 G  
Sc = 20%, 60%  
 $\alpha = 330, 360$

Centrifugation 57 G  
Test at 1 G  
Sc = 20%, 60%  
 $\alpha = 290, 330$

Figure 8.27 Crater Profiles Showing the Differences in Aspect Ratio due to Centrifugation Prior to Testing at 1 G.

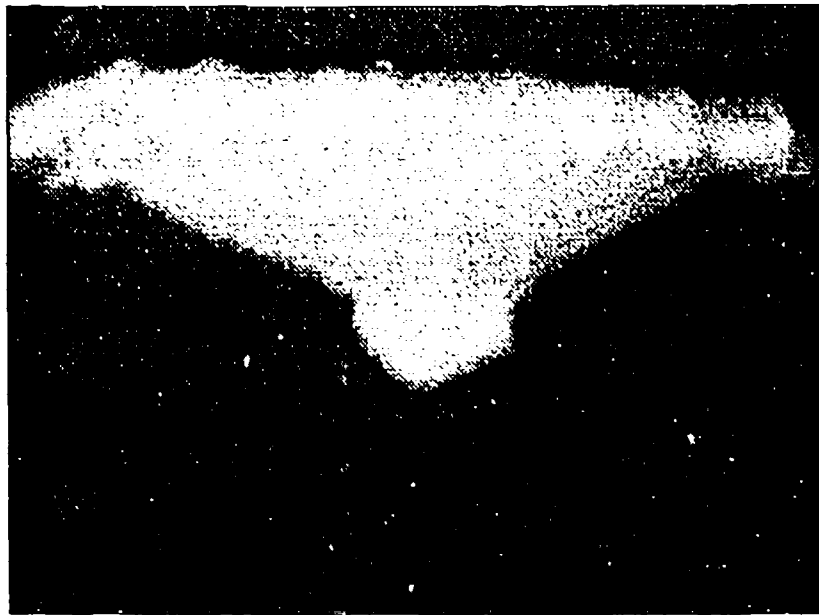
**TABLE 8.6.** THE DECREASE IN ACTUAL APPARENT CRATER DIMENSIONS DUE TO CENTRIFUGATION AT 57 G (179.5 RPM) PRIOR TO TESTING AT 1 G.

<u>Test Number</u> <u>(rpm-1G(sat)-#)</u>	<u>Inside</u> <u>Diameter</u> <u>(cm)</u>	<u>Depth</u> <u>(cm)</u>	<u>Volume</u> <u>(cm<sup>3</sup>)</u>
0.0-1G(20)-1	24.13	7.78	1368
179.5-1G(20)-3	23.02	6.48	1038
0.0-1G(60)-2	25.40	9.17	1869
179.5-1G(60)-4	24.45	7.94	1427

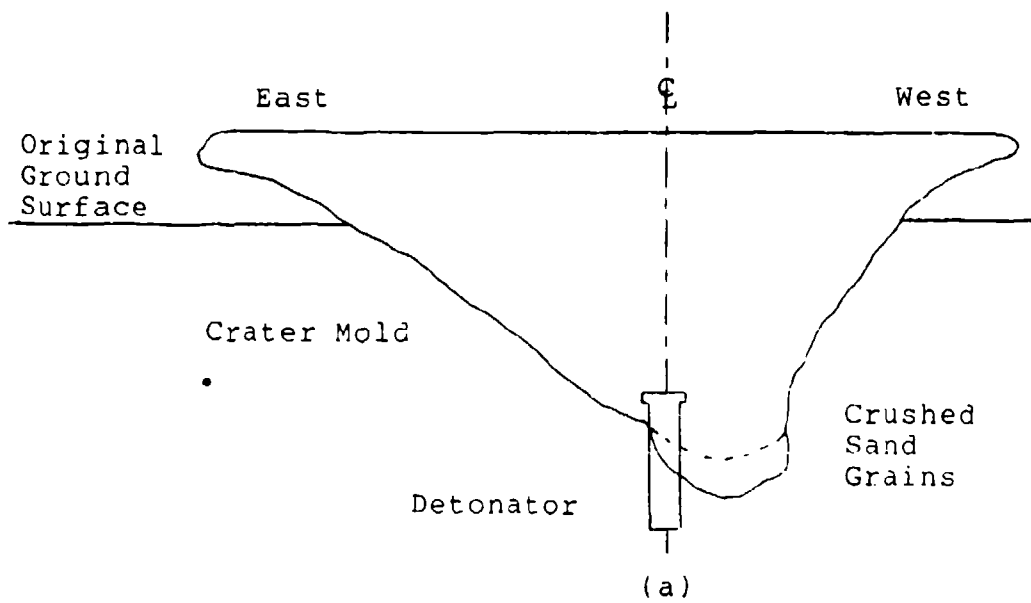
G. CORIOLIS EFFECT ON CRATER SHAPE

The asymmetry of the crater molds pictured in Appendix A is evidence that the use of centripetal acceleration distorts the shape of the apparent crater in sand. In every instance, the distortion occurs towards the West. Figure 8.28 shows the zone in which sand grains have been broken into fine particles by the blast is centered about the bottom of the apparent crater. Thus, there is an indication the true crater as well as the apparent crater is shifted towards the west.

In field tests, crater skewness is usually attributed to a tilted charge; a charge whose longitudinal axis is not vertical at the time of detonation. However, the bottom of all the craters formed on the centrifuge have been visibly skewed in the West direction, opposite the rotation of the centrifuge. Figure 8.29 shows the profile of test number



(b)



(a)

Figure 8.28 Typical Location of Crushed Sand Grains  
in the East-West Direction:  
a) Photograph; b) Schematic.

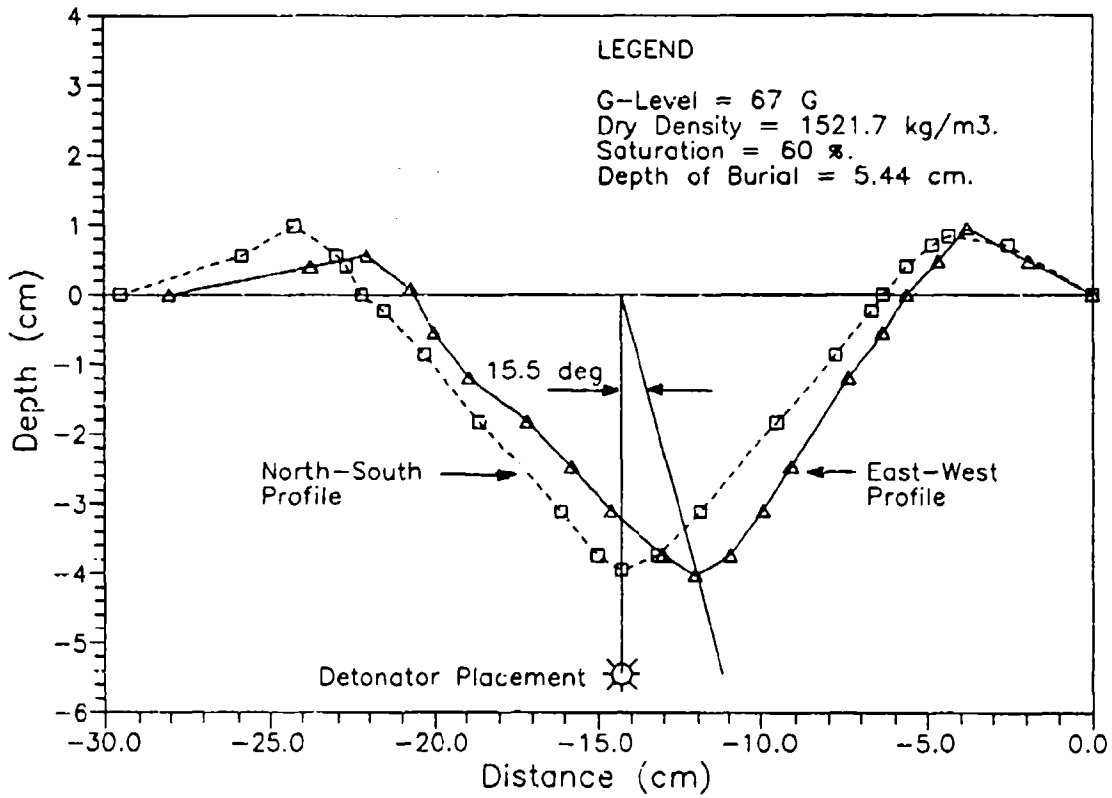


Figure 8.29 Crater Mold Profiles in the East-West and North-South Directions.

191.89-60-3 taken in the East-West and North-South directions. The procedure used to generate the profile is described in Appendix G. In the North-South direction, the apparent crater is symmetric about the axis of the detonator. If the Coriolis acceleration were not the cause of the distortion of the apparent crater shape, the asymmetry would not be confined to the East-West direction. Thus, the symmetry of the apparent crater in the North-South direction is further verification that the Coriolis acceleration is altering the shape of the apparent crater. The angle between the lines drawn from the intersection of the plane containing the detonator and the plane of the ground surface to the lowest point of each crater profile is 15.5°.

The skewness of several other craters was visually approximated. These approximations are listed in Table 8.7. The data indicate that greater G-levels produce greater apparent crater asymmetry (Appendix I), however, additional research is required.

Schmidt et al. (1986) and Steedman (1990) attribute apparent crater asymmetry to the uneven distribution of ejecta, but the Coriolis acceleration should effect more than just the ejecta. Because of high initial velocities produced by the blast, soil particles moving in directions other than the North-South direction should experience a Coriolis force. Thus, a vectorial analysis was performed to show how the Coriolis acceleration ( $a_c$ ) effects the rupture zone as well as

**TABLE 8.7. APPARENT CRATER ASYMMETRY DUE TO THE CORIOLIS ACCELERATION.**

Test (rpm-sat-#)	G-level (G)	Angle of Rotation (±2 deg)
102.00-70-3	18.85	11.0
120.63-70-4	26.34	13.0
120.63-60-1	26.34	12.8
164.71-20-5	49.11	15.7
164.71-40-4	49.11	19.8
164.71-60-4	49.11	20.0
191.89-20-4	66.65	18.6
191.89-40-3	66.65	16.0
191.89-60-3	66.65	15.5

the ejecta.

The blast is assumed to be a point source and the velocity vectors of the particles being ejected from the centrifuge bucket are separated into radial and tangential components. The Coriolis acceleration vectors are the vector cross products between the centrifuge rotation vector and the relative particle velocity vectors. The Coriolis force vector, however, will act in the direction opposite that of the Coriolis acceleration. The inertia force opposing the Coriolis acceleration will govern the movement of the soil particles.

Figure 8.30 shows the directions of the Coriolis force components drawn in the plane of the original ground surface about the edge of a spherical crater. The Coriolis force vectors derived from the tangential velocity of the particles point out of the bucket on the West side of the crater and

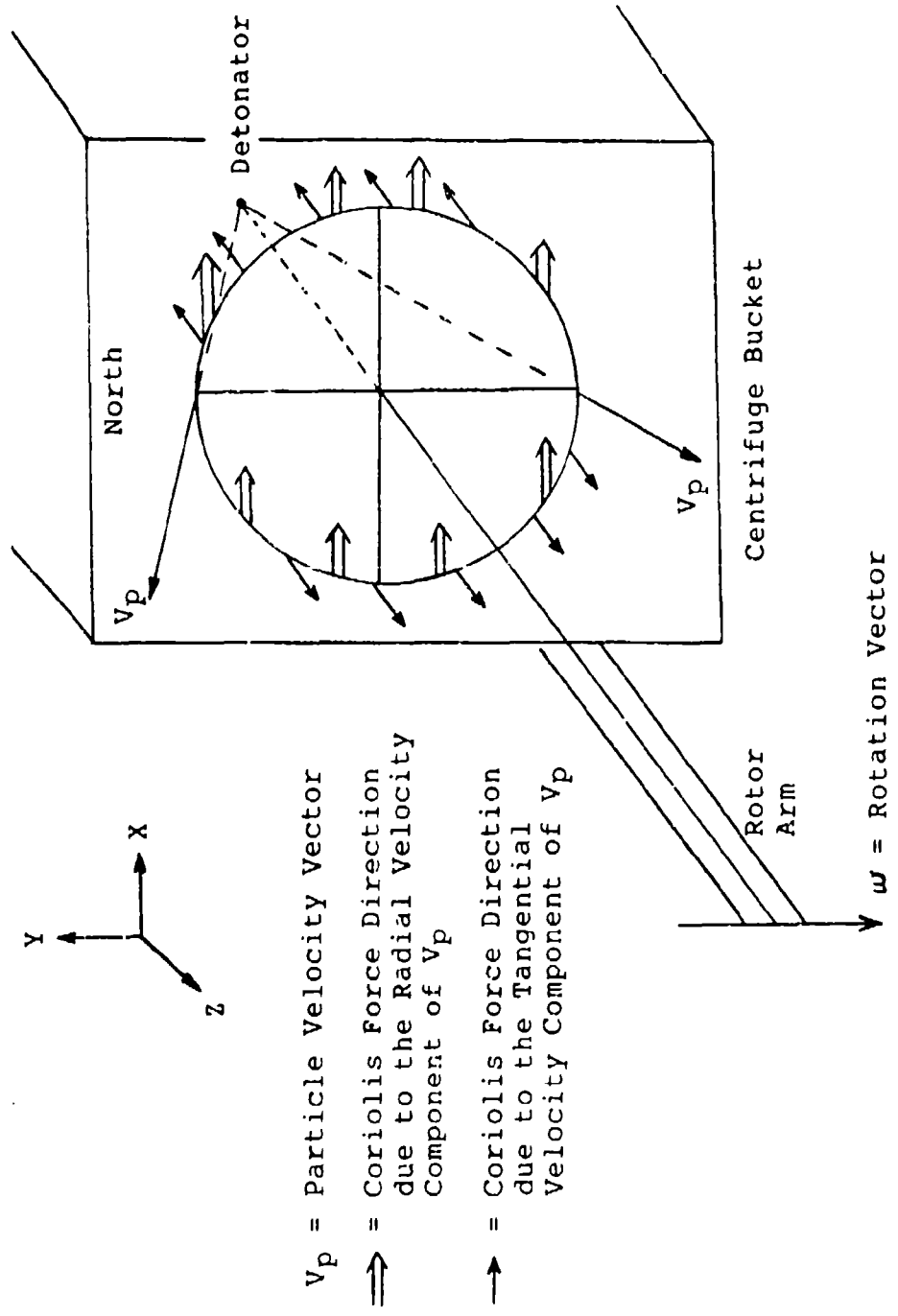


Figure 8.30 Direction of Coriolis Force Components Drawn in the Plane of the Original Ground Surface about the Edge of a Spherical Crater.

into the bucket on the East side of the crater. All of the Coriolis force vectors derived from the radial velocity of the particles point to the East. The Coriolis force acting on the soil below the detonator will be pointed to the West, assuming the Coriolis effect is reversed for particles accelerating down into the bucket. Therefore, during the explosion, the Coriolis forces tend to rotate the soil mass about the North-South axis at the detonator. The rotation of the soil mass surrounding the detonator by the Coriolis acceleration will shift the bottom of the crater to the West against the centrifuge rotation. Thus, the analytical result supports the skewed crater shape produced on the centrifuge.

## SECTION IX

### CONCLUSIONS AND RECOMMENDATIONS

#### A. CONCLUSIONS

##### 1. SCALING LAWS FOR DRY AND MOIST SAND

Craters induced by explosive detonations in dry and partially saturated Tyndall Beach Sand were modeled in a centrifuge. The apparent dimensions of the explosion-induced craters are analyzed as dimensional terms and dimensionless pi terms.

In the analysis of dimensional terms, the scaled apparent crater volume, radius, and depth are plotted against the TNT equivalent of the scaled explosive mass (Figures 8.1 to 8.6). The analysis shows through a comparison of yield exponents that the scaling laws for apparent crater dimensions are the same for dry and partially saturated sand (Table 9.1). The yield exponents of the current research are also similar to the yield exponents of crater dimensions produced on centrifuges by Goodings et al. (1988) and Schmidt and Holsapple (1978, 1980), and produced in the field by the U.S. Army Engineer Waterways Experiment Station (WES) (Strange et al., 1961; Rooke et al., 1974).

**TABLE 9.1. CRATER DIMENSION YIELD EXPONENTS FOR CHARGE MASS, W.**

Crater Dimension	Current Research	Goodings et al.	Schmidt & Holsapple	WES		
				(1974) <sup>b</sup>	(1974) <sup>b</sup>	(1961) <sup>c</sup>
	(1992) <sup>a</sup>	(1988)	(1978)	(1980)	(1974) <sup>b</sup>	(1961) <sup>c</sup>
	Tyndall Beach Sand	Ottawa Sand	Ottawa Sand	Desert Alluvium	Unspec. Sand	Unspec. Sand
Volume - Dry	0.831	0.84	0.842			
Volume - Moist	0.914			0.974	0.951	0.863
Radius - Dry	0.297	0.29	0.230			0.270
Radius - Moist	0.308			0.316	0.306	0.305
Depth - Dry	0.279	0.28	0.279			0.240
Depth - Moist	0.297			0.226	0.335	0.238

<sup>a</sup> Yield exponents for the dry test data do not include 1 G test results.  
<sup>b</sup> Yield exponents for the moist test data include 1 G test results.

<sup>b</sup> Rooke et al. (1974),  $1.1 < \lambda < 2.0$ .

<sup>c</sup> Strange et al. (1961),  $0.9 < \lambda < 1.1$ .

Conversely, in the analysis of the pi terms derived by Schmidt and Holsapple (1977) for buried charges, the apparent crater volume ( $\pi_v = V\rho/W$ ) and depth ( $\pi_d = d(\rho/W)^{1/3}$ ) data at compaction saturations of 20 and 60 percent do not parallel the data for dry beach sand when plotted in Figure 8.7 against the gravity scaled yield ( $\pi_2 = (G/Q)(W/\delta)^{1/3}$ ). The apparent crater volume and depth data support the material strength model developed by Schmidt and Holsapple (1979). At low gravity scaled yields the volume and depth curves are horizontal; the apparent cohesion of the partially saturated sand dominates the cratering process. The lower the compaction saturation and the larger the apparent cohesion, the higher the transition point becomes between cohesion dominated cratering and frictional shear resistance dominated cratering.

Thus, when dimensional terms are analyzed, the scaled apparent crater dimensions of volume, radius, and depth follow the same scaling relations in partially saturated sand as in dry sand. However, when the dimensionless pi terms are analyzed, the apparent crater volume and depth do not follow the same scaling relations in partially saturated sand as in dry sand. No conclusions can be drawn from the pi term for apparent crater radius.

## 2. DEPTH OF BURIAL EFFECT

In a second analysis of dimensional terms, the apparent crater dimensions are normalized (divided by the cube root of the explosive mass) and plotted against the normalized depth of charge burial (DOB). The normalized apparent crater diameter and depth data follow the best-fit prediction curves given in Figures 8.9 and 8.10 for sand derived by WES (Strange et al., 1961). The craters dimensions measured in dry sand plot below the crater dimensions measured in partially saturated sand. Amongst the partially saturated data, no trends due to the differences in compaction saturation are observed.

The apparent crater diameter data do not fall within the range from dry (field dry) to wet (saturated) sand predicted by the Air Force Protective Construction Design Manual and the Army design manual, Fundamentals of Protective Design for Conventional Weapons (Figure 8.11). The scaled apparent crater diameter data for craters formed in dry and partially saturated Tyndall Beach Sand are approximately 50 percent greater than the predicted apparent and true crater dimensions in "dry" and "wet" sand (Figure 8.12).

The scaled apparent crater depth data for craters formed in dry sand follow the curve predicted by the Air Force Protective Construction Design Manual and the Army design manual, Fundamentals of Protective Design for Conventional Weapons, for apparent crater depth in "dry" sand (Figure

8.12.a). In "wet" sand, the scaled apparent crater depth data at a normalized DOB of  $0.73 \text{ m/kg}^{1/3}$  bracket the predicted range for apparent and true crater depth (Figure 8.12.b).

### 3. DESATURATION DURING CENTRIFUGATION

Centrifugation is shown to cause desaturation in sand ranging in degrees of saturation from 20 percent (Figures 8.18). The desaturation is such that the water retention curve is reproduced within the specimen bucket (Appendix E). The greatest desaturation occurs at the top of the sample, and the higher the g-level, the greater the desaturation. The results indicate that capillary rise scales to the prototype saturation profile as  $1/N$ , where  $N$  is the model scale.

### 4. SATURATION VERSUS CRATER DIMENSION

The scaled apparent crater dimensions of crater volume, radius, and depth increase by 150, 20, and 100 percent respectively between 0 and 20 percent compaction saturation (Figures 8.20 and 8.23). If the influence of moisture on stress transmission ratios can be applied to cratering, the increase in scaled apparent crater dimensions will occur at the residual level of saturation. In Tyndall Beach Sand, the residual level of saturation is approximately 10 percent. Beyond 20 percent, the compaction saturation is not shown to influence apparent crater dimensions.

5. EFFECT OF MOISTURE ON APPARENT CRATER ASPECT RATIO

Craters in dry Tyndall Beach Sand have aspect ratios of approximately 3.2. An increase in the unit weight of the material or the addition of moisture lowers the aspect ratio. At the residual level of saturation, the aspect ratio falls to 1.3 and 1.4 for 19 G and 26 G, respectively. At the higher G-levels of 49 G and 67 G, the aspect ratio increases to 2.0 (Figure 8.21).

The crater wall angles of the craters measured in partially saturated sand are  $37.6^\circ$  and  $35.5^\circ$  from the horizontal for 19 G and 26 G, respectively. The decrease in apparent crater depth for tests performed at 49 G and 67 G, and the relatively low crater wall angles of the craters measured in dry sand ( $17.5^\circ$ ) and in the partially saturated sand at 49 G and 67 G ( $27.8^\circ$ ,  $26.6^\circ$ ) suggest slope failure as the mechanism causing large aspect ratios for craters formed in dry sand and at 49 G and 67 G. Centrifugation of a specimen prior to testing at 1 G is also shown to raise the aspect ratio.

6. CORIOLIS EFFECT ON CRATER SHAPE

Craters produced on a centrifuge by a buried charge are skewed in the plane of rotation against the direction of rotation (Figure 8.29). The skew of the crater is attributed to the Coriolis acceleration on particle motion. The effect of the Coriolis acceleration on the entire crater is to rotate

the soil mass of the crater about an axis centered at the charge and parallel to the angular rotation vector of the centrifuge.

#### B. RECOMMENDATIONS

Cratering depends on soil strength and in partially saturated sand, the apparent cohesion is often a significant component of soil strength. Thus, further study of cratering in partially saturated sand should begin with calculations of the apparent cohesion. An apparent cohesion/saturation curve would prove useful in subscale laboratory tests and full scale field tests. A known apparent cohesion would permit a measure of the true soil strength to be determined and the graphical analysis of a cohesion  $\pi$  term.

Secondly, colored sand layers should be placed above the detonator to map the distribution of ejecta. The relationship between apparent and true crater dimensions are not known for centrifuge crater models. The relationship may or may not be the same for full scale field tests.

Lastly, centrifuge results may not be consistent throughout all G-levels. The data in Figures 8.9, 8.10 and 8.11 indicate that, for a constant DOB, normalized apparent crater dimensions decline with an increase in G-level. Data collected by Goodings et al. (1988) and Schmidt and Holsapple (1980) support this observation (see Appendix L). Thus, the

effects of centripetal acceleration for explosion-induced crater formation requires further definition.

## LIST OF REFERENCES

1. ASTM D4253, (1988), Standard Test Methods for Maximum Index Density of Soils Using a Vibratory Table, Section 4, Vol. 04.08, Soil and Rock, Building Stones; Geotextiles, ASTM, 1916 Race Street, Philadelphia, Pennsylvania, pp. 554-565.
2. ASTM D4254, (1988), Standard Test Methods for Minimum Index Density of Soils and Calculation of Relative Density, Section 4, Vol. 04.08, Soil and Rock, Building Stones; Geotextiles, ASTM, 1916 Race Street, Philadelphia, Pennsylvania, pp. 566-572.
3. Baker, W. E., Kulesz, J. J., Westine, P. S., Cox, P. A., and Wilbeck, J. S., (1980), A Manual for the Prediction of Blast and Fragment Loading on Structures, Report No. DOE/TIC-11268, U. S. Army Engineer Division, Huntsville, Alabama, November.
4. Baker, W. E., Westine, P. S. and F. T. Dodge, (1981), Similarity Methods in Engineering Dynamics: Theory and Practice of Scale Modeling, Southwest Research Institute, San Antonio, Texas.
5. Buckingham, E., (1914), On Physically Similar Systems: Illustrations of the use of Dimensional Equations, Phys. Rev., Vol. 4, pp. 345-376.
6. Chabai, A. J., (1959), Crater Scaling Laws for Desert Alluvium, SC-4391 (RR), Sandia Corporation, Albuquerque, New Mexico.
7. Chabai, A. J., (1965), On Scaling Dimensions of Craters Produced by Buried Explosives, Journal of Geophysical Research, Vol. 70, No. 2, October 15, pp. 5075-5098
8. Charlie, W. A., (1989), Stress Wave Transmission from Contained Blasts in Moist Soils, Broad Agency Announcement Proposal, U.S. Air Force, HQ AFCEA/RACS, Tyndall AFB, Florida, October.
9. Charlie, W. A., and S. J. Pierce, (1989), High Intensity Stress Wave Propagation in Partially Saturated Sand, Final Report to AFOSR, 1988 USAF-UES SFRP Contract No. F49620-87-0004, Department of Civil Engineering, Colorado State University, Fort Collins, Colorado, September.

10. Dillon, L. A. (1972), The Influence of Soil and Rock Properties on the Dimensions of Explosion-Produced Craters. AFWL (DEV), Kirtland AFB, New Mexico, Technical Report No. AFWL-TR-71-144, February.
11. Drake, J. L., and C. D. Little, (1983), Ground Shock from Penetrating Conventional Weapons, Symposium Proceedings, The Interaction of Non-Nuclear Munitions with Structures, U.S. Air Force Academy, Colorado Springs, Colorado, May 10-13, pp.1-6.
12. Farr, J.V., (1990), One-Dimensional Loading-Rate Effects, Journal of Geotechnical Engineering, ASCE, Vol. 116, No. 1, January, pp. 119-135.
13. Felice, C. W., J. A. Brown, E. S. Gaffney, and J. M. Olsen, (1985), An Investigation into the High Strain-Rate Behavior of Compacted Sand Using the Split-Hopkinson Pressure Bar Technique, Proceedings of the Second International Symposium on the Interaction of Non-Nuclear Munitions with Structures, Panama City Beach, Florida, April 15-18, pp. 391-396.
14. Fredlund, D. G., (1986), Soil Mechanics Principles that Embrace Unsaturated Soils, Proceedings of the Eleventh International Conference on Soil Mechanics and Foundation Engineering, Society of Soil Mechanics and Foundation Engineering, San Francisco, California, Vol. 2, pp. 465-472.
15. Fragaszy, R. J. and T. A. Taylor, (1989) Centrifuge Modeling of Projectile Penetration in Granular Soils, HQ AFESC/RDCS, Tyndall AFB, Florida, Report No. ESL-TR-88-76, April.
16. Gaffney, E. S., C. W. Felice, and R. S. Steedman, (1989), Cratering by Buried Charges in Wet Media: Comparison of Centrifuge and Field Events, Proceedings of the Fourth International Symposium on the Interaction of Non-Nuclear Munitions with Structures (volume 1), Panama City Beach, Florida, April 17-21, pp. 402-407.
17. Goodings, D. J., W. L. Fourney, and R. D. Dick. (1988), "Geotechnical Centrifuge Modeling of Explosion Induced Craters - A Check for Scaling Effects," U.S. Air Force Office for Scientific Research, Washington, D.C., Report No. AFOSR-86-0095, July.
18. Gill, J. J. and S. T. Kuennen, (1991), Half-Space Modeling of Explosively-Formed Craters, Proceedings of International Conference Centrifuge 91, Boulder, Colorado, June 13-14, (Hon-Yim Ko and Francis G. McLean eds.) A. A. Balkema, Rotterdam. ISBN 90 6191 193 1, pp. 465-472.

19. Holsapple, K. A. and R. M. Schmidt, (1980), "On the Scaling of Crater Dimensions 1. Explosive Processes, Journal of Geophysical Research, Vol. 85, No. B12, December 10, pp. 7247-7256.
20. Holsapple, K. A., R. M. Schmidt, and R. L. Dyrdaahl, (1978), Gravity-Scaling Methods Applied to Crater-Induced Ground Motions and Effects, Nuclear Blast and Shock Simulation Symposium, Defense Nuclear Agency - SPSS, San Diego, California, Nov. 28-30.
21. James, R. G., (1978), Centrifuge Experiments on the Centrifuge, (2<sup>nd</sup> Series), University of Cambridge, England, Department of Civil Engineering, September.
22. Joseph, P. J., H. H. Einstein, and R. V. Whitman, (1988), A Literature Review of Geotechnical Centrifuge Modeling with Particular Emphasis on Rock Mechanics, HQ AFCEA/RACS Tyndall AFB, Florida, Report No. ESL-TR-87-23, June.
23. Kline, S. J., (1980), Similitude and Approximation Theory, McGraw-Hill Book Company, New York.
24. Knudson, H. L., J. W. Meyer, S. B. Price, and A. D. Rooke, Jr., (1972), Effects of Stemming on High-Explosive Cratering, U.S. Army Engineer Waterways Experiment Station, Vicksburg, Mississippi. Miscellaneous Paper N-72-6, May.
25. Kutter, B. L., L. M. O'Leary, and P. Y. Thompson, (1985), Centrifugal Modeling of the Effects of Blast Loading on Tunnels, Proc. of Second Symposium on the Interaction of Non-Nuclear Munitions with Structures, Panama City Beach, Florida, April 15-18, pp 1-6.
26. Meyer, R., (1987), Explosives, (3rd ed.), VCH Publishers, Suite 909, 220 East 23rd Street, New York, New York.
27. Nielsen, J. P., (1983), The Centrifugal Simulation of Blast Parameters, Tyndall AFB, Florida, Technical Report ESL-TR-83-12, December.
28. Piekutowski, A. J., (1974), Laboratory-Scale High Explosive Cratering and Ejecta Phenomenology Studies, AFWL-TR-72-155, Air Force Weapons Lab, Albuquerque, New Mexico, April.
29. Piekutowski, A. J., (1975), A Comparison of Cratering Effects for Lead Azide and PETN Explosive Charges, AFWL-TR-74-182, Air Force Weapons Lab, Albuquerque, New Mexico, May.
30. Pierce, S. J., (1989), High Intensity Compressive Stress Wave Propagation Through Unsaturated Sands, Master's Thesis, Colorado State University, Spring.

31. Rooke, A. D., B. L. Carnes, and L. K. Davis, (1974), Cratering by Explosives: A Compendium and an Analysis, U.S. Army Engineer Waterways Experiment Station, Vicksburg, Mississippi, Technical Report B024-657, January.
32. Ross, C. A., P. Y. Thompson, W. A. Charlie, and D. C. Doehring, (1989), Transmission of Pressure Waves in Partially Saturated Soils, Journal of Experimental Mechanics, Society for Experimental Mechanics, Vol. 29, No. 1, March, pp. 80-83.
33. Sager, R. A., C. W. Denzel, and W. B. Tiffany, (1960), Compendium of Crater Data, U.S. Army Engineering Waterways Experiment Station, CE: Cratering From High Explosive Charges, Technical Report No. 2-547, Report No. 1, Vicksburg, Mississippi, May.
34. Schmidt, R. M., (1977), A Centrifuge Cratering Experiment: Development of a Gravity-Scaled Yield Parameter, Impact and Explosion Cratering, (D.J. Roddy, R.O. Pepin, and R.B. Merrill, eds), Pergamon Press, New York, pp. 1261-1278.
35. Schmidt, R. M., (1979), Simulation of Large Scale Explosive Cratering and Ground Shock Using a 600-G Geotechnic Centrifuge, Proceedings of the Sixth International Symposium of Blast Simulation, Cahors, France, June 25-29, pp. 1-34.
36. Schmidt, R. M. and K. A. Holsapple, (1978), Centrifuge Cratering Experiments I: Dry Granular Soils, Defense Nuclear Agency Report DNA 4568F, Washington, D.C.
37. Schmidt, R. M. and K. A. Holsapple, (1979), Centrifuge Crater Scaling Experiment II, Material Strength Effects, Interim Report for Period 31 January 1978 - 31 January 1979, Prepared for the Defense Nuclear Agency, Washington D.C., Contract No. DNA 001-78-C-0149, May.
38. Schmidt, R. M. and K. A. Holsapple, (1980), Theory and Experiments on Centrifuge Cratering, Journal of Geophysical Research, Volume 85, No. B1, January 10, pp.235-252.
39. Schmidt, R. M., K. A. Holsapple, and L. D. Fisher, (1979), Statistical-Dimensional Analysis: An Application to the assessment of Crater Configuration, Final Report for Period 19 June 1978 - 31 January 1979, Report DNA 4904F, Prepared for the Defense Nuclear Agency, Washington, D.C., Contract No. DNA 001-78-C-0326, January.
40. Schmidt, R. M., K. A. Holsapple, and K. R. Housen, (1986), Gravity Effects in Cratering, Technical Report DNA-TR-86-182, Defense Nuclear Agency, Washington, DC, 30 May.

41. Schofield, A. N., (1981), Dynamic and Earthquake Geotechnical Centrifuge Modeling, State of the Art Review presented to the International Conference on Recent Advances in Geotechnical Earthquake Engineering and Soil Dynamics, April 26 - May 3, Session 5, Centrifuge Testing in Cyclic Loading, Cambridge University, Cambridge, UK.

42. Steedman, R. S., (1986), Centrifuge Modeling of the Effects of Blast Loading on Piles; Data Analysis, Final Report, WL-TR-90-33, Vol. II, Weapons Laboratory, Air Force Systems Command, Kirtland Air Force Base, New Mexico, July, pp. 22-26.

43. Strange, J. N., C. W. Denzel, and T. J. McLane, (1961), Analysis of Crater Data, U.S. Army Engineering Waterways Experiment Station, CE: Cratering From High Explosive Charges, Technical Report No. 2-547, Report No. 2, Vicksburg, Mississippi, June.

44. Veyera, G. E., and B. J. Fitzpatrick, (1990), Stress Transmission and Microstructure in Compacted Moist Sand, Final Report, Research Initiation Grant Program, Contract No. F49620-88-C-0053/SB5881-0378, Sponsored By Air Force Office of Scientific Research, December.

APPENDIX A

MEASURED, SCALED, AND NORMALIZED APPARENT CRATER DATA

CONSTANT NORMALIZED DOB SERIES

TEST DATA NOTES FOR TYNDALL BEACH SAND COMPACTED TO A DRY DENSITY OF 95 lb/ft<sup>3</sup> (1521.7 kg/m<sup>3</sup>).

<u>Saturation</u>	<u>Note</u>
17%, 20%	Test numbers 191.89-20-4 subjected to 93-g prior to being tested at 67-g.
40%	Test numbers 102.08-40-1 and 102.08-40-2 tested at a saturation of 35%, not a saturation of 40%.  Test number 120.63-40-1 subjected to 43-g prior to testing at 26-g.
70%	Test 102.08-70-1 had 1.0 in of water in the crater immediately after it was formed. Subtracting 1.0 in from a measured crater depth of 3.22 in places the water 2.22 in (5.64 cm) from the soil surface. Subtracting 5.64 cm from the total soil depth of 28 cm left a elevation of 22.4 cm. Scaling this elevation a prototype dimension requires multiplying the 22.4 cm by (18.86) <sup>3</sup> which is 421.73 cm.  Test 120.63-70-2 had 0.55 in of water in the crater immediately after it was formed. Subtracting 0.55 in from a measured crater depth of 2.28 in places the water 1.73 in (4.39 cm) from the soil surface. Subtracting 4.39 cm from the total soil depth of 26 cm left a elevation of 21.6 cm. Scaling this elevation a prototype dimension requires multiplying the 21.6 cm by (26.34) <sup>3</sup> which is 569.1 cm.  Test 102.08-70-3 and 120.83-70-4 prepared with one layer, the bottom layer, of dry sand to prevent a rise in the water table.

A separate test series in Ottawa sand is also included. The OT in the test number indicates Ottawa sand. In this series, the dry density of specimens were 100.67 lb/ft<sup>3</sup> in order to keep the relative density equal to that of the Tyndall sand specimens (39%).

# MEASURED APPARENT CRATER DIMENSIONS

TYNDALL BEACH SAND

SATURATION = 0%

SI System Dry Density of 1521.7 kg/m<sup>3</sup>

Sand	Test Number	RDX (mg)	g level (@ det)	Saturation (%)	Burial Depth (cm)	Outside Diameter (cm)	Inside Diameter (cm)	Depth (cm)	Volume (cm <sup>3</sup> )	Volume Error (%)
Beach Sand	102.08-0-7	1043	18.86	0	7.60	38.10	20.00	3.00	430.4	13.48
"	120.63-0-8	383	26.34	0	5.44	33.34	16.93	2.78	298.9	6.69
"	120.63-0-9	383	26.34	0	5.44	32.28	17.04	3.02	318.1	4.72
Ottawa 20/30	191.89-OT 0-10 *	383	66.65	0	5.44	29.85	17.54	2.02	235.8	31.08

English System Dry Density of 95 lb/ft<sup>3</sup>

Sand	Test Number	RDX (lb)	g level (@ det)	Saturation (%)	Burial Depth (in)	Outside Diameter (in)	Inside Diameter (in)	Depth (in)	Volume (in <sup>3</sup> )	Volume Error (%)
Beach Sand	102.08-0-7	0.00230	18.86	0	2.99	15.00	7.87	1.18	26.3	13.48
"	120.63-0-8	0.00084	26.34	0	2.14	13.13	6.67	1.09	18.2	6.69
"	120.63-0-9	0.00084	26.34	0	2.14	12.71	6.71	1.19	19.4	4.72
Ottawa 20/30	191.89-OT 0-10 *	0.00084	66.65	0	2.14	11.75	6.91	0.80	14.4	33.08

Note: Test number 102.08-0-7 indicates explosive detonation at 102.08 rpm, zero percent saturation series, test seven. A separate test series in Ottawa sand is also listed. The OT in the test number indicates Ottawa sand. \*The dry density of the Ottawa sand specimen was 1601.8 kg/m<sup>3</sup> (100.67 lb/ft<sup>3</sup>).

# SCALED APPARENT CRATER DIMENSIONS

TYNDALL BEACH SAND

SATURATION = 0%

SI System Dry Density of 1521.7 kg/m<sup>3</sup>

Test Number	Explosive Mass		Burial Depth (m)	Outside Diameter (m)	Inside Diameter (m)	Inside Radius (m)	Depth (m)	Volume (m <sup>3</sup> )
	RDX (kg)	TNT Eq. (kg)						
102.08-0-7	7.00	7.63	1.43	7.19	3.77	1.89	0.57	2.89
120.63-0-8	7.00	7.43	1.43	8.78	4.46	2.23	0.73	5.46
120.63-0-9	7.00	7.43	1.43	8.50	4.49	2.24	0.80	5.81
191.89-OT0-10 *	113.40	123.00	3.63	19.90	11.69	5.85	1.35	69.61

English System Dry Density of 95 lb/ft<sup>3</sup>

Test Number	Explosive Weight		Burial Depth (ft)	Outside Diameter (ft)	Inside Diameter (ft)	Inside Radius (ft)	Depth (ft)	Volume (ft <sup>3</sup> )
	RDX (lb)	TNT Eq. (lb)						
102.08-0-7	15.43	16.81	4.70	23.57	12.38	6.19	1.86	101.96
120.63-0-8	15.43	16.82	4.70	28.81	14.63	7.32	2.40	192.89
120.63-0-9	15.43	16.82	4.70	27.90	14.73	7.36	2.61	205.28
191.89-OT0-10 *	249.99	272.40	11.90	65.27	38.35	19.18	4.42	2465.38

\* Dry density of the Ottawa sand specimen was 1601.8 kg/m<sup>3</sup> (100 lb/ft<sup>3</sup>).

# NORMALIZED APPARENT CRATER DIMENSIONS

TYNDALL BEACH SAND

SATURATION = 0%

SI System      Dry Density of 1521.7 kg/m<sup>3</sup>

Test Number	Explosive Mass	Burial Depth	Outside Diameter	Inside Diameter	Inside Radius	Depth	Volume
102.08 - 0 - 7	7.63	0.728	3.65	1.92	0.96	0.29	1.47
120.63 - 0 - 8	7.63	0.728	4.46	2.27	1.13	0.37	2.77
120.63 - 0 - 9	7.63	0.728	4.32	2.28	1.14	0.40	2.95
191.89 - OT 0 - 10 *	123.60	0.728	3.99	2.35	1.17	0.27	14.02

English System      Dry Density of 95 lb/ft<sup>3</sup>

Test Number	Explosive Weight	Burial Depth	Outside Diameter	Inside Diameter	Inside Radius	Depth	Volume
102.08 - 0 - 7	16.81	1.835	9.20	4.83	2.42	0.72	39.80
120.63 - 0 - 8	16.82	1.835	11.25	5.71	2.86	0.94	75.29
120.63 - 0 - 9	16.82	1.835	10.89	5.75	2.87	1.07	80.12
191.89 - OT 0 - 10 *	272.49	1.835	10.07	5.92	2.96	0.68	380.28

\* Dry density of the Ottawa specimen was 1601.8 kg/m<sup>3</sup> (100 lb/ft<sup>3</sup>).

# MEASURED APPARENT CRATER DIMENSIONS

TYNDALL BEACH SAND

SATURATION = 17%, 20%

SI System Dry Density of 1521.7 kg/m<sup>3</sup>

Sand	Test Number	RDX (mg)	g level (@ det)	Saturation (%)	Burial Depth (cm)	Outside Diameter (cm)	Inside Diameter (cm)	Depth (cm)	Volume (cm <sup>3</sup> )	Volume Error (%)
Beach Sand	102.08 - 20 - 3	1043	18.86	17	7.60	40.20	21.80	8.30	995.6	11.45
"	120.63 - 20 - 2	383	26.34	17	5.44	32.39	17.15	6.03	no mold	---
"	164.71 - 20 - 5	383	49.11	20	5.44	32.07	17.04	4.52	415.7	3.61
"	191.89 - 20 - 4 *	383	66.65	20	5.44	32.38	15.34	4.24	303.5	9.23
Ottawa 20/30	162.38 - OT 20 - 7 **	1043	49.11	20	7.60	38.10	24.77	4.52	904.3	5.64
"	191.89 - OT 20 - 6 **	383	66.65	20	5.44	34.45	18.10	3.02	281.7	15.97

English System

Dry Density of 95 lb/ft<sup>3</sup>

Sand	Test Number	RDX (lb)	g level (@ det)	Saturation (%)	Burial Depth (in)	Outside Diameter (in)	Inside Diameter (in)	Depth (in)	Volume (in <sup>3</sup> )	Volume Error (%)
Beach Sand	102.08 - 20 - 3	0.00230	18.86	17	2.99	15.83	8.58	3.27	60.8	11.45
"	120.63 - 20 - 2	0.00084	26.34	17	2.14	12.75	6.75	2.37	---	---
"	164.71 - 20 - 5	0.00084	49.11	20	2.14	12.63	6.71	1.78	25.4	3.61
"	191.89 - 20 - 4 *	0.00084	66.65	20	2.14	12.75	6.04	1.67	18.5	9.23
Ottawa 20/30	162.38 - OT 20 - 7 **	0.00230	49.11	20	2.99	15.00	9.75	1.78	55.2	5.64
"	191.89 - OT 20 - 6 **	0.00084	66.65	20	2.14	13.56	7.13	1.19	17.2	15.97

\* Specimen spun to 93 G prior to test at 66.65 G.

\*\* Dry density of the Ottawa sand specimen was 1601.8 kg/m<sup>3</sup> (100 lb/ft<sup>3</sup>).

# SCALED APPARENT CRATER DIMENSIONS

TYNDALL BEACH SAND

SATURATION = 17%, 20%

SI System Dry Density of 1521.7 kg/m<sup>3</sup>

Test Number	Explosive Mass		Burial Depth (m)	Outside Diameter (m)	Inside Diameter (m)	Inside Radius (m)	Depth (m)	Volume (m <sup>3</sup> )
	RDX (kg)	TNT Eq. (kg)						
102.08 - 20 - 3	7.0	7.6	1.43	7.58	4.11	2.06	1.57	6.68
120.63 - 20 - 2	7.0	7.6	1.43	8.53	4.52	2.26	1.59	---
164.71 - 20 - 5	45.4	49.4	2.67	15.75	8.37	4.16	2.22	49.24
191.89 - 20 - 4	113.4	123.6	3.63	21.58	10.22	5.11	2.83	89.86
162.38 - OT 20 - 7 *	123.5	134.7	3.73	18.71	12.16	6.08	2.22	107.11
191.89 - OT 20 - 6	113.4	123.6	3.63	22.96	12.06	6.03	2.01	83.40

English System Dry Density of 95 lb/ft<sup>3</sup>

Test Number	Explosive Weight		Burial Depth (ft)	Outside Diameter (ft)	Inside Diameter (ft)	Inside Radius (ft)	Depth (ft)	Volume (ft <sup>3</sup> )
	RDX (lb)	TNT Eq. (lb)						
102.08 - 20 - 3	15.43	16.8	4.70	24.87	13.49	6.74	5.14	235.86
120.63 - 20 - 2	15.43	16.8	4.70	27.99	14.82	7.41	5.21	---
164.71 - 20 - 5	100.01	109.0	8.76	51.67	27.45	13.73	7.28	1738.72
191.89 - 20 - 4	250.00	272.5	11.90	70.80	33.54	16.77	9.27	3173.21
162.38 - OT 20 - 7 *	272.35	296.9	12.25	61.39	39.91	19.95	7.28	3782.35
191.89 - OT 20 - 6	250.00	272.5	11.90	75.33	39.57	19.79	6.59	2945.28

\* Dry density of the Ottawa sand specimens were 1601.8 kg/m<sup>3</sup> (100 lb/ft<sup>3</sup>).

# NORMALIZED APPARENT CRATER DIMENSIONS

TYNDALL BEACH SAND

**SATURATION = 17%, 20%**

**SI System**      Dry Density of 1521.7 kg/m<sup>3</sup>

Test Number	Explosive Mass	Burial Depth	Outside Diameter	Diameter		Inside Radius	Depth	Volume
				$\frac{m}{kg^{1/3}}$	$\frac{m}{kg^{1/3}}$			
102.08 - 20 - 3	7.6	0.728	3.85	2.09	1.04	0.80	3.39	
120.63 - 20 - 2	7.6	0.728	4.33	2.29	1.15	0.81	---	
164.71 - 20 - 5	49.4	0.728	4.29	2.28	1.14	0.60	13.41	
191.89 - 20 - 4	123.6	0.728	4.33	2.05	1.03	0.57	18.04	
162.38 - OT 20 - 7 *	134.7	0.728	3.65	2.37	1.19	0.43	20.90	
191.89 - OT 20 - 6	123.6	0.728	4.61	2.42	1.21	0.40	16.74	

**English System**      Dry Density of 95 lb/ft<sup>3</sup>

Test Number	Explosive Weight	Burial Depth	Outside Diameter	Diameter		Inside Radius	Depth	Volume
				$\frac{ft}{lb^{1/3}}$	$\frac{ft}{lb^{1/3}}$			
102.08 - 20 - 3	16.81	1.836	9.71	5.27	2.63	2.00	92.96	
120.63 - 20 - 2	16.82	1.835	10.92	5.78	2.89	2.03	---	
164.71 - 20 - 5	109.01	1.835	10.82	5.75	2.87	1.52	363.98	
191.89 - 20 - 4	272.50	1.835	10.92	5.17	2.59	1.43	489.46	
162.38 - OT 20 - 7 *	296.86	1.836	9.20	5.98	2.99	1.09	566.99	
191.89 - OT 20 - 6	272.50	1.835	11.62	6.10	3.05	1.02	454.30	

\* Dry density of the Ottawa sand specimens were 1601.8 kg/m<sup>3</sup> (100 lb/ft<sup>3</sup>).

# MEASURED APPARENT CRATER DIMENSIONS

## TYNDALL BEACH SAND

SATURATION = 35%, 40%

### SI System

Dry Density of 1521.7 kg/m<sup>3</sup>

Sand	Test Number	RDX (mg)	g level (@ det)	Saturation (%)	Burial Depth (cm)	Outside Diameter (cm)	Inside Diameter (cm)	Depth (cm)	Volume (cm <sup>3</sup> )	Volume Error (%)
Beach Sand	102.08 - 40 - 2	1043	18.86	35	7.60	39.90	23.00	8.00	1305.6	10.19
"	120.63 - 40 - 1 *	383	26.34	35	5.44	31.80	19.70	7.00	---	---
"	164.71 - 40 - 4	383	49.11	40	5.44	32.49	15.66	3.97	319.0	2.51
"	191.89 - 40 - 3	383	66.65	40	5.44	31.54	14.18	3.33	241.8	17.78
Ottawa 20/30	191.89 - OT 40 - 5 **	383	66.65	40	5.44	36.20	17.60	3.25	341.0	6.74

### English System

Dry Density of 95 lb/ft<sup>3</sup>

Sand	Test Number	RDX (lb)	g level (@ det)	Saturation (%)	Burial Depth (in)	Outside Diameter (in)	Inside Diameter (in)	Depth (in)	Volume (in <sup>3</sup> )	Volume Error (%)
Beach Sand	102.08 - 40 - 2	0.00230	18.86	35	2.99	15.71	9.06	3.15	79.7	10.19
"	120.63 - 40 - 1	0.00084	26.34	35	2.14	12.52	7.76	2.76	---	---
"	164.71 - 40 - 4	0.00084	49.11	40	2.14	12.79	6.17	1.56	19.5	2.51
"	191.89 - 40 - 3	0.00084	66.65	40	2.14	12.42	5.58	1.31	14.8	17.78
Ottawa 20/30	191.89 - OT 40 - 5 **	0.00084	66.65	40	2.14	14.25	6.93	1.28	20.8	6.74

\* Specimen spun to 43 G prior to test at 26.34 G.

\*\* Dry density of the Ottawa sand specimen was 1601.8 kg/m<sup>3</sup> (100 lb/ft<sup>3</sup>).

# SCALED APPARENT CRATER DIMENSIONS

## TYNDALL BEACH SAND

SATURATION = 35%, 40%

SI System Dry Density of 1521.7 kg/m<sup>3</sup>

Test Number	Explosive Mass RDX (kg)	TNT Eq. (kg)	Burial Depth (m)	Outside Diameter (m)	Inside Diameter (m)	Inside Radius (m)	Depth (m)	Volume (m <sup>3</sup> )
102.08 - 40 - 2	7.0	7.6	1.43	7.53	4.34	2.17	1.51	8.76
120.63 - 40 - 1	7.0	7.6	1.43	8.38	5.19	2.59	1.84	---
164.71 - 40 - 4	45.4	49.4	2.67	15.96	7.69	3.85	1.95	37.78
191.89 - 40 - 3	113.4	123.6	3.63	21.02	9.45	4.73	2.22	71.59
191.89 - OT 40 - 5 *	113.4	123.6	3.63	24.13	11.73	5.87	2.17	100.96

English System Dry Density of 95 lb/ft<sup>3</sup>

Test Number	Explosive Weight RDX (lb)	TNT Eq. (lb)	Burial Depth (ft)	Outside Diameter (ft)	Inside Diameter (ft)	Inside Radius (ft)	Depth (ft)	Volume (ft <sup>3</sup> )
102.08 - 40 - 2	15.43	16.82	4.70	24.69	14.23	7.12	4.95	309.30
120.63 - 40 - 1	15.43	16.82	4.70	27.48	17.02	8.51	6.05	---
164.71 - 40 - 4	100.00	109.00	8.76	52.35	25.23	12.62	6.40	1334.26
191.89 - 40 - 3	250.00	272.50	11.90	68.97	31.01	15.50	7.28	2528.11
191.89 - OT 40 - 5 *	250.00	272.50	11.90	79.16	38.49	19.24	7.11	3565.28

\* Dry density of the Ottawa sand specimen was 1601.8 kg/m<sup>3</sup> (100 lb/ft<sup>3</sup>).

# NORMALIZED APPARENT CRATER DIMENSIONS

TYNDALL BEACH SAND

**SATURATION = 358, 40%**

**SISystem      Dry Density of 1521.7 kg/m<sup>3</sup>**

Test Number	Explosive Mass	Burial Depth	Outside Diameter	Inside Diameter	Inside Radius	Depth	Volume
102.08 - 40 - 2	7.6	0.728	3.82	2.20	1.10	0.77	4.45
120.63 - 40 - 1	7.6	0.728	4.25	2.64	1.32	0.94	—
164.71 - 40 - 4	49.4	0.728	4.35	2.10	1.05	0.53	10.29
191.89 - 40 - 3	123.6	0.728	4.22	1.90	0.95	0.42	14.37
191.89 - OT 40 - 5 *	123.6	0.728	4.84	2.55	1.18	0.43	20.27

**English System      Dry Density of 95 lb/ft<sup>3</sup>**

Test Number	Explosive Weight	Burial Depth	Outside Diameter	Inside Diameter	Inside Radius	Depth	Volume
102.08 - 40 - 2	16.82	1.835	9.64	5.55	2.78	1.93	120.71
120.63 - 40 - 1	16.82	1.835	10.73	6.64	3.32	2.36	—
164.71 - 40 - 4	109.00	1.835	10.96	5.28	2.64	1.34	279.30
191.89 - 40 - 3	272.50	1.835	10.64	4.78	2.39	1.12	389.93
191.89 - OT 40 - 5 *	272.50	1.835	12.21	5.94	2.97	1.10	549.90

\* Dry density of the Ottawa sand specimen was 1601.8 kg/m<sup>3</sup> (100 lb/ft<sup>3</sup>).

# MEASURED APPARENT CRATER DIMENSIONS

TYNDALL BEACH SAND

SATURATION = 53%, 60%

## SI System

Dry Density of 1521.7 kg/m<sup>3</sup>

Sand	Test Number	RDX (mg)	g level (@ det)	Saturation (%)	Burial Depth (cm)	Outside Diameter (cm)	Inside Diameter (cm)	Depth (cm)	Volume (cm <sup>3</sup> )	Volume Error (%)
Beach Sand	102.08 - 60 - 2	1043	18.86	53	7.00	41.60	23.90	8.30	1300.8	2.31
"	120.63 - 60 - 1	383	26.34	53	5.44	37.50	18.10	5.60	443.2	5.64
"	164.71 - 60 - 4	383	49.11	60	5.44	32.49	15.88	3.93	340.3	8.23
"	191.89 - 60 - 3	383	66.65	60	5.44	29.21	15.24	3.81	285.7	3.15
Ottawa 20/30	191.89 - OT 60 - 5 **	383	66.65	60	5.44	34.90	17.00	2.18	294.6	49.56

## English System

Dry Density of 95 lb/ft<sup>3</sup>

Sand	Test Number	RDX (lb)	g level (@ det)	Saturation (%)	Burial Depth (in)	Outside Diameter (in)	Inside Diameter (in)	Depth (in)	Volume (in <sup>3</sup> )	Volume Error (%)
Beach Sand	102.08 - 60 - 2	0.00230	18.86	53	2.99	16.38	9.41	3.27	79.4	2.31
"	120.63 - 60 - 1	0.00084	26.34	53	2.14	14.76	7.13	2.20	27.0	5.64
"	164.71 - 60 - 4	0.00084	49.11	60	2.14	12.79	6.25	1.55	20.8	8.23
"	191.89 - 60 - 3	0.00084	66.65	60	2.14	11.50	6.00	1.50	17.4	3.15
Ottawa 20/30	191.89 - OT 60 - 5 **	0.00084	66.65	60	2.14	13.74	6.69	0.86	18.0	49.56

\*\* Dry density of the Ottawa sand specimen was 1601.8 kg/m<sup>3</sup> (100 lb/ft<sup>3</sup>).

# SCALED APPARENT CRATER DIMENSIONS

TYNDALL BEACH SAND

SATURATION = 53%, 60%

SI System Dry Density of 1521.7 kg/m<sup>3</sup>

Test Number	Explosive Mass		Burial Depth (m)	Outside Diameter (m)	Inside Diameter (m)	Inside Radius (m)	Depth (m)	Volume (m <sup>3</sup> )
	RDX (kg)	TNT Eq. (kg)						
102.08 - 60 - 2	7.0	7.6	1.43	7.85	4.51	2.25	1.57	8.73
120.63 - 60 - 1	7.0	7.6	1.43	9.88	4.77	2.38	1.48	8.10
164.71 - 60 - 4	45.4	49.4	2.67	15.96	7.80	3.90	1.93	40.31
191.89 - 60 - 3	113.4	123.6	3.63	19.47	10.16	5.08	2.54	84.59
191.89 - OT 60 - 5 *	113.4	123.6	3.63	23.26	11.33	5.67	1.45	87.22

English System Dry Density of 95 lb/ft<sup>3</sup>

Test Number	Explosive Weight		Burial Depth (ft)	Outside Diameter (ft)	Inside Diameter (ft)	Inside Radius (ft)	Depth (ft)	Volume (ft <sup>3</sup> )
	RDX (lb)	TNT Eq. (lb)						
102.08 - 60 - 2	15.43	16.81	4.70	25.74	14.79	7.39	5.14	308.16
120.63 - 60 - 1	15.43	16.82	4.70	32.41	15.64	7.82	4.84	286.01
164.71 - 60 - 4	100.01	109.01	8.76	52.35	25.59	12.79	6.33	1423.35
191.89 - 60 - 3	250.00	272.50	11.90	63.87	33.32	16.66	8.33	2987.10
191.89 - OT 60 - 5 *	250.00	272.50	11.90	76.31	37.17	18.59	4.77	3080.15

\* Dry density of the Ottawa sand specimen was 1601.8 kg/m<sup>3</sup> (100 lb/ft<sup>3</sup>).

# NORMALIZED APPARENT CRATER DIMENSIONS

TYNDALL BEACH SAND

**SATURATION = 53%, 60%**

SI System      Dry Density of 1521.7 kg/m<sup>3</sup>

Test Number	Explosive Mass	Burial Depth	Outside Diameter	Inside Diameter	Inside Radius	Depth	Volume	TNT Eq. (kg)	
								m	kg <sup>1/3</sup>
102.08 - 60 - 2	7.6	0.728	3.99	2.29	1.14	0.80	4.43		
120.63 - 60 - 1	7.6	0.728	5.02	2.42	1.21	0.75	4.11		
164.71 - 60 - 4	49.4	0.728	4.35	2.12	1.06	0.53	10.98		
191.89 - 60 - 3	123.6	0.728	3.91	2.04	1.02	0.51	16.98		
191.89 - OT 60 - 5 *	123.6	0.728	4.67	2.27	1.14	0.29	17.51		

English System      Dry Density of 95 lb/ft<sup>3</sup>

Test Number	Explosive Weight	Burial Depth	Outside Diameter	Inside Diameter	Inside Radius	Depth	Volume	TNT Eq. (lb)	
								ft	lb <sup>1/3</sup>
102.08 - 60 - 2	16.82	1.836	10.05	5.77	2.89	2.00	120.29		
120.63 - 60 - 1	16.82	1.835	12.65	6.10	3.05	1.89	111.63		
164.71 - 60 - 4	109.00	1.835	10.96	5.36	2.68	1.33	297.96		
191.89 - 60 - 3	272.50	1.835	9.85	5.14	2.57	1.29	460.75		
191.89 - OT 60 - 5 *	272.50	1.835	11.77	5.73	2.87	0.74	475.10		

\* Dry density of the Ottawa sand specimen was 1601.8 kg/m<sup>3</sup> (100 lb/ft<sup>3</sup>).

# MEASURED APPARENT CRATER DIMENSIONS

TYNDALL BEACH SAND

SATURATION = 70%

SI System Dry Density of 1521.7 kg/m<sup>3</sup>

Sand	Test Number	RDX (mg)	g level (@ det)	Saturation (%)	Burial Depth (cm)	Outside Diameter (cm)	Inside Diameter (cm)	Depth (cm)	Volume (cm <sup>3</sup> )	Volume Error (%)
Beach Sand	102.08 - 70 - 3 *	1043	18.86	70	7.60	43.26	22.86	8.18	1302.9	4.68
"	102.08 - 70 - 1	1043	18.86	70	7.60	39.65	24.13	8.18	1559.6	2.37
"	120.63 - 70 - 4 *	383	26.34	70	5.44	37.94	16.93	6.23	494.5	5.46
"	120.63 - 70 - 2	383	26.34	70	5.44	37.78	16.62	5.79	534.2	3.56

English System Dry Density of 95 lb/ft<sup>3</sup>

Sand	Test Number	RDX (lb)	g level (@ det)	Saturation (%)	Burial Depth (in)	Outside Diameter (in)	Inside Diameter (in)	Depth (in)	Volume (in <sup>3</sup> )	Volume Error (%)
Beach Sand	102.08 - 70 - 3 *	0.00230	18.86	70	2.99	17.03	9.00	3.22	79.5	4.68
"	102.08 - 70 - 1	0.00230	18.86	70	2.99	15.62	9.50	3.22	95.2	2.37
"	120.63 - 70 - 4 *	0.00084	26.34	70	2.14	14.94	6.67	2.45	30.2	5.46
"	120.63 - 70 - 2	0.00084	26.34	70	2.14	14.87	6.54	2.28	32.6	3.56

\* Test numbers 3 & 4 were prepared using 2 inches of dry sand for the first - bottom - layer.

# SCALED APPARENT CRATER DIMENSIONS

TYNDALL BEACH SAND

SATURATION = 70%

SI System Dry Density of 1521.7 kg/m<sup>3</sup>

Test Number	Explosive Mass RDX (kg)	TNT Eq. (kg)	Burial Depth (m)	Outside Diameter (m)	Inside Diameter (m)	Inside Radius (m)	Depth (m)	Volume (m <sup>3</sup> )
102.08 - 70 - 3	7.0	7.63	1.43	8.16	4.31	2.16	1.54	8.74
102.08 - 70 - 1	7.0	7.63	1.43	7.48	4.55	2.28	1.54	10.46
120.63 - 70 - 4	7.0	7.63	1.43	9.99	4.46	2.23	1.64	9.04
120.63 - 70 - 2	7.0	7.63	1.43	9.95	4.38	2.19	1.53	9.76

English System Dry Density of 95 lb/ft<sup>3</sup>

Test Number	Explosive Weight RDX (lb)	TNT Eq. (lb)	Burial Depth (ft)	Outside Diameter (ft)	Inside Diameter (ft)	Inside Radius (ft)	Depth (ft)	Volume (ft <sup>3</sup> )
102.08 - 70 - 3	15.43	16.82	4.70	26.77	14.14	7.07	5.06	308.66
102.08 - 70 - 1	15.43	16.82	4.70	24.55	14.93	7.47	5.06	369.47
120.63 - 70 - 4	15.43	16.82	4.70	32.79	14.63	7.32	5.38	319.12
120.63 - 70 - 2	15.43	16.82	4.70	32.65	14.36	7.18	5.00	344.74

# NORMALIZED APPARENT CRATER DIMENSIONS

TYNDALL BEACH SAND

**SATURATION = 70%**

SI System      Dry Density of 1521.7 kg/m<sup>3</sup>

Test Number	Explosive Mass	Burial Depth	Diameter		Inside Radius	Depth	Volume	
			Outside	Inside				
			m		kg <sup>1/3</sup>		m <sup>3</sup>	
			kg <sup>1/3</sup>				kg <sup>1/3</sup>	
102.08 - 70 - 3	7.63	0.728	4.14	2.19	1.10	0.78	4.44	
102.08 - 70 - 1	7.63	0.728	3.80	2.31	1.16	0.78	5.32	
120.63 - 70 - 4	7.63	0.728	5.08	2.27	1.13	0.83	4.59	
120.63 - 70 - 2	7.63	0.728	5.05	2.22	1.11	0.77	4.96	

English System      Dry Density of 95 lb/ft<sup>3</sup>

Test Number	Explosive Weight	Burial Depth	Diameter		Inside Radius	Depth	Volume	
			Outside	Inside				
			ft		lb <sup>1/3</sup>		ft <sup>3</sup>	
			lb <sup>1/3</sup>				lb <sup>1/3</sup>	
102.08 - 70 - 3	16.82	1.835	10.45	5.52	2.76	1.98	120.48	
102.08 - 70 - 1	16.82	1.835	9.58	5.83	2.91	1.98	144.22	
120.63 - 70 - 4	16.82	1.835	12.80	5.71	2.86	2.10	124.55	
120.63 - 70 - 2	16.82	1.835	12.74	5.61	2.80	1.95	134.55	

VARIATION IN DOB SERIES

# MEASURED APPARENT CRATER DIMENSIONS

TYNDALL BEACH SAND

SATURATION = 0% VARIOUS DEPTHS OF BURIAL - PLUVIATED

SI System Dry Density of 1521.7 kg/m<sup>3</sup>

Sand	Test Number	RDX (mg)	g level (@ det)	Burial Depth (cm)	Outside Diameter (cm)	Inside Diameter (cm)	Depth (cm)	Volume (cm <sup>3</sup> )	Volume Error (%)
Beach Sand	194.44 - V 0 - 1	823	65.07	2.20	30.80	20.32	4.13	554.6	5.59
"	185.57 - V 0 - 2	1043	60.13	4.44	33.02	23.26	4.88	922.5	5.42
"	167.17 - V 0 - 3	383	49.11	5.44	27.94	13.10	2.02	123.3	15.41
"	194.75 - V 0 - 4	383	66.65	5.44	22.78	14.29	2.10	141.6	26.84
"	201.76 - V 0 - 5	603	72.18	6.86	24.53	14.61	2.18	131.0	26.72
"	139.30 - V 0 - 6	1043	35.17	10.36	29.69	20.00	2.50	274.9	9.82
"	178.75 - V 0 - 7	603	57.29	8.64	23.89	13.97	1.55	120.3	34.91
"	189.94 - V 0 - 8	823	65.07	9.58	27.15	16.83	1.71	129.9	73.13

English System Dry Density of 95 lb/ft<sup>3</sup>

Sand	Test Number	RDX (lb)	g level (@ det)	Burial Depth (in)	Outside Diameter (in)	Inside Diameter (in)	Depth (in)	Volume (in <sup>3</sup> )	Volume Error (%)
Beach Sand	194.44 - V 0 - 1	0.00181	65.07	0.87	12.13	8.00	1.63	33.8	5.59
"	185.57 - V 0 - 2	0.00230	60.13	1.75	13.00	9.16	1.92	56.3	5.42
"	167.17 - V 0 - 3	0.00084	49.11	2.14	11.00	5.16	0.80	7.5	15.41
"	194.75 - V 0 - 4	0.00084	66.65	2.14	8.97	5.63	0.83	8.6	26.84
"	201.76 - V 0 - 5	0.00133	72.18	2.70	9.66	5.75	0.86	8.0	26.72
"	139.30 - V 0 - 6	0.00230	35.17	4.08	11.69	7.88	0.98	16.8	9.82
"	178.75 - V 0 - 7	0.00133	57.29	3.40	9.41	5.50	0.61	7.3	34.91
"	189.94 - V 0 - 8	0.00181	65.07	3.77	10.69	6.63	0.67	7.9	73.13

# SCALED APPARENT CRATER DIMENSIONS

TYNDALL BEACH SAND

SATURATION = 0% VARIOUS DEPTHS OF BURIAL - PLUVIATED

SI System Dry Density of 1521.7 kg/m<sup>3</sup>

Test Number	Explosive Mass		Burial Depth (m)	Outside Diameter (m)	Inside Diameter (m)	Inside Radius (m)	Depth (m)	Volume (m <sup>3</sup> )
	RDX (kg)	TNT Eq. (kg)						
194.44 - V 0 - 1	226.75	247.15	1.43	20.04	13.22	6.61	2.69	152.80
185.57 - V 0 - 2	226.76	247.16	2.67	19.85	13.98	6.99	2.94	200.56
167.17 - V 0 - 3	45.36	49.45	2.67	13.72	6.43	3.22	0.99	14.60
194.75 - V 0 - 4	113.40	123.61	3.62	15.18	9.52	4.76	1.40	41.92
201.76 - V 0 - 5	226.76	247.15	4.95	17.70	10.54	5.27	1.57	49.26
139.30 - V 0 - 6	45.37	49.46	3.64	10.44	7.03	3.52	0.88	11.96
178.75 - V 0 - 7	113.38	123.59	4.95	13.69	8.00	4.00	0.89	22.62
189.94 - V 0 - 8	226.75	247.15	6.23	17.66	10.95	5.47	1.11	35.79

English System Dry Density of 95 lb/ft<sup>3</sup>

Test Number	Explosive Weight		Burial Depth (ft)	Outside Diameter (ft)	Inside Diameter (ft)	Inside Radius (ft)	Depth (ft)	Volume (ft <sup>3</sup> )
	RDX (lb)	TNT Eq. (lb)						
194.44 - V 0 - 1	500.00	545.00	4.70	65.75	43.38	21.69	8.81	5396.07
185.57 - V 0 - 2	500.00	545.00	8.76	65.14	45.88	22.94	9.63	7082.64
167.17 - V 0 - 3	100.00	109.00	8.76	45.02	21.10	10.55	3.26	515.74
194.75 - V 0 - 4	250.00	272.50	11.89	49.82	31.24	15.62	4.60	1480.54
201.76 - V 0 - 5	500.00	545.00	16.24	58.08	34.59	17.29	5.17	1739.71
139.30 - V 0 - 6	100.00	109.00	11.96	34.26	23.08	11.54	2.88	422.33
178.75 - V 0 - 7	250.00	272.50	16.23	44.91	26.26	13.13	2.91	798.84
189.94 - V 0 - 8	500.00	545.00	20.44	57.96	35.92	17.96	3.64	1263.88

# NORMALIZED APPARENT CRATER DIMENSIONS

TYNDALL BEACH SAND

**SATURATION = 0% VARIOUS DEPTHS OF BURIAL - PLUVIATED**

SI System      Dry Density of 1521.7 kg/m<sup>3</sup>

Test Number	Explosive Mass	Burial Depth	Diameter		Inside Radius	Depth	Volume
			Outside	Inside			
TNT Eq.(kg)		m		kg <sup>1/3</sup>		m <sup>3</sup> kg <sup>1/3</sup>	
194.44 - V 0 - 1	247.15	0.228	3.19	2.11	1.05	0.43	24.35
185.57 - V 0 - 2	247.16	0.426	3.16	2.23	1.11	0.47	31.96
167.17 - V 0 - 3	49.45	0.727	3.74	1.75	0.88	0.27	3.98
194.75 - V 0 - 4	123.60	0.727	3.05	1.91	0.96	0.28	8.42
201.76 - V 0 - 5	247.17	0.789	2.82	1.68	0.84	0.25	7.85
139.30 - V 0 - 6	49.46	0.993	2.84	1.92	0.96	0.24	3.26
178.75 - V 0 - 7	123.59	0.993	2.75	1.61	0.80	0.18	4.54
189.94 - V 0 - 8	247.15	0.993	2.81	1.74	0.87	0.18	5.70

English System      Dry Density of 95 lb/ft<sup>3</sup>

Test Number	Explosive Weight	Burial Depth	Diameter		Inside Radius	Depth	Volume
			Outside	Inside			
TNT Eq.(lb)		ft		lb <sup>1/3</sup>		ft <sup>3</sup> lb <sup>1/3</sup>	
194.44 - V 0 - 1	545.00	0.576	8.05	5.31	2.66	1.08	660.61
185.57 - V 0 - 2	545.00	1.073	7.97	5.62	2.81	1.18	867.09
167.17 - V 0 - 3	109.00	1.833	9.42	4.42	2.21	0.68	107.97
194.75 - V 0 - 4	272.50	1.833	7.68	4.82	2.41	0.71	228.37
201.76 - V 0 - 5	545.00	1.988	7.11	4.23	2.12	0.63	212.98
139.30 - V 0 - 6	109.00	2.503	7.17	4.83	2.42	0.60	88.41
178.75 - V 0 - 7	272.50	2.504	6.93	4.05	2.03	0.45	123.22
189.94 - V 0 - 8	545.00	2.503	7.10	4.40	2.20	0.45	154.73

1 G SERIES

# MEASURED APPARENT CRATER DIMENSIONS

TYNDALL BEACH SAND

## 1g TESTS

### SI System

Dry Density of 1521.7 kg/m<sup>3</sup>

Sand	Test Number	RDX (mg)	g level (@ det)	Saturation (%)	Burial Depth (cm)	Outside Diameter (cm)	Inside Diameter (cm)	Depth (cm)	Volume (cm <sup>3</sup> )	Volume Error (%)
Beach Sand	rpm - 1g 20 - 1	603	1.00	20	6.32	36.83	24.13	7.78	1367.7	2.78
"	179.48 - 1g 20 - 3	603	1.00	20	5.32	37.06	23.02	6.48	1037.7	3.47
"	rpm - 1g 60 - 2	603	1.00	60	6.32	34.45	25.40	9.17	1869.3	10.70
"	179.48 - 1g 60 - 4	603	1.00	60	6.32	35.85	24.45	7.94	1426.8	1.05
"	vibrated - 1g 0 - 5	603	1.00	0	6.32	26.67	15.88	2.22	330.4	33.29
"	pluviated - 1g 0 - 6	603	1.00	0	6.32	26.04	15.24	1.75	132.4	5.29

### English System

Dry Density of 95 lb/ft<sup>3</sup>

Sand	Test Number	RDX (lb)	g level (@ det)	Saturation (%)	Burial Depth (in)	Outside Diameter (in)	Inside Diameter (in)	Depth (in)	Volume (in <sup>3</sup> )	Volume Error (%)
Beach Sand	rpm - 1g 20 - 1	0.00133	1.00	20	2.49	14.50	9.59	3.06	83.5	2.78
"	179.48 - 1g 20 - 3	0.00133	1.00	20	2.49	14.59	9.06	2.55	63.3	3.47
"	rpm - 1g 60 - 2	0.00133	1.00	60	2.49	13.56	10.00	3.61	114.1	10.70
"	179.48 - 1g 60 - 4	0.00133	1.00	60	2.49	15.36	9.63	3.13	87.1	1.05
"	vibrated - 1g 0 - 5	0.00133	1.00	0	2.49	10.50	6.25	0.88	20.2	33.29
"	pluviated - 1g 0 - 6	0.00133	1.00	0	2.49	10.25	6.00	0.69	8.1	5.29

# SCALED APPARENT CRATER DIMENSIONS

TYNDALL BEACH SAND

## 1g TESTS

### SI System

Dry Density of 1521.7 kg/m<sup>3</sup>

Test Number	Explosive Mass		Burial Depth (m)	Diameter (m)		Inside Diameter (m)	Inside Radius (m)	Depth (m)	Volume (m <sup>3</sup> )
	RDX (g)	TNT Eq. (kg)		Outside Diameter (m)	Inside Diameter (m)				
rpm - 1g 20 - 1	0.603	0.00066	0.0632	0.3683	0.2413	0.1207	0.0778	0.00137	
179.48 - 1g 20 - 3	0.603	0.00066	0.0632	0.3706	0.2302	0.1151	0.0648	0.00104	
rpm - 1g 60 - 2	0.603	0.00066	0.0632	0.3445	0.2540	0.1270	0.0917	0.00187	
179.48 - 1g 60 - 4	0.603	0.00066	0.0632	0.3885	0.2445	0.1222	0.0794	0.00143	
vibrated - 1g 0 - 5	0.603	0.00066	0.0632	0.2667	0.1588	0.0794	0.0222	0.00033	
pluviated - 1g 0 - 6	0.603	0.00066	0.0632	0.2604	0.1524	0.0762	0.0175	0.00013	

### English System

Dry Density of 95 lb/ft<sup>3</sup>

Test Number	Explosive Weight		Burial Depth (ft)	Diameter (ft)		Inside Diameter (ft)	Inside Radius (ft)	Depth (ft)	Volume (ft <sup>3</sup> )
	RDX (lb)	TNT Eq. (lb)		Outside Diameter (ft)	Inside Diameter (ft)				
rpm - 1g 20 - 1	0.0013	0.0014	0.2073	1.2083	0.7917	0.3958	0.2552	0.04830	
179.48 - 1g 20 - 3	0.0013	0.0014	0.2073	1.2158	0.7552	0.3776	0.2125	0.03665	
rpm - 1g 60 - 2	0.0013	0.0014	0.2073	1.1302	0.8333	0.4167	0.3008	0.06601	
179.48 - 1g 60 - 4	0.0013	0.0014	0.2073	1.2748	0.8021	0.4010	0.2604	0.05039	
vibrated - 1g 0 - 5	0.0013	0.0014	0.2073	0.8750	0.5208	0.2604	0.0729	0.01167	
pluviated - 1g 0 - 6	0.0013	0.0014	0.2073	0.8542	0.5000	0.2500	0.0573	0.00468	

# NORMALIZED APPARENT CRATER DIMENSIONS

TYNDALL BEACH SAND

## 1g TESTS

SI System Dry Density of 1521.7 kg/m<sup>3</sup>

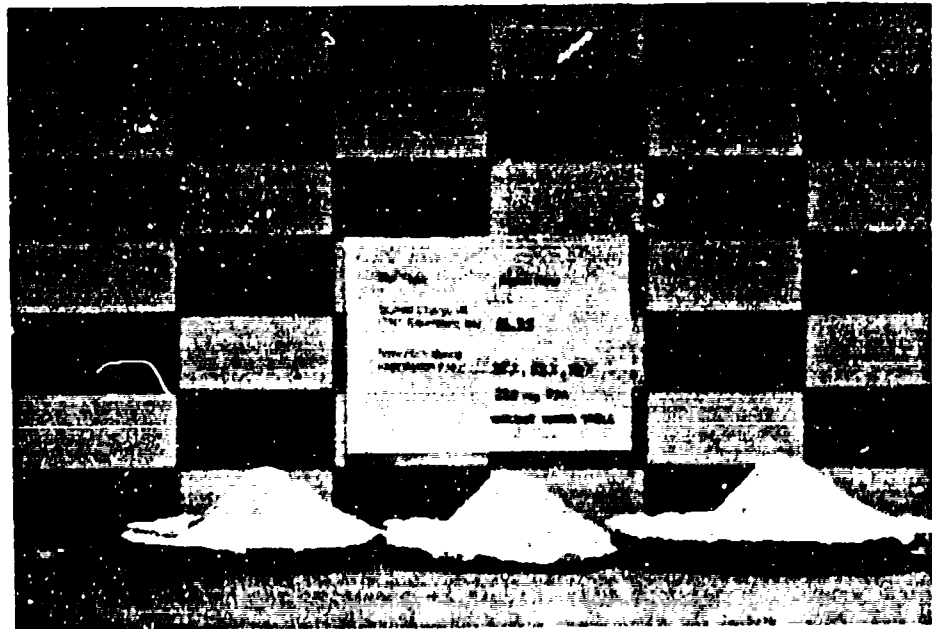
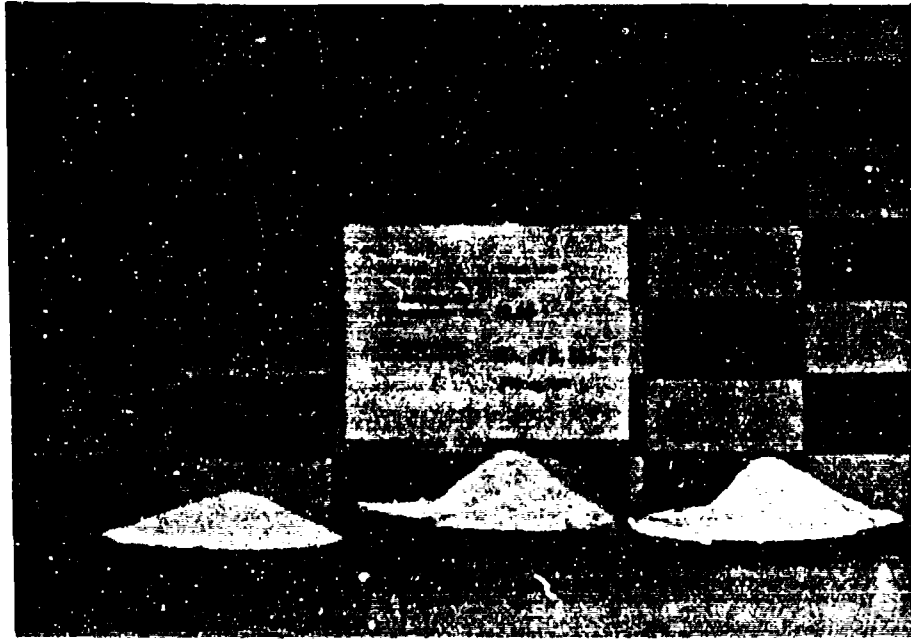
Test Number	Explosive Mass	Burial Depth	Outside Diameter	Inside Diameter	Inside Radius	Depth	Volume
rpm - 1g 20 - 1	0.00066	0.727	4.236	2.775	1.388	0.895	0.01573
179.48 - 1g 20 - 3	0.00066	0.727	4.262	2.647	1.324	0.745	0.01194
rpm - 1g 60 - 2	0.00066	0.727	3.962	2.921	1.461	1.054	0.02150
179.48 - 1g 60 - 4	0.00066	0.727	4.469	2.812	1.406	0.913	0.01641
vibrated - 1g 0 - 5	0.00066	0.727	3.067	1.826	0.913	0.256	0.00380
pluviated - 1g 0 - 6	0.00066	0.727	2.994	1.751	0.876	0.201	0.00152

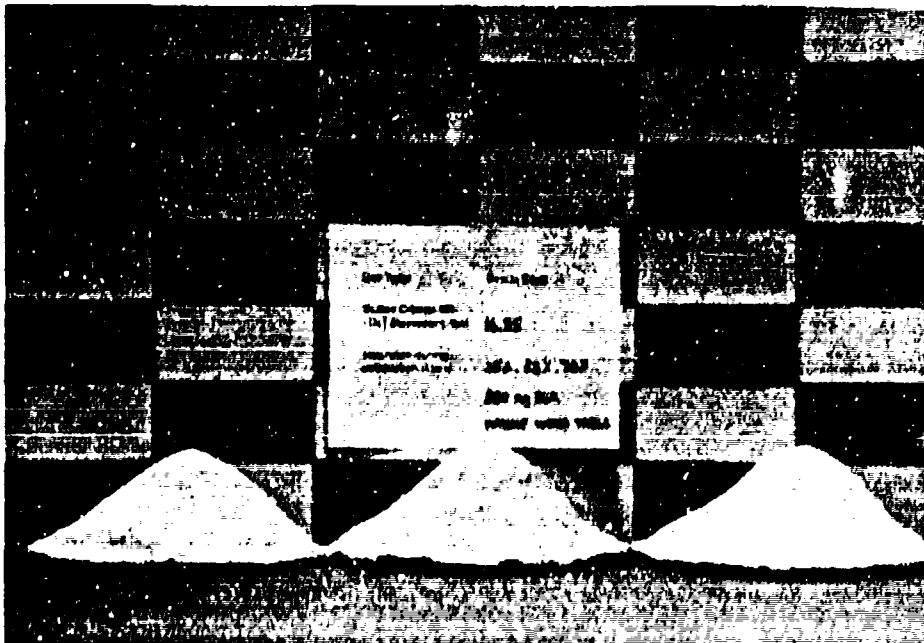
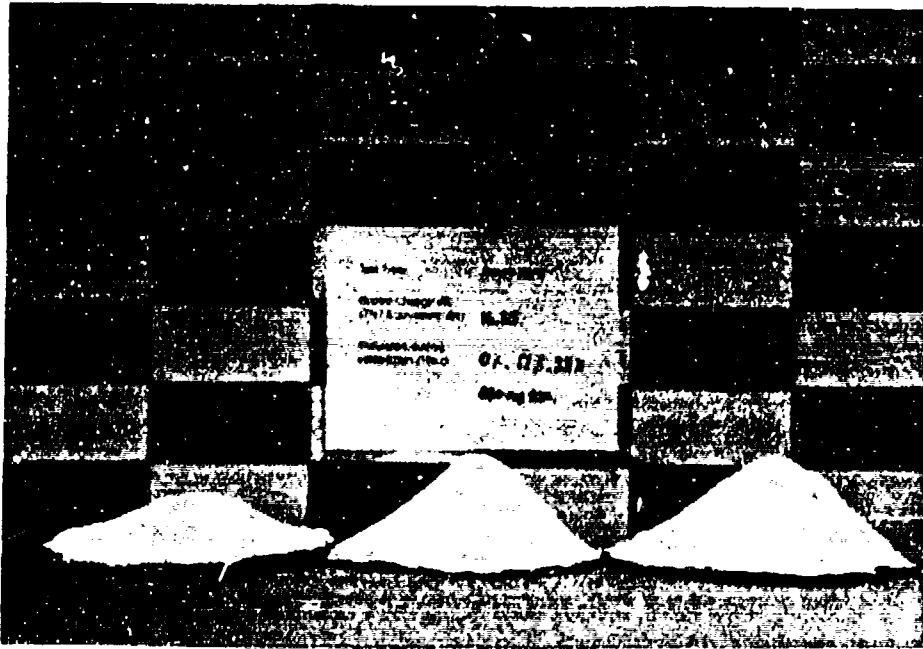
English System Dry Density of 95 lb/ft<sup>3</sup>

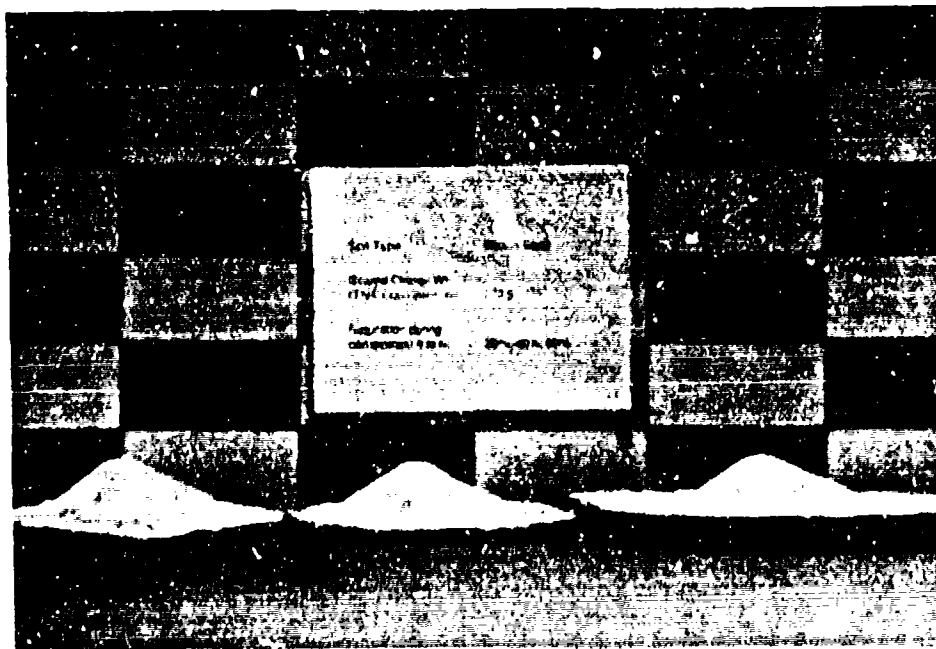
Test Number	Explosive Weight	Burial Depth	Outside Diameter	Inside Diameter	Inside Radius	Depth	Volume
rpm - 1g 20 - 1	0.0014	1.832	10.678	6.996	3.498	2.255	0.42683
179.48 - 1g 20 - 3	0.0014	1.832	10.744	6.674	3.337	1.878	0.32384
rpm - 1g 60 - 2	0.0014	1.832	9.988	7.364	3.682	2.658	0.58337
179.48 - 1g 60 - 4	0.0014	1.832	11.265	7.088	3.544	2.301	0.44527
vibrated - 1g 0 - 5	0.0014	1.832	7.732	4.603	2.301	0.644	0.10311
pluviated - 1g 0 - 6	0.0014	1.832	7.548	4.419	2.209	0.506	0.04132

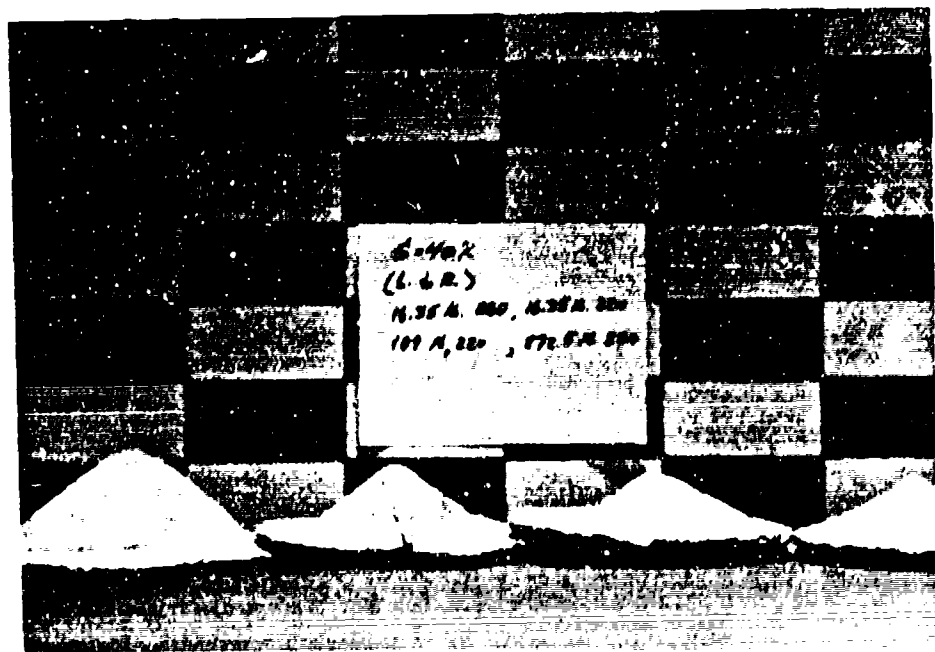
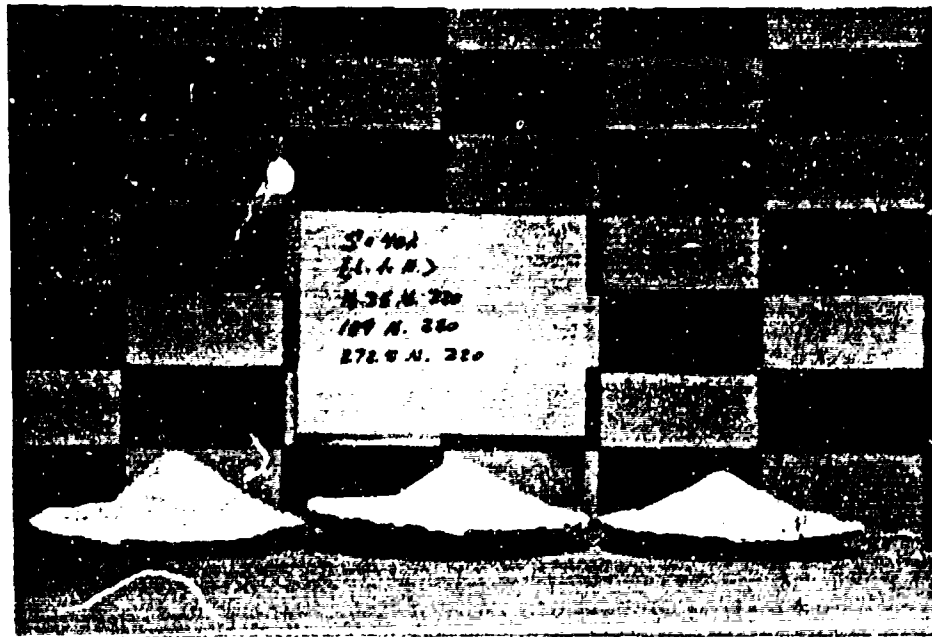
APPENDIX B

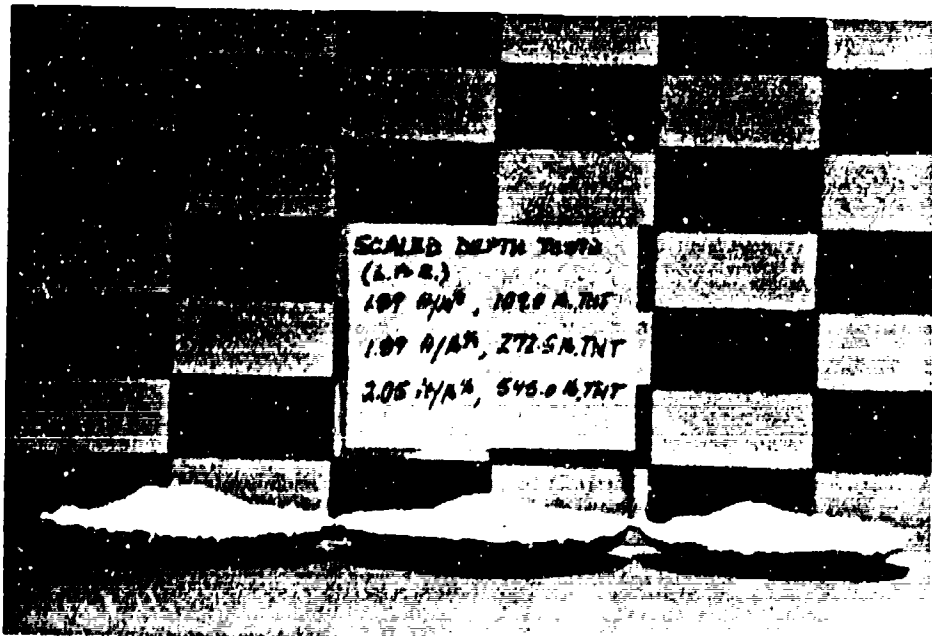
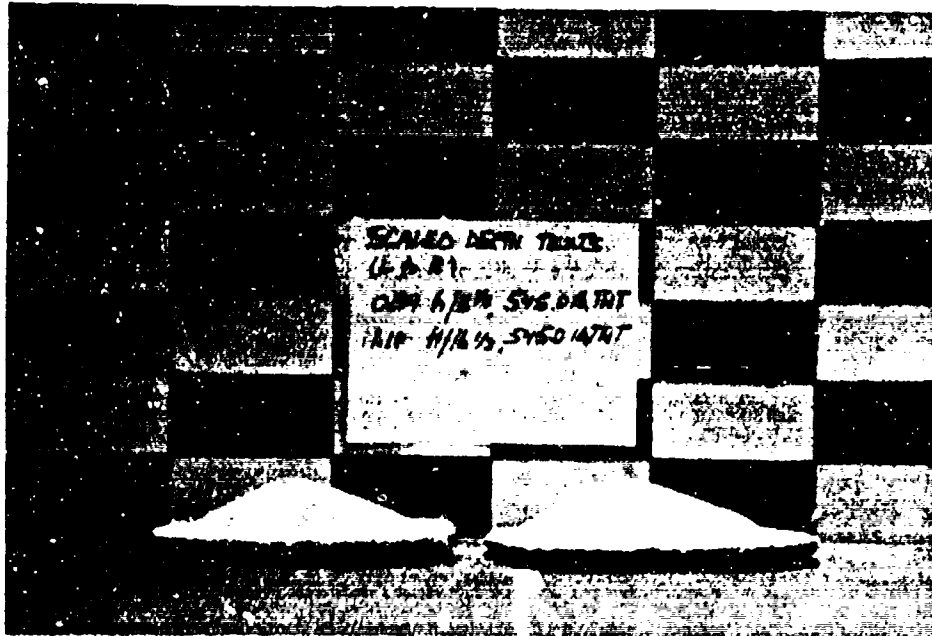
CRATER MOLD PHOTOGRAPHS

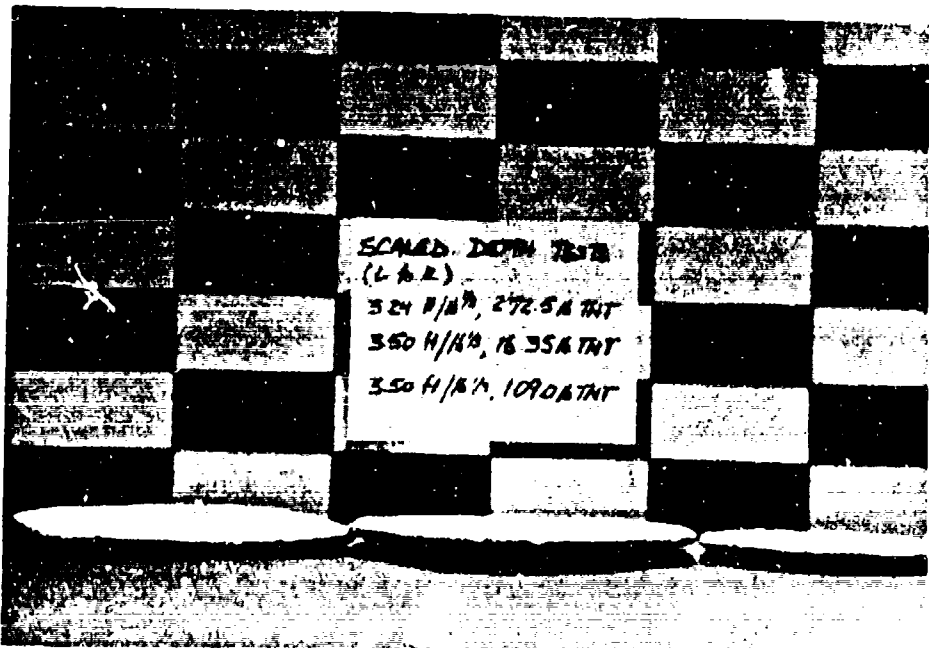
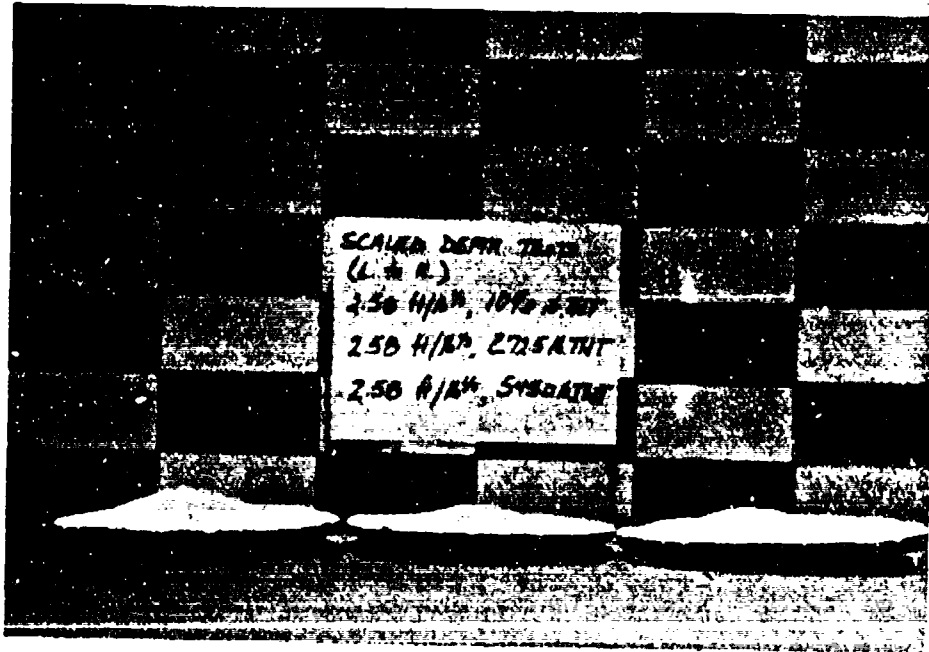


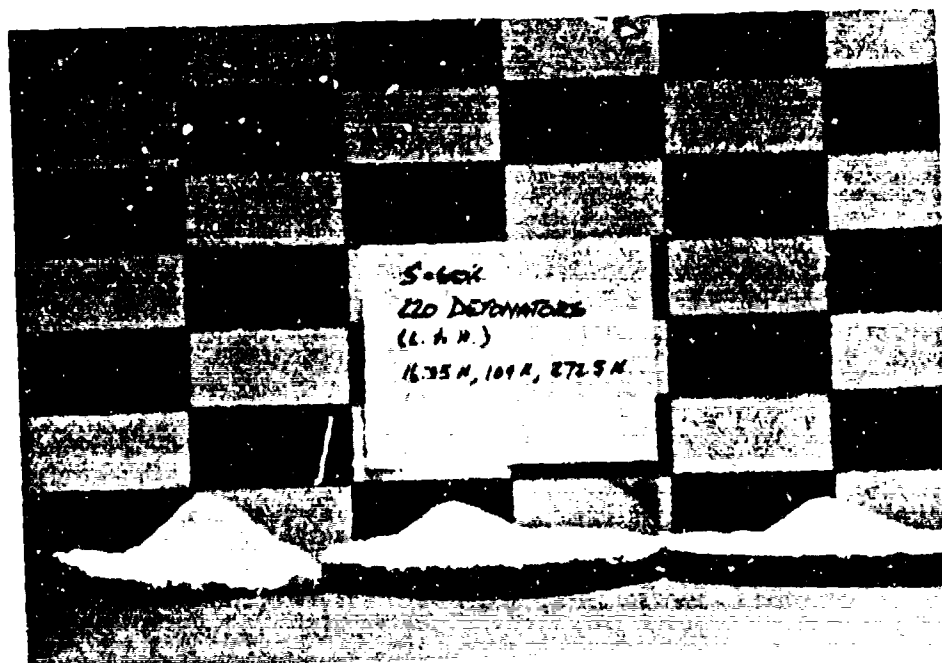
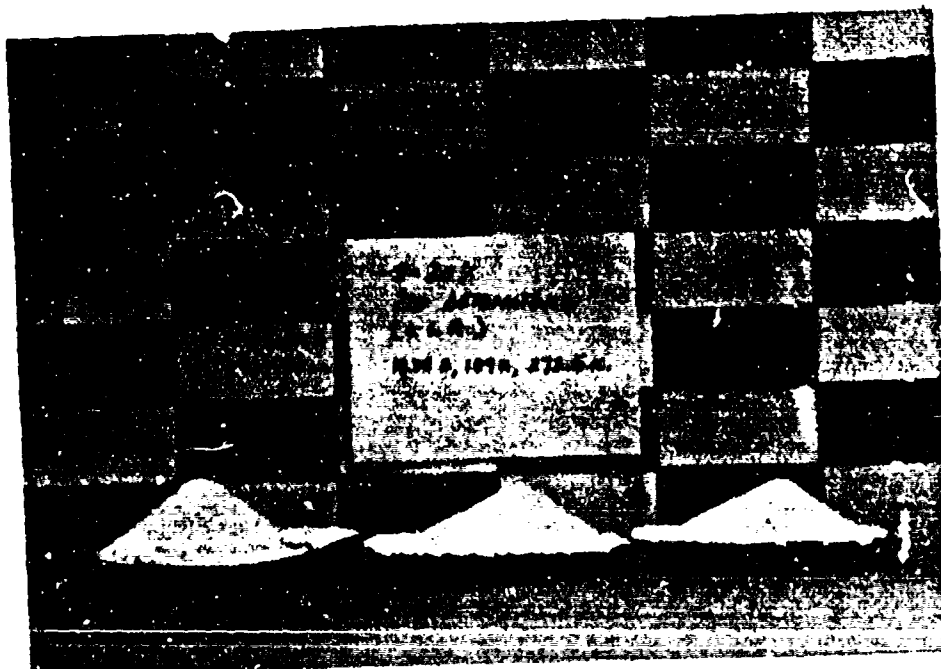




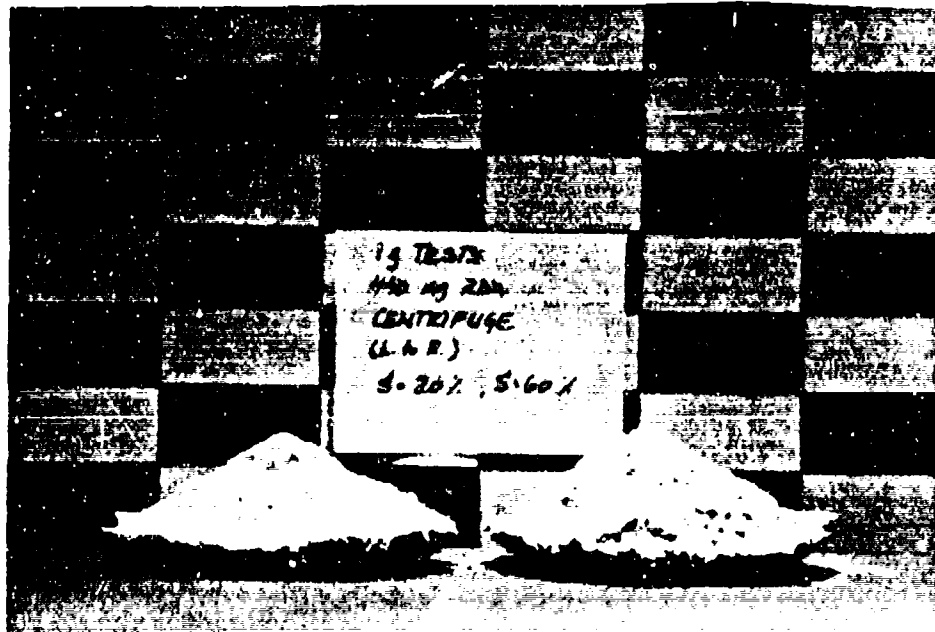


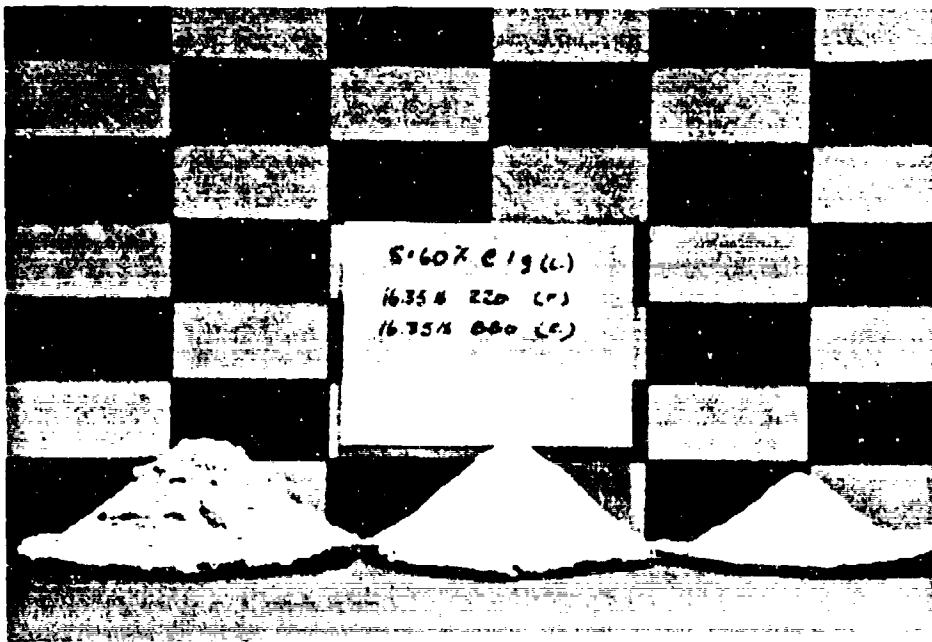
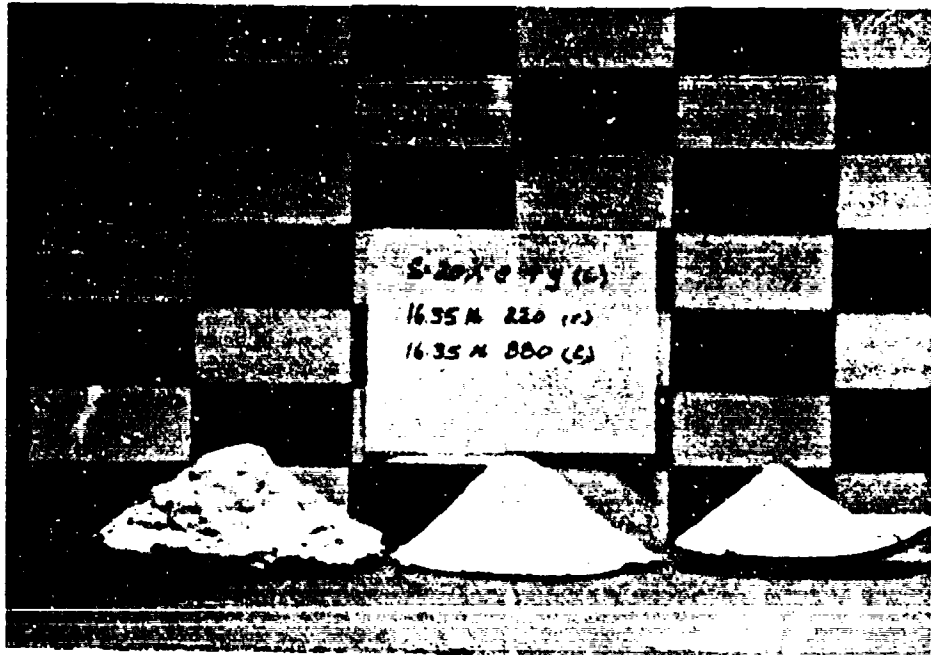


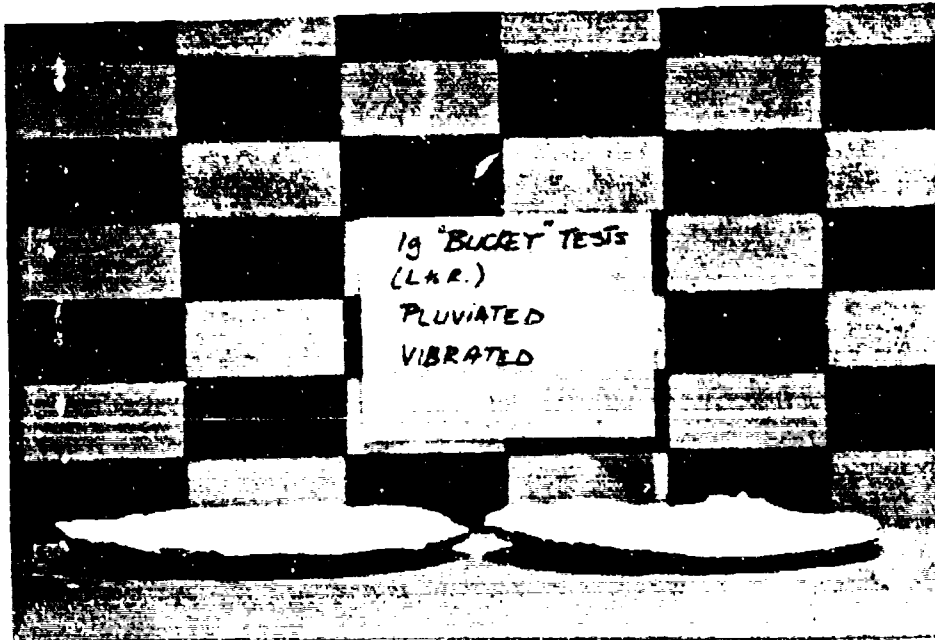


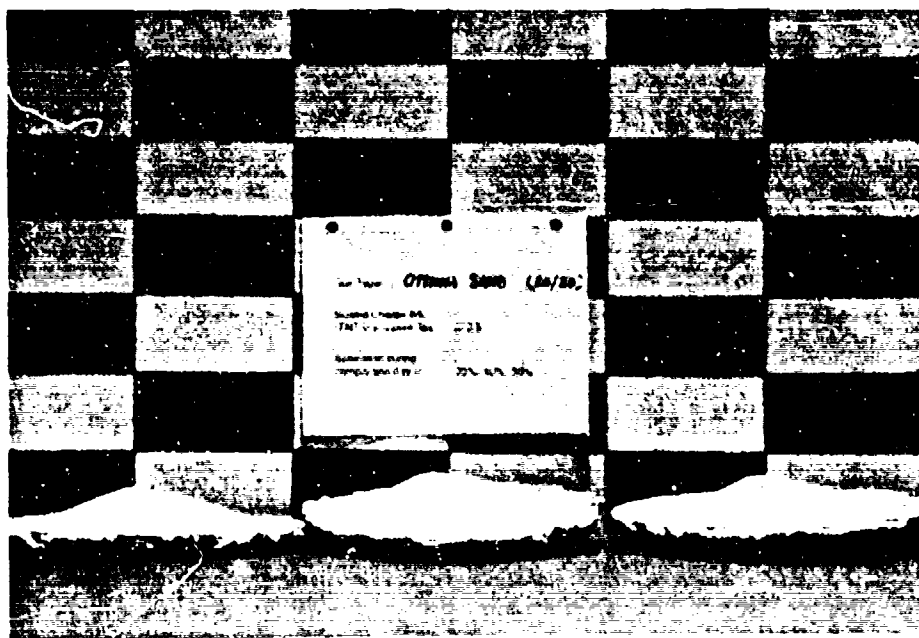
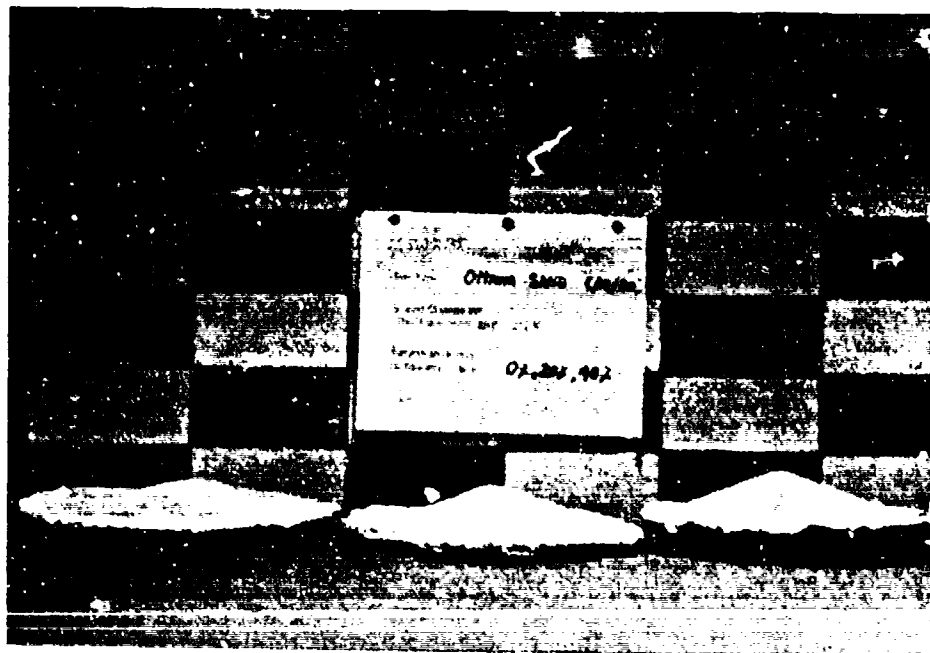












APPENDIX C

MOISTURE CONTENT-SATURATION CONVERSION CURVE

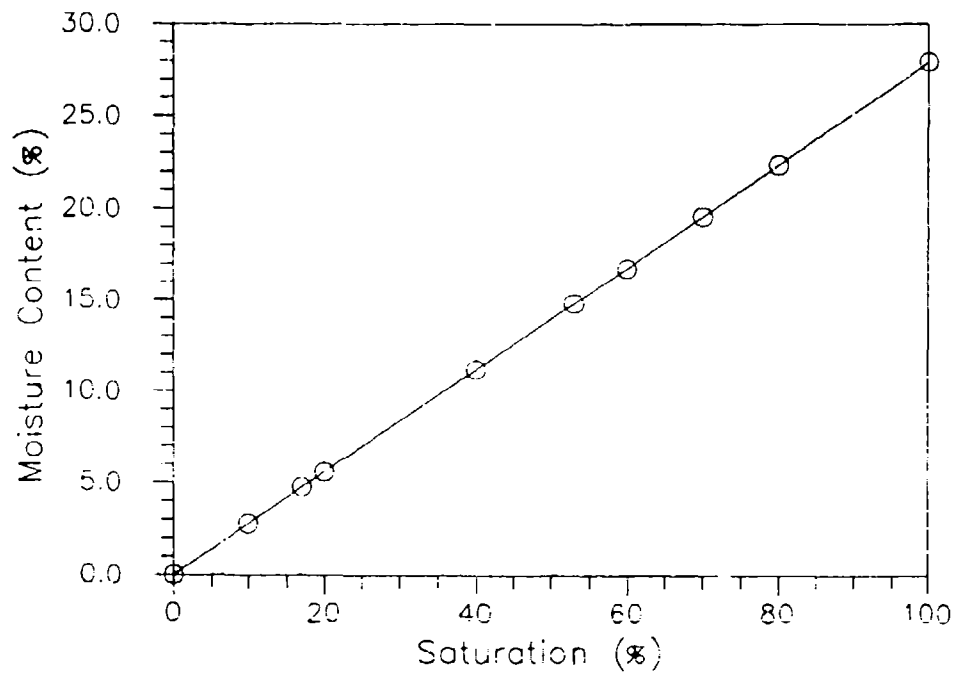


Figure C.1 Moisture Content-Saturation Conversion Curve for Tyndall Beach Sand.

APPENDIX D

MOISTURE CONTENT DATA

NOTES FOR MOISTURE CONTENT DATA.

<u>Test No.</u>	<u>Note</u>
120.63-40-1	Run up to 43-g prior to testing at 26-g (Balance light did not come on). One side of the bucket consistently wetter than the other, 12 o'clock versus 3 o'clock. Moisture contents were 20 and 15 percent which led to saturations of 71 and 54 percent respectively.
191.89-20-4	Run up to 93-g prior to testing at 26-g (Balance light did not come on). There was a high range within the moisture content measurements. Moisture contents ranged from 10 to 18%. Saturations ranged from 38 to 64%.
120.63-60-1	Eliminated one point; A moisture content of 3.31% mid way down the specimen was inconsistent with the moisture content data above and below it. Bottom measurements are actually 2 to 4 inches off the bottom of the centrifuge bucket.
102.08-40-2	More water was measured in the center of the specimen than by the side of the centrifuge bucket. Moisture content: 20.6% vs. 17%; Saturation: 74% vs. 50%. Also, the top and middle points of the 12 o'clock sample location were switched.
191.89-60-3	Moisture content measurements were larger at the center of the specimen than along the side of the centrifuge bucket. The top measurements showed moisture contents of 4.6% at the center and 2.65% at the side which correspond to saturations of 16.4% and 9.5% respectively.
164.71-20-5	Moisture content measurements were larger at the center of the specimen than along the side of the centrifuge bucket. The bottom measurements showed moisture contents of 12.2% at the center and 7.6% at the side which correspond to saturations of 43.8% and 27.4% respectively.

TABLE D.1 SPECIMEN MOISTURE CONTENT DATA  
 TYNDALL BEACH SAND - DRY DENSITY OF 95 lb/ft<sup>3</sup> (1521.7 kg/m<sup>3</sup>)

Test No. (rpm-Sat #)	g	RP-83 Size	S (%)	w (%)	wave (%)			Save (%)			
					top	middle	bottom	top	middle	bottom	
102.08-20-3	18.86	880	17	4.75	2.66	3.55	9.53	12.7	-	-	
102.08-40-2	18.86	880	40	11.18	2.73	4.23	18.92	15.15	67.71	67.71	
102.08-60-2	18.86	880	53	14.81	2.99	4.42	22.09	15.82	79.04	79.04	
102.08-70-1	18.86	880	70	19.56	6.51	21.92	26.72	78.41	95.59	95.59	
(1" water in crater)					Alt. Depths 1-2"			5-6"	7-8"	9-10"	10-12"
102.08-70-3	18.86	880	70	19.56	w	2.67	3.51	5.33	8.75	15.12	18.01
(2" dry sand)					S	9.56	12.57	19.08	31.32	54.10	64.45
120.63-20-2	26.34	220	17	4.75	2.78	3.44	9.93	12.30	-	-	
120.63-40-1	26.34	220	40	11.18	2.47	2.93	17.48	10.48	62.55	62.55	
120.63-60-1	26.34	220	53	14.81	2.71	5.04	22.12	18.03	79.16	79.16	
120.63-70-2	26.34	220	70	19.56	9.73	19.00	24.33	68.01	87.03	87.03	
(0.55" water in crater)					Alt. Depths 1-2"			3-4"	5-6"	7-8"	9-10"
120.63-70-4	26.34	220	70	19.56	w	3.20	5.11	8.02	11.02	18.37	
(2" dry sand)					S	11.45	18.27	28.69	39.41	65.73	
164.71-20-5	49.11	220	20	5.59	2.62	3.66	9.94	13.10	35.58	35.58	
164.71-40-4	49.11	220	40	11.18	w	2.75	3.87	5.21	8.55	11.99	
164.71-60-4	49.11	220	60	16.77	S	9.84	13.84	18.63	30.59	42.90	
					w	3.54	5.58	1.70	15.32	21.24	
					S	12.65	19.96	41.87	54.83	75.98	
191.89-20-4	66.65	220	20	5.59	2.48	2.92	13.70	8.88	10.47	49.03	
191.89-40-3	66.65	220	40	11.18	2.38	2.50	16.20	8.52	8.94	57.96	
191.89-60-3	66.65	220	60	16.77	3.63	21.30	21.94	76.22	78.50	78.50	

Alternate depths measured from the top of the centrifuge bucket.

TABLE D.2 SPECIMEN MOISTURE CONTENT STATISTICS  
 TYNDALL BEACH SAND - DRY DENSITY OF 95 lb/ft<sup>3</sup> (1521.7 kg/m<sup>3</sup>)

Test No. (rpm-Sat #)	g	RP-83 Size	top		middle		bottom		# Points
			mean	std dev	mean	std dev	mean	std dev	
102.08-20-3	18.86	880	9.53	0.56	12.70	0.32	-	-	4
102.08-40-2	18.86	880	9.77	0.65	15.15	1.32	67.71	7.57	4
102.08-60-2	18.86	880	10.71	0.98	15.82	1.39	79.04	3.72	4
102.08-70-1 (1" water in crater)	18.86	880	23.28	1.46	78.41	2.10	95.59	2.90	2
102.08-70-3 (2" dry sand)	18.86	880							5
120.63-20-2	26.34	220	9.93	0.52	12.30	0.13	-	-	4
120.63-40-1	26.34	220	8.83	0.46	10.48	0.67	62.55	10.51	4
120.63-60-1	26.34	220	9.66	0.50	18.03	0.13	79.16	1.70	4
120.63-70-2 (0.55" water in crater)	26.34	220	34.80	15.14	68.01	0.60	87.03	1.30	2
120.63-70-4 (2" dry sand)	26.34	220							5
164.71-20-5	49.11	220	9.36	0.11	13.10	0.19	35.58	11.63	2
164.71-40-4	49.11	220							5
164.71-60-4	49.11	220							5
191.89-20-4	66.65	220	8.88	0.51	10.47	0.12	49.03	11.33	4
191.89-40-3	66.65	220	8.52	0.05	8.94	0.15	57.96	0.41	2
191.89-60-3	66.65	220	12.96	4.93	76.22	10.59	78.50	3.31	2

Regression statistics were not run on test data having five sample depths of 1-2", 3-4", 5-6", 7-8", and 9-10".

APPENDIX E

WATER RETENTION (DESATURATION) CURVE

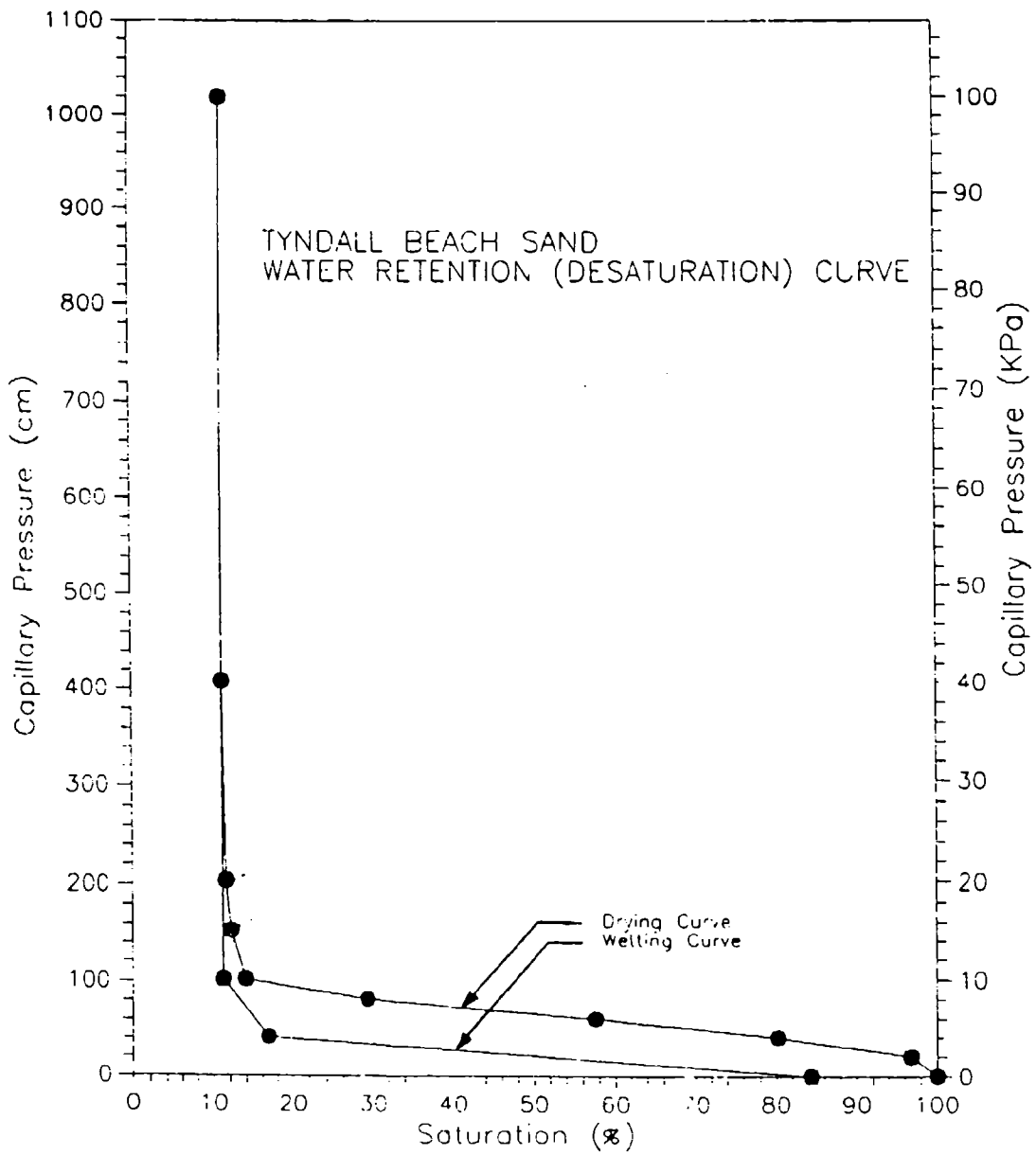


Figure E.1 Water Retention (Desaturation) Curve for Tyndall Beach Sand.

APPENDIX F

ACTUAL DRY DENSITY OF PLUVIATED DRY SPECIMENS

TABLE F.1 ACTUAL DRY DENSITIES FOR THE PLUVIATED SPECIMENS.

Test no.	Measured Weight (lb)	Bucket Weight (lb)	Bucket Volume (ft <sup>3</sup> )	Actual Density (lb/ft <sup>3</sup> )	Actual Density (kg/m <sup>3</sup> )
1	196.13	29.10	1.76	94.96	1521.04
2	197.38	29.75	1.77	94.65	1516.15
3	195.75	29.10	1.76	94.74	1517.63
4	195.50	29.75	1.77	93.59	1499.19
5	195.75	29.10	1.76	94.74	1517.63
6	196.50	29.75	1.77	94.16	1508.23
7	198.63	29.75	1.77	95.36	1527.45
8	195.00	29.10	1.76	94.32	1510.80
9	198.38	29.75	1.77	95.21	1525.19
10	195.50	29.10	1.76	94.60	1515.35
11	195.38	29.10	1.76	94.53	1514.21

Only first eight tests reported.

APPENDIX G

APPARENT CRATER MEASUREMENT PROCEDURE

## APPARENT CRATER MEASUREMENT PROCEDURE

### A. Inside Diameter, and Depth

The apparent crater depth and inside diameter were measured immediately following the test. All measurements were taken using the original ground surface as a frame of reference. A Wang word processing ruler having metric units was placed across the crater and pushed down through the crater lip to the original ground surface. The apparent crater diameter was measured as the distance along the ruler bounded by the intersections of the ruler with the crater wall (Figure G.1). Using a second ruler, the apparent crater depth was measured as the distance from the original ground surface as established by the Wang ruler to the deepest point of the crater (Figure G.1).

Indentations left by the Wang ruler are shown in Figure G.2. The two indentations shown in the North-South direction indicate the distance between the observed center of the apparent crater and the location of the deepest point in the crater. For the crater shown, the diameter measurement in the North-South direction was made at the crater center along the eastern most North-South indentation, while the depth measurement was made along the western most North-South indentation.

The apparent crater depth and diameter measurements were taken in two perpendicular directions. The directions of measurement were those providing the greatest accuracy. No attempt was made to limit crater measurement to specific directions or orientations. Thus, the dimensions reported in Appendix B are an average of the two measurements taken for each crater.

### B. Volume

Previously, crater volume measurements have been made using surveying instrumentation or a profilometer. Both techniques measure distances from an arbitrary datum, set parallel to the original ground surface, to different elevations within the crater and approximate crater volume using concentric disks. The result is a topographic representation of the crater.

Although these techniques are sufficiently accurate, an alternative method of measuring crater volume was designed. A concrete mold was made of the crater which was then used to make a clay replica. When the clay replica was filled with water, the weight of water in grams equaled the crater volume in cubic centimeters (Figure G.3).

Permaplast, artist modeling clay, was used to make the clay replicas (Figure G.4). Saran wrap was used to keep the clay from sticking to the concrete mold. After being molded

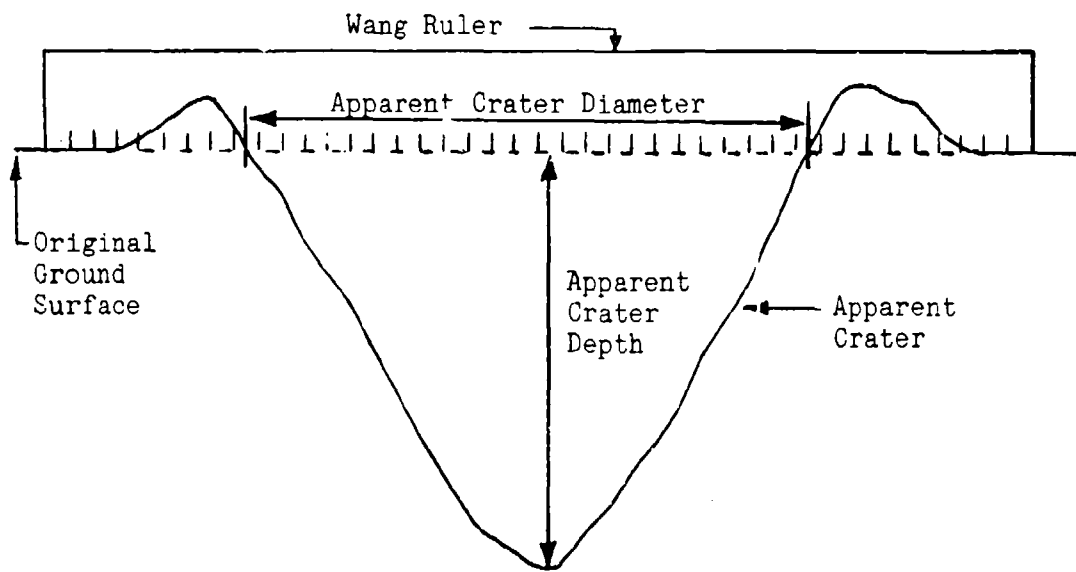


Figure G.1 Apparent Crater Depth and Inside Diameter Measured using the Original Ground Surface as a Frame of Reference.

North

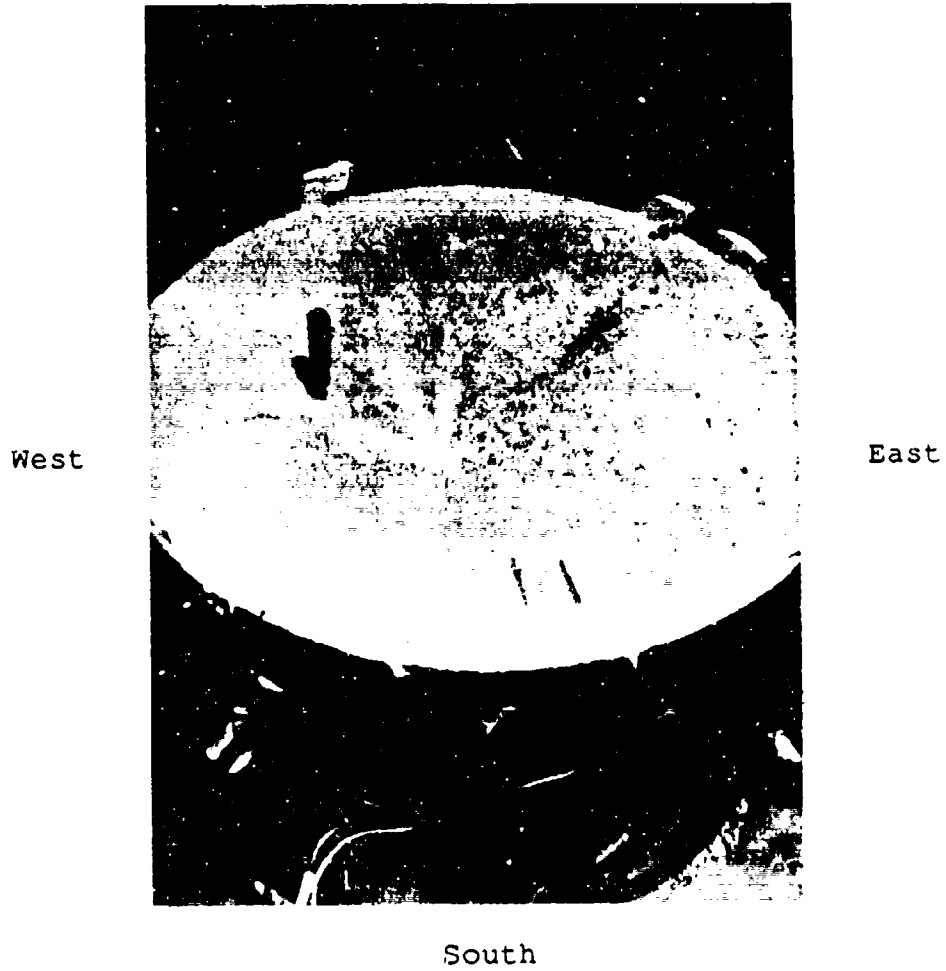


Figure G.2 Indentations Left in the Apparent Crater by the Wang Ruler.



Figure G.3 Clay Replica Filled With Water.  
Apparent Crater Volume Assumed to  
be the Weight of Water  
(1 gram water = 1 cubic centimeter).



Figure G.4 Permoplast Clay Placement Over the  
Concrete Mold to Make the Clay Replica.

to the shape of the apparent crater, the clay was covered with masking tape to prevent the shape of the crater from changing when the concrete mold was removed (Figure G.5).

Rarely could the apparent crater depth and inside diameter be duplicated when the clay replica was filled with water even when the indentations left by the Wang ruler were used as reference points. Either one of the apparent crater dimensions, diameter or depth, could be matched, but matching both dimensions at once often proved impossible. Therefore, two apparent crater volume measurements were made for every concrete mold.

The first measurement was taken at the apparent crater dimension perceived as being the most accurate, and the second measurement was taken at the least accurate dimension. Thus, the second apparent crater volume measurement established an upper or lower bound for the first measurement. The difference between the first and second measurements is the potential error associated with the apparent crater volume. The potential error is assumed to be symmetric so that the difference between the first and second apparent crater volume measurements is interpreted as a 95 percent confidence interval.

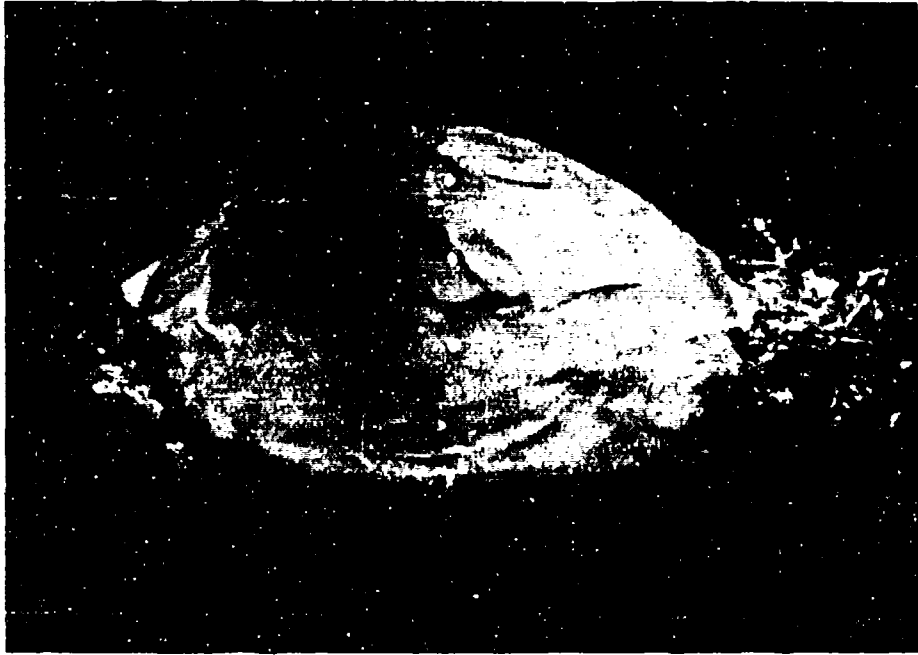


Figure G.5 Clay Replica Covered With Masking Tape to Prevent the Shape of the Crater From Changing When the Concrete Mold was Removed.

APPENDIX H

CRATER MOLD MEASUREMENT PROCEDURE

## CRATER MOLD MEASUREMENT PROCEDURE

1. The crater is leveled such that three reference points all have approximately the same vertical distance,  $d_{ref}$ , from a horizontal datum (Figure H.1). These reference points are located on the edge of the mold beyond the crater lip. They should be close to the original sand surface.

The purpose for leveling the crater mold is to attain the same orientation present when it was removed from the specimen. In this manner, the angle  $\theta$  can be measured.

2. The ruler is leveled to insure the measurements are indeed vertical.

3. Using the arrow scored on the underside of the mold, the ruler is oriented perpendicular to the rotor. This is to place the profile along the East-West direction, the line of Coriolis acceleration.

4. Record the location,  $x$  distance of each of the reference points.

5. Calculate the center of the center of a symmetrical crater by dividing the distance between reference points in half.

6. Measure the vertical distance from the ruler to the crater mold at intervals between the reference points.

7. Calculate the difference,  $x$  distance, between the location of the maximum unskewed crater depth and the location of the maximum skewed crater depth.

8. Determine the angle of rotation,  $\phi$ .

$$\tan\phi = \frac{\text{distance separating maximum crater depths}}{\text{maximum skewed crater depth}}$$

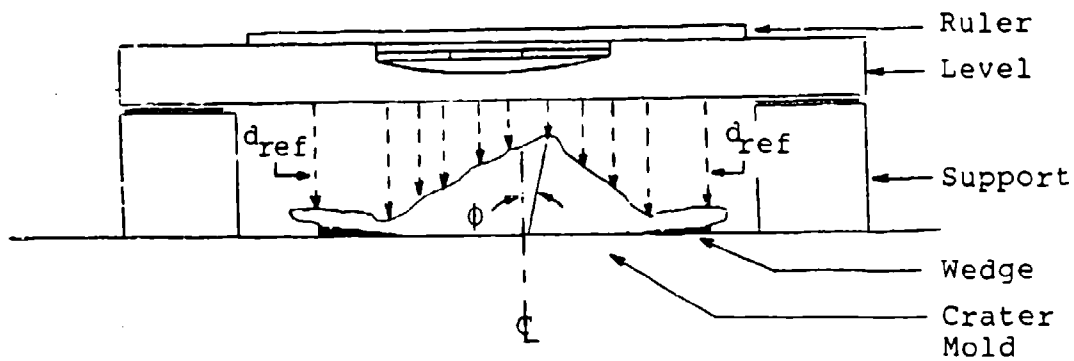


Figure H.1 Diagram Illustrating the Apparent Crater Mold Measurement Procedure.

APPENDIX I

APPARENT CRATER DIMENSIONS VERSUS CHARGE MASS, TNT  
EQUIVALENT (FIGURES 8.1 - 8.6) WITHOUT 1 G DATA

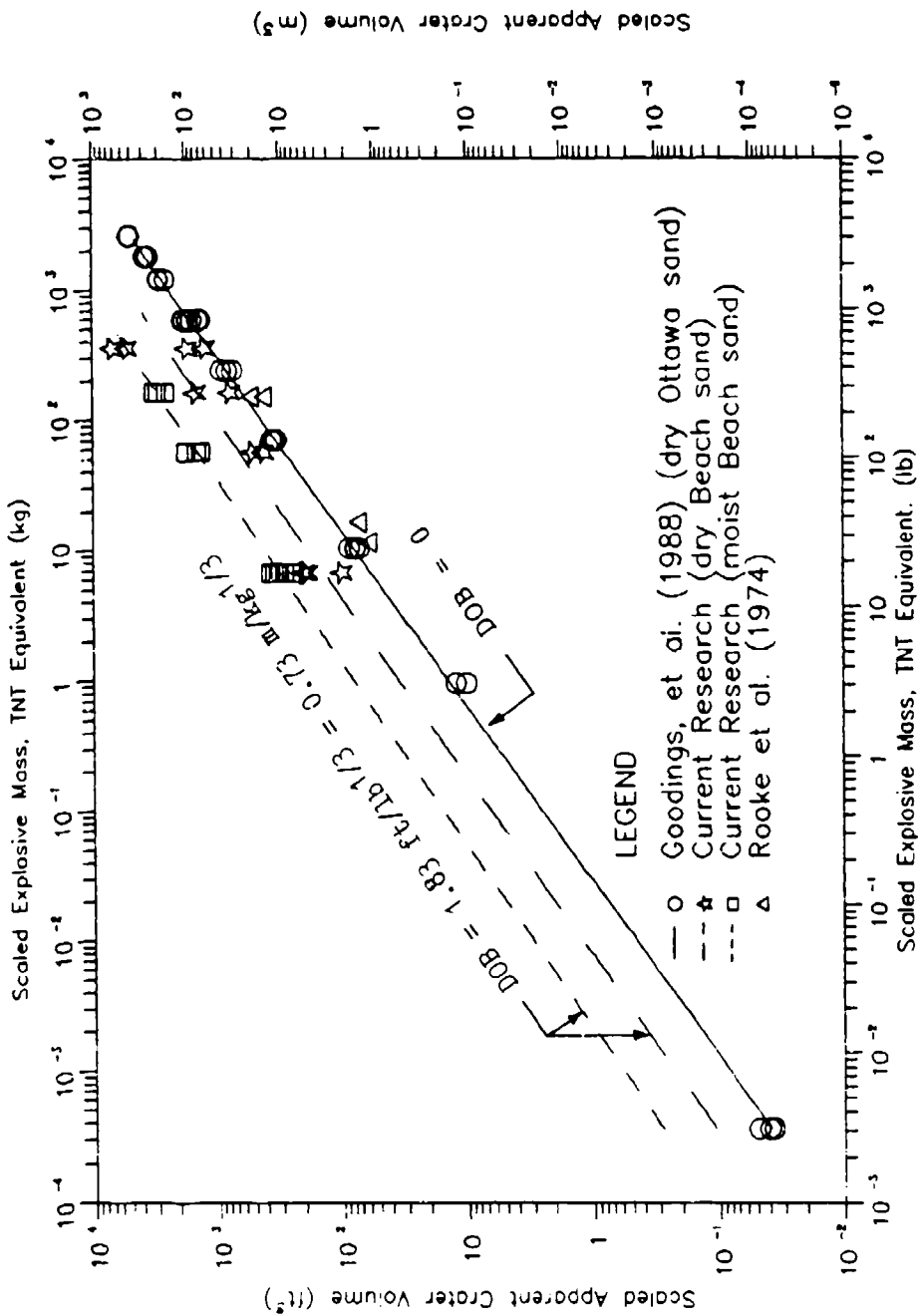


Figure I.1 Scaled Apparent Crater Volume Versus Scaled Explosive Mass, TNT Equivalent. (Conversions:  $0.0283\text{ft}^3 = 1.0\text{m}^3$ ,  $0.454\text{lb} = 1.0\text{kg}$ ).

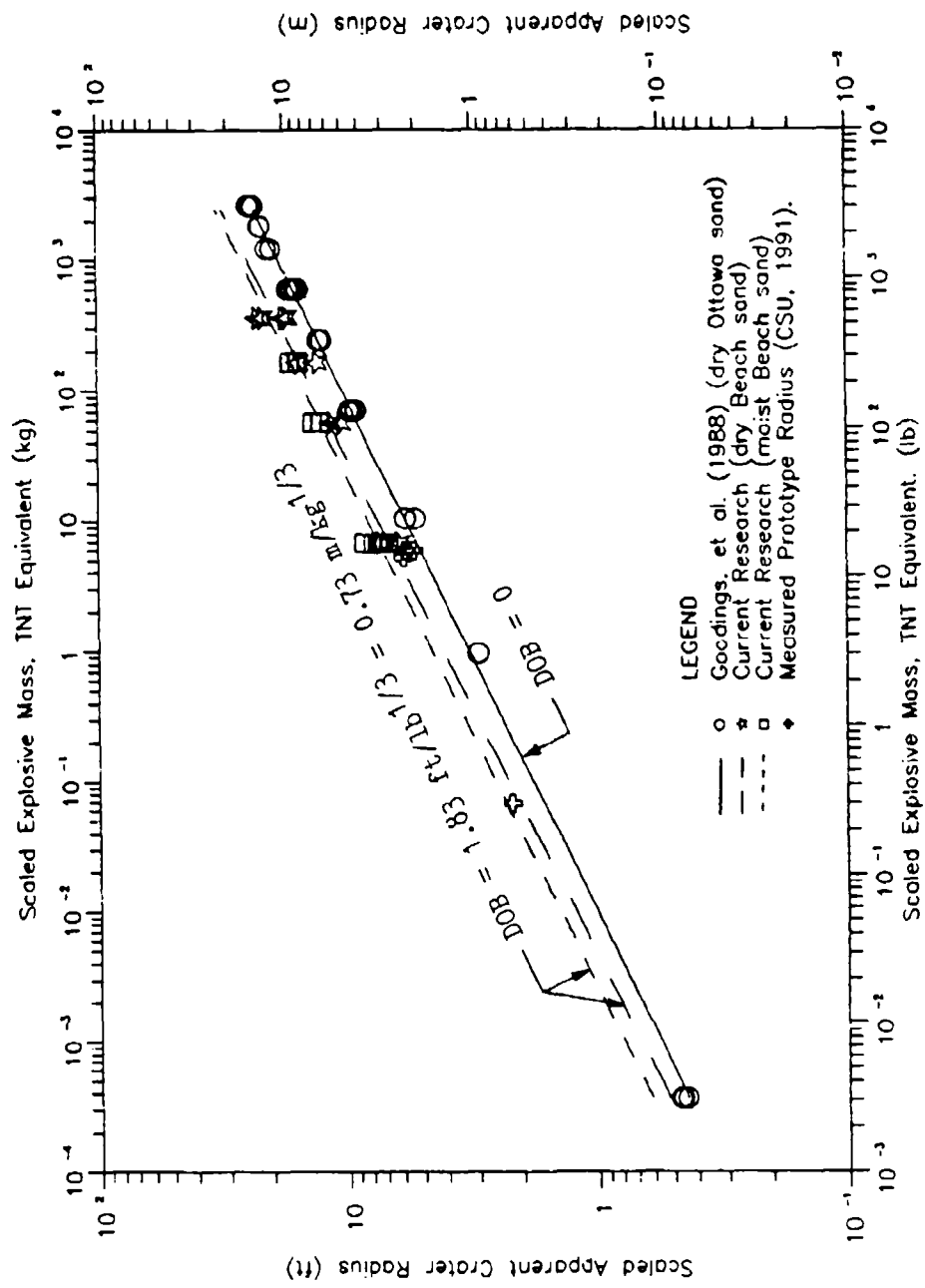


Figure 1.2 Scaled Apparent Crater Radius Versus Scaled Explosive Mass, TNT Equivalent. (Conversions: 0.305ft = 1.0m, 0.454lb = 1.0 kg).

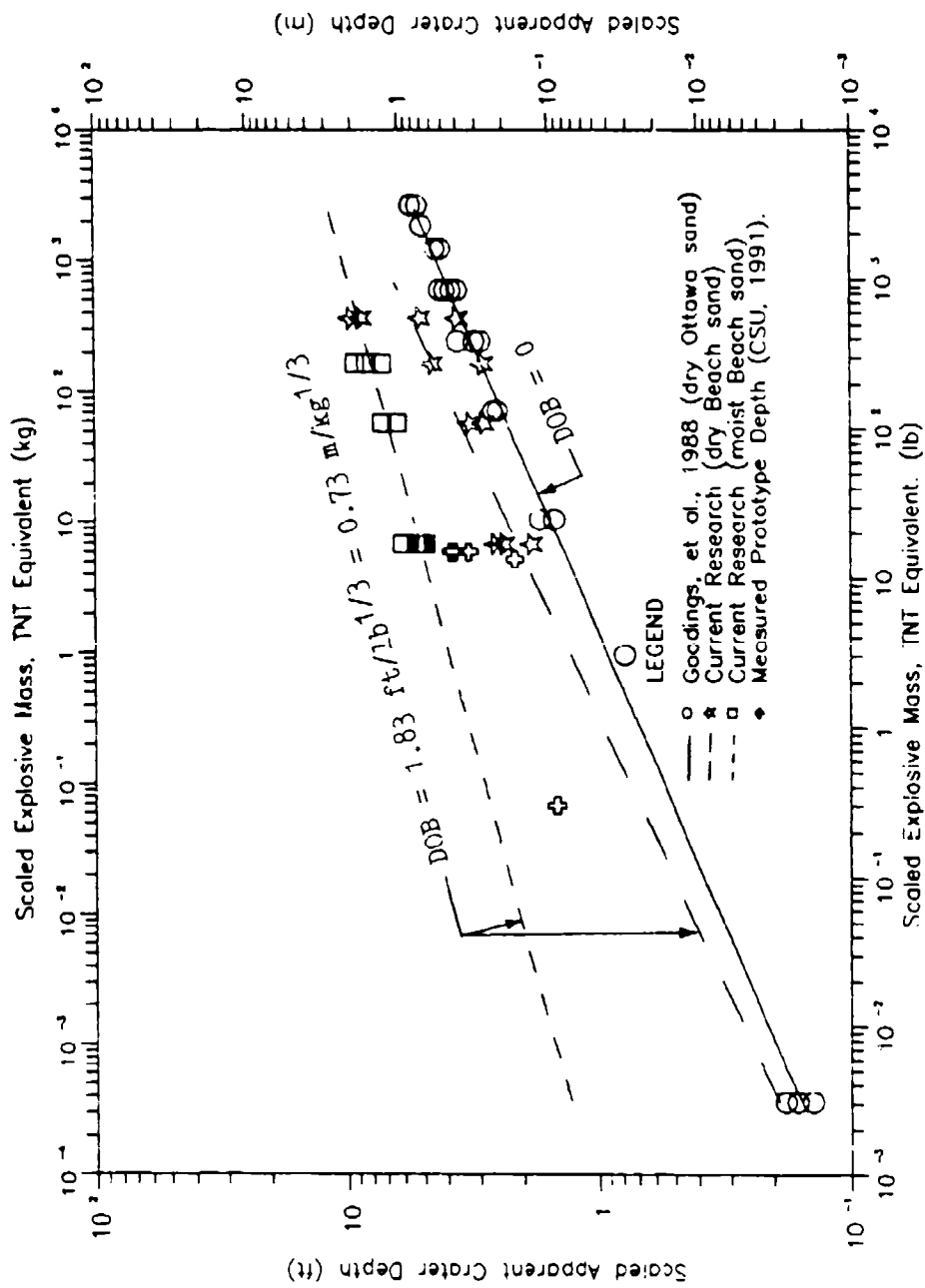


Figure I.3 Scaled Apparent Crater Depth Versus Scaled Explosive Mass, TNT Equivalent, (Conversions:  $0.305\text{ft} = 1.0\text{m}$ ,  $0.454\text{lb} = 1.0\text{kg}$ ).

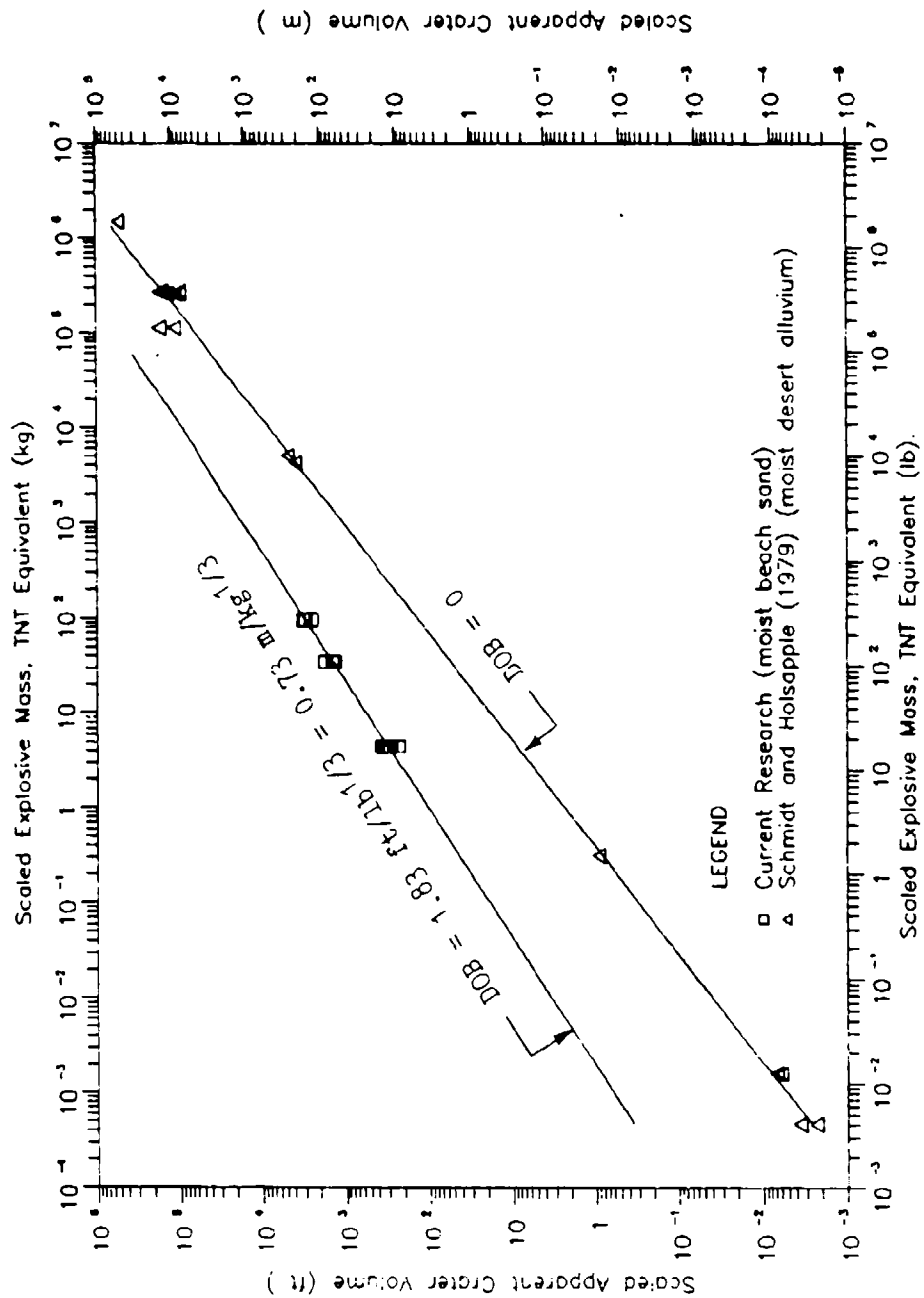


Figure I.4 Scaled Apparent Crater Volume Versus Scaled Explosive Mass, TNT Equivalent. (Conversions:  $0.0283 \text{ ft}^3 = 1.0 \text{ m}^3$ ,  $0.454 \text{ lb} = 1.0 \text{ kg}$ ).

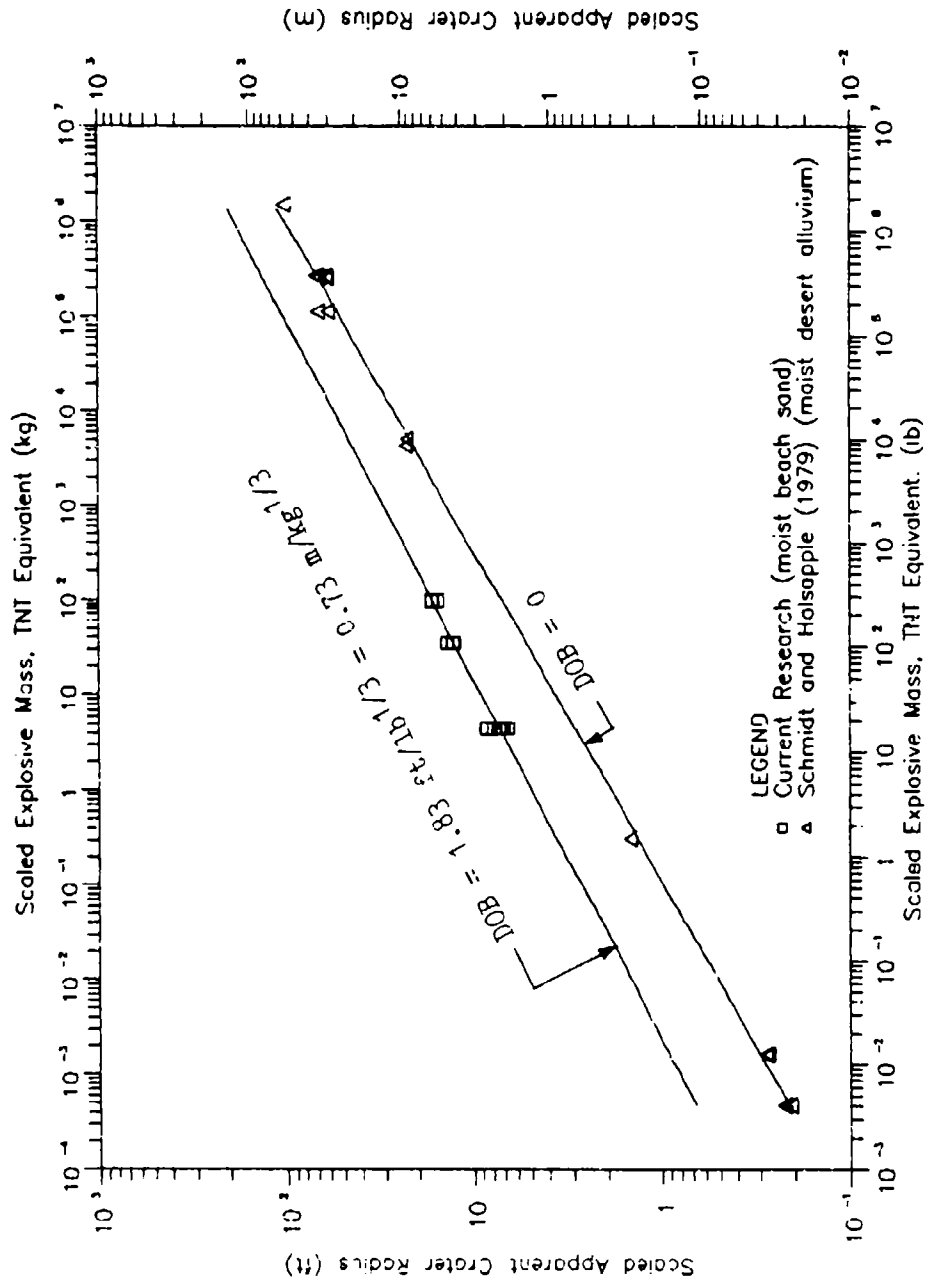


Figure I.5 Scaled Apparent Crater Radius Versus Scaled Explosive Mass, TNT Equivalent. (Conversions: 0.305ft = 1.0m, 0.454lb = 1.0kg).

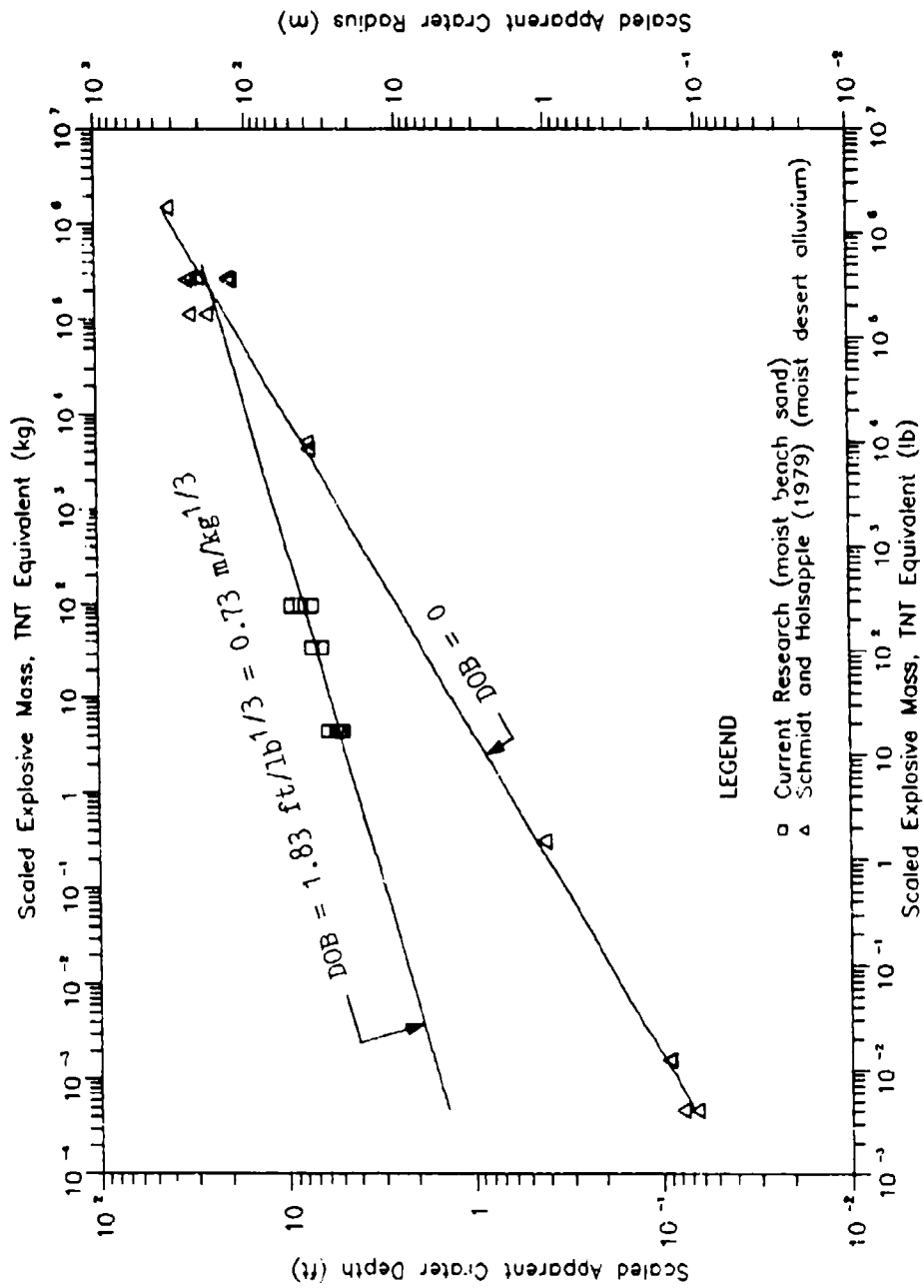


Figure I.6 Scaled Apparent Crater Depth Versus Scaled Explosive Mass, TNT Equivalent. (Conversions: 0.305ft = 1.0 m, 0.454lb = 1.0kg).

TABLE I.1 YIELD EXPONENTS FOR BEST-FIT LINES WITHOUT 1 G DATA.

	Dry (S=0%)	Moist (S=17% to 70%)
Volume	0.831	0.813
Radius	0.297	0.289
Depth	0.279	0.159

TABLE I.2 CORRELATION COEFFICIENTS FOR BEST-FIT LINES WITHOUT 1 G DATA.

	Dry (S=0%)	Moist (S=17% to 70%)
Volume	0.825	0.982
Radius	0.939	0.975
Depth	0.622	0.867

APPENDIX J

TORQUE PRODUCED ON THE CRATER SOIL MASS BY THE CORIOLIS FORCE

## TORQUE PLACED ON THE CRATER SOIL MASS BY THE CORIOLIS FORCE

Figure J.1 shows the torque placed on the ejected soil mass by the Coriolis force ( $F_c$ ). Given a spherical control volume of radius R centered at the detonator, the torque (T) at any point can be expressed as the triple integral:

$$\bar{T} = \iiint \rho \bar{r} \times \bar{F}_c \, d\rho \, d\theta \, \rho \sin\phi \, d\phi \quad (J.1)$$

where  $rR$  is the particle velocity,  $\phi$  is the angle between  $r$  and the  $z$  axis, and  $\theta$  is the angle between the trace of  $r$  in the  $x$ - $y$  plane and the  $x$  axis. The Coriolis force is

$$\bar{F}_c = -m\bar{a}_c \quad (J.2)$$

which can be rewritten as

$$\bar{F}_c = -2m\bar{\omega}(-\hat{k}) \times \bar{V}_p(\rho) \quad (J.3)$$

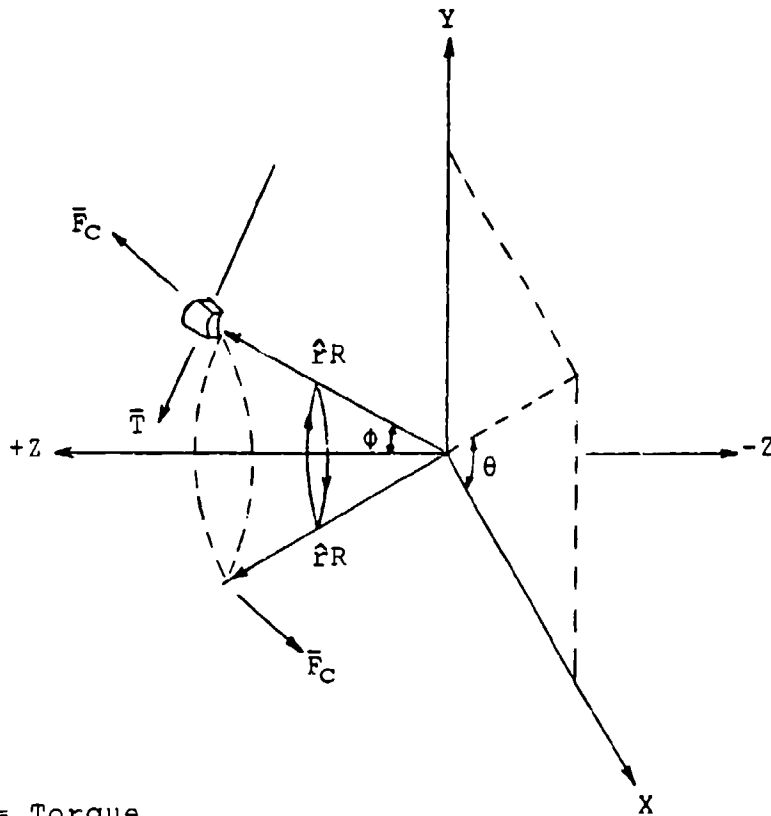
or

$$\bar{F}_c = -2m\bar{\omega}(-\hat{k}) \times \bar{V}_p(\hat{i}\cos\theta\sin\phi + \hat{j}\sin\theta\sin\phi + \hat{k}\cos\phi) \quad (J.4)$$

where  $m$  is a unit mass,  $a_c$  is the Coriolis acceleration,  $\omega$  is the angular velocity,  $V_p$  is the particle velocity, and  $i$ ,  $j$ , and  $k$  are unit vectors in the  $x$ ,  $y$ , and  $z$  directions respectively. Thus, the torque at radius R becomes

$$\begin{aligned} \bar{T} = \int_0^\pi \int_0^{2\pi} 2m\bar{\omega}V_p [\hat{k}(\cos\theta\sin\phi)^2 + \hat{k}(\sin\theta\sin\phi)^2 \\ + (-\hat{i}\cos\phi\cos\theta\sin\phi \\ - \hat{j}\cos\phi\sin\theta\sin\phi)] \, d\theta \, \rho \sin\phi \, d\phi \quad (J.5) \end{aligned}$$

The integration of the torque with respect to  $\theta$  from 0 to  $2\pi$  produces a rotational vector for which the X and Y components cancel out. By definition, the torque is perpendicular to  $V_p$  and  $F_c$ , so the plane containing T and  $V_p$  passes through the origin. For every velocity vector,  $V_p$ , there is a second velocity vector with an equal and opposite X and Y components.



where  $\vec{T}$  = Torque  
 $\vec{F}_C$  = Coriolis Force  
 $R$  = Spherical Control Volume Radius  
 $\hat{f}$  = Unit Velocity Vector

Figure J.1 Torque Placed on the Moving Soil Mass by the Coriolis Force.

APPENDIX K

CENTRIFUGE CRATER ROTATION VERSUS G-LEVEL

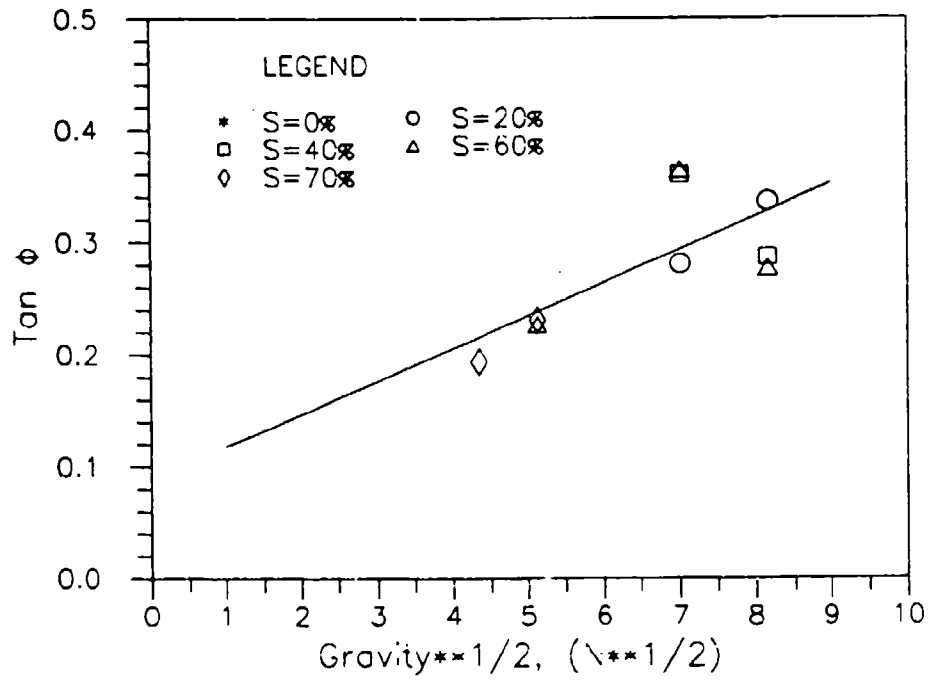


Figure K.1 Centrifuge Crater Rotation Versus G-Level where  $\phi$  is the Angle Shown in Figure H.1.

APPENDIX L

DECLINE OF NORMALIZED APPARENT CRATER DIMENSIONS  
WITH INCREASED G-LEVEL, SCHMIDT AND HOLSAPPLE  
(1980), AND GOODINGS ET AL. (1988).

An analysis of the normalized apparent crater depth data presented in Figure 8.11 was made to determine the separation observed in the data. The results of the analysis are shown in Table L.1. The normalized apparent crater depth decreases with an increase in G-level. Figures L.1 through L.4 add the data reported by Schmidt and Holsapple (1978) and Goodings et al., (1988) to Figures 8.9 and 8.10.

**Table L.1** NORMALIZED APPARENT CRATER DEPTH DATA.

		Apparent Crater Depth/W <sup>1/3</sup>	
Sat	G	W = "880"	W = "220"
(%)		(m/kg <sup>1/3</sup> )	(m/kg <sup>1/3</sup> )
17, 20	19	0.80	
	26		0.81
	49		0.60
	67		0.57
35, 40	19	0.77	
	26		0.94
	49		0.53
	67		0.45
53, 60	19	0.80	
	26		0.75
	49		0.53
	67		0.51
70	19	0.78, 0.78	
	26		0.83, 0.77
	49		
	67		

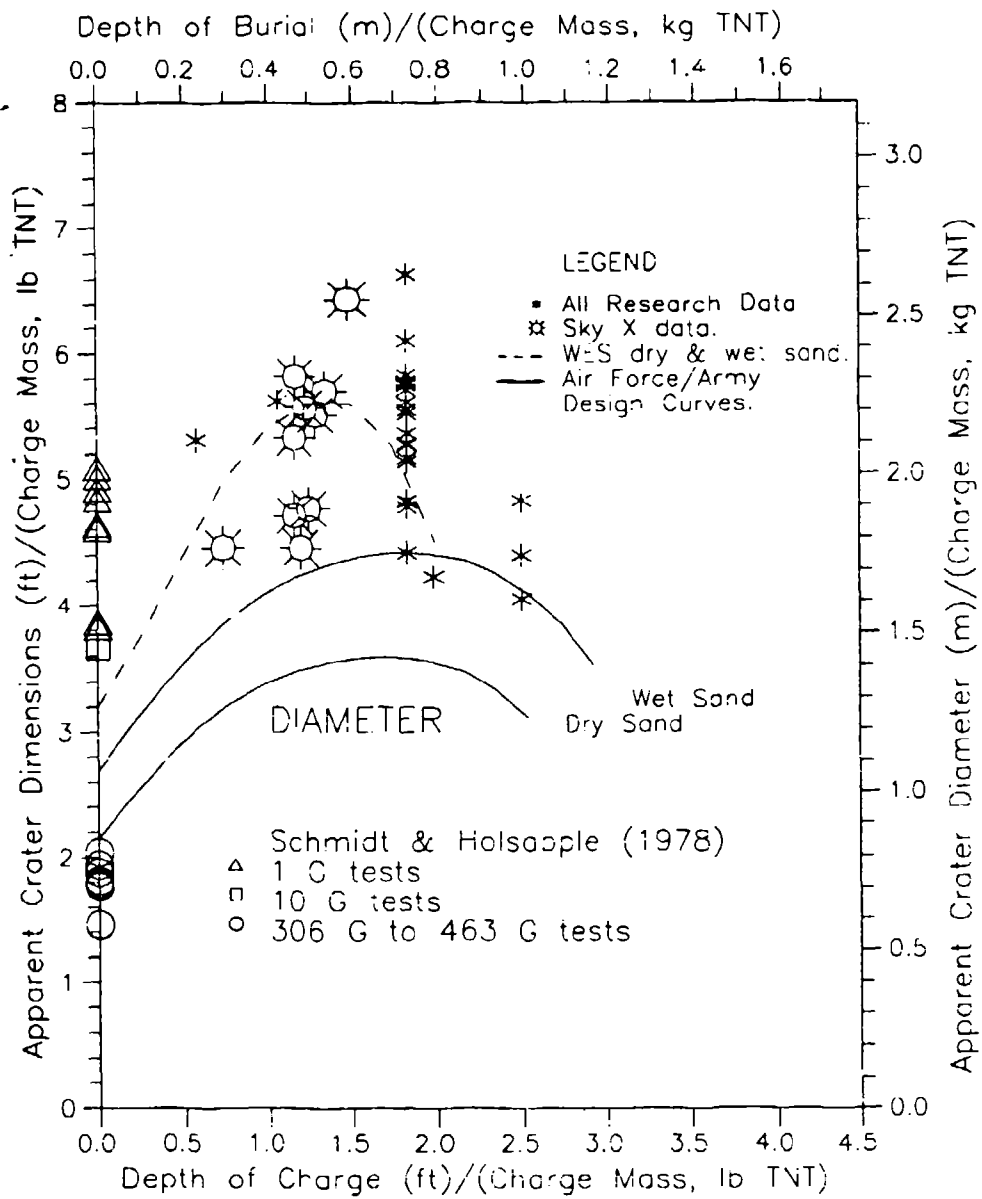


Figure L.1 Normalized Apparent Crater Diameter Data Reported by Schmidt and Holsapple (1978) Plotted in Figure 8.9.

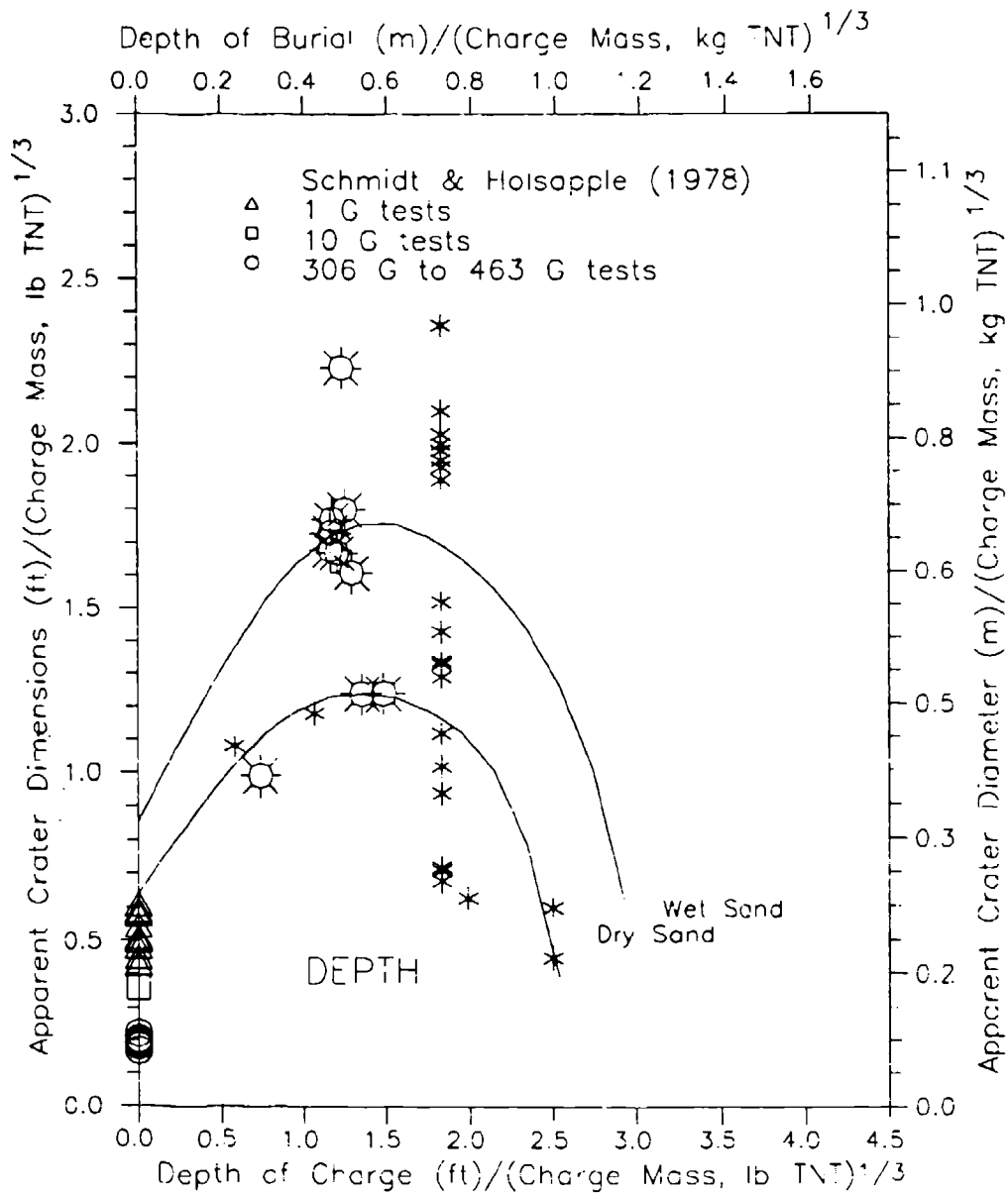


Figure L.2 Normalized Apparent Crater Depth Data Reported by Schmidt and Holsapple (1978) Plotted in Figure 8.10.

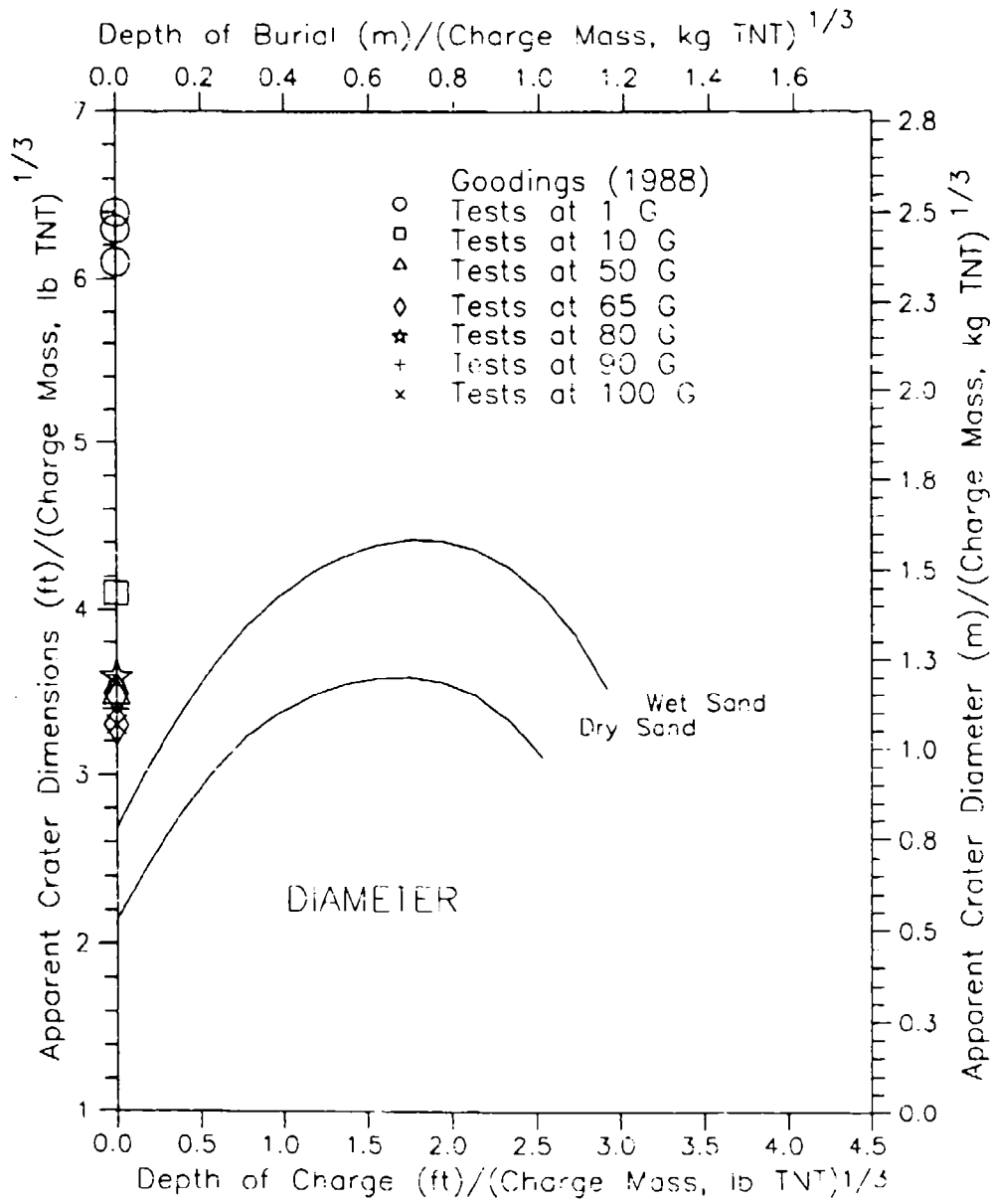


Figure L.3 Normalized Apparent Crater Diameter Data Reported By Goodings et al. (1983) Plotted in Figure 8.9.

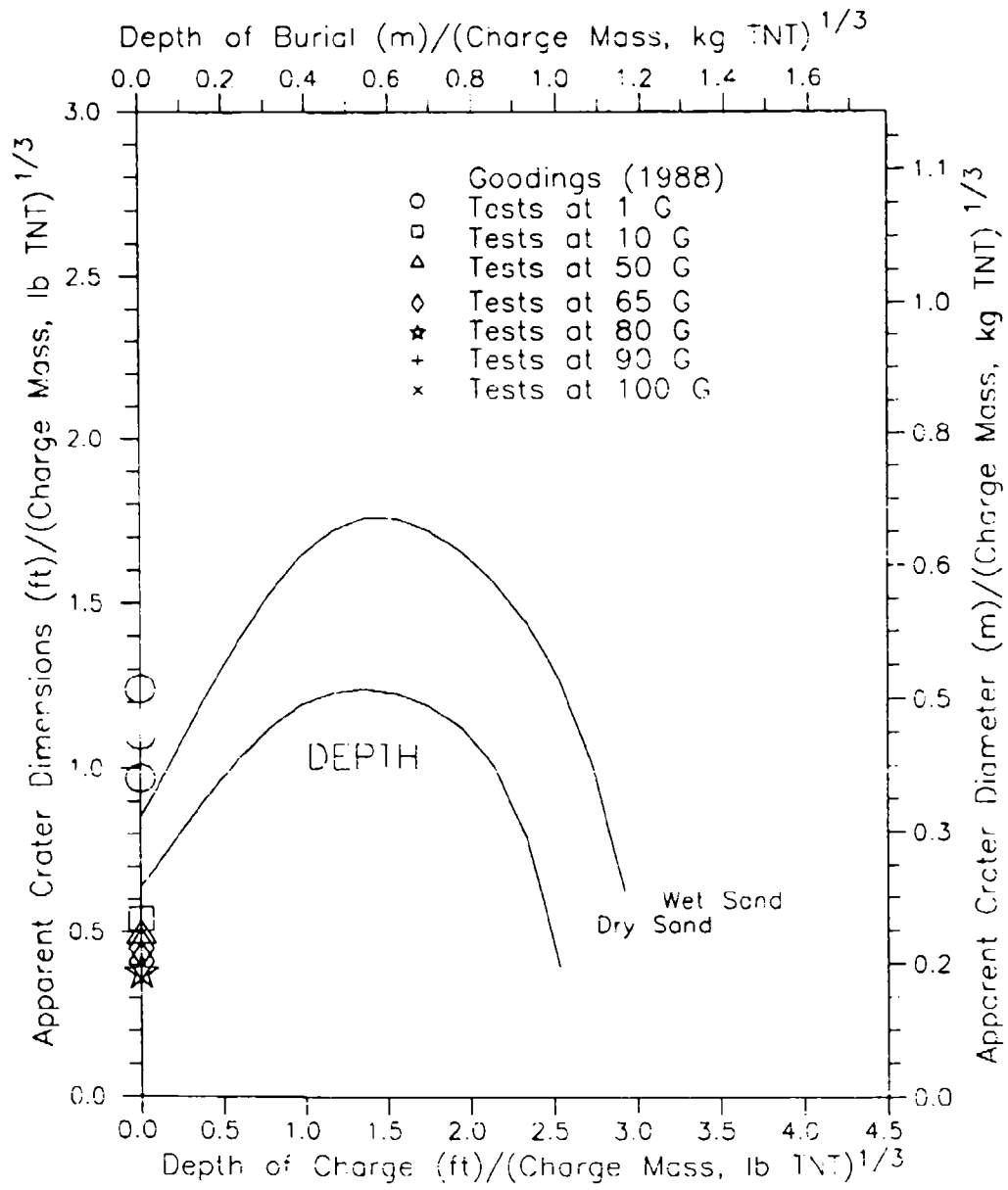


Figure L.4 Normalized Apparent Crater Depth Data  
 Reported by Goodings et al. (1988)  
 Plotted in Figure 8.10.